

# 22<sup>nd</sup> ABAF

BRNO 2021

Advanced Batteries, Accumulators  
and Fuel Cells

INTERNATIONAL CONFERENCE

August 22<sup>nd</sup> - August 25<sup>th</sup> 2021

**Organised by:**

**Department of Electrical and Electronic Technology,**  
Faculty of Electrical Engineering and Communication,  
Brno University of Technology

**Organizing committee:**

Marie Sedlaříková  
Tomáš Kazda

co-sponsored by



**Honourary Scientific Committee:**

- Petr Vanýsek, *Northern Illinois University, DeKalb, Illinois, USA*
- Arnaldo Visintin, *INIFTA, La Plata, Argentina*
- Günter Fafílek, *TU Wien, Vienna, Austria*
- Elena Shembel, *USCTU, Dnipro, Ukraine*
- Vito Di Noto, *University of Padova, Padova, Italy*
- Alexei Kornyshev, *Imperial College, London, UK*
- Boris Markovsky, *Bar-Ilan University, Tel Aviv, Israel*
- Philipp Adelhelm, *Friedrich Schiller University, Jena, Germany*
- Laurence Hardwick, *University of Liverpool, Liverpool, UK*
- Renata Oriňáková, *UPJŠ, Košice, Slovakia*
- Grzegorz Lota, *Poznan University of Technology, Poznan, Poland*
- Mariusz Walkowiak, *Institute of Non-Ferrous Metals, Poznan, Poland*

**Organisation Committee:**

- Marie Sedlaříková, *FEEC BUT, Brno, Czech Republic*
- Tomáš Kazda, *FEEC BUT, Brno, Czech Republic*
- František Klein, *Brno, Czech Republic*
- Vítězslav Novák, *FEEC BUT, Brno, Czech Republic*
- Miroslav Zatloukal, *FEEC BUT, Brno, Czech Republic*
- Jiří Libich, *FEEC BUT, Brno, Czech Republic*
- Josef Máca, *FEEC BUT, Brno, Czech Republic*
- Tomáš Binar, *FEEC BUT, Brno, Czech Republic*
- Jiří Švarc, *University of Defence, Brno, Czech Republic*
- Pavlína Sedlaříková, *Brno, Czech Republic*

**Program Committee:**

- Marie Sedlaříková, *FEEC BUT, Brno, Czech Republic*
- Mariusz Walkowiak, *Institute of Non-Ferrous Metals, Poznan, Poland*
- Arnaldo Visintin, *INIFTA, La Plata, Argentina*
- Petr Vanýsek, *Northern Illinois University, DeKalb, Illinois, USA*
- Günter Fafílek, *TU Wien, Vienna, Austria*
- Boris Markovsky, *Bar-Ilan University, Tel Aviv, Israel*
- Alexei Kornyshev, *Imperial College, London, UK*
- Philipp Adelhelm, *Friedrich Schiller University, Jena, Germany*
- Laurence Hardwick, *University of Liverpool, Liverpool, UK*
- Josef Máca, *FEEC BUT, Brno, Czech Republic*
- Vítězslav Novák, *FEEC BUT, Brno, Czech Republic*
- Petr Bača, *FEEC BUT, Brno, Czech Republic*
- Tomáš Kazda, *FEEC BUT, Brno, Czech Republic*
- Helena Polsterová, *FEEC BUT, Brno, Czech Republic*
- Miroslav Zatloukal, *FEEC BUT, Brno, Czech Republic*
- Kristýna Jandová, *FEEC BUT, Brno, Czech Republic*
- Andrea Fedorková-Straková, *UPJŠ, Košice, Slovakia*
- Jiří Libich, *FEEC BUT, Brno, Czech Republic*
- Tomáš Binar, *FEEC BUT, Brno, Czech Republic*
- Jiří Švarc, *University of Defence, Brno, Czech Republic*

Main sponsor:



**CEZ GROUP**

Other sponsors:



co-sponsored by



We would like to express our thanks to the Brno University of Technology, Faculty of Electrical Engineering and Communication for support and help with organising 22<sup>nd</sup> ABAF conference.



## Contents

### Lithium Batteries and Related Systems

- P. Blažek, P. Guricová, O. Klvač, T. Kazda, A. Břínek, T. Zikmund and J. Kaiser*  
**Multiscale 3D analysis of defects and temporal development of electrode morphology in lithium-ion batteries by X-ray computed tomography** ..... 11
- M. Broszkiewicz*  
**Imidazole-based lithium salt as an additive for lithium-conducting electrolytes** ..... 14
- B. Eschelmüller, K. Froehlich, W. Pessenhofer, H. Besser, W. Pflöging, M. Jahn, F. Pichler*  
**Laser structuring of NMC 811 high energy electrodes in battery production for enhancing the electrochemical performance for xEV energy storage systems** ..... 15
- K. Froehlich, A. Gigl, B. Eschelmüller, M. Jahn*  
**Process standardisation of EU research pilot lines for prototype cell production** ..... 17
- M. Kasprzyk, A. Zalewska, M. Broszkiewicz, J. Tańska, W. Wieczorek*  
**The Study of Lithium PVdF-HFP Electrolytes Based on Non-Crystallizing Solutions** ..... 18
- T. Kazda, V. Gavalierová, J. Tichý*  
**Influence of long-term cycling at low temperature on the performance of Li-ion batteries** ..... 20
- V. Knap, M. Molhanec, A. Gissero, and D.-I. Stroe*  
**Calendar degradation and self-discharge occurring during short- and long-term storage of NMC based Lithium-ion batteries**..... 23
- L. Neidhart, K. Froehlich, M. Jahn, F. Winter*  
**Critical Parameter Evaluation of Thick, Multi-Layer Cathodes in Li-Ion Batteries**..... 24
- K. Rogala, N. Zaremba, M. Broszkiewicz, D. Jamroz, T. Trzeciak, L. Niedzicki*  
**Non-Fluorine Salts for Safer and Less Hazardous Lithium-ion Batteries** ..... 26
- R.D. Apostolova, S.P. Kuksenko*  
**Electrochemical Behavior of SiO<sub>2</sub>-Containing Electrodes in Lithium Battery Systems: Effect of the SiO<sub>2</sub> Production Methods**..... 28
- D. Csik, D. Zalka, K. Saksl, A. Straková, Fedorková, D. Capková*  
**Spinel Structured High Entropy Oxide (CoFeCrNiAl)<sub>3</sub>O<sub>4</sub> as Anode Active Material in Lithium-ion Batteries** ..... 32
- M. Fibek, J. Libich, J. Máca and A. Šimek*  
**Lithium-Titanate as Electrode Material for Aprotic Systems**..... 35
- P. Guricová, O. Čech, T. Kazda*  
**The study of cathode material stability after disassembly of Li-ion cell** ..... 37

<i>W. Kurpiel</i> <b>Research on lithium-iron-phosphate cells (LiFePO<sub>4</sub>) in terms of temperature hazard during operation.....</b>	41
<i>J. Libich, J. Máca, M. Sedlaříkova, A. Šimek, P. Čudek, A. Chekannikov and G. Fafílek</i> <b>Rate Capability Testing of Graphite Electrode Material .....</b>	42
<i>T. V. Lisnycha, Yu. V. Shmatok, N. I. Globa, S. A. Kirillov</i> <b>Surface characteristics of TiO<sub>2</sub> and their effect on specific capacity in lithium and sodium systems .....</b>	44
<i>S. Peterová, I. Veselkova and M. Sedlaříková</i> <b>Comparison of Gel Polymer Electrolytes Containing Lithium and Sodium Salts .....</b>	46
<i>K. Rogala</i> <b>New Ionic Liquid for Lithium-Ion Batteries.....</b>	49
<i>M. Šedina and T. Kazda</i> <b>LIBs with anode subside by silicon and their reaction on pressure.....</b>	50
<i>J. Tańska, M. Kasprzyk, D. Jamroz, T. Trzeciak, and L. Niedzicki</i> <b>Solid-State Electrolytes Based on New Polymer DAIKIN® Fluoropolymer for Li-ion Batteries .....</b>	53
<i>P. Maule, J. Vanek and K. Jandova</i> <b>Measuring the electrical capacity of lithium batteries and implementing the values in the warranty conditions of BEV and PHEV battery manufacturers.....</b>	54
<i>D. Zalka, D. Csík, A. Straková Fedorková, K. Saks</i> <b>A new high entropy sulfide material for lithium ion battery anodes.....</b>	57
<i>A. Zsigmond and J. Libich</i> <b>The Effect of Electrode Binders To Electrochemical Properties Of Negative Electrode Materials.....</b>	59
<b>Supercapacitors</b>	
<i>R. Holze</i> <b>Self-discharge of supercapacitors - A new look at a persistent problem.....</b>	61
<i>G. Lota, S. Znanięcki, K. Szwabińska, J. Wojciechowski, A. Skrzypeczak, K. Lota</i> <b>Long-term Performance of Electrochemical Capacitors .....</b>	63
<i>Haojie Fei, N. Kazantseva, M. Jurča, P. Sába</i> <b>Carbon coating on Nb<sub>2</sub>O<sub>5</sub> for high-rate anode for Li-ion capacitors.....</b>	65
<b>Fuel Cells</b>	
<i>M. O. Danilov, G. I. Dovbeshko, I. A. Rusetskyi, V. N. Byckov, O. P. Gnatyuk, S. S. Fomanyuk, G.Ya. Kolbasov</i> <b>Synthesis and Application of Graphite-Like Carbon Nitride as an Electrode Material for the Oxygen Electrode of a Fuel Cell.....</b>	67

*M. Paidar, A. Giurg, F. Zenith*  
**Potential of hydrogen powered trains in Czech Republic**..... 70

*M. Carda, N. Adamová, D. Budáč, M. Paidar, K. Bouzek*  
**Preparation and properties of YSZ ceramic electrolyte for solid oxide cells**..... 72

## **Aqueous Batteries**

*G. Abbas, F. J. Sonia, Z. A. Zafar, P. Jiříček, M. Bouša, M. Kalbáč, J. Červenka, O. Frank*  
**Electrochemical intercalation of anion into graphite using concentrated aqueous electrolyte** .... 74

*P. Mazúr, M. Mikešová, J. Kvičala, Z. Burešová, M. Klikar, F. Bureš, J. Akrman, L. Kubáč*  
**Pyridinium-based anolytes for redox flow battery** ..... 75

*J. Mrlík, P. Mazúr, J. Pociďič, J. Vrána, J. Charvát, M. Marek, J. Kosek*  
**Study of deactivation of vanadium redox flow battery negative graphite felt electrode in single electrolyte setup** ..... 76

*P. Vanýsek*  
**Visualizing Impedance Spectroscopy Response for Interpretation of Collected Data**..... 77

*A. I. Volkov, A. O. Efremova, E. G. Tolstopyatova, and V. V. Kondratiev*  
**Electrochemically Deposited Binder-Free MnO<sub>2</sub> Cathode for Aqueous Zinc-Ion Batteries** ..... 80

*L. Chladil and H. Hálová*  
**Study of Negative Electrode for Lead-acid Batteries Using Operando Confocal Laser Microscopy** ..... 83

*M. A. Kamenskii, S. N. Eliseeva, V. V. Kondratiev*  
**The Electrochemical Performance of  $\delta$ -MnO<sub>2</sub> Cathode Material for Aqueous Zinc-Ion Batteries: the Role of Current Collector** ..... 86

*P. Kędzior, W. Rzeszutek, J. Wojciechowski, G. Lota*  
**Ionic liquids as additive modifying electrolyte of lead-acid battery** ..... 89

*P. Křivík, P. Bača, J. Kazelle*  
**Impedance Measurements of AGM Solar Battery for RAPS Systems**..... 91

*R. Płowens, M. Baraniak, M. Bajsert, G. Lota*  
**Carbon additives effect on lead-acid battery properties**..... 95

*J. Smejkal and L. Chladil*  
**Study of Surface Processes Taking Place on the Surface of the Negative Electrode of Lead-acid Batteries Using XRD** ..... 98

*J. Zimáková, P. Bača, M. Langer, T. Binar*  
**Monitoring The Influence Of The Temperature On The Properties Of Lead-acid Battery** ..... 101

## **New Systems of Batteries**

*J. Bitenc, A. Vižintin, K. Pirnat, R. Dominko*  
**Organic Multivalent Batteries**..... 105

<i>L. Kavan, M. Vinarčíková, M. Zlámalová and M. Zúkalová</i> <b>Titania Containing Cathodes for Lithium-Sulfur Batteries: Case Studies by Electrochemical Impedance Spectroscopy</b> .....	106
<i>T. Syrový, J. Černý, T. Kazda, L. Kubáč, L. Syrová</i> <b>Printed electrode for sodium ion batteries based on organic compounds</b> .....	107
<i>Z. A. Zafar, K. Knizek, G. Abbas, M. Silhavik, and J. Cervenka</i> <b>Perchlorate Based "Water-in-Salt" Electrolyte for Beyond Li-ion Electrochemical Energy Storage Systems</b> .....	111
<i>M. Zúkalová, M. Vinarčíková and L. Kavan</i> <b>Influence of carbonaceous and inorganic additives on electrochemical performance of the sulfur-composite cathode for Li-sulfur batteries</b> .....	112
<i>D. Capková, T. Kazda, J. Macko, O. Petruš, A. Baskevich, E. Shembel, A. Straková Fedorková</i> <b>Pyrite as a Low-Cost Additive in Sulfur Cathode Material for Stable Cycle Performance</b> .....	113
<i>O. Čech, T. Kazda, L. Chladil, D. Kusmič, G. Fafílek, P. Čudek, M. Sedlaříková</i> <b>Amorphous Sulfur Copolymer for Li-S Batteries Prepared By Inverse Vulcanization</b> .....	116
<i>N. I. Globa, Yu. V. Shmatok, V. A. Sirosh, S. A. Kirillov</i> <b>Ion-exchange reaction in Li-Na systems as an effective method for the synthesis of sodium-ion battery electrode materials</b> .....	119
<i>K. Jaššo, T. Kazda, P. Čudek, and D. Capková</i> <b>Determining the Optimal Height of The Active Layer for the Positive Electrode of Lithium-Sulfur Batteries</b> .....	122
<i>T. Kutsch, M. Gehring, H. Tempel, H. Kungl, R.-A. Eichel</i> <b>Influence of carbonization temperature on morphology and oxygen reduction activity of electrospun Ni/NiO-decorated carbon fibre mats as self-standing cathodes for metal-air batteries</b> .....	125
<i>J. Maca, J. Libich, T. Kazda and K. Jasso</i> <b>Deposited Layers as Negative Electrodes</b> .....	127
<i>Marjan Motiei, Haojie Fei, Elif Vargun, Constantin Bubulinca, Natalia Kazantseva, Qilin Cheng, Gengchao Wang, Hua Bao, Petr Saha</i> <b>Hollow structure of MnO<sub>2</sub> wrapped sulfur microsphere to suppress the volume changes in lithium-sulfur battery</b> .....	129
<i>O. Ovchinnikova, Yu. Polishchuk, K. Sukhyi, E. Shembel</i> <b>Non-Aqueous Ionic Liquids Based on Quaternary Ammonium Salts for Lithium-Sulfur Batteries</b> .....	131
<i>Y. Polishchuk, E. Shembel, V. Kyrychenko, A. Straková Fedorková, V. Redko, B. Blyuss and O. Girin</i> <b>Melanin's Semiconductor Nature and his Polymer Structure Successfully Modifies Sulfur Cathode and Increase Efficiency on Li-S batteries</b> .....	133
<i>A. V. Potapenko, O. V. Potapenko, O. V. Krushevskiy</i> <b>EIS Analysis of Sulfur Cathodes with Water-Soluble Binder NV-1A for Lithium-Sulfur Batteries</b> .....	140

*S. Dubinevych, V. Redko, B. Blyuss, E. Shembel, O. Girin, and N. Zaderey*  
**Graphene's Correlation of Electrical and Magnetic Properties Manages the Modification and Increasing the Energy of Li Batteries** ..... 142

*Yu. V. Shmatok, N. I. Globa, S. A. Kirillov*  
**Structure, morphology and electrochemical characteristics of  $\text{Na}_x\text{MnO}_2$  ( $x = 0.44, 0.67$  and  $0.8$ ) as cathode materials for Na-ion batteries** ..... 143

*I. Veselkova, K. Jaššo, T. Kazda and M. Sedlaříková*  
**Study of Gel Polymer Electrolytes for Li-S batteries** ..... 146

## **Photovoltaics**

*S. Gavranović, J. Pospíšil, V. Novák and P. Vanýsek*  
**Perovskite Single Crystals for Energy Conversion of Solar Radiation** ..... 148

*T. Binar, J. Zimáková, J. Fridrich, M. Sedlaříková*  
**Use of Photovoltaic Panels to Power Variable Traffic Signs** ..... 152

*K. Jandova, M. Janda*  
**Solar-Powered Irrigation System** ..... 155

*F. Langer, J. Vanek, K. Jandova, P. Maule*  
**The influence of environmental conditions of the recycling of solar modules** ..... 158

## **Corrosion, Applications and Simulations**

*M. Mačák, K. Jaššo, P. Vyroubal, T. Kazda, P. Čudek*  
**Numerical Simulation of Cathode Structure Influence on Lithium-Sulphur Battery Behaviour** ..... 161

*K. Mairhofer, B. Kipper-Pires, G. Fafilek*  
**Photoassisted Electrodeposition of Cuprous Oxide Thin Films** ..... 164

*P. Šabacká, J. Maxa, A. Maxová*  
**Mathematical and Physical Analysis of the effect of conical and detached shock waves at the tip of a static probe in an experimental chamber** ..... 165

*P. Šabacká, J. Maxa, F. Maxa*  
**Mathematical-physical analysis of Drag Force of a .223 REM caliber projectile** ..... 169

*Amrit Kumar Thakur, Ravishankar Sathyamurthy*  
**A critical review of recent development of novel Li-ion battery cooling methods using phase change materials for fast charging application** ..... 173

*R. Bayer*  
**Mathematical and Physical Analysis of Pressure Gradient in the Experimental Chamber for Subsequent Comparison with Optical Methods** ..... 174

*T. Binar, J. Zimáková, M. Šustr, L. Řehořek, M. Sámel, M. Sedlaříková*  
**Use of Cold Kinetic Deposition Technology on Materials Used in Electrical Engineering** ..... 179

<i>T. Binar, J. Zimáková, P. Bača, J. Fridrich, M. Sedlaříková</i> <b>Power Supplies For Variable Traffic Signs</b> .....	183
<i>T. Binar, J. Zimáková, M. Šustr, M. Sámel, M. Sedlaříková</i> <b>Example of Application of Cold Spray Technology in Electrical Engineering</b> .....	187
<i>T. Binar, J. Zimáková, J. Šteiniger, L. Řehořek, P. Křivík, P. Čudek, M. Sedlaříková</i> <b>Evaluation of the Use of Cold Kinetic Deposition Technology on Materials Used in Electrical Engineering</b> .....	192
<i>J. Zimáková, T. Binar, P. Šafla, M. Sedlaříková</i> <b>A tool for effective management of the logistics process with a direct link to the material life cycle</b> .....	196
<i>T. Binar, J. Zimáková, P. Šafl, M. Sedlaříková</i> <b>Impacts of Simulated Climate Change on Vehicle Engine Function Parts</b> .....	200
<i>R. Cipin, M. Toman, P. Prochazka, and I. Pazdera</i> <b>Using Neural Network for Estimation of Li-ion Battery Depth of Discharge</b> .....	204
<i>D. Dobrocky, J. Sedlak, A. Polzer, Z. Joska, J. Prochazka, Z. Studeny and E. Svoboda</i> <b>Influence of Machining Parameters on the Surface Quality of Technical Plastics</b> .....	207
<i>J. Dokoupil a J. Starý</i> <b>Effect of temperature cycling on IMC growth and solder joint strength of SAC305 solder alloy and REL61 low silver alloy</b> .....	208
<i>V. Horák, B. T. Phan, and L. Dobšáková</i> <b>Thermodynamics of Moist Air for Vacuum Technology</b> .....	210
<i>L. Horák, J. Kazelle</i> <b>Ecological Epoxy Casting Systems for Electrical Engineering Applications</b> .....	214
<i>O. Klvač, T. Kazda, Y. Fam, L. Novák</i> <b>Preparation of an electrochemical cell inside a scanning electron microscope</b> .....	217
<i>D. Kusmič, L. Klakurková, M. Juliš, P. Gejdoš, J. Viliš, O. Čech</i> <b>The Corrosion Resistance of anodized EN AW 7075 T6 Alloy</b> .....	220
<i>M. Mačák, T. Kazda, K. Jaššo, P. Vyroubal</i> <b>Equivalent Circuit Modelling of Li-S Batteries</b> .....	221
<i>M. Mačák, P. Vyroubal</i> <b>Modelling of Electrochemical Magnetohydrodynamics in Ansys Fluent</b> .....	224
<i>H. Ch. Nguyen, E. Svoboda, J. Prochazka</i> <b>Effects of Hybrid Surface Treatment Composed of Plasma Nitriding and CrN Coating on Friction-Wear Properties and Adhesion Strength of Stainless Steel</b> .....	227
<i>P. N. Nam, J. Leuchter, P. K. Lam, R. Bystřický, and D. Q. Huy</i> <b>Battery Monitoring System using Microcontroller ESP32 and Internet of Things</b> .....	228
<i>H. Polsterová</i> <b>Dielectric properties of nanocomposit based on epoxy resin</b> .....	231

<i>A. Pražanová, V. Knap</i> <b>Electrical circuit model of Lithium-ion batteries and revisiting of its parametrization procedures</b> .....	237
<i>J. Prochazka, D. Dobrocky, Z. Joska, H. Ch. Nguyen, J. Sedláček, J. Sedlák, A. Polzer, and P. Sliwková</i> <b>Modification of surface structure by diffusion processes</b> .....	238
<i>M. Sedlaříková, M. Zatloukal, J. Hrabovský, P. Čudek</i> <b>Corrosion Processes of Sintered Materials Based on Fe-Mg</b> .....	241
<i>M. Sedlaříková, M. Zatloukal, J. Bachmayer, P. Čudek</i> <b>Corrosion of Sintered Materials Based on Fe.Si-Ag-Mg</b> .....	245
<i>V. Sítař, T. Vysloužil, L. Raková, Z. Pazdera</i> <b>Impact of Electric Vehicles Charging on Electric Distribution Grids in Small Villages</b> .....	249
<i>J. Starý</i> <b>Electromigration and Flux Residues</b> .....	250
<i>Z. Studeny, D. Dobrocky, L. Dobsakova and J. Prochazka</i> <b>Resistance of PLA material prepared by additive technology</b> .....	253
<i>J. Maxa, P. Šabacká, R. Bayer</i> <b>Analysis of the effect of reflected shock waves in the experimental chamber</b> .....	256
<i>P.Šafl, J. Zimáková, T.Binar, M. Sedlaříková</i> <b>Observation of environmental impact on HIPS material for 3D printing</b> .....	260
<i>P.Šafl, J. Zimáková, T.Binar, M. Sedlaříková</i> <b>Reducing internal stress by annealing</b> .....	264
<i>P. Vorel, J. Martis</i> <b>Battery Powered Lawn Mower</b> .....	268
<i>P. Vyroubal, T. Kazda, M. Mačák</i> <b>CFD Simulation of Thermal Abuse in Lithium-Ion Battery Pac</b> .....	271
<i>P. Vyroubal, M. Mačák, T. Kazda</i> <b>Numerical Modeling of Reactions at the Level of an Electrochemical Cell</b> .....	274
<i>R. Kutil, T. Binar, M. Sedlaříková, J. Zimáková</i> <b>Analysis of Time Delays in the Supply of Rechargeable Batteries in a Specific Inventory System</b> .....	277

## Multiscale 3D analysis of defects and temporal development of electrode morphology in lithium-ion batteries by X-ray computed tomography

P. Blažek<sup>a</sup>, P. Guricová<sup>b</sup>, O. Klvač<sup>b</sup>, T. Kazda<sup>b</sup>, A. Břínek<sup>a</sup>, T. Zikmund<sup>a</sup>, and J. Kaiser<sup>a</sup>

<sup>a</sup> Central European Institute of Technology, Brno University of Technology, Brno, Czech Republic

<sup>b</sup> Department of Electrical and Electronic Technology, Faculty of Electrical Engineering and Communication, Technická 10, 616 00 Brno, Czech Republic

X-ray computed tomography is a 3D imaging technique which is able to provide information about both inner and outer parts of battery cells without their destruction. We will present this technique allowing us access to the batteries data in whole range of scales – from the analysis of whole cells down to microstructure of electrodes. We will focus on the changes in the structure during the aging process of the battery.

### Introduction

The development of batteries aiming towards better performance, higher energy density, and a higher lifetime can be advantageously supported by X-ray micro-computed tomography (CT). CT is a 3D imaging method enabling analysis of both inner and outer features of samples with a high-resolution (typically down to  $1\ \mu\text{m}^3$  or even less spatial voxel resolution) in a non-destructive manner. It may provide information about position of components or presence of defects in different scales (micro-CT – mm lengths with ten micrometers linear voxel size, submicron/nano CT with sub-micrometer linear voxel size). With submicron/nano CT, we can measure and analyze microstructure of electrodes (1-3).

Here we present helical CT scanning of the whole cylindrical cell which is imaged with sufficient resolution to distinguish all important components, detect defects in electrodes and track morphological changes due to cell aging in one overview scan. With region of interest (ROI) scanning, part of the volume is imaged with two times higher resolution. From the ROI scan, we can focus on the specific region or defect which may be then analyzed in more detail. We will disassemble the battery and cut a piece of electrode selected from ROI CT scan for submicron CT to analyze size of the active particles. The results from CT will be complemented by electron microscopy analysis.

### Material and methods

The sample used for the defect analysis and aging study was cylindrical NMC based cell INR18650-29E manufactured by Samsung SDI. The battery was scanned in fresh state and after 200 cycles at 1C (90-15% SoC). The overview battery scan and ROI scan were performed using HeliScan microCT (Thermo Fisher Scientific) with 150 kV tube voltage, 0.55 s exposure time, space-filling helical trajectory, and voxel size  $8\ \mu\text{m}$ , and 120 kV, 0.7 s exposure time and voxel size  $4\ \mu\text{m}$ , respectively. The battery was then cut, gradually polished by 30, 15, 8, and  $5\ \mu\text{m}$  grain size SiC grinder papers, and dried. The final surface polishing was performed using broad ion beam polisher Model 1061 SEM Mill (Fischione Instruments) at 3 kV for 4 hours with cryo cooling. Images were taken using Scios 2 scanning electron microscope (Thermo Fischer Scientific). After battery

disassembly, a piece of the cathode was cut and imaged using Rigaku nano3DX with Mo target, 50 kV tube voltage, and voxel size of 0.54  $\mu\text{m}$ .

## Results and discussion

From the scan of the whole battery, we can detect a presence of defects, but the resolution is not sufficient for quantitative analysis. Using ROI scan, we can achieve two times better resolution providing us with more information about position and shape of the defects (Figure 1 a-d). The comparison of the battery cell in fresh and aged state (Figure 1 e, f) revealed delamination across the whole battery and large deformation of electrodes in the region close to the central pin.

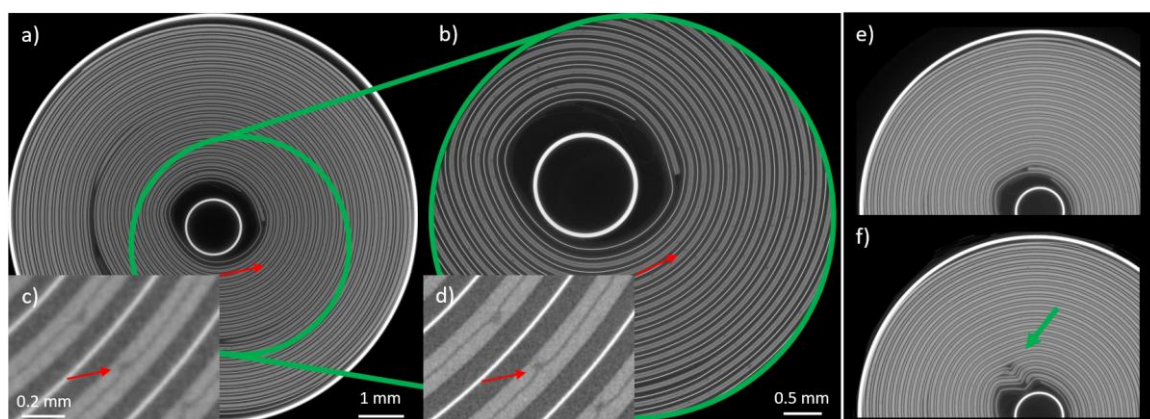


**Figure 1.** Tomographic cross-sections of the 18650 battery cell. Red arrow shows the position of a same defect. a) Overview scan of the whole battery and b) result of the ROI scan. Green circle shows the position in the overview scan. c) Detail of the defects in lower resolution overview scan. d) Detail of the defects in the higher resolution ROI scan. e) Battery in fresh state, f) battery after 200 cycles. Green arrow shows deformation which occurred during cycling.

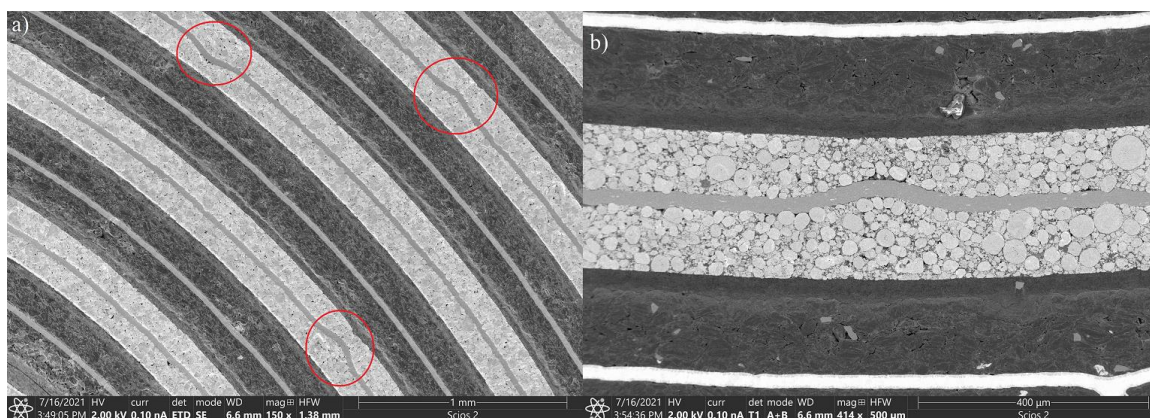


**Figure 2.** Cross-section SEM battery images. a) Larger field of view, three defects are highlighted by red circles. b) Detail of bulged region.

SEM images (Figure 2) of defects *c* and *d* show the presence of bulging regions, which were probably caused by the uneven distribution of the material during coating process.

With submicron CT we were able to assess the microstructure of the battery cathode. The resolution is sufficient to distinguish active particles and analyze their size and shape (Figure 3). The mean diameter of particles is 8  $\mu\text{m}$ .

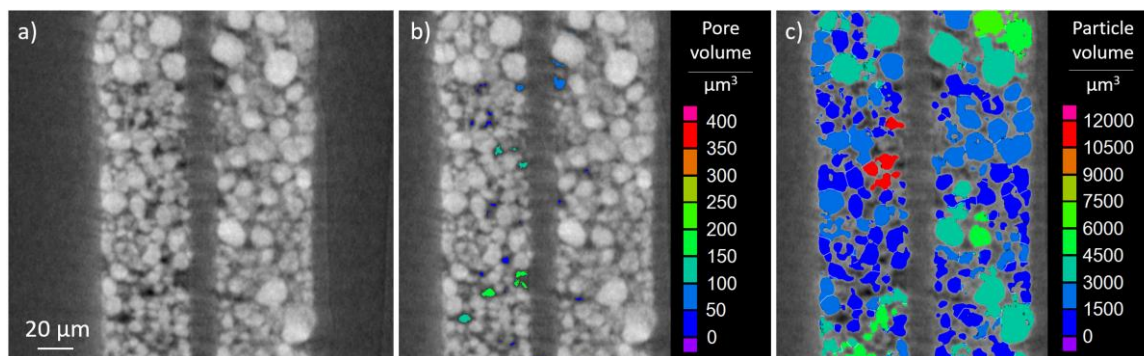


**Figure 3.** a) Tomographic cross-sections of the submicron CT scan of the cathode b) Visualization of porosity, c) visualization of active particles (volume is color-coded).

### Conclusion

With space-filling trajectory scan, we were able to image the whole cylindrical cell 18650. The resolution was sufficient to distinguish all components (electrodes, current collectors, separators) and detect defects. The ROI scan was able to show the defects in more detail while still being non-destructive. We were also able to detect changes in electrode geometry due to aging processes. SEM images of the polished battery cross-section show that the defects are areas of bulged aluminum foil that are likely to be caused by inhomogeneous distribution of electroactive material during the coating process. With sub-micron CT we analyzed an extracted piece of electrode providing information about shape and size of active particles.

### Acknowledgments

We acknowledge CzechNanoLab Research Infrastructure supported by MEYS CR (LM2018110), thank to the support of grant CEITEC VUT-K-21-6938 and specific graduate research of the Brno University of Technology No. FEKT-S-20-6206.

### References

1. P. Pietsch and V. Wood, *Annu. Rev. Mater. Res.* **47**, 451–479 (2017).
2. D. Di Lecce, S. Levchenko, F. Iacoviello, D. J. L. Brett, P. R. Shearing and J. Hassoun, *ChemSusChem* **12**(15), 3550–3561 (2019).
3. X. Lu, A. Bertei, D. P. Finegan, C. Tan, S. R. Daemi, J. S. Weaving, K. B. O’Regan, T. M. M. Heenan, G. Hinds, E. Kendrick, D. J. L. Brett and Paul R. Shearing, *Nat. Commun.* **11**(1), 1–13 (2020).

## Imidazole-based lithium salt as an additive for lithium-conducting electrolytes

M. Broszkiewicz

Lithium salt LiHDI (lithium 4,5-dicyano-2-(*n*-heptafluoropropyl)imidazolidide) is proposed as a solid electrolyte interface stabilizing additive for lithium-ion batteries. It was chosen as an additive for lithium electrolytes because out of the imidazole-based family of lithium salts (LiTDI, LiPDI, LiHDI) it's electrolytes exhibited the best interfacial stability versus metallic lithium even when at low concentration. Electrolytes containing either LiTDI or battery standard LiPF<sub>6</sub> were tested with various amounts of LiHDI additive. Chemical stability in a presence of water and thermal stability of LiHDI are on par with LiTDI. Being a lithium salt itself, and that of similar conductivity in solutions to LiTDI, LiHDI additive does not negatively affect properties of electrolytes. Conductivity measurements of solutions, galvanostatic cycling of graphite-LiFePO<sub>4</sub> cells at room temperature, cells' cycling at 60°C, internal cell resistance monitoring during cycling and X-ray photoelectron spectroscopy analysis of electrodes' surfaces after cycling have been performed. LiHDI, unlike FEC-VC mixture, does not negatively affect properties of the electrolyte. Cycling at room temperature showed improved capacity retention with LiHDI additive, both with graphite and LFP as capacity limiting electrodes. Samples with LiHDI also exhibited better capacity retention than samples with FEC-VC during cycling at elevated temperatures. Internal cell resistance can be correlated with capacity retention. XPS results show changes in composition of SEI and CEI depending on the composition of electrolyte and the duration of cycling. To conclude, LiHDI is a promising interface stabilizing additive which can be added in lower amount than FEC-VC to be at least as effective. It shows especially promising results during cycling at elevated temperatures.

## **Laser structuring of NMC 811 high energy electrodes in battery production for enhancing the electrochemical performance for xEV energy storage systems**

B. Eschelmüller<sup>a</sup>, K. Froehlich<sup>a</sup>, W. Pessenhofer<sup>b</sup>, H. Besser<sup>c</sup>, W. Pfleging<sup>c</sup>, M. Jahn<sup>a</sup>, F. Pichler<sup>d</sup>

<sup>a</sup>Electric Vehicle Technologies, AIT Austrian Institute of Technology GmbH, Vienna, Austria

<sup>b</sup>New coatings, Miba eMobility GmbH, Vorchdorf, Austria

<sup>c</sup>Institute for Applied Materials (IAM-AWP), Karlsruhe Institute of Technology, P.O. Box 3640, 76021, Karlsruhe, Germany

<sup>d</sup>Virtual Vehicle Research GmbH, Graz, Austria

Layered oxide cathodes, especially thick-film electrodes like lithium nickel manganese cobalt oxide, NMC, are under continuously investigation to meet the ambitious requirements, e.g. 700 Wh/l, for future Li-ion batteries in electric drive applications. The objective of the most current studies is to reduce the Co content with a concurrent increasing Ni-content in the NMC cathodes such as NMC 811 [1]. It must not leave the fact out of consideration, that NMC cathodes suffer from low high rate capability and corresponding low capacity retention at high C-rates. In particular, the negative impact is even higher for thick-film high energy cathodes. To counteract the negative effect, high repetition ultrafast laser ablation is applied to create appropriate 3D electrode designs [2]. New Li<sup>+</sup>-diffusion pathways, applied by the laser structuring process, shell enhance electrolyte wettability and reduce overpotentials at high C-rates.

It is attempted to integrate the laser structuring into a continuous roll-to-roll electrode production process. In this way, the positive properties achieved through 3D structuring can also be obtained for Li-ion batteries that are produced on a large scale. By using this novel production technology, future NMC batteries can be produced with improved performance characteristics for xEV applications. Furthermore, this technology can also be applied for other generation 3b battery cells. This work is performed under the frame of the RealLi! project, in which the following aspects are covered:

- a) Development of thick film NMC811 electrodes with high areal capacity
- b) Passivation approach to improve cycle stability and lifetime
- c) Cell Assembly and electrochemical characterization
- d) Holistic evaluation of the potential environmental impact of the NMC811 cells via life cycle assessment
- e) An experimentally validated electrochemical model to describe electrode structures and their optimization.
- f) Improved electrochemical performance of NMC811 electrodes on a laboratory scale by using 3D laser structuring.
- g) Scale up of the 3D laser structuring process and corresponding improved electrochemical performance of NMC811 electrodes in pouch cell format by using 3D laser ablation.

### **Acknowledgments**

This work was in the course of project 873396 financially supported by the Austrian Federal Ministry for Climate Action, Environment, Energy, Mobility, Innovation and Technology (bmk).

### **References**

1. C. of the European Parliament, Tackling the Challenges in commodity markets on raw materials, “Tackling the Challenges in commodity markets on raw materials”, 2011.
2. W. Pfleging, “Recent progress in laser texturing of battery materials: a review of tuning electrochemical performances, related material development, and prospects for large-scale manufacturing”, *Int. J. Extrem. Manuf.*, vol. 3, 2020.

## Process standardisation of EU research pilot lines for prototype cell production

K. Froehlich<sup>a</sup>, A. Gigl<sup>a</sup>, B. Eschelmüller<sup>a</sup>, M. Jahn<sup>a</sup>

<sup>a</sup>Electric Drive Technologies, AIT Austrian Institute of Technology GmbH, Vienna, Austria

From a European perspective, battery cell production can score internationally mainly in two different factors: sustainability and quality. To achieve high quality in terms of cell production, well-defined processing standards are required, should be retained and therefore pre-defined precisely. The conduction of an interlaboratory, so-called round-robin test, can accelerate this process.

As LiPLANET network [1], our mission and aim are to create a European innovation and production ecosystem and reinforce the position of the European Union (EU) in the Lithium battery cell manufacturing market.

As part of the activities, different European research pilot lines have come together to sound out this future standardization by means of a round-robin test.

The test was sorted out and initialized, setting up a protocol using materials on a non-competitive basis and at the beginning, different questions were raised:

Which process parameters are considered critical?

Which tolerances at different production steps are acceptable?

How does the final prototype cell format influence those?

The focus of the round-robin test is set on widespread cell chemistries to cover as many pilot lines as possible and gain knowledge on the influence of the production processes on different cell properties on a non-competitive basis.

Materials and compositions have been chosen and the test protocol was defined accordingly. For the initial run, the consortium agreed to apply NMC622 cathode and artificial graphite anode active material and defined to produce prototype cells consisting of 10 cathodes, resulting in different final cell capacities depending on the individual research pilot line facilities. Round-robin test results will be compared and shared within the network and cell manufacturing community.

So how can we ensure and retain high quality and environmentally friendly cell production within the European Union? If we want to realize sustainable, innovative and high-class production processes, standardization of the individual processes and continuous qualification of pilot lines is a step towards the right direction.

### Acknowledgments

This project has received funding from the European Union's Horizon 2020 research and innovation programme under grant agreement No 875479.

### References

1. <https://www.liplanet.eu/> .

## The Study of Lithium PVdF-HFP Electrolytes Based on Non-Crystallizing Solutions

M. Kasprzyk <sup>a,\*</sup>, A. Zalewska <sup>a</sup>, M. Broszkiewicz <sup>a</sup>, J. Tańska <sup>a</sup>, W. Wiczorek <sup>a</sup>

<sup>a</sup> Faculty of Chemistry, Warsaw University of Technology, Warsaw 00-664, Poland

This work is concentrated on usage of non-crystallizing liquid electrolytes to form gel-type electrolytes with PVdF-HFP (poly(vinylidene fluoride-co-hexafluoropropylene)). The mixtures of ethylene carbonate (EC) with poly(ethylene glycol)s (PEGs) are making base for the electrolytes preparation. Liquid electrolyte based on such solvent mixture do not exhibit any crystallization or melting points. The gel electrolyte show great mechanical properties and quite high conductivity also at temperatures below 0°C. The electrochemical study of these electrolytes will be presented herein.

### Introduction

Lithium-ion batteries are still developing very fast due to, among other factors, increasing interest in electric vehicles. The amount of portable devices is also increasing, so that energy source must be reliable and light in weight.

It is well known that modern lithium-ion batteries use mostly liquid electrolytes, however those exhibit multiple disadvantages. The first one is the risk of crystallization at temperatures below 0°C. For most of electrolytes it is impossible to still conduct at temperatures below -20°C. Crystallization and the sudden drop in conductivity are the main issues with liquid electrolytes. Also due to crystallization, the cracking of electrodes may be observed. Thus, even heating back to room temperature after freezing may not bring back the original properties of the battery. Significant changes in its properties may include the drop in capacity of electrodes as well as the critical damage incapacitating the battery may occur. That is why the non-crystallizing electrolytes may be an answer to this important issue.

The second issue with liquid electrolytes is the possibility of electrolyte leakage and possibility of solvent evaporation causing a significant increase in the inner pressure of the battery. Such behavior may lead to explosion or to incineration. Both of these situations may be extremely hazardous to user and to the environment. The answer to such an issue may be use of gel electrolyte, which lowers the risk of fire outbreak by far. However, the outstanding issue with gel electrolytes is to increase their conductivity at lower temperatures.

### Experimental and results

The presented work is about gel electrolytes and their electrochemical properties. PVdF-HPF porous membrane synthesis was conducted with so-called Bellcore method. The microscopic images will be presented. The electrolytes with both LiPF<sub>6</sub> (lithium hexafluorophosphate) and LiTDI (lithium 4,5-dicyano-2-(trifluoromethyl)imidazole) salts will be shown. The certain mixtures of EC:PEG with different chain length will be used as the basis for gel electrolyte preparation.

The conductivity, cyclic voltammetry, lithium transference number and other electrochemical measurements will be shown.

These electrolytes exhibit quite high conductivity (around 1 mS cm<sup>-1</sup> at 20°C) in comparison to other gel electrolytes. They show relatively high conductivity at temperatures below 0°C as well. The high electrochemical stability window of these electrolytes is also observed, up to 4.7 V vs. Li.

### Acknowledgments

This work was financially supported by Faculty of Chemistry, Warsaw University of Technology.

### References

1. M.C. Smart, B.V. Ratnakumar, S. Surampudi, *J. Electrochem. Soc.*, **149(4)**, A361 (2002).
2. M. Kasprzyk, A. Zalewska, L. Niedzicki, A. Bitner, M. Marcinek, W. Wieczorek, *Solid State Ionics*, **308**, 22 (2017).
3. M. Kasprzyk, A. Zalewska, W. Wieczorek, *J. Phys. Chem. C.*, **124(9)**, 5046 (2020).

## **Influence of long-term cycling at low temperature on the performance of Li-ion batteries**

T. Kazda<sup>a</sup>, V. Gavalierová<sup>a</sup>, J. Tichý<sup>a</sup>

<sup>a</sup> Department of Electrical and Electronic Technology, Faculty of Electrical Engineering and Communication, BUT, Technická 10, 616 00 Brno, Czech Republic

Lithium-ion batteries are the most popular battery system for portable devices and electromobility. Their importance will increase in the future with the further development of electromobility. One of the often discussed topics is the stability of batteries during their operation at low temperatures. In this paper, we focus on the effect of long-term cycling for 200 cycles at the temperature of -10°C on the performance of Li-ion batteries.

### **Introduction**

Lithium-ion batteries are crucial for many applications nowadays. Current and future development of electric vehicles is heavily dependent on the development of Li-ion batteries. Compared with other applications of Li-ion batteries like cell phones or notebooks, electric vehicles are exposed to a wider extent of external factors like temperature or humidity. The range of temperatures in which cars are operated is approximately from -25°C through 40°C depending on location. Temperatures in the Czech Republic are usually between -10°C and 35°C. The optimal temperature range for Li-ion batteries is 15°C–35°C 1. It is evident that there are temperatures outside the optimal range both on the positive and negative side of the real range even if we omit the heating of the battery by discharging during driving. Some older types of electric cars do not have active heating of batteries. They are only able to cool the battery which means they cannot heat the battery during a ride in winter. The battery temperature can also drop when the electric car is parked outside in winter when all systems are switched off. At low temperatures, the internal resistance of the cell increases, which leads to increased losses, which leads to increased battery heating during charging and discharging, which subsequently leads to a reduction of the internal resistance 2. Low temperature leads to a decrease in electrolyte viscosity and conductivity 3. In the case of electrode materials, the diffusion of Li<sup>+</sup> ions into the structure of the electrodes is slowed down 4. These changes lead to a decrease in the capacity of the battery and at the same time to the reduction of the maximum load of the battery. The most crucial drawback of Li-ion batteries at low temperatures is lithium plating on the anode surface during charging. Usually, it is not recommended to charge the battery if the temperature is lower than 0°C. Due to the high resistance, the voltage on the anode side can drop too low, which leads to lithium plating on the anode surface instead of lithium intercalation into the graphite structure. This effect leads to capacity reduction and formation of lithium dendrites during cycling. Lithium dendrites can subsequently grow through the separator and short-circuit the battery. In the worst case, the battery may ignite and the entire device may be destroyed 1. In this article, we focused on monitoring the capacity drop at a very low temperature of -10° C during cycling for 200 cycles at maximum load.

## Experimental

Two commercial cylindrical cells Samsung INR18650-29E (2850 mAh) were chosen for long-term cycling at room temperature and at the temperature of  $-10^{\circ}\text{C}$  for 200 cycles. The lowest recommended temperature for discharging is  $-20^{\circ}\text{C}$  and it is  $0^{\circ}\text{C}$  for charging. The test was performed at a temperature  $10^{\circ}\text{C}$  lower than the lowest recommended charging temperature. Both cells were charged/discharged at  $0.1\text{ C}$  at room temperature before and after cycling in the full range of  $2.5\text{--}4.2\text{ V}$ . The long-term cycling was performed at  $2750\text{ mA}$  (maximal recommended charging current) for charging and  $2850\text{ mA}$  for discharging in the range of  $90\%$  SoC and  $90\%$  DoD. This limitation was set because of battery cycle life extension and as well as because of lithium plating limitation at the low temperature in the case of the second battery. It is evident that the cell at room temperature provided higher capacity during the whole cycling, see Figure.1. The capacity of the battery *INR18650-29E\_room temperature* at the beginning of cycling was  $2165\text{ mAh}$  and it was  $1646\text{ mAh}$  in the case of the battery *INR18650-29E\_ $-10^{\circ}\text{C}$* . The capacity drop after 200 cycles in the case of the battery *INR18650-29E\_room temperature* was  $20.4\%$  ( $0.104\%$  per cycle). The capacity of the battery *INR18650-29E\_ $-10^{\circ}\text{C}$*  decreased by  $24.1\%$  ( $0.121\%$  per cycle). A comparison of the discharge capacity at  $0.1\text{ C}$  at room temperature before and after cycling is shown in Figure 2. Capacities before cycling were practically identical for both batteries:  $2874\text{ mAh}$  for *INR18650-29E\_room temperature* and  $2860\text{ mAh}$  for *INR18650-29E\_ $-10^{\circ}\text{C}$* . The capacity after cycling at low temperature was approximately  $1.1\%$  lower compared to the battery cycled at room temperature.

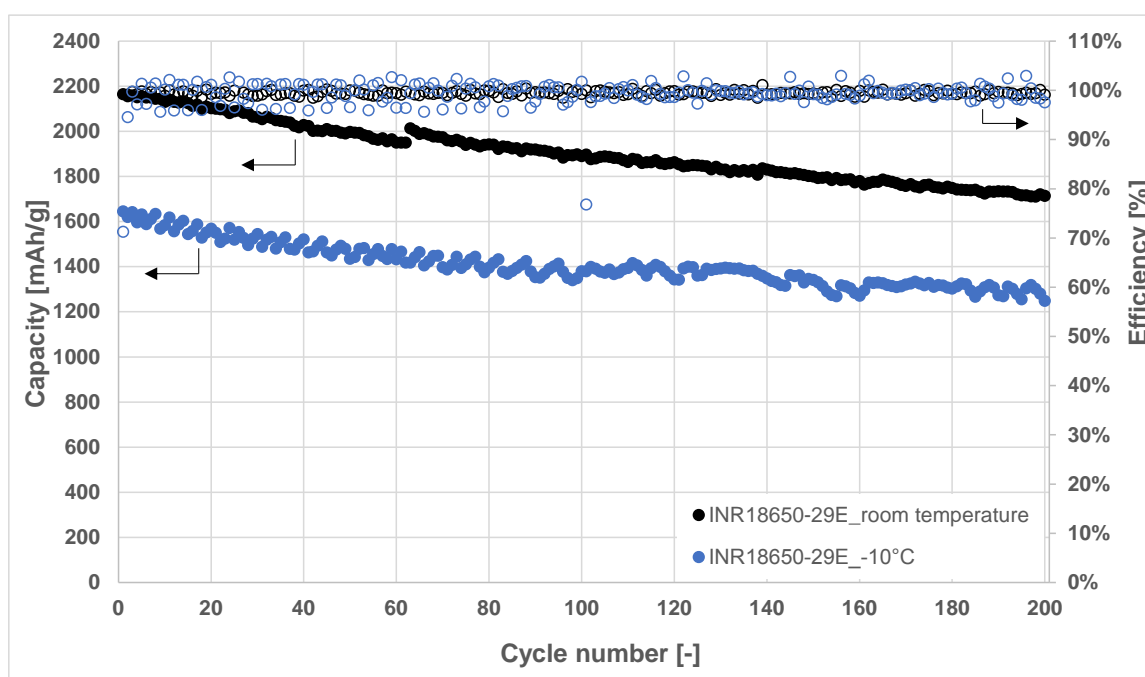


**Figure 1.** Comparison of the capacities and efficiency of the INR18650-29E cells during long term cycling at  $1\text{ C}$  at room temperature and at  $-10^{\circ}\text{C}$

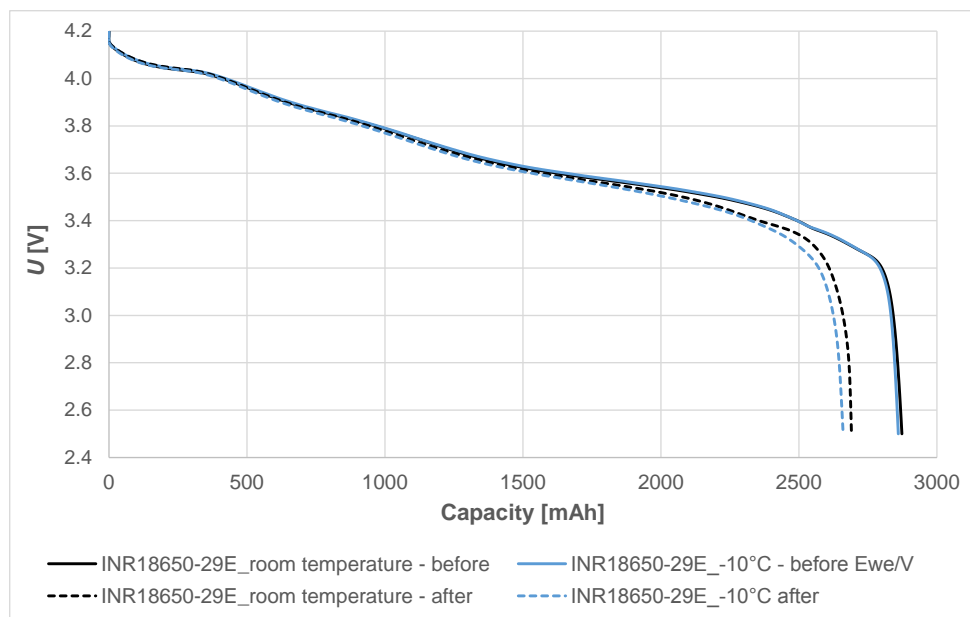


**Figure 2.** Comparison of discharge profiles of the INR18650-29E cells at 0.1 C before and after long term cycling at room temperature and at -10°C

## Conclusion

The performed measurements show that cycling at a very low temperature of -10 ° C leads to a slightly faster decrease of capacity and a subsequent decrease of capacity during re-cycling at room temperature. The difference is not significant even when the recommended temperature limits are greatly exceeded. At the same time, it is clear that a battery operating at low temperatures is not immediately destroyed.

## Acknowledgments

Authors gratefully acknowledge the financial support from BUT specific research programme (project No. FEKT-S-20-6206).

## References

1. S. Ma, M. Jiang, P. Tao, C. Song, J. Wu, J. Wang, T. Deng and W. Shang, *Progress in Natural Science: Materials International*, **vol. 28**, 653-666 (2018).
2. Y. Ji, Y. Zhang and C. Wang, *Journal of The Electrochemical Society*, **vol. 160**, A636-A649 (2013).
3. H. Shiao, D. Chua, H. Lin, S. Slane and M. Salomon, *Journal of Power Sources*, **vol. 87**, 167-173 (2000).
4. S. Zhang, K. Xu and T. Jow, *Electrochimica Acta*, **vol. 48**, 241-246 (2002).

## Calendar degradation and self-discharge occurring during short- and long-term storage of NMC based Lithium-ion batteries

Vaclav Knap<sup>a,b,c</sup>, Martin Molhanec<sup>b</sup>, Alejandro Gismero<sup>c</sup>, and Daniel-Ioan Stroe<sup>c</sup>

<sup>a</sup> GomSpace A/S, Aalborg Denmark

<sup>b</sup> Faculty of Electrical Engineering, Czech Technical University in Prague, Czech Republic

<sup>c</sup> Department of Energy Technology, Aalborg University, Aalborg, Denmark

Nowadays, Lithium-ion (Li-ion) batteries are found in many various applications, from consumable and wearable electronics, over traction, mobility, aerospace, up to large stationary storages. Over a lifetime in an application, Li-ion batteries experience a capacity loss. This loss is either reversible, in that case, it is seen as a self-discharge, or it is irreversible, and then it is described as degradation. Even though Li-ion batteries have relatively a low self-discharge in comparison to previous battery technologies, it is still an important performance parameter that influences battery readiness (available stored charged after long storage), and economics. Next to it, battery degradation and its related capacity fade receive great interest, as it directly limits an application lifetime. Thus, it is desirable to avoid conditions causing a severe deterioration and it is also desired to predict such degradation.

In this work, a systematic study was conducted, where Li-ion cells were stored at various state-of-charge and temperature conditions. A reference performance test was periodically performed to check their status and evaluate their capacity loss. The obtained data were analyzed and used for self-discharge and capacity decay modelling. Especially for the calendar capacity model, it is common to store cells for a shorter period (e.g., one month) and then build a model from those data. However, storage periods can significantly vary, and the validity of such a model might be questioned. Thus, short, and long storage periods were selected to address this question. Specifically, groups of cells were stored for two and six months repeatedly. The models were characterized from the cells checked every two months and then they were validated and evaluated on the cells stored for six months continuously. Consequently, the predictions can be used in an application to estimate a useable life and to select preferable operating conditions.

## Critical Parameter Evaluation of Thick, Multi-Layer Cathodes in Li-Ion Batteries

L.Neidhart<sup>a,b</sup>, K. Froehlich<sup>a</sup>, M. Jahn<sup>a</sup>, F. Winter<sup>b</sup>

<sup>a</sup>Electric Vehicle Technologies, AIT Austrian Institute of Technology GmbH, Vienna, Austria

<sup>b</sup>Technical University of Vienna, Institute of Chemical, Environmental and Bioscience Engineering, Vienna, Austria

Increasing the energy density in Li-ion batteries is an issue that needs to be addressed in future automotive applications due to increasing demand for longer range and lower prices for batteries in xEVs. A possible solution is maximizing the ratio between active and inactive material within the cell. A straight forward way to fulfil this goal is to develop thick electrode coatings [1,2]. Unfortunately, this approach bears multiple challenges such as ensuring mechanical stability of the electrode and suppressing the extend of defects like cracking and cavities inside the coating. Intralayer material distribution can also be strongly affected during the drying process of thick electrodes. The effect of binder particle accumulation at the top of the coating intensifies due to uncontrollable binder migration [3–7]. This can not only cause insufficient adhesion or even full delamination from the current collector foil, but also blockage of the Li-ion channels within the electrode [8]. These problems can be held accountable for negative consequences on electrochemical performance. Multilayer coated electrodes are a strategy to circumvent these problems [9]. Several coatings performed on top of each other not only enhance total coating height but can also be used for vertically functionalisation of the electrode. Thorough studies of the electrode parameters are needed to help understand how coating compositions affect the performance of the electrode.

Porosity is one such parameter, which is known to play an important role for ion diffusivity throughout electrodes used in Li-ion batteries. It can be quantified by calculations or Hg-porosimetry [10]. However, especially for coatings with enhanced thickness, the diffusion coefficient needs to be adapted by the tortuosity of the system [11]. Effective tortuosity is not only related to the extension of ionic transport pathways inside an electrode, but also takes dead ends, surface morphologies and geometrical effects into account [12].

The tortuosities of cathodes consisting of Ni-rich lithium nickel manganese cobalt oxides (NMC811), as active material, are investigated in this work. Electrodes with varying thicknesses, porosities and solvents (N-Methyl-2-pyrrolidone (NMP) and water) are characterized by obtaining electrochemical impedance spectra. Symmetrical cells are tested in a blocking state to receive ionic resistances to calculate the tortuosity factor [13–15]. Additionally, multi-layered electrodes are tested with the same method. Lower tortuosity values are measured for both NMP and water-based systems, compared to single coated electrodes – supporting the applicability of the multi-layer technique.

The impact of electrode parameters on resulting tortuosities are presented and discussed.

### Acknowledgments

This work was financially supported by the Austrian Federal Ministry for Climate Action, Environment, Energy, Mobility, Innovation and Technology (bmk).

## References

1. Z. Du, D.L.W. Iii, C.D.S. Kalnaus, J. Li, Understanding limiting factors in thick electrode performance as applied to high energy density Li-ion batteries, *J. Appl. Electrochem.* 47 (2017) 405–415. <https://doi.org/10.1007/s10800-017-1047-4>.
2. Y. Kuang, C. Chen, D. Kirsch, L. Hu, Thick Electrode Batteries: Principles, Opportunities, and Challenges, *Adv. Energy Mater.* 9 (2019). <https://doi.org/10.1002/aenm.201901457>.
3. F. Font, B. Protas, G. Richardson, J.M. Foster, Binder migration during drying of lithium-ion battery electrodes: Modelling and comparison to experiment, *J. Power Sources.* 393 (2018) 177–185. <https://doi.org/10.1016/j.jpowsour.2018.04.097>.
4. M. Müller, L. Pfaffmann, S. Jaiser, M. Baunach, V. Trouillet, F. Scheiba, P. Scharfer, W. Schabel, W. Bauer, Investigation of binder distribution in graphite anodes for lithium-ion batteries, *J. Power Sources.* 340 (2017) 1–5. <https://doi.org/10.1016/j.jpowsour.2016.11.051>.
5. L.S. Kremer, A. Hoffmann, T. Danner, S. Hein, B. Prifling, D. Westhoff, C. Dreer, A. Latz, V. Schmidt, M. Wohlfahrt-Mehrens, Manufacturing Process for Improved Ultra-Thick Cathodes in High-Energy Lithium-Ion Batteries, *Energy Technol.* 8 (2020) 1–14. <https://doi.org/10.1002/ente.201900167>.
6. S. Jaiser, M. Müller, M. Baunach, W. Bauer, P. Scharfer, W. Schabel, Investigation of film solidification and binder migration during drying of Li-Ion battery anodes, *J. Power Sources.* 318 (2016) 210–219. <https://doi.org/10.1016/j.jpowsour.2016.04.018>.
7. B.G. Westphal, A. Kwade, Critical electrode properties and drying conditions causing component segregation in graphitic anodes for lithium-ion batteries, *J. Energy Storage.* 18 (2018) 509–517. <https://doi.org/10.1016/j.est.2018.06.009>.
8. M. Baunach, S. Jaiser, S. Schmelzle, H. Nirschl, P. Scharfer, W. Schabel, Delamination behavior of lithium-ion battery anodes: Influence of drying temperature during electrode processing, *Dry. Technol.* 34 (2016) 462–473. <https://doi.org/10.1080/07373937.2015.1060497>.
9. R. Diehm, J. Kumberg, C. Dörner, M. Müller, W. Bauer, P. Scharfer, W. Schabel, In Situ Investigations of Simultaneous Two-Layer Slot Die Coating of Component-Graded Anodes for Improved High-Energy Li-Ion Batteries, *Energy Technol.* (2020). <https://doi.org/10.1002/ente.201901251>.
10. L. Froboese, P. Titscher, B. Westphal, W. Haselrieder, A. Kwade, Mercury intrusion for ion- and conversion-based battery electrodes – Structure and diffusion coefficient determination, *Mater. Charact.* 133 (2017) 102–111. <https://doi.org/10.1016/j.matchar.2017.09.002>.
11. L. Shen, Z. Chen, Critical review of the impact of tortuosity on diffusion, *Chem. Eng. Sci.* 62 (2007) 3748–3755. <https://doi.org/10.1016/j.ces.2007.03.041>.
12. J. Landesfeind, J. Hattendorff, A. Ehrl, W.A. Wall, H.A. Gasteiger, Tortuosity Determination of Battery Electrodes and Separators by Impedance Spectroscopy, *J. Electrochem. Soc.* 163 (2016) A1373–A1387. <https://doi.org/10.1149/2.1141607jes>.
13. T.T. Nguyen, A. Demortière, B. Fleutot, B. Delobel, C. Delacourt, S.J. Cooper, The electrode tortuosity factor: why the conventional tortuosity factor is not well suited for quantifying transport in porous Li-ion battery electrodes and what to use instead, *Npj Comput. Mater.* 6 (2020). <https://doi.org/10.1038/s41524-020-00386-4>.
14. F. Pouraghajan, H. Knight, M. Wray, B. Mazzeo, R. Subbaraman, J. Christensen, D. Wheeler, Quantifying Tortuosity of Porous Li-Ion Battery Electrodes: Comparing Polarization-Interrupt and Blocking-Electrolyte Methods, *J. Electrochem. Soc.* 165 (2018) A2644–A2653. <https://doi.org/10.1149/2.0611811jes>.
15. N. Ogihara, S. Kawauchi, C. Okuda, Y. Itou, Y. Takeuchi, Y. Ukyo, Theoretical and Experimental Analysis of Porous Electrodes for Lithium-Ion Batteries by Electrochemical Impedance Spectroscopy Using a Symmetric Cell, *J. Electrochem. Soc.* 159 (2012) A1034–A1039. <https://doi.org/10.1149/2.057207jes>.

## Non-Fluorine Salts for Safer and Less Hazardous Lithium-ion Batteries

K. Rogala<sup>a</sup>, N. Zaremba<sup>a</sup>, M. Broszkiewicz<sup>a</sup>, D. Jamroz<sup>a</sup>, T. Trzeciak<sup>a</sup>, L. Niedzicki<sup>a,\*</sup>

<sup>a</sup> Faculty of Chemistry, Warsaw University of Technology, Noakowskiego 3, 00-664 Warsaw, Poland

Due to the increasing environmental consciousness, increasing significance of sustainable economy and recycling/reuse, the push for less toxic chemicals and longer use of devices is getting stronger around the world, especially in Europe. Fluorine-free electrolytes might be for lithium-ion batteries what has been the lead-free gasoline for cars. This work is showing the potential of the non-fluorine salts and electrolytes based on them.

### Introduction

In the recent years the European Union, as well as multiple other countries and organizations push for the decrease of the raw materials usage, higher rate and yield of recycling and dropping of toxic and/or non-abundant materials/elements. On one hand the increasing environmental consciousness is not only putting a priority on the sustainable and circular economy but also for longer use of devices/machines so there would be a smaller need for the primary raw materials. This would mean drop in mining operations and other activities that unnecessarily destroy or harm the environment. On the other hand, resigning from non-abundant or inaccessible materials in the region (e.g. EU) increases economic/technologic/material independence but also makes smaller demand for long distance transport. Use of fluorine in high-tech devices (e.g. energy storage/power sources) is touching both these issues. That is why resigning from the fluorine may be the answer to a lot of the issues, including easier recycling (less degraded recycled materials and higher yield of recycling), smaller demand for discarded water treatment, fumes filtering, etc.

In the recent years, the PIRG team at Warsaw University of Technology has been involved in the design, synthesis and development of the non-fluorine lithium salts for lithium-ion cells (1,2). In the presentation it will be shown that such salts are on par with the existing commercially available salts and can easily substitute them in the typical batteries.

### Results

The salts have been tested in both model solvent (PC) and typical battery solvent mixture (i.e. EC:DMC, 1:2 w/w ratio – abbreviated EC:2DMC) for their static properties. Those are total ionic conductivity ( $\sigma$ ), lithium cation transference number ( $T_{Li^+}$ ) and resulting lithium cation conductivity ( $\sigma_{Li^+}$ ) - effective conductivity which is calculated as a product of ionic conductivity and lithium cation transference number.

The LiPCP salt (lithium 1,1,2,3,3-pentacyanopropenide) has the maximum ionic conductivity of 8.2 mS/cm at 20°C in EC:2DMC. The lithium cation transference number is in 0.4-0.8 range, yielding at least two concentration ranges that exhibit lithium cation conductivity of 5.5 mS/cm. This effective conductivity is higher than that of the commercially available LiPF<sub>6</sub> in typical battery solvent mixtures (EC:2DMC, EC:DEC:DMC, etc.), where it reaches up to 3.5 mS/cm. The main

advantage of the LiPCP salt is high transference number, which translates to higher efficiency of the whole cell system.

LiHCAP (lithium 1,1,2,4,5,5-hexacyano-3-azapenta-1,4-diene) is a second presented salt. It also exhibits ionic conductivities above 8 mS/cm.

Both non-fluorine salts are forming solutions that are thermally stable in wide range of the temperatures (below -20°C and above 80°C) with pure salts stability much above that of LiPF<sub>6</sub>. During presentation, thermal, electrochemical and chemical stability will be discussed. Tests in half cells and full cells will be presented as well.

The main argument behind using non-fluorine/fluorine-free salts is lack of the fluorine in their content. However, as the presentation will prove, there are other advantages of using them, namely better conductivity and stability.

### Acknowledgments

This work has been financially supported by the Warsaw University of Technology.

### References

1. L. Niedzicki, M. Bukowska, T. Trzeciak, A. Bitner, P. Szczecinski, M. Marcinek, W. Wieczorek, *Polish patent PL232856* (2019).
2. L. Niedzicki, T. Trzeciak, J. Niewiedzial, *Polish patent PL227209* (2017).

## Electrochemical Behavior of SiO<sub>2</sub>-Containing Electrodes in Lithium Battery Systems: Effect of the SiO<sub>2</sub> Production Methods

R.D. Apostolova<sup>1</sup>, S.P. Kuksenko<sup>2</sup>

<sup>1</sup> Ukrainian State University of Chemical Technology, Dnipro, 49005 Ukraine, e-mail apostolova.rd@gmail.com<sup>1</sup>

<sup>2</sup> Chuiko Institute of Surface Chemistry, National Academy of Sciences of Ukraine, General Naumov str. 17, Kyiv, 03164 Ukraine

SiO<sub>2</sub> dioxide with a high theoretical capacity (1784 mAh g<sup>-1</sup>) belongs to a series of materials being developed to replace the less energy consuming graphite (372 mAh g<sup>-1</sup>) in the negative electrodes of commercial lithium-ion batteries (LIBs). The actual capacity of SiO<sub>2</sub> dioxide is less than the theoretical one, since it depends on a number of reasons that restrain the expanded industrial production of LIBs based on it. There are 16 SiO<sub>2</sub> polymorphs, the electrochemical properties of which are largely determined by the manufacturing process. This presentation shows different electrochemical behavior SiO<sub>2</sub>-containing electrodes prepared using different technologies, with an emphasis on the need to identify the true mechanisms of effective electrode processes, excluding harmful side effects.

### Electrodes with "nano-Si/SiO<sub>2</sub>" and "nano-Si@SiO<sub>2</sub>" powders

The electrochemical behavior of the two types of electrodes have been studied (Fig. 1): from a silicon nanopowder with a natural layer of silicon oxide on its surface (is marked as "nano-Si/SiO<sub>2</sub>") and micropowder of silicon clusters embedded into a matrix of silicon dioxide (is marked as "nano-Si@SiO<sub>2</sub>"), which was obtained by heat treatment SiO at 1100 °C in the stream of Ar. When the silicon nanopowder is stored in air, its surface oxidizes to give a natural oxide layer with a thickness of ~6 nm. The "nano-Si/SiO<sub>2</sub>" powder is constituted by highly structured aggregates of ~30 nm particles with the specific surface area of 70–80 m<sup>2</sup>/g and bulk density (weight divided by geometric volume) of approximately 0.08 g/cm<sup>3</sup>. The broadening of the peaks for (111) and (220) faces in the X-ray diffraction pattern indicates that the size of single-crystal regions does not exceed 19–20 nm (the crystallite size was calculated by the Scherrer equation). The "nano-Si@SiO<sub>2</sub>" powder is constituted by amorphous ~5 nm silicon clusters distributed in volume of SiO<sub>2</sub>. Electrodes were fabricated from "nano-Si/SiO<sub>2</sub>" and "nano-Si@SiO<sub>2</sub>" powders using synthetic graphite KS6 (TIMCAL, Switzerland) with isometric particles 6.5 μm in size (D<sub>90</sub>) and a specific surface area of 20.0 m<sup>2</sup>/g as electrochemically active and electrically conductive additive: 4KS6+1nano-Si/SiO<sub>2</sub> (with 15 wt.% PVDF) and 2KS6+1nano-Si@SiO<sub>2</sub> (with 8 wt.% PVDF). The electrode paste suspensions were uniformly deposited as viscous substances (as a 100–110 μm thick layer) onto a 20 μm thick Cu-foil serving as a current collector. The electrode layers were then compacted by rolling to a working thickness of ~80 μm. The electrode cycling parameters were studied with half-cells of R2016 size, in which lithium metal acted simultaneously as counter and reference electrode. As electrolyte served 1M solution of LiPF<sub>6</sub> in a mixture of FEC+EMC (30:70 vol.%) with addition of VC (3 wt.%) and ES (2 wt.%) [1–3]. The half-cells cycling was performed at 25°C (Fig. 1, a) and 50°C (Fig. 1, b) in the *cc/cv* (charge) and *cc* (discharge) modes: 250 mA/g,

10 mV, 25 mA/g and 250 mA/g, 1.0 V (Fig. 1, *a*); 60 mA/g, 10 mV, 6 mA/g and 60 mA/g, 1.0 V (Fig. 1, *b*).

The charge-discharge curves of both electrodes are identical except for some voltage plateau on the charging curve Fig. 1, *a*, which becomes more pronounced in subsequent cycles after the first one [4]. Its appearance is explained by the formation of intermetallic  $\text{Li}_{15}\text{Si}_4$ , which is impossible in the case of amorphous silicon (Fig. 1, *b*). The using of "nano-Si/SiO<sub>2</sub>" in the electrode contributes to its stable cycling (charge-discharge curves are practically superimposed on each other after the first cycle). In the case of "nano-Si@SiO<sub>2</sub>" is observed characteristic only of a-Si and graphite the course of charge-discharge curves.

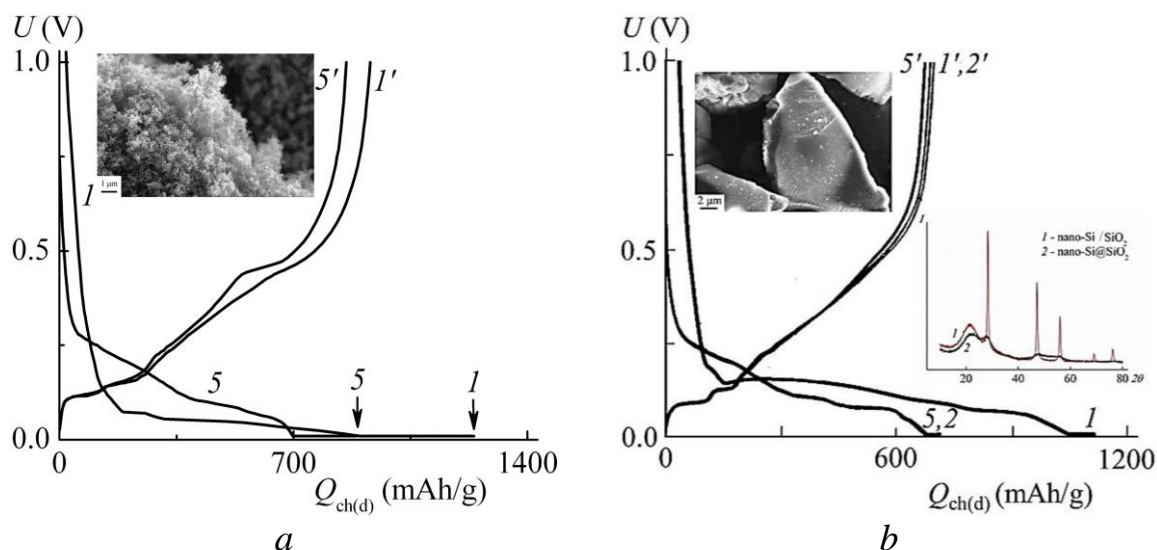


**Figure 1.** Charge-discharge curves of the half-cells with "nano-Si/SiO<sub>2</sub>"- (*a*) and "nano-Si@SiO<sub>2</sub>"-based electrodes in cc/cv (charge) and cc (discharge) modes. Inserts: micrographs of "nano-Si/SiO<sub>2</sub>" (*a*), "nano-Si@SiO<sub>2</sub>" (*b*) powders and their X-ray diffraction spectrums (*b*).

In the case of both electrodes, we found no evidence of direct electrochemical reduction of SiO<sub>2</sub>.

### Galvanic synthesis method and the advantages of synthesized product electrochemical characteristics

It was proposed an electrochemical synthesis of a thin-layer SiO<sub>2</sub>/Ni composite and demonstrates the features of its electrochemical interaction with lithium. Silicon dioxide was obtained by sulfuric-acid-driven precipitation from a solution of sodium-based liquid glass  $\text{Na}_2\text{SiO}_3 \cdot m\text{H}_2\text{O}$  with a density of 1.08 g/cm<sup>3</sup>. The SiO<sub>2</sub> precipitate was used for galvanic preparation of the SiO<sub>2</sub>/Ni composite [5]. The thin-layer composite was deposited on a cathode made of nickel foil in an electrolytic cell with a nickel anode. The cathode was positioned horizontally, and the suspension of SiO<sub>2</sub> in an electrolyte for nickel-plating was poured into the electrolytic cell. At the first, the precipitation of SiO<sub>2</sub> particles onto the nickel electrode occurred in the absence of current. Then, the current was switched for galvanic fixing of SiO<sub>2</sub> particles onto the nickel electrode. The electrolyte composition for deposition of the composite (in g/L) was as follows: NiSO<sub>4</sub>·7H<sub>2</sub>O, 150; Na<sub>2</sub>SO<sub>4</sub>·5H<sub>2</sub>O, 25; H<sub>3</sub>BO<sub>3</sub>, 15; KCl, 10; SiO<sub>2</sub>, 2; pH = 5–6.:  $S_{\text{cathode}} : S_{\text{anode}} = 1 : 20$ ;  $i_{\text{cathode}} = 1.5\text{--}2.0 \text{ mA/cm}^2$ . Heat treatment of SiO<sub>2</sub>/Ni composite: 105°C for 6–7 h. Here  $S_{\text{cathode}} : S_{\text{anode}}$  are the cathode and anode surface area, respectively, cm<sup>2</sup>. The electrochemical characteristics of SiO<sub>2</sub> were studied with galvanostatic charge-discharge cycling using a prototyping LIB with

2016 dimensions, on a test bench equipped with computer software. The prototyping battery was filled with an electrolyte with the following composition: dimethoxyethane (Merck), dioxolane (Acros), and 1 mol/L LiBF<sub>4</sub> (Advanced Research Chemicals).

On the XRD data, synthesized oxide belongs to an amorphous modification (Fig. 2a). The synthesized silicon dioxide has the following parameters: the mass part of moisture is 6.2%, the specific surface area is 202 m<sup>2</sup>/g, and the bulk density is 220 g/dm<sup>3</sup>. In accordance with the size distribution histogram for SiO<sub>2</sub> particles, their maximum size does not exceed 22 nm and reaches 12–16 nm in the main fraction (Fig. 2b). The reversible performance of SiO<sub>2</sub> occurrences at current density of 30 μA/cm<sup>2</sup> (Fig. 2c, the part of the charge curve 1 without the fluctuations). At the 80 μA/cm<sup>2</sup> the fluctuations arise as the result of the volume of expansion of the active electrode component, and the second horizontal voltage area with a slope appears below 0.1 V. The advantage of the synthesized material is the possibility of obtaining stable cycling at an almost fixed voltage. This is facilitated by the encapsulation of the oxide with a homogeneous distribution in a rigid nickel matrix. This effect is not achieved in an electrode with synthesized SiO<sub>2</sub> in a composition with graphite filler and a binder in the presence of domains and aggregates of active material particles (Fig. 2d).

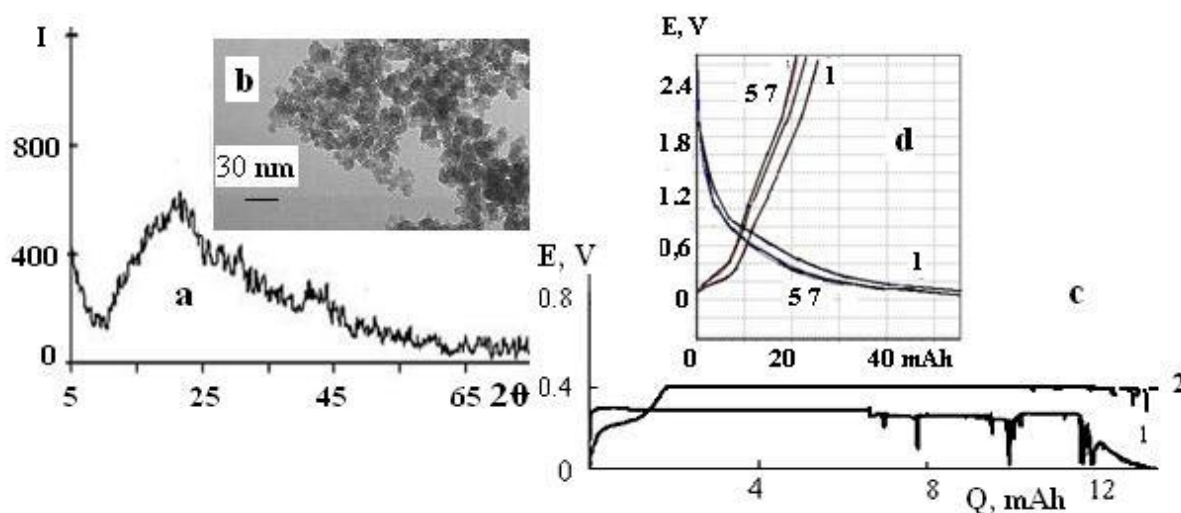


**Figure 2.** The investigation data of SiO<sub>2</sub>/Ni composite (a, c) and SiO<sub>2</sub> (b, d): a – XRD pattern, b – the image in CEM, c, d – charge-discharge curves.

## Conclusion

Thus, we did not find confirmation of SiO<sub>2</sub> electrochemical reduction in electrodes with "nano-Si/SiO<sub>2</sub>" and "nano-Si@SiO<sub>2</sub>" powders and also with synthesized domains and aggregates SiO<sub>2</sub> in a composition with graphite filler and a binder. The advantage of the SiO<sub>2</sub>/Ni composite is the possibility of obtaining stable cycling at an almost fixed voltage.

## References

1. Kuksenko S.P., Kovalenko I.O. Synthesis of a Silicon–Graphite Composite for the Hybrid Electrode of Lithium-Ion Batteries. *Russ. J. Appl. Chem.* 2010. **83**(10): 1811.
2. Kuksenko S.P., Kovalenko I.O. Silicon Nanopowder as Active Material for Hybrid Electrodes of Lithium-Ion Batteries. *Russ. J. Appl. Chem.* 2011. **84**(7): 1179.

3. Kuksenko S.P. Aluminum Foil as Anode Material for Lithium–Ion Batteries: Effect of Electrolyte Compositions on Cycling Parameters. *Russ. J. Electrochem.* 2013. **49**(1): 67.
4. Kuksenko S.P., Kaleniuk H.O., Tarasenko Yu.O., Kartel M.T. Stable silicon electrodes with polyvinilidenfluoride-binder for lithium-ion batteries. *Him. Fiz. Tehnol. Poverhn.* 2020. **11**(1): 58 [in Ukrainian].
5. Pat. UA118820. Apostolova R.D., Matsiyevsky M.A., Gladun V.A., Savchenko M.O.. Method of electrochemical obtaining of thin-layer SiO<sub>2</sub>/Ni composite electrodes for lithium-ion batteries. Publ. 2019.

## Spinel Structured High Entropy Oxide (CoFeCrNiAl)<sub>3</sub>O<sub>4</sub> as Anode Active Material in Lithium-ion Batteries

D. Csik<sup>a,b</sup>, D. Zalka<sup>b,c</sup>, K. Saks<sup>b,d</sup>, A. Straková Fedorková<sup>c</sup>, D. Capková<sup>c</sup>

<sup>a</sup> Department of Materials Science, Faculty of Materials, Metallurgy and Recycling, Technical University of Košice, Letná 9, 042 00, Košice, Slovak Republic

<sup>b</sup> Institute of Materials Research, Slovak Academy of Sciences, Watsonova 47, 040 01, Košice, Slovak Republic

<sup>c</sup> Department of Physical Chemistry, Faculty of Sciences, Pavol Jozef Šafárik University in Košice, Moyzesova 11, 041 54, Košice, Slovak Republic

<sup>d</sup> Institute of Physics, Faculty of Sciences, Pavol Jozef Šafárik University in Košice, Park Angelium 9, 040 01, Košice, Slovak Republic

Transition-metal based high entropy oxides (HEO) are a new type of active materials in lithium-ion batteries which possess high specific capacity and cyclability and can efficiently alleviate volume changes during charging and discharging. Here, a novel spinel structured high entropy oxide (CoFeCrNiAl)<sub>3</sub>O<sub>4</sub> is synthesized. Single phase HEO was prepared oxidizing a high entropy alloy (CoFeCrNiAl) at 1000 °C under pure oxygen atmosphere. X-ray diffraction was used to reveal the phase composition of the alloy and the oxide. Electrochemical properties of the HEO were investigated in half-cells (vs. Li metal). The initial discharge capacity of the HEO was 533 mAh.g<sup>-1</sup>. The discharge potential plateau was around 0.25 V vs. Li/Li<sup>+</sup>.

### Introduction

On 14 July 2021, the European Commission adopted legislative proposals to achieve climate neutrality in the EU by 2050 (1). Electric mobility can help the European Union to achieve its goals, e.g. reducing greenhouse gas emissions, air pollution and dependence on oil (2). Lithium-ion batteries (LIB) are evaluated as one of the best choices because of their high specific energy and energy density. Commercial LIBs have theoretical capacity approx. 200-300 mAh.g<sup>-1</sup>, but their actual capacities are lower, around 100-200 mAh.g<sup>-1</sup>. Because of that, their weight in an electric vehicle is around 200-500 kg which means a range of up to 200-400 km. The most used commercial anode active material is graphite which is limited by its relatively low gravimetric capacity. Alternative materials to graphite are intercalation materials, such as Si, P, Sb and conversion materials, such as metal oxides which can deliver considerably higher capacity, but both types of materials suffer from pulverization and volume changes during the cycling process, resulting in capacity fading. Recently, it has been shown that high entropy oxides exhibit superior electrochemical properties as anode active materials due to their entropy stabilization effect (3-7). They can deliver remarkable reversible capacity (1235 mAh.g<sup>-1</sup> at current density 100 mA.g<sup>-1</sup>) (7), high-rate capability (500 mAh.g<sup>-1</sup> at current density 2000 mA.g<sup>-1</sup>) (7) and cycle stability (500 cycles without significant capacity fading) (5).

In this work, we prepared a novel spinel structured high entropy oxide  $(\text{CoFeCrNiAl})_3\text{O}_4$  and analyze its electrochemical properties in lithium-ion battery configuration. Without any optimization of the electrode, we obtained for the prepared HEO relatively high discharge capacity, around  $533 \text{ mAh.g}^{-1}$ .

## Experimental

Pure elements (Co, Fe, Cr, Ni, Al – 99.9 wt.%) were used to prepare a high entropy alloy by arc melting under Ar atmosphere in a Mini Arc Melter. The so-called pre-alloy was then milled into powder by a vibration mill. Subsequently the powder particles of the pre-alloy were oxidized at high temperature ( $1000 \text{ }^\circ\text{C}$ ) under  $\text{O}_2$  atmosphere in a tube furnace. The final step of the preparation involved vibration milling of the obtained high entropy oxide. The crystalline structure of the high entropy alloy and oxide was examine using an X-ray diffractometer with a Cu  $K\alpha$  radiation source.

Electrochemical performance test was carried out in an El-Cell. The HEO active material (80 wt. %) and amorphous carbon (10 wt. %) were mixed in a mortar. PVDF (10 wt. %) were dissolved in NMP then the mixture of the HEO and carbon was added to the binder solution and mixed on a magnetic stirrer for 24 h. Subsequently the slurry was cast onto copper foil (the thickness of the wet film was  $100 \text{ }\mu\text{m}$ ) and dried at  $80 \text{ }^\circ\text{C}$  for 24 h. The electrodes were cut out in the diameter of 18 mm and pressed (50 MPa). The active material loading was approx.  $\sim 2.6 \text{ mg.cm}^{-2}$ . The half cells with Li metal foil ( $\text{Ø} 18 \text{ mm}$ ) and glass fiber separator (Whatman GF/A -  $\text{Ø} 18 \text{ mm}$ ) were assembled in an argon filled glovebox ( $\text{H}_2\text{O}$  and  $\text{O}_2$  content  $< 1 \text{ ppm}$ ). The electrolyte used was 1 M  $\text{LiPF}_6$  in a mixture of EC/DMC 50/50 vol. %.

The XRD analysis of the materials revealed that the high entropy alloy has a single-phase cubic structure of the Im-3m space group (COD no. 00-151-2502),  $R_{\text{wp}}=1.62 \text{ \%}$ . After the oxidizing process in an oxygen atmosphere the crystal structure changed into a single-phase cubic structure of the Fd-3m space group (COD no. 00-900-2323),  $R_{\text{wp}}=2.89 \text{ \%}$ . The low  $R_{\text{wps}}$  indicate the results of refinement are highly reliable. To analyze the electrochemical performance of the obtained HEO galvanostatic charge-discharge measurement was carried out. The initial discharge capacity was around  $533 \text{ mAh.g}^{-1}$  at a current density of  $45 \text{ mA.g}^{-1}$ , which is significantly lower than the theoretical capacity of the HEO (approx.  $995 \text{ mAh.g}^{-1}$ ). The discharge potential plateau was around  $0.25 \text{ V}$  vs.  $\text{Li/Li}^+$ . In the subsequent cycles the capacity was extremely reduced to  $11 \text{ mAh.g}^{-1}$  in the third cycle (Figure 1.). The SEM examination revealed that carbon dissolution occurred during the cycling which causes loss of the electrical contact of the active material.

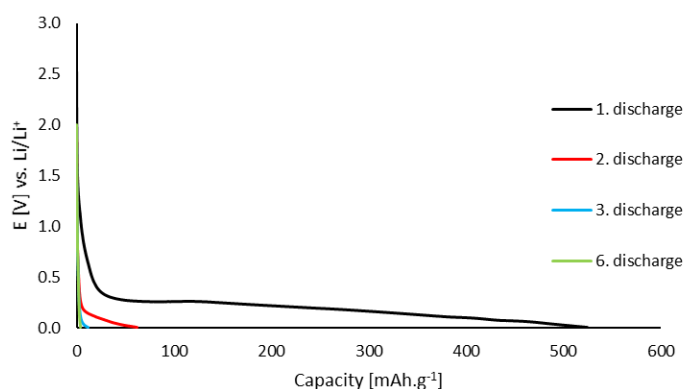


**Figure 1.** Discharge capacities of the  $(\text{CoFeCrNiAl})_3\text{O}_4$  electrode at current density of  $45 \text{ mA.g}^{-1}$

## Conclusions

In this work, a novel high entropy oxide (CoFeCrNiAl)<sub>3</sub>O<sub>4</sub> is described as a potential anode active material in lithium-ion batteries. To best of our knowledge, this preparation method has not yet been used to prepare high entropy oxides. Without any optimization of the electrode and cell design, a relatively high discharge capacity was obtained (533 mAh.g<sup>-1</sup>) in the first cycle. The discharge potential plateau was a little bit higher than that of lithium (0.25 V vs. Li/Li<sup>+</sup>) which is necessary to obtain high voltage electrochemical full cells. Further examination of the electrochemical properties of the synthesized high entropy oxide requires optimization of the electrode preparation process. This work highlights the potential usage of high entropy oxides as anode active materials in lithium-ion batteries.

## Acknowledgments

This work was realized within the frame of the project „Research centre for progressive materials and technologies for present and future applications „PROMATECH“, ITMS 26220220186; supported by the Operational Program “Research and Development” financed through European Regional Development Fund, by the projects of Slovak Research and Development Agency APVV-20-0138, APVV-15-0202, PP-COVID-20-0025 and of Slovak Grant Agency VEGA 2/0021/16.

## References

1. EU Emissions Trading System. (2021). European Commission. [https://ec.europa.eu/clima/policies/ets\\_en](https://ec.europa.eu/clima/policies/ets_en)
2. M. Niestadt and A. Bjørnåvold, Electric road vehicles in the European Union: Trends, impacts and policies. (2019) [https://www.europarl.europa.eu/RegData/etudes/BRIE/2019/637895/EPRS\\_BRI\(2019\)63789\\_5\\_EN.pdf](https://www.europarl.europa.eu/RegData/etudes/BRIE/2019/637895/EPRS_BRI(2019)63789_5_EN.pdf)
3. N. Qiu, H. Chen, Z. Yang, S. Sun, Y. Wang, Y. Cui, A high entropy oxide (Mg<sub>0.2</sub>Co<sub>0.2</sub>Ni<sub>0.2</sub>Cu<sub>0.2</sub>Zn<sub>0.2</sub>O) with superior lithium storage performance, *J. Alloys Compd.* 777 (2019) 767–774.
4. D. Wang, S. Jiang, C. Duan, J. Mao, Y. Dong, K. Dong, Z. Wang, S. Luo, Y. Liu, X. Qi, Spinel-structured high entropy oxide (FeCoNiCrMn)<sub>3</sub>O<sub>4</sub> as anode towards superior lithium storage performance, *J. Alloys Compd.* 844 (2020) 156158.
5. A. Sarkar, L. Velasco, D. Wang, Q. Wang, G. Talasila, L. de Biasi, C. Kübel, T. Brezesinski, S.S. Bhattacharya, H. Hahn, B. Breitung, High entropy oxides for reversible energy storage, *Nat. Commun.* 9 (2018).
6. H. Chen, N. Qiu, B. Wu, Z. Yang, S. Sun, Y. Wang, A new spinel high-entropy oxide (Mg<sub>0.2</sub>Ti<sub>0.2</sub>Zn<sub>0.2</sub>Cu<sub>0.2</sub>Fe<sub>0.2</sub>)<sub>3</sub>O<sub>4</sub> with fast reaction kinetics and excellent stability as an anode material for lithium ion batteries, *RSC Adv.* 10 (2020) 9736–9744.
7. T.X. Nguyen, J. Patra, J.K. Chang, J.M. Ting, High entropy spinel oxide nanoparticles for superior lithiation-delithiation performance, *J. Mater. Chem. A.* 8 (2020) 18963–18973.

## Lithium-Titanate as Electrode Material for Aprotic Systems

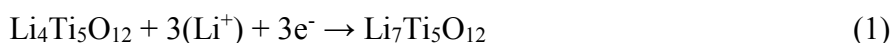
M. Fíbek<sup>a</sup>, J. Libich<sup>a</sup>, J. Máca<sup>a</sup> and A. Šimek<sup>a</sup>

<sup>a</sup>Department of Electrical and Electronic Technology, The Faculty of Electrical Engineering and Communication, Brno University of Technology, Technická 3058/10 616 00, Brno, Czech Republic

This article briefly describes experiments which investigate the mutual compatibility of aprotic solvents with higher fire safety and Lithium Titanate Oxide (LTO) as the negative electrode material for lithium-ion batteries. The work follows the current trend of enhancing fire safety by using new kinds of aprotic solvents along with a new generation of electrode materials which fulfil the intended using of lithium-ion batteries for high power applications, e.g. electric vehicle propulsion. In our work, the examiner of using sulfolane electrolyte (SL) and  $\text{Li}_4\text{Ti}_5\text{O}_{12}$  (LTO) under various ambient temperatures. The influence of electrolyte on the proper operation and stability of negative electrode material was considered. The measurements were performed in the temperature range from 25 °C up to 80 °C with half-cell connection. Our main objective of these experiments was to prove and investigate a proper operation of an aprotic electrolyte with higher fire safety together with LTO negative material under high ambient temperatures.

### Introduction

Lithium-ion batteries are extended to many application areas due to their advantageous ratio of energy stored per kilogram of battery weight and environmental friendliness. Today they are used mainly in the application of small portable electronic devices. With the development of electromobility, it represents space for a new power application of lithium-ion batteries and the associated increased demands on their power load, stability and safety. In the field of negative electrode materials for lithium-ion batteries, graphite still dominates, mainly due to its price and the established technological process of processing. Lithium Titanate Oxide,  $\text{Li}_4\text{Ti}_5\text{O}_{12}$  (LTO), can be considered as a suitable replacement, this material works on a similar principle of intercalation (insertion) of lithium ions into the structure of the material. Unlike graphite, however, it has a spinel (tunnel) structure and when lithium ions interact with its structure, conversion occurs, ie the incorporation of lithium atoms into the structure of the material, see the notation of the half-reaction in equation [1] below. As can be seen in Figure 1, there is three electron exchange during charging-discharging process.



The LTO work potential is significantly higher than the graphite potential (0.2 V vs. Li /  $\text{Li}^+$ ) of approximately 1.55 V vs. Li /  $\text{Li}^+$ , this disadvantage can be partially compensated by using more

positive positive electrode materials, their working potential is approximately 5 V vs. Li / Li<sup>+</sup>. In contrast, the higher working potential has the advantage of a very thin Solid Electrolyte Interface (SEI) layer, which represents a lower irreversible capacity loss during the first initialization cycle. Furthermore, the higher working potential limits the growth of lithium dendrites, which can cause the cell to short-circuit in cases where it penetrates the separator. Another disadvantage of LTO material over graphite is its lower theoretical capacity of 175 mAh/g (graphite 372 mAh/g). A significant safety advantage of LTO is its thermal stability and safety LTO material is able to withstand higher current loads than graphite without thermal decomposition, experiments with DSC (Differential Scanning Calorimetry) have shown that fully lithium (charged) LTO material exhibits thermal flow 383 J/g, which is several times less than in the case of graphite 2700 J/g, which is an important aspect of fire safety of the material.

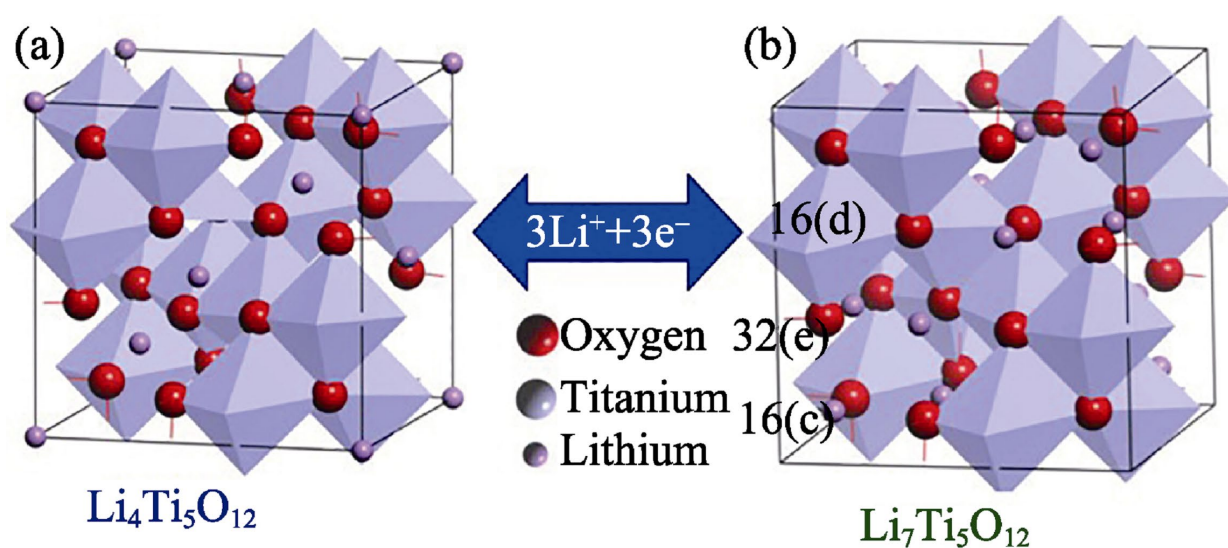


**Figure 1.** Crystal structure of LTO negative electrode material and its changes during charge and discharge (2).

### Acknowledgment

This work was supported by the specific graduate research of the Brno University of Technology No. FEKT-S-20-6206.

### References

1. A. N. Yi, X. U. E. Bing, Journal of Inorganic Materials, 33 (5) (2018).

## The study of cathode material stability after disassembly of Li-ion cell

P. Guricová<sup>1</sup>, O. Čech<sup>1</sup>, T. Kazda<sup>1</sup>

<sup>1</sup> Department of Electrical and Electronic Technology, Faculty of Electrical Engineering and Communication, BUT, Technická 10, 616 00 Brno, Czech Republic

Structural changes in cathode material extracted from LiCoO<sub>2</sub> (LCO) type cell as a function of aging and storage time was studied. Ex-situ X-ray diffraction analysis was used for observation of differences between materials separated from cell in a fresh state and aged cell. Phase transition happening in the LiCoO<sub>2</sub> material during cycling of the battery but also when in contact with air are discussed. Shift of the main peak (0 0 3) and (1 0 4) for the aged cathode material are displayed and discussed.

### Introduction

With rapidly growing production of Li-ion accumulators in the last couple of years, many researches have been focused on recycling the cathode materials. Before recycling however, it is important to understand the ongoing processes happening inside material structure. During repeated cycling of the battery there is gradual degradation resulting in capacity loss over time. When recovering such material, restoring its original concentration of lithium ions is important. In addition, the stability of the separated material is significant in the means of longer storage times after separation. After demounting of the battery is cathode apart from defects after cycling affected also by other ongoing processes like self-discharging or interaction of certain elements with air [1].

Lithium cobalt oxide (LiCoO<sub>2</sub>), which is a commonly used cathode material in Li-ion accumulators because of its high specific energy and good reliability. It can exist in two forms: low-temperature (LT) and high-temperature (HT) LiCoO<sub>2</sub>. HT LiCoO<sub>2</sub> is preferred as a cathode material due to its hexagonal structure with space group R-3m. This order of atoms ensures more efficient intercalation process. During this process (Li<sup>+</sup> insertion/extraction) three-order phase transition takes place, causing distortion of lattice structure and decrease in capacity. After the active material has been isolated from the cell, exposure to air can also lead to undesirable reactions and to the degradation of material. It was found that during aging for longer times formation of the spinel phase appears. Self-discharge, which occurs mainly as a result of reactions between electrodes and electrolyte and phase transition from hexagonal to cubic phase are also considered to be the reason for capacity loss [2][3].

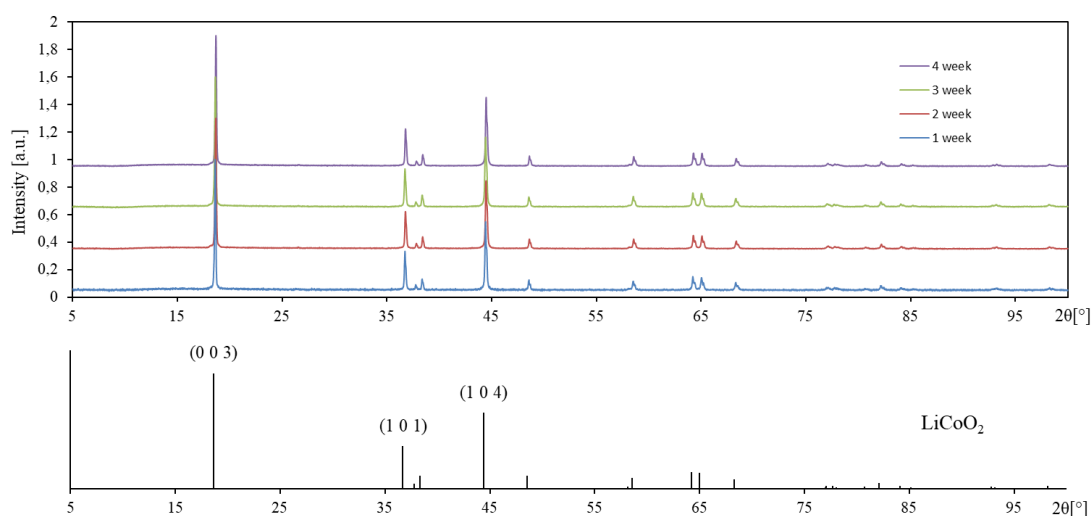
### Experimental

Two Samsung ICR 18650-20R cells were chosen for the experiment. First one was in fresh state and the second cell was first cycled with 500 cycles and 1C rate. After aging of the second battery, both cells were discharged to 2.5 V and disassembled in a hood. Separated cathode materials were extracted from aluminium collector using organic solvent DMSO (dimethylsulfoxide) heated to 50°C. Substance was left on air during one month. Structure of the material was observed every week using X-ray diffraction analysis (XRD).

For the XRD measurements was used a Rigaku MiniFlex 600 diffractometer in 2Theta/Theta configuration with Cu-K $\alpha$  radiation. The sample was fixed in glass sample holder.

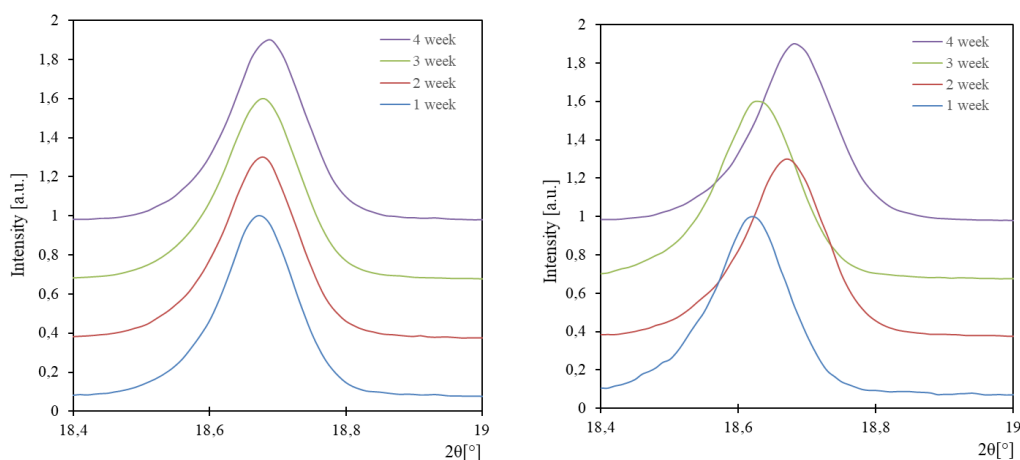
## Discussion

Figure 1 shows XRD patterns of the cathode material extracted from commercial cell Samsung 18650-20R after aging. X-ray scan confirmed that the studied material has a structure of LiCoO<sub>2</sub> with space group R-3m belonging to the trigonal system. The two most intense peaks of the spectrum are peak (0 0 3) at  $\approx 18.5^\circ$  and (1 0 4) at  $\approx 44.5^\circ$ . No considerable changes are visible on the overall spectrum, however there are changes in peak position in closer display of single peaks.



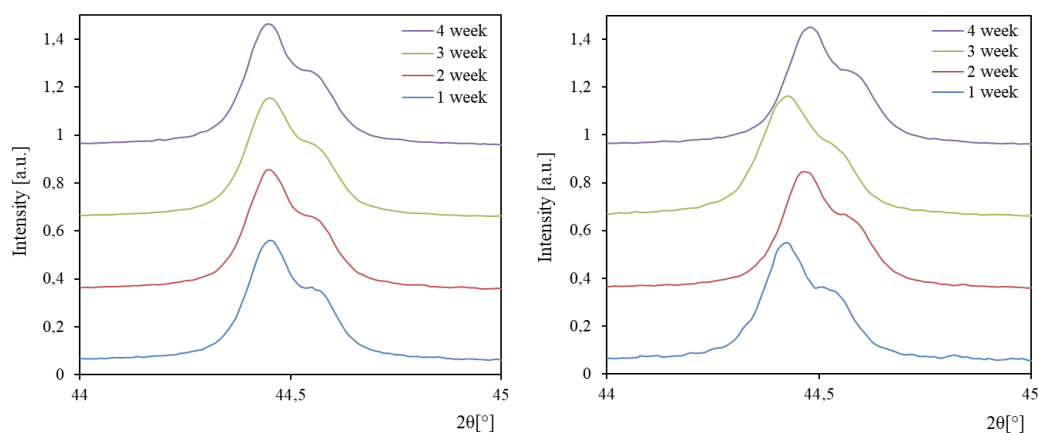
**Figure 1.** Diffractogram for LiCoO<sub>2</sub> cathode material after aging

Figure 2 displays the most intense peak (0 0 3) of the LiCoO<sub>2</sub> structure. It is visible that for the fresh cell the peaks are in good accordance for all measurements during longer period of time. However, for the aged cell there is visible shift in the peak position, which is similar to the shift of the structure during charging of the battery (delithiation). This process is followed by change of lattice constants.



**Figure 2.** Comparison between the main peak (0 0 3) of cathode material extracted from fresh state cell (left) and aged cell (right)

Figure 3 shows evolution of peak (1 0 4). Similarly to the results shown in Figure 3, peaks for the aged cell show the same tendency in the direction of drift, they are moving to higher angles. Diffraction patterns for the cell in fresh state were again found to be consistent with a single phase.



**Figure 3.** Comparison between the peak (1 0 4) of cathode material extracted from fresh state cell (left) and aged cell (right)

XRD results demonstrate that all diffraction peaks of the measured samples are in good accordance with that of the pure  $\text{LiCoO}_2$  layered structure in the R-3m space group. That means that during longer times when the material is in contact with air, no impurities are being formed. However, in close-up look we can see that some reactions are taking place on the material structure similar to the delithiation. During this particular time period, the delithiation was not so intense to change the space group from hexagonal to monoclinic.

### Conclusion

A comparison between measured data for the cell in a fresh state did not reveal any significant differences unlike the results for aged cell. In contrary, cycled cathode material has somehow disordered structure of lithium ions because of aging, therefore it is more likely to undergo delithiation after disassembly of the battery. We conclude that the apparent shift in peaks upon storage is not due to structural changes, but rather due to delithiation reactions on the  $\text{LiCoO}_2$  electrode.

### Acknowledgement

This work was supported by the specific graduate research of the Brno University of Technology No. FEKT-S-20-6206.

### References

1. OZAWA, Yasunori, Rachid YAZAMI a Brent FULTZ. An XRD Study of Chemical Self-Discharge in Delithiated Cobalt Oxide. *Electrochemical and Solid-State Letters*. 2004, 8(1), 38-41. Dostupné z: doi:10.1149/1.1830395
2. PEGORETTI, V.C.B, P.V.M DIXINI, P.C SMECELLATO, S.R BIAGGIO a M.B.J.G FREITAS. Thermal synthesis, characterization and electrochemical study of high-temperature (HT) LiCoO<sub>2</sub> obtained from Co(OH)<sub>2</sub> recycled of spent lithium ion batteries. *Materials research bulletin*. Elsevier, 2017, 86, 5-9. ISSN 0025-5408. Dostupné z: doi:10.1016/j.materresbull.2016.09.032
3. FANG, Ting, Jenq-gong DUH a Shyang-roeng SHEEN. LiCoO<sub>2</sub> cathode material coated with nano-crystallized ZnO for Li-ion batteries. *Thin solid films*. Elsevier B.V, 2004, 469-470, 361-365. ISSN 0040-6090. Dostupné z: doi:10.1016/j.tsf.2004.08.151

## **Research on lithium-iron-phosphate cells (LiFePO<sub>4</sub>) in terms of temperature hazard during operation**

W. Kurpiel

The presentation will present the results of hazard tests, especially the temperature, for selected lithium-ion-phosphate cells operated, however, in accordance with the manufacturer's recommendations, but used in arduous mining conditions. This applies to the performance of the cells in the battery packs without any management system (BMS). This especially applies to threats in the case of accidental, cyclical, slight overloads and discharge of cells.

## Rate Capability Testing of Graphite Electrode Material

J. Libich<sup>a</sup>, J. Máca<sup>a</sup>, M. Sedlaříkova<sup>a</sup>, A. Šimek<sup>a</sup>, P. Čudek<sup>a</sup>, A. Chekannikov<sup>b</sup> and G. Fafilek<sup>c</sup>

<sup>a</sup>Department of Electrical and Electronic Technology, FEEC, Brno University of Technology, 616 00 Brno, Czech Republic

<sup>b</sup>Moscow Institute of Physics and Technology, 9 Institutskiy per., Dolgoprudny, Moscow, 141701, Russian Federation

<sup>c</sup>Vienna University of Technology, Getreidemarkt 9, 1060 Vienna, Austria

The paper deals with the investigation of natural graphite electrode materials for lithium-ion batteries. These negative electrode materials operate on the intercalation principle where graphite plays a host role for lithium ions. There is a solid electrolyte interphase (SEI) layer which originates from electrode-electrolyte interphase. The SEI layer is a fundamental part of lithium-ion battery system and its quality defines and highly affects the overall quality of lithium-ion battery itself. Growth of the SEI layer is connected with the formation of new compounds. The process of SEI layer formation is linked to energy consumption (energy loss). What is most important is the fact that the growth of SEI layer consumes a significant amount of lithium ions provided from a limited positive electrode (cathode) source. In this work, the lithiation method was employed to reduce these undesirable side effects of the SEI growth.

### Introduction

It is not necessary to introduce the lithium-ion batteries, from their discovery in the market since 1991 they undergo concentrated research and development which make the lithium-ion battery the best battery system of all times.

The working potential of the negative electrode is related to the formation of a solid polymer compound at the interface between the fixed electrode and the liquid electrolyte. This layer, called the Solid Electrolyte Interface (SEI) in English, has the characteristics that affect the entire lithium-ion battery system. This layer is formed both at the interface between the negative electrode and the electrolyte and at the interface between the positive electrode and the electrolyte. Its chemical and physical properties differ depending on the working potential window of the individual electrodes. In the case of a negative electrode, at a low reduction potential, approximately 0.2 V vs. Li/Li<sup>+</sup> begins to form at the interface a polymer layer formed by the decomposition products of the electrolyte. The formation of the SEI layer is necessary for the function of the lithium-ion battery. The function of this layer consists primarily (from the point of view of the negative electrode) in preventing the reduction of lithium cations present in the electrolyte, thus maintaining the electron charge in the negative electrode. The SEI layer represents a selective membrane, thanks to which lithium ions can pass through the layer, but for electrons the layer is insulating, i.e. non-conductive. The layer is formed

during the first and second charging cycles, the so-called formatting cycles, in subsequent cycles the layer is already stable. The electrolyte decomposes on the surface of the negative electrode to form a polymer film composed of inorganic and organic components of the electrolyte and the electrode. This layer ensures stability between the electrolyte and the electrode and prevents further decomposition, on the other hand, the layer consumes and irreversibly binds part of the lithium during its formation, thus reducing the capacity of the lithium-ion cell. The composition, thickness, morphology and density of the SEI layer significantly affect the performance of the whole article. The amount of irreversible lithium losses during the formation of the SEI layer depends on the specific area of the electrode, ie the area of the electrode-electrolyte interface. The larger the specific surface area of the electrode (porosity), the larger the area covered by the SEI layer, and thus the greater the cell capacity losses. In general, the magnitude of the loss of theoretical capacity of the cell caused by the formation of the SEI layer in the range of 18% to 45% is reported. Figure 1 shows a lithiation system consisting of metallic lithium, a lithiated material such as graphite, this material being deposited on a copper collector.

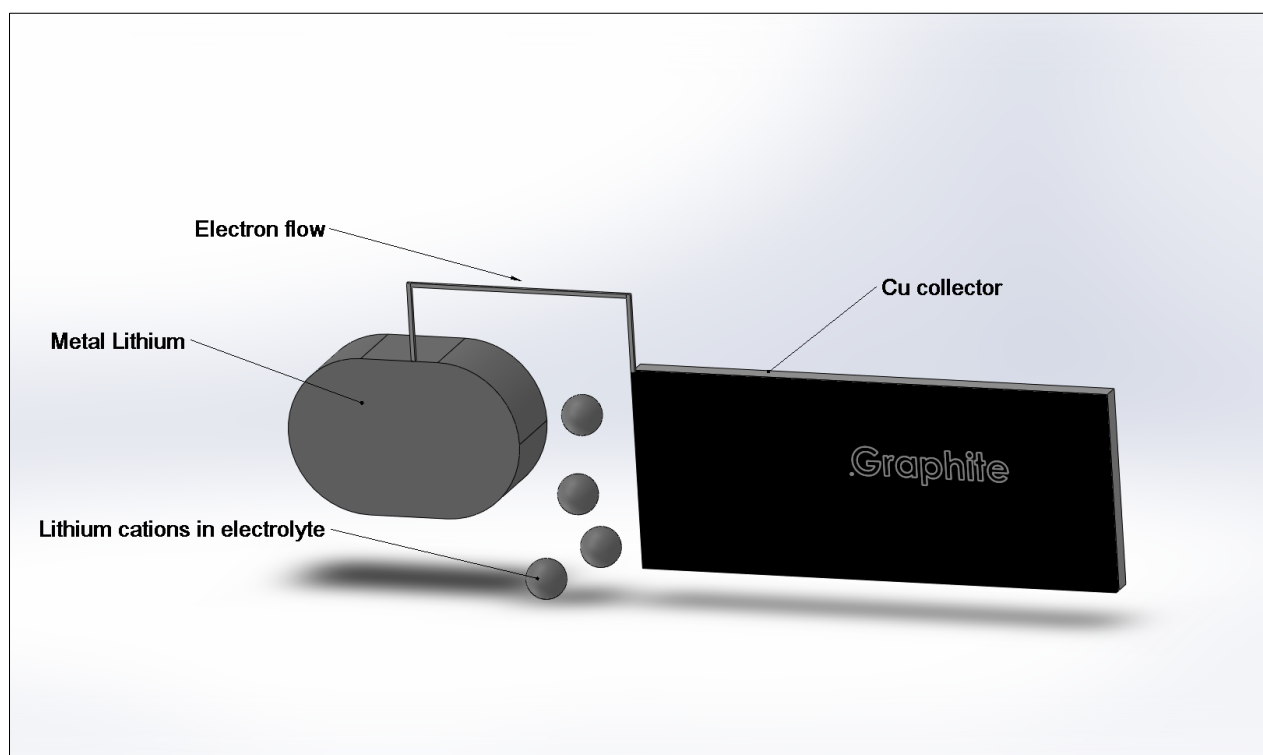


**Figure 1.** Simplified illustration of lithiation cell.

### Acknowledgments

This work was supported by specific graduate research project of the Brno University of Technology: Materialy a technologie pro elektrotechniku IV., reg. no. FEKT-S-20-6206.

## Surface characteristics of TiO<sub>2</sub> and their effect on specific capacity in lithium and sodium systems

T. V. Lisnycha, Yu. V. Shmatok, N. I. Globa, S. A. Kirillov

Joint Department of Electrochemical Energy Systems,

38A Vernadsky Ave., 03680 Kyiv, Ukraine

The paper presents the results of studies of nanosized titanium dioxide (TiO<sub>2</sub>) samples synthesized by alkaline hydrolysis. The surface properties of the samples were changing by applying different temperature treatment conditions, which made it possible to obtain TiO<sub>2</sub> with a specific surface area of 31-204 m<sup>2</sup>/g. It is shown that the electrochemical behavior of TiO<sub>2</sub>, specific capacity and its stability during cycling depend on the nature of the alkali metal cation and the surface properties of TiO<sub>2</sub>.

### Introduction

Environmental friendliness, low cost, insignificant volumetric expansion and the presence of a large number of polymorphic structures (rutile, anatase, brookite) make TiO<sub>2</sub> a promising material for use in lithium and sodium batteries. The thermodynamics and kinetics of charge/discharge processes of TiO<sub>2</sub> with different structures, e.g. anatase and rutile, differ significantly in lithium-ion systems. At the same time, the charge/discharge mechanisms of anatase and rutile in sodium-ion systems are similar. However, even within the same crystal structure, the capacitive and kinetic characteristics of TiO<sub>2</sub> depend on the size and surface properties of TiO<sub>2</sub> particles.

The aim of this work was to establish a correlation between the surface properties of TiO<sub>2</sub> with the rutile structure and its electrochemical properties in lithium and sodium electrochemical systems.

### Experimental

To obtain the rutile form of TiO<sub>2</sub> a “soft chemistry” approach was used consisting in the slow hydrolysis of dilute TiCl<sub>4</sub> solutions, in which the formation of rutile TiO<sub>2</sub> occurs at the moment of precipitation. The obtained TiO<sub>2</sub> precipitates were dried at 150 °C and then annealed at 200-470 °C. The physico-chemical properties of the materials obtained were characterized using X-ray diffraction (XRD), porosimetry, and scanning electron microscopy (SEM) methods. Electrochemical studies were carried out in 2016 coin cells with a lithium or sodium metal anode. The cathode included TiO<sub>2</sub>, Super P carbon black, graphite and PVDF binder taken in a mass ratio of 7:1:1:1. A 1 M solution of LiPF<sub>6</sub> in a mixture of ethylene carbonate and dimethyl carbonate (1:1 by volume) and a 1 M solution of NaBF<sub>4</sub> in tetraethylene glycol dimethyl ether were used as electrolytes in lithium and sodium cells, respectively. Cells and electrolytes were prepared in dry glove boxes in an argon atmosphere. A Neware Battery Testing System (China) was used in galvanostatic studies.

## Results and Discussion

After heat treatment, the XRD patterns of the samples obtained correspond to crystalline TiO<sub>2</sub> with the rutile structure. Calculated by the Scherrer equation, crystallite sizes are 6-10 nm. According to the porosimetry data, an increase in the annealing temperature and its duration led to a decrease in the specific surface area of TiO<sub>2</sub> from 204 to 31 m<sup>2</sup>/g. All TiO<sub>2</sub> samples synthesized have mesoporous structure with dominant pore size in a range of 2-8 nm. Using SEM (Figure 1), it was found that TiO<sub>2</sub> samples consist of nanoparticles of 10-40 nm in size that form mesoporous spheres with the diameter up to 3 μm.

The tables summarize the results of galvanostatic cycling of TiO<sub>2</sub> in lithium (Table 1) and sodium (Table 2) electrochemical cells. In lithium cells, the specific surface area does not significantly affect the specific capacity, which remains stable more over 100 cycles.

In sodium cells, the relationship between the specific surface area and specific capacity is manifested to a much greater extent. At the first cycle, the dependence of the specific capacity on the specific surface area is almost linear. The stability of the specific capacity of TiO<sub>2</sub> during cycling in sodium cells is much worse.

**Table 1.** Cycling characteristics of TiO<sub>2</sub> in lithium cells at the current rate of C/8.

Specific surface area, m <sup>2</sup> /g	1 cycle, mAh/g			5 cycle, mAh/g			100 cycle,
	Q <sub>dch</sub>	Q <sub>ch</sub>	Q <sub>ch</sub> /Q <sub>dch</sub>	Q <sub>dch</sub>	Q <sub>ch</sub>	Q <sub>ch</sub> /Q <sub>dch</sub>	Q <sub>dch</sub>
143	264	186	0.70	161	170	1.06	183
113	328	218	0.66	183	171	0.93	191
82	310	200	0.65	171	159	0.93	174
61	323	200	0.62	158	156	0.98	167

**Table 2.** Cycling characteristics of TiO<sub>2</sub> in sodium cells at the current density of 50 μA/cm<sup>2</sup>.

Specific surface area, m <sup>2</sup> /g	1 cycle, mAh/g			Q <sub>dch</sub> , mAh/g			
	Q <sub>dch</sub>	Q <sub>ch</sub>	Q <sub>ch</sub> /Q <sub>dch</sub>	5 cycle	10 cycle	20 cycle	50 cycle
143	270	145	0.54	149	140	120	102
113	231	105	0.45	199	181	139	97
82	200	79	0.4	170	150	118	86
49	164	50	0.3	72	86	58	35

## Conclusions

Nanosized TiO<sub>2</sub> with rutile structure synthesized by a hydrolysis method was investigated in lithium and sodium cells. Using the galvanostatic cycling method, the dependences of the specific capacity, coulombic efficiency and discharge rate on the specific surface area of TiO<sub>2</sub> were found. In lithium cells, the surface properties of TiO<sub>2</sub> do not significantly affect the specific capacity and its stability during long-term cycling, but influence the rate characteristics under the discharge current densities up to 20 C. In sodium cells, the specific surface area of TiO<sub>2</sub> is the main factor determining the specific capacity and its stability under cycling conditions.

## Comparison of Gel Polymer Electrolytes Containing Lithium and Sodium Salts

S. Peterová<sup>a</sup>, I. Veselkova<sup>a</sup> and M. Sedlářiková<sup>a</sup>

<sup>a</sup> Department of Electrical and Electronic Technology, Brno University of Technology, Technická 10, 616 00 Brno, Czech Republic

This article deals with the comparison of gel polymer electrolytes (GPEs) containing lithium and sodium salts. The research was carried out with lithium salts  $\text{LiClO}_4$ ,  $\text{LiPF}_6$  and sodium salts  $\text{NaClO}_4$  and  $\text{NaPF}_6$ . Gel polymer electrolytes were prepared with monomers ethyl methacrylate (EMA) and methyl methacrylate (MMA). The polymerization of the sample of GPE was initiated by UV radiation and benzoin ethyl ether (BEE) was used as initiator. Conductivity and electrochemical stability measurements were performed on the prepared samples of gel polymer electrolytes. Part of the research is also implementation of thermal analysis of prepared samples.

### Introduction

Gel polymer electrolytes suitably combine the ionic properties of the liquid phase and the mechanical properties of the gel. The basic requirements for these electrolytes are high ionic conductivity over a wide range of heat, good mechanical properties, thermal and electrochemical stability and long-life service. The current trend of development is the effort to replace lithium ions in electrolytes with another more common element. In addition to lithium, alkali metals also include sodium. Sodium is more available in nature than lithium and it is also cheaper. The other advantage, beside of the higher occurrence in nature, is low atomic weight, high reduction potential and also non-toxicity. [1] [2]

### Chemical composition of GPE

The method of preparing gel polymer electrolytes is based on mixing monomers with a salt, a polymerization initiator and a crosslinker in an aprotic solvent. Every part of the gel preparation takes place in an inert atmosphere, because of the need of an inert atmosphere, glow-boxes are usually used. It is necessary to initiate polymerization of samples of gel polymer electrolytes with thermal or ultraviolet radiation. In case of this research ultraviolet radiation was used.

The GPE consisted of the following materials:

- Salt Lithium hexafluorophosphate ( $\text{LiPF}_6$ )  
Lithium perchlorate ( $\text{LiClO}_4$ )  
Sodium hexafluorophosphate ( $\text{NaPF}_6$ )  
Sodium perchlorate ( $\text{NaClO}_4$ )
- Solvent ethyl carbonate and diethyl carbonate (EC/DEC in weight 1:1)
- The initiator of UV polymeration benzoin ethyl ether (BEE)
- Crosslinking agent Ethylene glycol dimethacrylate (EDMA)
- Monomer ethyl methacrylate (EMA) and methyl methacrylate (MMA)

## Experiment

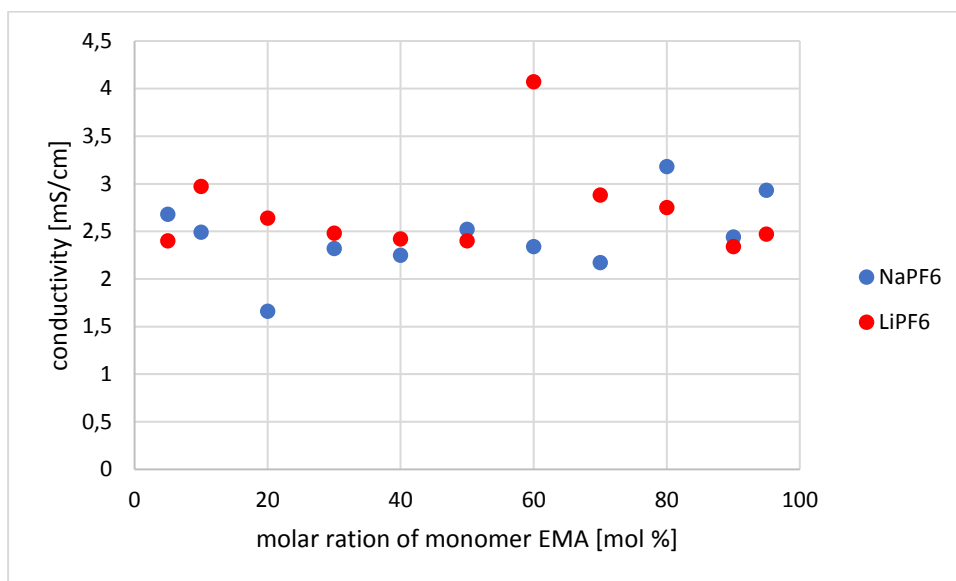


**Figure 1.** Conductivity values of GPE containing salts NaPF<sub>6</sub> and LiPF<sub>6</sub>

Firstly, gel polymer electrolytes containing LiPF<sub>6</sub> and NaPF<sub>6</sub> salts were measured. The average value of conductivity of GPE containing the LiPF<sub>6</sub> is 2,7 mS/cm and NaPF<sub>6</sub> is 2,45 mS/cm. The conductivity values are similar for both types of salt. Most of the prepared samples reached a conductivity in the range of 2,25 mS/cm to 3mS/cm.

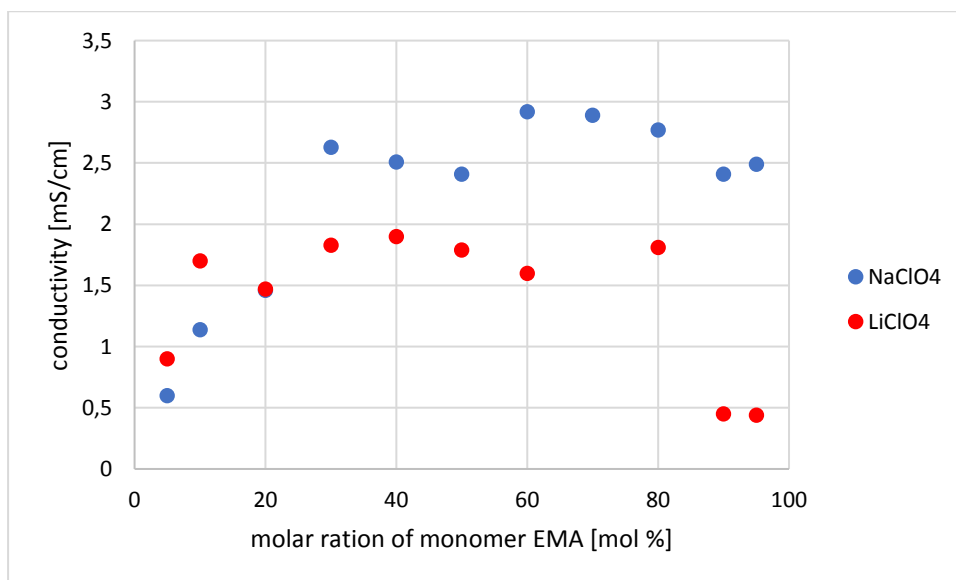


**Figure 2.** Conductivity values of GPE containing salts NaClO<sub>4</sub> and LiClO<sub>4</sub>

Secondly, samples containing NaClO<sub>4</sub> and LiClO<sub>4</sub> were measured. The measurement results show that the average value of conductivity of GPE with NaClO<sub>4</sub> is 2,2 mS/cm and LiClO<sub>4</sub> 1,39 mS/cm. In this case of measurement, we can see that the conductivity increases with increasing molar proportion of monomer EMA. For the last two samples containing LiClO<sub>4</sub> salt a measurement error is probably present. The reason may be in increased humidity in the glove box. These salts reached a lower conductivity compared to LiPF<sub>6</sub> or NaPF<sub>6</sub>.

### Conclusion

The aim of this research was to compare the conductivity and electrochemical stability of samples of gel polymer electrolytes with salts containing sodium and lithium ions. Samples with  $\text{LiPF}_6$ ,  $\text{NaPF}_6$  and  $\text{LiClO}_4$ ,  $\text{NaClO}_4$  were compared. The  $\text{LiPF}_6$  salt, which is used in lithium-ion batteries in the liquid form of electrolyte, turned out the best. In the case of gel polymer electrolytes, the samples containing this salt does not achieve sufficient conductivity for wide use.

### Acknowledgments

This work was supported by the grant FEKT-S-20-6206 "Materiály a technologie pro elektrotechniku III"

### References

1. Isa, K.B.M., Othman, L., Zainol, N.H., Samin, S.M., Chong, W.G., Osman, Z., Arof, A.K.M., *Studies on Sodium Ion Conducting Gel Polymer Electrolytes*. KEM 594–595, 786–792. (2013)
2. Othman, L., Isa K.B.M., Osman, Z., Yahya, R. *Ionic Transport Studies of Gel Polymer Electrolytes Containing Sodium Salt*. 5122-5129 (2017)

## New Ionic Liquid for Lithium-Ion Batteries

K. Rogala

In recent years, interest in researching new materials for lithium-ion battery is increasing. One of the main research subjects is electrolytes. There are many types of electrolytes used in lithium-ion batteries. Among them ionic liquids (ILs) seem to be a very promising electrolyte component. The main advantages of the ILs are very low vapor pressure, non-flammability, favorable solvating properties for a range of polar and non-polar compounds, thermal stability and wide range of electrochemical stability. These properties can help solve the problems faced by the battery industry.

This work concerned the synthesis and analysis of the properties of a new IL with a non-standard organic anion TDI – **1-methyl-1-propylpyrrolidinium 4,5-dicyano-2-(trifluoromethyl)imidazolate (MPPyrTDI)** – for application as a solvent in electrolytes used in lithium-ion cells.

The first stage of the research was the synthesis and estimation solubility of lithium salt (LiTDI) in the tested IL. Subsequently electrolyte solutions were prepared by dissolving LiTDI salt in MPPyrTDI in whole range of solubility. Then were tested physicochemical and electrochemical properties. The electrochemical stability of the MPPyrTDI relative to the lithium anode was tested using Linear Sweep Voltammetry (LSV). IL and the resulting electrolytes were tested for thermal stability using differential scanning calorimetry (DSC) on a TA apparatus. Ionic conductivity was tested by means of Electrochemical Impedance Spectroscopy (EIS) and measurements of the lithium cation transference numbers performed at room temperature by means of d.c. polarization method with Bruce and Vincent correction. All electrochemical tests were performed on a multi-channel potentiostatic-galvanostat VMP3 by Biologic Science Instruments with the function analysis of the frequency response.

## LIBs with anode subsided by silicon and their reaction on pressure

M.Šedina<sup>a</sup> and T.Kazda<sup>a</sup>

<sup>a</sup> Department of Electrotechnology, Brno university of technology, Brno 61600, Czech Republic

Conversion materials, especially silicon, are promising materials for the evolution of anode materials. Today it is used as a composite material together with graphite. However, this opens up problems that need to be solved. One way to solve parts of the problem is to apply external pressure to the batteries.

### Introduction

We use batteries every day of our lives. We can find them in the devices, which we use daily, whether they are mobile phones, watches, computers, etc. or in today's evolving mobility, which includes electric cars, scooters, bicycles, etc. Battery technology continues to evolve dynamically, opening up new challenges that need to be solved.

### Anode materials

The current generation of batteries uses two types of anode materials. The most common material used by most batteries is graphite. Its theoretical capacity for  $\text{LiC}_6$  is 372 mAh/g. The second type of anode material used is ceramic LTO. LTO is used for LMO and NMC cathode materials. The theoretical capacity of  $\text{Li}_4\text{Ti}_5\text{O}_{12}$  is 175 mAh/g.

Today's research deals with how to increase this capacity. Silicon appears to be one of the promising materials for increasing the capacity of the anode. The theoretical capacity of  $\text{Li}_{15}\text{Si}_4$  is 3580 mAh/g, which is ten times more than today's commonly used graphite. Another advantage of silicon is its large number of sites (about 25 % of Earth's crust) and low ecological impact. In any case, there are several problems that make it impossible to use this material. Today, batteries are using Si/C composite, where silicon is represented by 5 %. The subsidence is expected to increase by up to 40 % in the future.[1][2]

### Problems connected with usage of silicon

One of the problems with the use of silicon is its large volume change during cycling (up to 300 %), this increase in volume results in damage of the formed SEI layer and its re-increase. Another problem is that the silicon particles crack and disintegrate. Due to this problem, batteries with a silicon anode are characterized by a rapid decrease of capacity, which makes their practical use impossible. Volume changes are shown in Figure 1.[2]

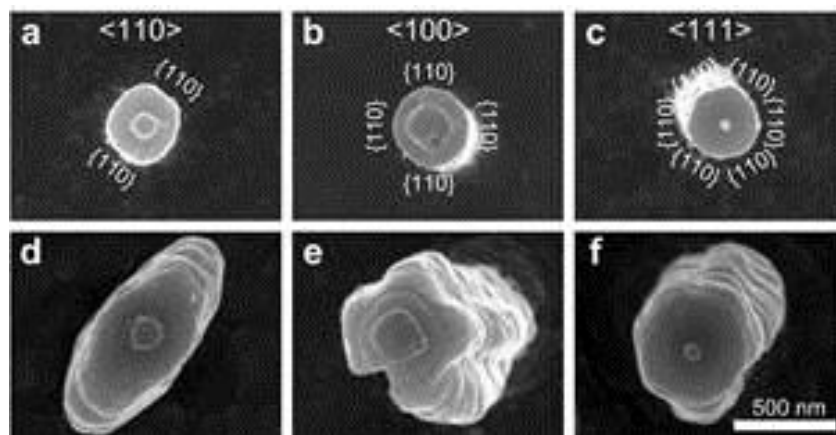


**Figure 1.** Volume change of Si particular under SEM [Chyba! Nenalezen zdroj odkazů.]

### Measure battery under pressure

In my research, I want to focus on measure the battery under constant pressure and find how moderate pressure affects battery parameters as capacity drop, battery impedance and the number of life cycles.

#### Previous studies

There are several studies, which are focused on study batteries under pressure. The results of the study show that, when you moderate the right amount of pressure on the battery, the battery will have lower internal resistance and it will inflate less. a is showing that the pressure stabilizes the capacity drop and made him more linear than the uncompressed battery. b shows how can moderated pressure can reduce battery inflation. When you combine these results you can see that the right amount of pressure increase battery parameters. [4]

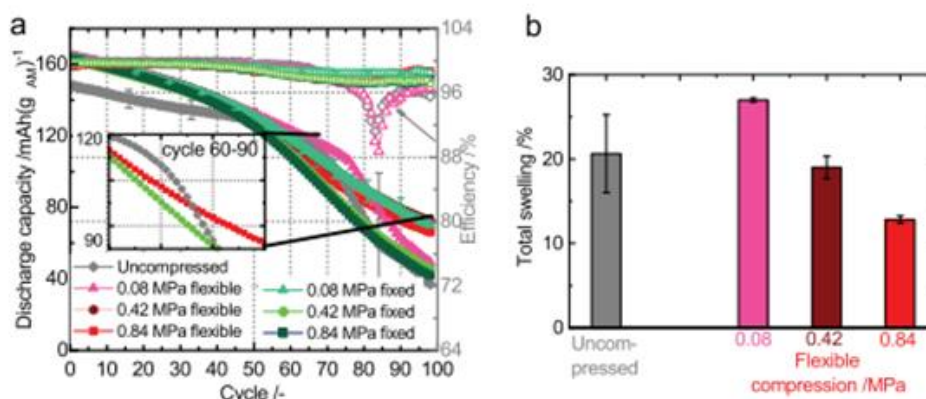


**Figure 2.** Effect of compression on battery with Si anode [4]

#### Device for moderate pressure

For that experiment, I designed a device that serv for moderation pressure on the battery. It is made from four metal clamps and two wooden desks, as you can see in **Figure 3**. Wooden desks serve for the distribution of the pressure on the battery and as an insulator of metal parts from the

battery. Metal clamps are made from two metal strips and two springs. Pressure is moderate by stressing the springs and for the setting, we use equation [1], where  $F$  is the spring force,  $R$  is the spring constant and  $s$  is the spring stroke.

$$F = -R * s \quad [1]$$

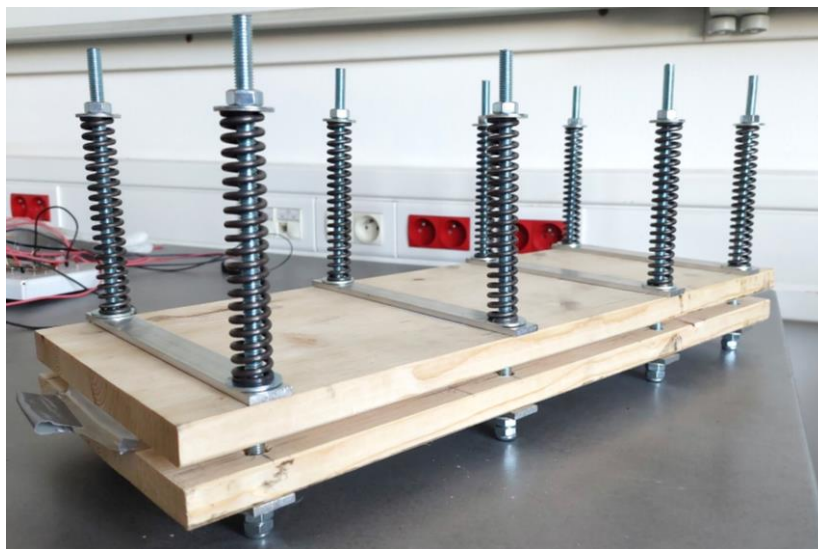


**Figure 3.** Device for moderate pressure

### Acknowledgements

This work was supported by the specific graduate research of the Brno University of Technology No. FEKT-S-20-6206.

### References

1. XU, Yu Hong, Ge Ping YIN a Peng Jian ZUO. Geometric and electronic studies of Li<sub>15</sub>Si<sub>4</sub> for silicon anode. *Electrochimica Acta* [online]. 2008, **54**(2), 341-345 [cit. 2021-7-9]. ISSN 00134686.
2. LUO, Fei, Bonan LIU, Jieyun ZHENG, Geng CHU, Kaifu ZHONG, Hong LI, Xuejie HUANG a Liquan CHEN. Review—Nano-Silicon/Carbon Composite Anode Materials Towards Practical Application for Next Generation Li-Ion Batteries. *Journal of The Electrochemical Society* [online]. 2015, 162(14), A2509-A2528 [cit. 2021-7-9]. ISSN 0013-4651.
3. High Capacity Silicon Anodes: Volume Expansion and Mechanics of Fracture. *Lithium Battery Research* [online]. [cit. 2021-7-8]. Dostupné z: <https://www.lithiumbatteryresearch.com/high-capacity-silicon-anodes-volume-expansion-and-mechanics-of-fracture/>
4. MÜLLER, Verena, Rares-George SCURTU, Karsten RICHTER, Thomas WALDMANN, Michaela MEMM, Michael A. DANZER a Margret WOHLFAHRT-MEHRENS. Effects of Mechanical Compression on the Aging and the Expansion Behavior of Si/C-Composite|NMC811 in Different Lithium-Ion Battery Cell Formats. *Journal of The Electrochemical Society* [online]. 2019, **166**(15), A3796-A3805 [cit. 2021-6-23]. ISSN 0013-465

## Solid-State Electrolytes Based on New Polymer DAIKIN® Fluoropolymer for Li-ion Batteries

J. Tańska<sup>a</sup>, M. Kasprzyk<sup>a</sup>, D. Jamroz<sup>a</sup>, T. Trzeciak<sup>a</sup>, and L. Niedzicki<sup>a</sup>

<sup>a</sup> Faculty of Chemistry, Warsaw University of Technology, Warsaw, Poland

The aim of the research was to obtain solid electrolytes based on new polymer – DAIKIN® Fluoropolymer (FP) for the new generation of Li-ion batteries that will find application in electric vehicles. An important aspect is to obtain electrolytes that will be as safe for the environment as possible. Thus the salts used in the research (as well as their ionic liquids derivatives) are non-fluorine or of the low fluorine content (less than typical anions – PF<sub>6</sub><sup>-</sup> or TFSI<sup>-</sup>) (1). The synthesis of the DAIKIN® FP-based SPEs was done with the use of acetonitrile as a solvent. In the investigation two types of salts (LiTDI and LiPCP) and two different ionic liquids (MPPyrTDI and MPPyrPDI) were used.

The ingredients were mixed for 15 hours at 30°C and then for 5 hours at 40°C. In the next step the membranes were casted on Teflon® surface and then cured under vacuum at 30°C for 24 hours and then at 60°C for 48 hours. The microstructure of the obtained SPEs was analyzed and the conductivity and cyclic voltammetry measurements were performed.

The results have shown that higher addition of the ionic liquid increased the flexibility of the membranes and improved their conductivity (for both LiTDI and LiPCP) while maintaining the solid state of matter.

### Acknowledgments

This work has been financially supported from the European Union's Horizon 2020 research and innovation programme under grant agreement No 875029.

### References

1. L. Niedzicki, P. Oledzki, P. Wieczorek, M. Marcinek, and W. Wieczorek, *Synth. Met.*, **223** (2017).

## Measuring the electrical capacity of lithium batteries and implementing the values in the warranty conditions of BEV and PHEV battery manufacturers

P. Maule, J. Vanek and K. Jandova

Faculty of Electrical Engineering and Communication, Brno University of Technology,  
Technická 10, 612 00 Brno

The work deals with the quality of batteries in electric vehicles manufactured today's and the determination of warranty conditions and guarantees for built-in lithium batteries. However, the design, testing, prototyping and creation of new vehicles is not without errors, as the experience of some manufacturers, including the more inexperienced Mercedes, shows now. On a tested sample of the Mercedes E350e PHEV, a capacity loss of more than 30% from the original nominal value was measured after 18 months of vehicle operation, well above the manufacturer's expectations and declarations. After the first practical results on the quality of mass-produced EVs, the manufacturer removed all or part of the physical parameters of the battery (nominal energy) and introduced general warranty rules for the battery - limited by the number of years or mileage.

### Introduction

The actual electrical capacity depends on temperature, discharge current and final discharge voltage. The index digit following C specifies the discharge/charge time in hours that the battery needs to be charged/discharged with current to use this storage capacity. For example, a capacity value of C10 = 100 Ah means that the battery has a capacity of 100 Ah when discharged evenly for 10 hours until the final discharge voltage is reached. The discharge current in this example is  $100 \text{ Ah} / 10 \text{ h} = 10 \text{ A}$ . If the cell is charged and the maximum charging voltage is reached on the cell, then we speak of reaching the rated capacity and we refer to this state as SOC = 100%. If the maximum voltage is exceeded, irreversible damage may occur in the cell leading to a shortened lifetime or even a safety risk.

Determining the value of the final discharge voltage has a major impact on the overall electrical capacity. The higher the value of the discharge voltage is set, the smaller the total capacitance will be and vice versa. A suitable cell material composition (1) can achieve cell voltages up to 4.8V. Thus, with the same number of battery cells, we are able to achieve an overall higher voltage of the composite battery, a higher capacity value, and with the same required motor power of the vehicle means a reduction in the average operating current and an increase in the efficiency of the battery assembly.

In practice, the capacity of a battery can be measured in a simplified way by connecting a power resistor R to a previously fully charged battery and measuring the time it takes for the battery voltage to drop to the maximum discharge voltage (the state when the battery is considered discharged). During the discharging process, we measure the voltage  $U$  on the battery at well-defined times, preferably automatically (but also manually during the measurement). From two consecutive voltage measurements, we calculate the so-called average battery voltage  $U_x = U_{(t)} - U_{(t+1)}$  and then from the formula the capacity

$$C = \frac{U_x \cdot t}{R} \quad [1]$$

The disadvantage of this measurement is the gradual reduction of the discharge current when the battery voltage is reduced, which is not entirely appropriate. For the measurement, it may be recommended to replace the power resistor with a precision current source (controlled resistor) that will match the declining current waveform to a constant level, as shown in the discharge area in Figure 1.

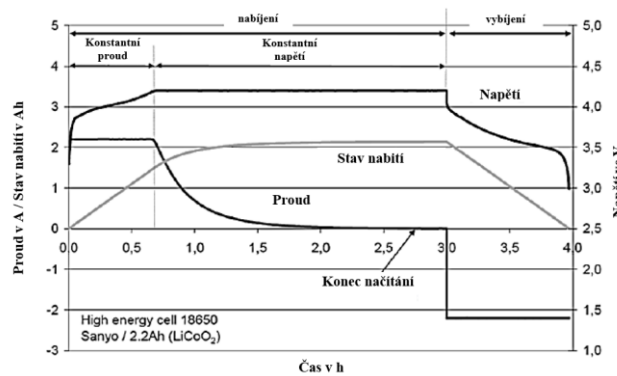


**Figure 1.** Time course of charging and discharging a lithium cell - A. Jossen (2)

### Evolution in the use of electrical capacity data for the battery warranty at Mercedes

For the first mass-produced BEV since 2015, according to (3), nominal energy in kWh was used to define consumer warranty conditions. The B250e has a capacity of 28 kWh, and if it drops below 19.6 kWh, the battery has exceeded the manufacturer's product warranty of 70% of rated capacity.

PHEVs experience more frequent and repeated charging and discharging, and the batteries have aged faster than the manufacturers liked. Therefore, only the capacity in Ah is now used in warranty terms for both BEVs and PHEVs (except B250e). As of 2020, Mercedes does not provide a warranty for the amount of battery capacity for PHEVs. This is a major and unprecedented intervention in the warranty conditions of such a renowned manufacturer. For the BEV types EQV, EQC, EQA, EQS, the battery capacity is defined in Ah and the lowest absolute value in Ah is set for each individual type. For EQV it is 180 Ah, for EQC it is 162 Ah, for Smart it is 36 Ah.

### Practical measurements for determining the remaining battery capacity of PHEVs

The measurement of the current battery capacity cannot be measured directly for any BEV or PHEV without interference with the vehicle design, we are forced to use indirect measurements. It consists in observing the conditions for capacity measurement - i.e. full battery charge, constant discharge current, outdoor and operating battery temperature of 25°C. The condition of maximum full charge is usually not a problem and can be ensured by sufficient time left on the charger with full charge reporting, maintaining temperatures with sufficient time interval after recharging, and appropriate timing of the experiment. For an approximately constant discharge current, we chose a flat road, with no possible road or other obstacles or stops, so that the performed driving would be generally steady and sustained, without the need for further acceleration and deceleration of the vehicle - unlike the NEDC standard. In the experiment, a constant speed of 50 km/h was used, with slow braking required at three points, followed by slow vehicle acceleration.

We used the vehicle's internal on-board computer to measure driving parameters and consumption. After a full charge and a four-hour interval, to drop any elevated battery temperature during charging, an experiment was conducted. A distance of 16 km was driven, with an average consumption of 23.1 kWh/100 km, an average speed of 29 km/h and with 16% of the remaining battery capacity, as shown in the photograph of the displays in Fig. 2.



**Figure 2.** Screenshot of the internal measurement displays of the MB E350e

With a measured average energy consumption of 231 Wh/km, 16 km have been driven, which is the electrical work done  $(231 \cdot 16) / 1000 = 3.696$  kWh. With a remaining battery capacity of 16%, 84% of the stored energy in the battery has been consumed, and the calculation  $C = 3.696 / 0.84 = 4.400$  kWh gives the actual actual battery capacity. Comparing the declared original nominal capacity of 6,4 kWh, there has been a reduction of 31,25 % of the capacity in just 18 months since the car was manufactured and put into service.

## Conclusion

With the claimed capacity reduction and 6-year warranty on the E350e, if the capacity were to continue to drop in a linear fashion, the battery would be fully depleted before the six-year warranty period was reached, a deterrent example of the quality of this manufacturer's batteries. The manufacturer's measured capacity of the battery is 19,1 Ah, or 86,93 %. The difference between capacity and rated energy is 18,18 %. Such a significant difference is the absence of a time-voltage relationship and points to consumer detriment. Presumably because of the higher quality of the batteries, Mercedes will manufacture in Germany's own town of Kamenec.

## References

1. HASELHUHN, Ralf a Petr MAULE, 2017. Fotovoltaické systémy: energetická příručka: pro elektrikáře, techniky, instalátory, projektanty, architekty, inženýry, energetiky, manažery, stavitele, studenty, učitele, ostatní odborné a profesní soukromé nebo veřejné instituce a zájemce o fotovoltaický obor a energetickou nezávislost. Plzeň: Česká fotovoltaická asociace. ISBN 978-80-906281-5-1.
2. JOSSEN, Andreas a Wolfgang WEYDANZ, 2006. Moderne Akkumulatoren richtig einsetzen: 2. überarbeitete Auflage. Druhé. Gottingen: Cuvilier Verlag.
3. Mercedes-Benz Cars UK Limited: Plug-in Hybrid and Electric Drive Battery Certificate, 2020. MERCEDES [online]. UK: Mercedes-Benz, 9.12.2020 [cit. 2021-5-12]. Dostupné z: <https://www.mercedes-benz.co.uk/passengercars/being-an-owner/warranty/warranty.module.html>

## A new high entropy sulfide material for lithium ion battery anodes

D. Zalka<sup>1,2</sup>, D. Csík<sup>2</sup>, A. Straková Fedorková<sup>1</sup>, K. Saks<sup>2</sup>

<sup>1</sup>Department of Physical Chemistry, Faculty of Sciences, Pavol Jozef Šafárik University in Košice, Moyzesova 11, 04154, Košice, Slovak Republic

<sup>2</sup>Slovak Academy of Sciences, Institute of Materials Research, Watsonova 47, 04001 Košice

Li-ion batteries are a unique combination of high energy and power density which approves these electrochemical systems to be applied in portable electronic devices, power tools and hybrid/full electric vehicles. However, there are some issues regarding to Li-ion batteries such as the lifetime of Li and transition metals which are used in Li-ion batteries are short and many of these systems miss electrochemical stability, good reversibility and operate inefficiently. In recent years the concept of entropy stabilization of crystal structures in oxide [1] and in sulfide [2] systems has created a new research area which aims to increase the storage capacity and cyclic stability of Li-ion batteries.

In this study a high entropy sulfide material with composition of  $\text{Cu}_5\text{SnMgGeZnS}_9$  was investigated. This material is a single-phase, high entropy compound [2] and it was never tested in Li-ion batteries as anode material. The high entropy sulfide powder was prepared by ball milling of the precursor materials. The electrode material was prepared by the mixing of  $\text{Cu}_5\text{SnMgGeZnS}_9 + \text{C} + \text{PVDF}$  in the wight ratio 80:10:10 wt% in NMP and dried for 24 h after stirring, coated to copper foil and pressed with  $300 \text{ kg/cm}^2$ . The material characterization was made by X-Ray Diffraction, Scanning Electron Microscopy and Energy Dispersive X-Ray Spectrometry. Cyclic voltammetry, electrochemical impedance spectroscopy and galvanostatic cyclization with potential limitation techniques were used for the investigation of the electrochemical behavior.

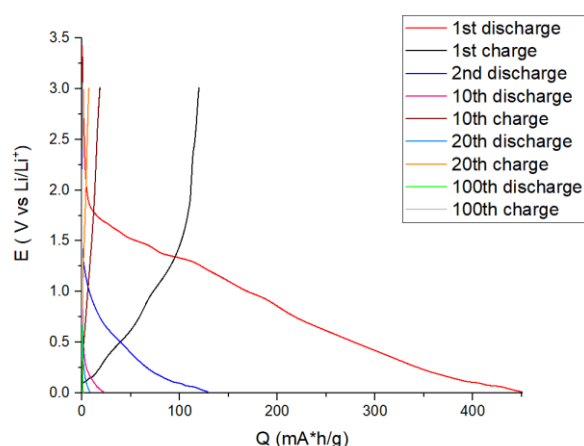


**Figure 1.** Charge and discharge capacities of  $\text{Cu}_5\text{SnMgGeZnS}_9 + \text{C} + \text{PVDF}$  electrode at 1 C rate

The initial capacity of the material was 450 mAh/g with 1 C charge-discharge rate between 0.01-3.0 V (Fig. 1). The improvement of the capacity retention and electrochemical stability of the electrode requires further research.

### **References**

1. A. Sarkar et al., High entropy oxides for reversible energy storage, Nature Comm., 9 (2018)
2. Rui-Zhi Zhang et al., Data-Driven Design of Ecofriendly Thermoelectric High-Entropy Sulfides, Inorg. Chem. 5 (2018) 13027-13033

### **Acknowledgement**

Support from the Slovak Research and Development Agency under the contract No. APVV-20-0138 is gratefully acknowledged.

## The Effect of Electrode Binders To Electrochemical Properties Of Negative Electrode Materials

A. Zsigmond<sup>a</sup> and J. Libich<sup>a</sup>

<sup>a</sup>Department of Electrical and Electronic Technology, Faculty of Electrical Engineering and Communication, Brno University of Technology, 616 00 Brno, Czech Republic

This paper deals with various types of electrode binders used in lithium-ion batteries. The electrode binders play important role in battery, the binders directly affect almost all aspect of electrode characteristics. As the one of the most import parameter is the electrode charge-discharge long term stability. The three binders have been tested in context of negative electrode in lithium-ion battery. The natural graphite has been chosen as an active electrode material. The natural graphite takes majority as negative electrode material on commercial market with lithium-ion batteries. The three kind of binders was established for testing: polyvinylidene fluoride (PVDF), styrene-butadiene rubber (SBR) and polyimide P84. The influence of these binders on charge-discharge stability are evaluated and described in this paper.

### Experiments and Results

#### Electrode binders

In the production of lithium ion battery electrodes, the binder plays an important role. It not only binds the active materials and the conductive additive to the current collectors, but also strongly affects the electrode processing and the electrochemical performance of the laminate. Polyvinylidene fluoride (PVDF) is the generally used binder, which requires the use of the volatile, organic compound N-methyl pyrrolidone in its application. Recently, sodium salt of carboxymethyl cellulose (CMC) and styrenebutadiene rubber (SBR) have been introduced as a suitable replacement in the manufacture of lithium ion anodes. The use of the water soluble binder system leads to a cheaper and greener electrode processing.

Polyvinylidene fluoride (PVDF) is a highly non-reactive and pure thermoplastic fluoropolymer. It is produced by the polymerization of vinylidene difluoride and is used in applications requiring the highest purity, strength, and resistance to solvents, acids, bases and heat. Compared to other fluoropolymers, it has a lower melting point, around 177 °C, also a lower density (1.78 g/cm<sup>3</sup>). It is available as piping products, sheet, tubing, films, plate and an insulator for premium wire. It can be injected, molded or welded and is commonly used in the chemical, semiconductor, medical and defense industries, as well as in lithium ion batteries. Strong piezoelectricity was observed in PVDF, ten times larger than in any other polymer. During the observation PVDF was placed under a strong electric field to induce a net dipole moment. The poled thin films had a piezoelectric coefficient of 6- 7 pC/N. PVDF has a 50-60 % crystalline structure with a glass transition temperature (T<sub>g</sub>) of -35 °C. The material is mechanically stretched to orient the molecular chains and then poled under tension to achieve piezoelectric properties.

When poled, PVDF also has ferroelectric polymer and pyroelectric properties, making it useful in sensor and battery applications. PVDF can be used as binder material in the production of

composite electrodes for lithium ion batteries. A weight solution of 1-2 % PVDF dissolved in N-methyl-2- pyrrolidone (NMP) is mixed with an active lithium storage material (graphite, silicon, tin, LiCoO<sub>2</sub>, LiMn<sub>2</sub>O<sub>4</sub>, LiFePO<sub>4</sub>) and a conductive additive (carbon black, carbon 36 nanofibers). This slurry is cast onto a metallic current collector and the NMP is evaporated to form a composite or paste electrode. The advantage of using PVDF is that it is chemically inert over the potential range used and does not react with the electrolyte or lithium. PVDF can be used in a variety of situations, such as insulation on electrical wires, tactile sensor arrays, inexpensive strain gauges, lightweight audio transducers. In the biomedical sciences PVDF is used in immunoblotting as an artificial membrane.

Styrene-butadiene rubber (SBR) or styrene-butadiene rubber (SBR) is derived from styrene and butadiene, a type of synthetic rubber. These materials have good abrasion resistance and good aging stability when protected by additives. SBR is not to be confused with a thermoplastic elastomer made from the same monomers, styrene-butadiene block copolymer. Latex (emulsion) SBR is extensively used in coated papers, being one of the cheapest resins to bind pigmented coatings. It is also used in building applications, as a sealing and binding agent behind renders, an alternative to PVA. SBR can be used to 'tank' damp rooms or surfaces, a process in which the rubber is painted onto the entire surface (sometimes both the walls, floor and ceiling) forming a continuous, seamless damp-proof liner; a typical example would be a basement. It is also used by speaker driver manufacturers as the material for Low Damping Rubber Surrounds. Additionally, it is used in some rubber cutting boards.

Polyimide P84 can be produced in different forms. The base material for P84 fibres is composed of aromatic backbone units. Despite the non-melting aromatic, halogen free structure it is classified as non-flammable. P84 fibers are used as filter media for high temperature filtration, protective clothing, sealing materials for space craft and high temperature applications such as thermal insulation. Another form is a solution of P84, a fully imidized polyimide. It is used for coatings in the electric and electronics industry, due to its low dielectric constant or high dielectric strength. Available solvents are dimethylformamide (DMF) or N-methyl pyrrolidone (NMP) or N-ethyl pyrrolidone (NEP). The third form of P84 is polyimide powder. This powder shows typical properties of polyimide, high temperature stability up to 350 °C, chemical resistance, high mechanical strength, a low friction coefficient and minimal abrasion. It can be used in industrial applications, such as automotive industry, aerospace applications and office machines.

### Acknowledgments

This work was supported by specific graduate research project of the Brno University of Technology: reg. No. FEKT-S-20-6206.

## Self-discharge of supercapacitors - A new look at a persistent problem<sup>1</sup>

Rudolf Holze<sup>I,II,III,2</sup>

<sup>I</sup>State Key Laboratory of Materials-oriented Chemical Engineering, School of Energy Science and Engineering, Nanjing Tech University, Nanjing, 211816, Jiangsu Province, China

<sup>II</sup>Saint Petersburg State University, Institute of Chemistry, St. Petersburg, 199034, Russia

<sup>III</sup>Chemnitz University of Technology, Institut für Chemie, AG Elektrochemie, D-09107 Chemnitz, Germany

A charged device for electrochemical energy storage is in a state of high free reaction enthalpy (Gibbs energy), thus from a thermodynamic point of view it strives to reach a state of lower energy by discharge and/or self-discharge. The former is the users intent, the latter is driven by nature independently of the users intention. Self-discharge is a significant drawback of primary and secondary batteries, negatively affecting their performance, limiting their shelf life, even posing security risks when the battery powers a smoke detector, a critical sensor or emergency lighting. To handle this problems various approaches are employed: Predict, at least estimate, self-discharge and consider it when planning an application or applying a continuous trickle charge if possible. A more basic approach going beyond taking care of the symptoms is research into the causes and mechanisms of self-discharge aiming at limiting or even suppressing self-discharge.

**Table I.** Typical values of self-discharge<sup>3</sup>

	System	self-discharge
primary	Alkali-manganese cell	0.5 % per month
	Leclanché cell	0.5 % per month
	Lithium	0.5 % per month
secondary	Lithium-ion	4 % per month
	NiMH	25 % per month
	LSD-NiMH <sup>4</sup>	4 % per month
	NiCd	20 % per month
	RAM <sup>5</sup>	0.5 % per month
supercapacitor	EDLC <sup>6</sup>	1.8 % per day

Supercapacitors, although operating according to a completely different principle (the accumulation of charges in the electrochemical double layer), are affected by self-discharge even worse than batteries because charge and thus energy storage does primarily not proceed via materials transformation. Ion redistribution plays a significant role in voltage decay associated with self-discharge. Given the considerable self-discharge of most known supercapacitors it comes as a slight surprise that only limited attention is paid to it, in many publications the topic is still ignored. Nevertheless information about self-discharge is highly relevant for many applications. Thus it is quite necessary to rise awareness of this unwelcome phenomenon, to improve the understanding of the

<sup>1</sup> A full version of this overview will be published in *Electrochemical Energy Technology*

<sup>2</sup> Correspondence author, Email: rudolf.holze@chemie.tu-chemnitz.de

<sup>3</sup> Y. Wu, R. Holze: *Electrochemical Energy Conversion and Storage*. Wiley-VCH, Weinheim 2021.

<sup>4</sup> LSD: Low self-discharge rechargeable alkaline-manganese

<sup>5</sup> RAM: Rechargeable alkaline-manganese

<sup>6</sup> EDLC: electrochemical double layer capacitor

causes of the various modes of self-discharge, to consider factors influencing self-discharge and to search for options to suppress, at least to reduce self-discharge.

This presentation will provide an overview, highlight some research results, options and developments. It also provides recommendations regarding reporting of data.

### **Acknowledgments**

Preparation of this report has been supported within a research project grant № 26455158 and № 70037840 at St. Petersburg State University.

## Long-term Performance of Electrochemical Capacitors

G. Lota<sup>a,b</sup>, S. Znaniecki<sup>b</sup>, K. Szwabińska<sup>b</sup>, J. Wojciechowski<sup>b</sup>, A. Skrzypczak<sup>b</sup>, K. Lota<sup>a</sup>

<sup>a</sup>Łukasiewicz Research Network, Institute of Non-ferrous Metals Division in Poznan Central Laboratory of Batteries and Cells, Forteczna 12, 61-362 Poznan, Poland

<sup>b</sup>Institute of Chemistry and Technical Electrochemistry, Poznan University of Technology, Berdychowo 4, 60-965 Poznan, Poland

[grzegorz.lota@claio.poznan.pl](mailto:grzegorz.lota@claio.poznan.pl)

[grzegorz.lota@put.poznan.pl](mailto:grzegorz.lota@put.poznan.pl)

### Introduction

Electrochemical capacitors (also called supercapacitors or ultracapacitors) store the energy by the formation of the electrical double-layer at the electrode/electrolyte interface. These devices are characterized by high power density, short charge/discharge time and excellent cycling stability. The main goal of supercapacitor development nowadays is to increase their energy density and mentioned cycling stability. The former parameter could be improved by increasing the capacitance or operating voltage of the system, while the second by preserving current collectors from electrochemical corrosion phenomena. The increase of capacitance could be realized by the so-called pseudocapacitance effect, which can originate from the quick faradaic reactions at the electrode/electrolyte interface. These reactions can be induced by the appropriate modification of electrode in order to enforce the pseudocapacitive effect [1-6]. Electrochemical capacitors are composed of two electrodes separated by a separator and soaked in the electrolyte solution. Electrode material (mainly activated carbon) is coated on the surface of the current collectors made either of metals or stainless steel. In such a case, current collectors are exposed to corrosive electrolytes and can be subjected to corrosion processes [7-11]. There are several methods that are utilized to protect metals and steel from the harmful effects of electrochemical corrosion. One of them is the utilization of ionic liquids (ILs), which are added to an aggressive aqueous environment [12]. They act as corrosion inhibitors. This form of protection is being discussed in the scientific literature from about 20 years. A majority of articles describes the ability of this class of compounds to provide anti-corrosive protection for metal and steel. For these materials, an inhibitive influence on corrosion processes has been documented for dozens of ILs, vastly diversified in their chemical structure. A list of almost 90 investigated substances can be found in the literature [12]. Ionic liquids (ILs) are organic compounds which exhibit ionic structure and melting points below 100 degrees of Celsius. Due to their numerous advantageous properties, from some decades ILs stay in the scope of intense scientific interest, what results in the extensive research on possible ways to utilize them industrially. It covers various fields of IL application, for example as a solvent, an electrolyte, a catalyst, as a pharmaceutical or as corrosion inhibitors.

In this work, the influence of ionic liquids additives on the performance of electrochemical capacitors is presented. Strictly, ionic liquids have been added to aqueous 1 M Na<sub>2</sub>SO<sub>4</sub> electrolyte to inhibit corrosion processes on the surface of 316L stainless steel current collectors, which also influence the performance of electrochemical capacitors. Ionic liquids compounds were based on a common 2,5-dihydroxybenzenesulfonic anion.

### Acknowledgments

The authors would like to acknowledge for the financial support of the National Science Centre (Poland), grant no. 2018/31/B/ST8/01619 and the Ministry of Education and Science, 2021 (Poland).

### References

1. F. Béguin and E. Frackowiak (Ed.), *Supercapacitors: Materials, Systems and Applications*, Wiley-VCH, Weinheim (2013).
2. F. Béguin, V. Presser, A. Balducci, E. Frackowiak, *Adv. Mater.*, 26, 2219 (2014).
3. T. Brousse, D. Bélanger, J.W. Long, *J. Electrochem. Soc.*, 162, A5185 (2015).
4. K. Kopczyński, G. Milczarek, G. Lota, *Electrochem. Commun.*, 68, 28 (2016).
5. M. Graś, Ł. Kolanowski, J. Wojciechowski, G. Lota, *Electrochem. Commun.*, 68, 28 (2018).
6. K. Fic, G. Lota, M. Meller, E. Frackowiak, *Energy & Environmental Science*, 5, 842 5 (2012).
7. J. Wojciechowski, Ł. Kolanowski, A. Bund, G. Lota, *J. Power Sources* 368, 18 (2017).
8. E. McCafferty, *Introduction to Corrosion Science*, Springer, New York (2010).
9. N. Perez, *Electrochemistry and Corrosion Science*, Kluwer Academic Publishers, Boston (2004).
10. R.W. Revie, H.H. Uhlig, *Corrosion and Corrosion Control*, fourth ed., John Wiley & Sons, New Jersey (2008).
11. R.W. Revie, *Uhlig's Corrosion Handbook*, third ed., John Wiley & Sons, New Jersey (2011).
12. C. Verma, E.E. Ebenso, M.A. Quraishi, *J. Mol. Liq.*, 233, 403 (2017).

## Carbon coating on Nb<sub>2</sub>O<sub>5</sub> for high-rate anode for Li-ion capacitors

Haojie Fei<sup>1</sup>, Natalia Kazantseva<sup>1</sup>, Marek Jurča<sup>1</sup>, Petr Sába<sup>1,2</sup>

Email: haojie@utb.cz

<sup>1</sup>Centre of Polymer Systems, Tomas Bata University in Zlín, Zlín 76001 Czech Republic

<sup>2</sup>University Institute, Tomas Bata University in Zlín, Zlín 76001 Czech Republic

Fast charging/discharging capability is one of the key parameters for next-generation energy storage devices.<sup>1</sup> Li-ion capacitors have been proposed as an alternative approach to overcome the low energy density of conventional electrochemical double layer capacitors (EDLCs). A higher energy density could be achieved by replacing one activated carbon electrode with a Li-ion insertion/deinsertion electrode, which has a much higher specific capacity. The selection of this type of electrodes for Li-ion capacitors is the key to achieve desired performances. Nb<sub>2</sub>O<sub>5</sub> are one of the promising high-power anode materials. The Nb<sub>2</sub>O<sub>5</sub> based Li-ion capacitors working in the safe voltage range are free of the potential safety problems associated with the electrolyte decomposition, which can result in stable cycle life. However, further progress of Nb<sub>2</sub>O<sub>5</sub> anodes for practical applications faces challenges due to their intrinsic poor electric conductivity ( $\sim 3 \times 10^{-6}$  S cm<sup>-1</sup>).<sup>2</sup>

In this study, polyaniline (PANI) was coated on Nb<sub>2</sub>O<sub>5</sub> particles. After the carbonization, Nb<sub>2</sub>O<sub>5</sub>/Carbon composites were obtained with different carbon contents. They were investigated through various tools such as electron microscopes and X-ray diffraction. Their electrochemical performance was tested in coin cell 2032 with the lithium anode. As a result, the application of carbon enhances the rate capability of the cell. However, the optimization of carbon content was necessary.

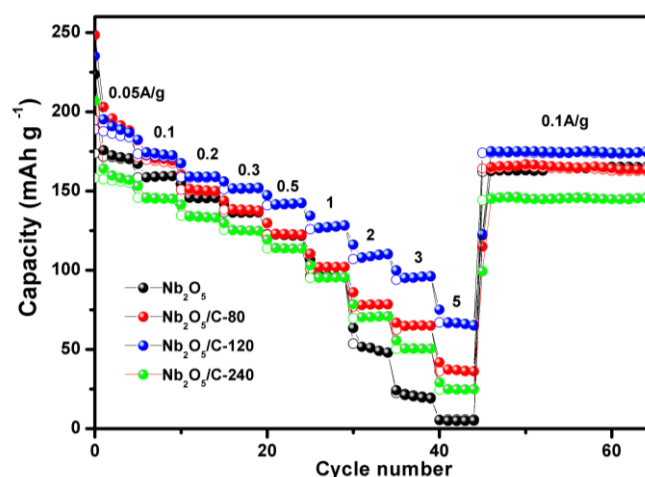


**Figure 1.** Rate capability of different Nb<sub>2</sub>O<sub>5</sub>/C composites at various current densities.

### **Acknowledgments**

This work is supported by the Ministry of Education, Youth, and Sports, Czech Republic (INTER-EXCELLENCE programme under the grant agreement No. LTT20005. It is also supported by project RP/CPS/2020/005.

### **Reference**

1. H. Ding et. al, Mater. Today Nano, 11 (2020) 100082.
2. W. Zuo et. al, Adv. Sci, 4 (2017) 1600539.

## Synthesis and Application of Graphite-Like Carbon Nitride as an Electrode Material for the Oxygen Electrode of a Fuel Cell.

M. O. Danilov<sup>a</sup>, G. I. Dovbeshko<sup>b</sup>, I. A. Rusetskyi<sup>a</sup>, V. N. Byckov<sup>b</sup>, O. P. Gnatyuk<sup>b</sup>,  
S. S. Fomanyuk<sup>a</sup>, G. Ya. Kolbasov<sup>a</sup>

<sup>a</sup>Institute of General and Inorganic Chemistry of the NAS of Ukraine,  
32/34 Academic Palladin Avenue, Kyiv, 03142, Ukraine.

<sup>b</sup>Institute of Physics of the NAS of Ukraine, 46 Nauky avenue, Kyiv, 03039, Ukraine.

\*Corresponding Author E-mail Address: danilovmickle@rambler.ru

### Introduction

It has been shown that carbon nanotubes and graphenes doped with nitrogen (1, 2) are good metal-free catalysts in the oxygen reduction reaction. It was noted in (3) that doping with nitrogen is the most effective method for improving the electrocatalytic activity of carbon nanomaterials. So, it can be assumed that carbon nitrides with a high nitrogen content are promising metal-free electrocatalysts. Carbon nitrides have two allotropic crystal structures. These are tetrahedral carbon nitride ( $\beta$ -C<sub>3</sub>N<sub>4</sub>) and graphite-like carbon nitride g-C<sub>3</sub>N<sub>4</sub> (3). The  $\beta$ -C<sub>3</sub>N<sub>4</sub> must have high hardness and low compressibility, like diamond, while g-C<sub>3</sub>N<sub>4</sub> is considered as the most stable substance under environmental conditions (4). There are studies in the literature on the use of carbon nitride as a catalyst in the oxygen reduction reaction. The aim of our work was to create a new composite of graphite-like carbon nitride and study the conditions for its preparation for use as a metal-free catalyst for the oxygen electrode of a fuel cell.

### Results and Discussion

We have developed a thermochemical method for the synthesis of layered composites based on graphite-like carbon nitride. This method involves heating urea and melamine in a lidded crucible to 550 ° C for 4 hours. We investigated various ratios of urea and melamine, and also investigated the properties of the obtained material depending on the location of melamine in the crucible on top of urea or with uniform stirring. Sample No. 1 C<sub>3</sub>N<sub>4</sub> (56.5:1) melamine on top, Sample No. 2 C<sub>3</sub>N<sub>4</sub> (2:1) melamine on top, Sample No. 3 C<sub>3</sub>N<sub>4</sub> (1:1) the mixture is mixed, Sample No. 4 (C<sub>3</sub>N<sub>4</sub> (1:1) melamine on top. Two-layer oxygen electrodes were prepared by pressing. The studies were carried out on a fuel half-cell, with a zinc electrode used as the anode. The fuel half-cell was described in (5). For the comparing parameters of the investigated electrodes we used multiwalled carbon nanotubes with deposited platinum black in an amount of 10 wt.%.

Figure 1 shows an X-ray diffraction pattern of hybrid nanocomposites of graphite-like carbon nitride obtained at various ratios of melamine and urea when melamine is placed in a crucible on top of urea. The X-ray diffraction pattern for samples with the same composition but different mixture arrangements was identical. A small peak at about  $\approx 13.2^\circ$  can be attributed to the (100) face of graphite-like carbon nitride and the corresponding period of alternation of structural heptazine blocks within individual carbon nitride monolayers with a distance of 0.68 nm (Figure 1). There is a reflex at  $2\theta \approx 27^\circ$ , which corresponds to the interplanar distance between monolayers  $d = 0.321$  nm of the (002) face of graphite-like carbon nitride. This value is in the range typical for graphite-like carbon nitride - from 0.319 to 0.326 nm. Other small (100) peak at around  $\approx 21.3^\circ - 21.4^\circ$  can be ascribed to the in-plane repeated units of fully polymerized triazine. The peak at 22.3 is

responsible for carbonated urea residues, and the peak at 23.8 is responsible for carbonated melamine residues.

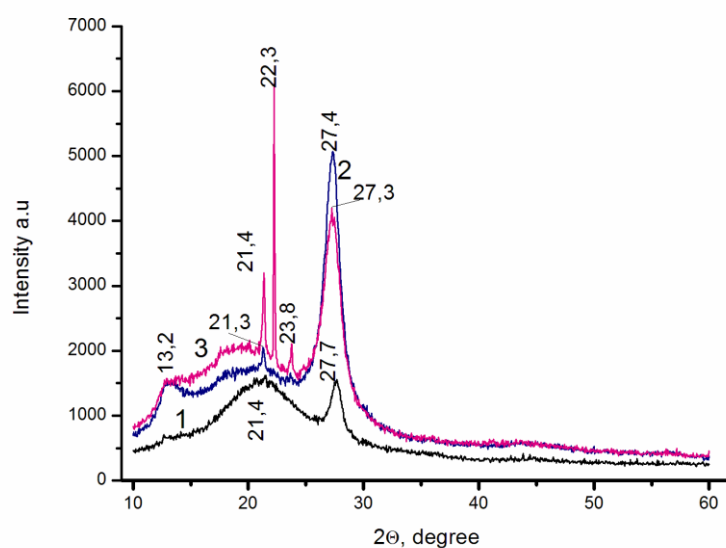


**Figure 1.** X-ray diffraction pattern of carbon nitride at different ratios of urea and melamine in the synthesis: 56.5: 1(1); 1: 1(2); 2: 1(3).

The micrograph of transmission electron microscopy showed that the  $C_3N_4$  sample consists of very small particles with a size of the order of nm, that is, several parameters of the crystal lattice (Figure 2).

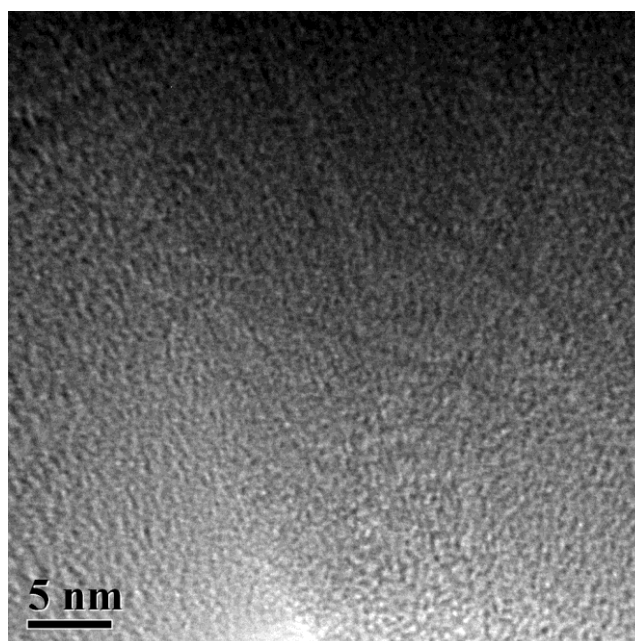


**Figure 2.** Micrograph of a thin fragment of the  $C_3N_4$  sample (56.5:1), illustrating its fine-crystalline structure.

As can be seen from Figure 3, the location of melamine in the crucible does not significantly affect the electrochemical characteristics of the electrodes. The best characteristics are obtained for electrodes made with a ratio of urea to melamine (2:1). Electrochemical studies have established that the obtained g-C<sub>3</sub>N<sub>4</sub> composites are promising materials as metal-free materials for oxygen electrodes of fuel cells, and their characteristics are close to those of electrodes containing platinum.

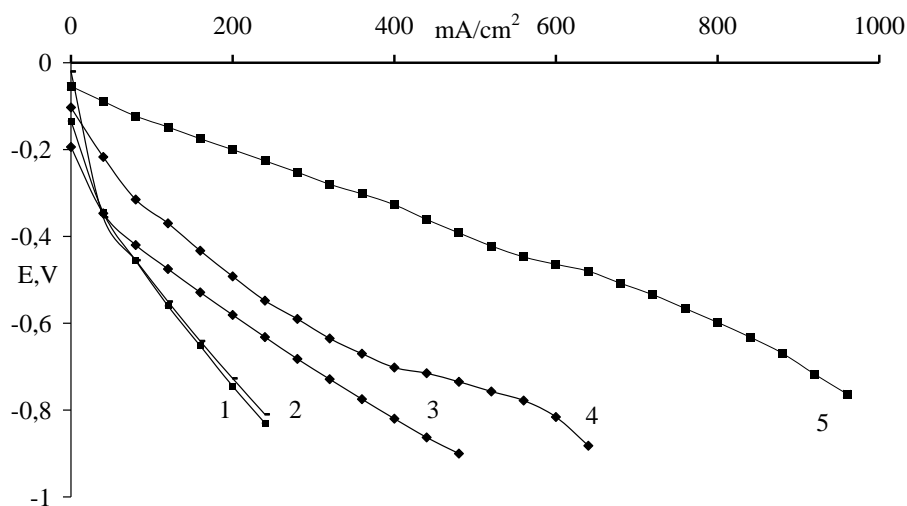


**Figure 3.** Current-voltage characteristics of oxygen electrodes with an active layer made of various electrode materials: 1 - g-C<sub>3</sub>N<sub>4</sub> (1:1) - melamine on top; 2 - g-C<sub>3</sub>N<sub>4</sub> (1:1) the mixture is stirred; 3 - g-C<sub>3</sub>N<sub>4</sub> (56.5:1); 4 - g-C<sub>3</sub>N<sub>4</sub> (2:1); 5 – multiwalled carbon nanotubes with deposited platinum in an amount of 10 wt. %.

It is worth to mention that the produced materials were stable over six months subject to testing in the fuel half-cell by galvanostatic mode at the current density of 200 mA cm<sup>-2</sup> on the oxygen electrodes.

## Conclusions

The thermochemical synthesized nanocomposite of carbon nitride, which is confirmed by X-ray diffraction and TEM analysis. Electrochemical studies have established that the obtained composites are promising materials as a non-metallic catalyst for oxygen electrodes of fuel cells.

## References

1. D. Yu, Q. Zhang, L. Dai, *J. Am. Chem. Soc.*, **132**, 15127 (2010).
2. L. Qu, Y. Liu, J.-B. Baek, L. Dai, *ACS Nano*, **4**, 1321 (2010).
3. M. Wang, Z. Wu, L. Dai, *Journal of Electroanalytical Chemistry*, **753**, 16 (2015).
4. A. Y. Liu, M. L. Cohen, *Science*, **245**, 841 (1989).
5. M. O. Danilov, I. A. Rusetskii, G. I. Dovbeshko, S. S. Fomanyuk, G. Ya. Kolbasov. *ECS Trans.* **95**(1), 273 (2019).

## Potential of hydrogen powered trains in Czech Republic

Martin Paidar<sup>1</sup>, Adam Giurg<sup>1</sup>, Federico Zenith<sup>2</sup>

<sup>1</sup>University of Chemistry and Technology, Prague  
Technická 5, Prague 6 Dejvice, 166 28, The Czech Republic

<sup>2</sup>SINTEF AS, Strindvegen 4, 7034 Trondheim, NORWAY

paidarm@vscht.cz

The European Union and also other countries declare strong ambitions to decarbonise their economies and thus change currently used processes based on fossil fuels. This aim requires big changes in all sectors of economy like households, industry and transportation. New technologies have to be implemented to maintain living standards but without carbon dioxide production. Transportation is responsible for approximately one third of all carbon dioxide emission in the Czech Republic, most of which produced by cars: thus, current governmental activities are focused on building electric vehicles chargers and hydrogen filling infrastructure. Rail transportation is often presented as an ecological alternative with minimal carbon footprint. However, the source of electricity for electric trains is frequently coal power plants, and not all rail tracks are electrified. The diesel-powered locomotives, passenger trains and locally operated shunters generate not only CO<sub>2</sub> emissions but also NO<sub>x</sub> and other pollutants. There are several possibilities to decarbonise diesel-powered trains: one is the construction of catenary electrification; battery-powered locomotives are suitable for short distances; hydrogen-powered trains with fuel cells can provide longer range without extensive infrastructure. The decision of new technology installation is connected with high expenses, thus serious analysis is required. This analysis is subject of currently running project RegioHyt.

From studies previously realized within the EU financed programme Shift2Rail follows that regional passenger trains (Regional Multiple Units) have highest potential for economic conversion to hydrogen. The current railway network in the Czech Republic is being analysed with main focus on non-electrified rails; future plans for electrification were also considered. Selected railways must be analysed with respect to local parameters to calculate the required performance of trains and also their expected hydrogen consumption. For calculations, the already existing products Alstom Coradia iLint and Siemens Mireo are used with known consumption in various terrain and operation modes.

The decarbonisation of rail transportation by use of hydrogen can be successful only if hydrogen with low carbon footprint will be used. One train has capacity for approx. 250 kg of hydrogen; with average consumption of 25 kg of H<sub>2</sub> per 100 km, the operating range is up to 1000 km. Similarly, shunters need for 1h of operation approx. 5.6 kg H<sub>2</sub>; it is clear that one operating shunter or Multiple Unit need a sufficient source of hydrogen. It is possible to use current production sources mainly located at industrial regions: it enables to ensure hydrogen supply for hydrogen trains implementation but its contribution to decarbonisation is problematic. Almost all hydrogen produced by chemical industry in Czech Republic does not fulfil the criteria for low carbon hydrogen. Therefore, a screening of potential sources of hydrogen has been realized. The use of low carbon footprint electricity and water electrolysis is the shortest way to obtain high quality hydrogen. To generate required amounts of hydrogen, the electricity source capable to produce at least 80 tons of H<sub>2</sub> yearly is needed. With average energy requirement 52 MWh / t(H<sub>2</sub>), it represents sources generating 5 GWh/year. Therefore, only large photovoltaic power plants and

nuclear power plants are capable to provide this amount of energy in the Czech Republic, unfortunately, wind power plants are usually localized far from railways. Beside the performance, the location close to the potential hydrogen filling station is crucial for economic operation of hydrogen powered trains. The last option studied is the production of hydrogen from biogas: the process is based on steam methane reforming, which does produce CO<sub>2</sub>, but in the case of biogas this does not count as emission from fossil fuel; the produced hydrogen can therefore be counted as low carbon hydrogen. Again, a sufficient source of biogas is necessary, thus only large capacity biogas stations are considered for the study.

From combination of local hydrogen accessibility, railway parameters and required passenger loads the economic viability will be calculated. The results will be compared to other options such as building catenary or battery powered trains.

### **Acknowledgments**

This project is financed by the Technology Agency of the Czech Republic under grant TO01000324, in the frame of the KAPPA programme, with funding from EEA Grants and Norway Grants.

## Preparation and properties of YSZ ceramic electrolyte for solid oxide cells

Michal Carda, Nela Adamová, Daniel Budáč, Martin Paidar, Karel Bouzek

*University of Chemistry and Technology, Prague  
Technická 5, Prague 6 Dejvice, 166 28, The Czech Republic  
cardam@vscht.cz*

Involvement of renewable energy sources in power grids significantly increased demand for efficient large-scale energy storage. This demand originates from the unstable power output of these energy sources, which are strongly dependent on weather, daytime etc. Among the most suitable processes for the large-scale energy storage is the direct conversion of electricity to the easily storable chemical energy of hydrogen molecule. In general, hydrogen economy concept consists of hydrogen production by water electrolysis during energy surplus and consequently direct electricity production from the electrochemical reaction of hydrogen and oxygen in a fuel cell device during energy shortages. Apparently, a device capable of water electrolysis and a fuel cell mode is desired for space utilization. In the case of low temperature technologies e. g. PEM systems a reversible operation is difficult. In opposition, high temperature systems such as solid oxide cells (SOCs) are particularly suitable for water electrolysis to produce hydrogen and later utilize hydrogen in fuel cell mode without any internal structural changes. In addition, high operating temperature (600 – 900 °C) enhances electrode reaction kinetics and enables operation without expensive PGM catalysts. These are the main advantages of SOCs which are especially important for large-scale stationary applications. However, high operating temperature also significantly enhances degradation processes and requires chemically stable and thermomechanically compatible materials. These disadvantages represent main obstacles for SOCs industrial utilization.

The SOC unit is comprised of three key components – two electrodes and electrolyte. The electrolyte must be non-porous, gas tight and ionically conductive. Yttria stabilized zirconia ( $ZrO_2 - Y_2O_3$ ; YSZ) is still considered a viable material for electrolyte due to its stability, thermomechanical compatibility and negligible undesired interaction with most of electrode materials. YSZ has a cubic crystalline structure derived from  $ZrO_2$ , where partial replacement of quadrivalent  $Zr^{4+}$  with trivalent  $Y^{3+}$  ions leads to formation of oxygen vacancies. Dopant ( $Y_2O_3$ ) content is a decisive factor for the mechanical stability and ionic conductivity of the electrolyte. At low concentration of dopant higher mechanical stability is achieved, however with much diminished ionic conductivity. On the other hand, high concentration of dopant provides higher ionic conductivity, however mechanical as well as thermal stability becomes a limiting factor. In available literature, 8 mol. % of  $Y_2O_3$  is considered as the best trade-off between stability and conductivity. Yet, based on SOC design different electrolyte properties may be required. Moreover, in open literature there are several major discrepancies regarding the dependence of the ionic conductivity of YSZ on dopant content.

The aim of this work is to describe a detailed procedure to prepare in-house YSZ electrolytes with desired dopant content based on commercially available Zr/Y nitrates as precursors. Subsequently, to morphologically and electrochemically characterize prepared electrolytes and compare them with commercially available YSZ electrolytes.

At first, YSZ powders with variable  $Y_2O_3$  content were prepared by combustion synthesis. Morphology and composition were characterized by SEM, XRF and laser diffraction. These powders were then uniaxially moulded and sintered to fabricate self-supporting YSZ button electrolytes. To determine their ionic conductivity symmetrical electrochemical cells were prepared

by depositing silver electrodes and subsequently these cells were characterized by electrochemical impedance spectroscopy at various temperatures.

Results indicate that YSZ powder postprocessing after combustion synthesis and sintering procedure are decisive for YSZ electrolyte morphological structure. Our in-house prepared YSZ powders have different morphology compared to commercial powders, therefore a modified sintering process to achieve fully sintered electrolyte is required. Overall, we have developed a procedure to fabricate YSZ electrolytes of required composition, which have comparable structural properties. Consequently, for different electrolyte compositions we successfully determined YSZ ionic conductivity, which was similar compared to commercial electrolytes of the same  $Y_2O_3$  content.

### **Acknowledgement**

This work was supported by Czech Science Foundation (GACR), contract No: 19-142-44-J and from the grant of Specific university research – grant No (A2\_FCHT\_2021\_083).

## Electrochemical intercalation of anion into graphite using concentrated aqueous electrolyte

Ghulam Abbas<sup>1,2</sup>, Farjana J. Sonia<sup>1</sup>, Zahid Ali Zafar<sup>2,3</sup>, Petr Jiříček, Milan Bouša<sup>1</sup>, Martin Kalbáč<sup>1</sup>, Jiří Červenka<sup>3</sup>, Otakar Frank<sup>1</sup>

Rechargeable dual ion batteries are very promising candidates for achieving high electrochemical performance due to the participation of both the cation and anion in the process of charge/discharge. In our study, reversible, anion (de)intercalation is proposed for graphitic materials in a concentrated  $\text{Al}(\text{ClO}_4)_3$  aqueous electrolyte through extensive electrochemical studies, with both *in-situ* and *ex-situ* characterization. The presence of the surface-controlled processes of charge storage has also been observed along with the diffusion-controlled dual ion intercalation in the graphitic structure. In addition, stable electrochemical performance with high coulombic efficiency of 83% up to 100 cycles has been achieved, highlighting the potential of concentrated aqueous electrolyte solutions in sustainable energy storage.

## Pyridinium-based anolytes for redox flow battery

P. Mazúr<sup>a</sup>, M. Mikešová<sup>a</sup>, J. Kvíčala<sup>b</sup>, Z. Burešová<sup>c</sup>, M. Klikar<sup>c</sup>, F. Bureš<sup>c</sup>, J. Akrman<sup>d</sup>, L. Kubáč<sup>d</sup>

<sup>a</sup>University of Chemistry and Technology Prague, Dept. of Chemical Engineering,  
Technická 5, 166 28 Prague, Czech Republic, [mazurp@vscht.cz](mailto:mazurp@vscht.cz);

<sup>b</sup>University of Chemistry and Technology Prague, Dept. of Organic Chemistry,  
Technická 5, 166 28 Prague, Czech Republic

<sup>c</sup>University of Pardubice, Faculty of Chemical technology, Institute of Organic Chemistry and  
Technology, Studentská 573, 532 10 Pardubice

<sup>d</sup>Centre for Organic Chemistry, Rybitví 296, 533 54 Rybitví, Czech Republic

Redox flow batteries (RFB) represent safe, reliable and long-lasting energy storage technology. Besides the traditional electrolytes based on metal ions, such as vanadium, zinc or iron, the novel organic redox couples are intensively searched in order to improve technico-economical features of the battery.[1, 2]

In our study a series of pyridinium-based molecules was designed, synthesized and tested for the application in aqueous RFB negative electrolytes. The effect of molecular structure on the relevant electrochemical properties was studied using glassy carbon rotating disc electrode and in a flow battery half-cell, both in neutral and acidic environment. The most promising derivative, 1,1'-bis(3-sulfonatopropyl)-4,4'-bipyridinium, was finally tested in a RFB single-cell using various positive electrolytes. The cell internal components and electrolyte compositions were optimized with the respect to the performance and the stability.

### Acknowledgments

The work was supported from European Regional development Fund-Project "Organic redox couple based batteries for energetics of traditional and renewable resources (ORGBAT)" No.CZ.02.1.01/0.0/0.0/16\_025/0007445.



EVROPSKÁ UNIE  
Evropské strukturální a investiční fondy  
Operační program Výzkum, vývoj a vzdělávání



MINISTERSTVO ŠKOLSTVÍ,  
MLÁDEŽE A TĚLOVÝCHOVY

### References

1. Leung, P., et al., Recent developments in organic redox flow batteries: A critical review. *Journal of Power Sources*, 2017. 360: p. 243-283.
2. Winsberg, J., et al., Redox-Flow Batteries: From Metals to Organic Redox-Active Materials. *Angewandte Chemie International Edition*, 2017. 56(3): p. 686-711.

## Study of deactivation of vanadium redox flow battery negative graphite felt electrode in single electrolyte setup

J. Mrlík<sup>a</sup>, P. Mazúr<sup>a</sup>, J. Pcedič<sup>b</sup>, J. Vrána<sup>b</sup>, J. Charvát<sup>a</sup>, M. Marek<sup>a</sup>, J. Kosek<sup>a</sup>

<sup>a</sup>University of Chemistry and Technology Prague, Dept. of Chemical Engineering, Technická 5, 166 28 Prague, Czech Republic, [mazurp@vscht.cz](mailto:mazurp@vscht.cz)

<sup>b</sup>Pinflow energy storage, s.r.o., Křižovnická 86/6, 110 00 Prague, Czech Republic

The vanadium redox flow battery is one of the most promising technologies for storing of electric energy from renewables. Its advantages are power and capacity independency, high efficiency, and long lifetime.

Main reason for decrease of vanadium redox flow battery voltage efficiency is usually deactivation of negative felt electrode.<sup>1</sup>

To study this phenomenon we used single electrolyte setup<sup>2</sup>, which provides possibility of tests under defined conditions (SoC of electrolyte, just oxidation or reduction on one electrode), instead of standard charge-discharge cycling alterations of conditions during each cycle.

We have observed that the main source of negative electrode felt deactivation is purely chemical deactivation due to negative electrolyte without current load with negligible changes due different SoC (+25 – +95 %) and that mild acceleration of deactivation takes place on reduction felt, whereas a bit stronger deceleration on oxidation felt under current density loads (150 – 500 mA cm<sup>-2</sup>) compared to purely chemical conditions.

### Acknowledgments

The work was supported from European Regional development Fund-Project "Organic redox couple based batteries for energetics of traditional and renewable resources (ORGBAT),, No. CZ.02.1.01/0.0/0.0/16\_025/0007445 and from grants of Specific university research – grant A1\_FCHI\_2021\_004 and A2\_FCHI\_2021\_022.



EVROPSKÁ UNIE  
Evropské strukturální a investiční fondy  
Operační program Výzkum, vývoj a vzdělávání



MINISTERSTVO ŠKOLSTVÍ,  
MLÁDEŽE A TĚLOVÝCHOVY

### References

1. Mazur, P.; Mrlík, J.; Pcedič, J.; Vrána, J.; Dundalek, J.; Kosek, J.; Bystron T., Effect of graphite felt properties on the long-term durability of negative electrode in vanadium redox flow battery. *J. Power Sources* 2019, 414, 354-365.
2. Darling, R.M.; Perry, M.L. Half-Cell Steady-State Flow-Battery Experiments. *ECS Trans.* 2013, 53, 31–38.

## Visualizing Impedance Spectroscopy Response for Interpretation of Collected Data

P. Vanýsek<sup>a</sup>

<sup>a</sup> Department of Electrical and Electronic Technology, FEKT, Brno University of Technology, Technická 3058/10, 616 00 Brno, Czech Republic

Measurements and interpretation of electrical impedance in electrochemistry and in related studies has become recently fairly commonplace as both the hardware and the interpretation software are more and more standard part of electrochemical potentiostats. With the interpretation software it is possible to model the studied system in any conceivable way, even if the physical reality may not follow the chosen model. An example is given where a circuit consisting of a capacitor with resistors in series and parallel are evaluated as if the circuit were just a pure capacitor. The method of plotting the results as complex permittivity and complex modulus is also shown. Finally, a result of lead acid battery electrode impedance, treated by the emerging method of distribution of relaxation times (DRT) is also given.

### What Is Impedance and How to Graph It

Electrical impedance spectroscopy method consists of an experiment in which frequency dependent resistance to current flow, measured over a broad (typically at least 4 to 5 order of magnitude) frequency range, is collected. The information at each frequency consists of two data values; the resistance as a ratio of potential divided by current and a phase shift between the imposed potential and the resulting current flowing through the studied system. The obtained data are conveniently treated as complex numbers with the attendant various methods of notation as well as a variety of graphical presentations.

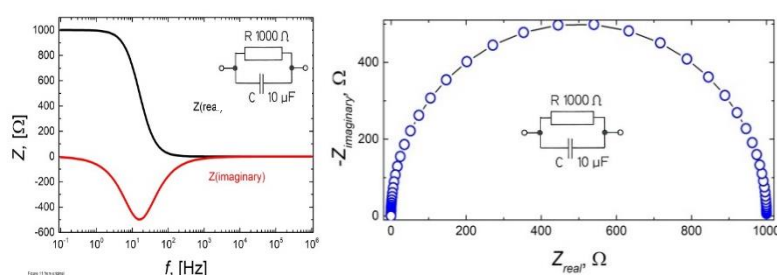


**Figure 1. and 2.** Bode (1) and Nyquist (2) graphical depiction of a simple RC circuit

Most readily used presentations are Bode and Nyquist diagrams. For a simple parallel RC circuit a possible Bode plot representations is in Fig. 1. Due to wide spectrum of frequencies used the x-axis will be always logarithmic. The y-axis could be linear or logarithmic, or one axis could represent the impedance vector and another phase shift. The Nyquist plot depicts (Fig. 2, for the same circuit) real vs. imaginary impedance. The axes should be isometric, which assures that the RC response is a perfect semicircle, a good guide for visual interpretation. Besides graphing the Nyquist of Bode plots with impedance values, it is also possible to use admittance, capacitance, inductance,

permittivity, or other related values, some of which may be useful, but some of which may cause confusion, as will be shown later.

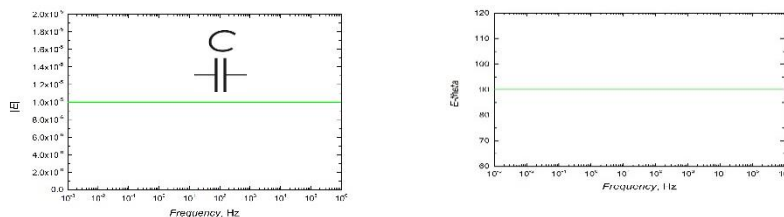


**Figure 3.** Permittivity response of a simple ideal capacitor.

### Plotting other parameters than impedance.

Software usually supplied with impedance analyzers allows plotting data using different parameters in addition to impedance or admittance. These involve calculation transformation with *a priori* assumption that the measured response can be actually meaningfully transformed. Most notable are plots of permittivity (real and imaginary, or the vector value and phase angle) or modulus, which is the inverse of permittivity.

Fig. 3 depicts the vector and phase angle theta of permittivity evaluated from response from an ideal capacitor. In this case, the response is frequency independent as for an ideal capacitor the dielectric maintains its value regardless of applied frequency.

On the face of this, one would assume that any circuit with an ideal capacitor and some resistors, which have also resistance independent of frequency, would give a response with the permittivity or modulus independent of frequency. However, this is not the case, as demonstrated in Figs. 4 and 5.

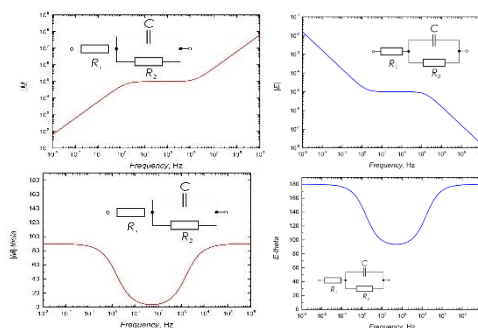


**Figure 4. and 5.** Permittivity and modulus response of an R(RC) circuit.

This may bring into question some results reported throughout literature, where authors describe results documenting permittivity dependent on frequency. While at very high frequencies permittivity will be function of frequency, at the low values, e.g., in the range of acoustic frequencies, one would more reasonable expect frequency independent behavior.

### Method of Distribution of Relaxation Times

Another interesting and possibly useful approach to obtain a better insight into collected impedance results may be the use of mathematical method DRT (distribution of relaxation times). A few years ago, this method of evaluation appeared in the literature [1, 2], although this concept is not entirely new. Yager published a paper on the distribution of relaxation times in dielectrics already in 1936 [3]. What has sparked the recent interests is the possibility of mathematical processing on a PC.

The available method (DRTtools) is an application of the MATLAB program and was used in publications [4] and [5]. Here (Fig. 6, 7) we give an example outcome of processed data, using previously obtained data by Petr Krivik during his study of charging and discharging a sealed lead-acid battery (impedance results interpreted in [6]).

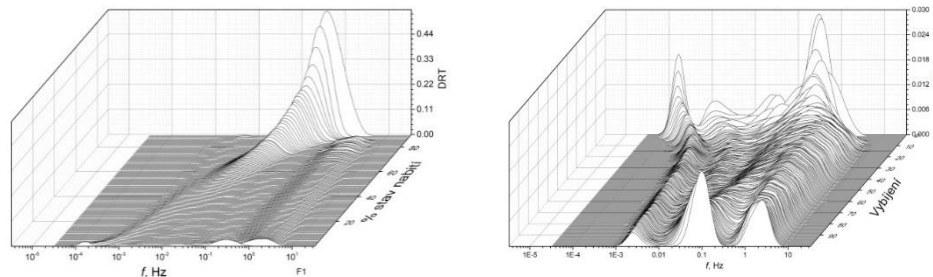


**Figure 6. and 7.** DRT method applied to a large set of impedance measurements during charging (6) and discharging (7) a lead acid cell. Data courtesy P. Krivik.

### Acknowledgments

This work was supported by a specific research grant of the Brno Technical University; project FEKT-S-20-62060 and in part by the Czech Science Foundation project GA ČR GA19-23718S.

### References

1. BioLogic, Distribution of Relaxation Times (DRT): an introduction, BioLogic, Editor. 2017.
2. Weese, J., A reliable and fast method for the solution of Fredholm integral equations of the first kind based on Tikhonov regularization. *Computer Physics Communications*, 1992. **69**(1): p. 99-111.
3. Yager, W.A., The Distribution of Relaxation Times in Typical Dielectrics. *Physics*, 1936. **7**(12): p. 434-450.
4. Shoar Abouzari, M.R., et al., On the physical interpretation of constant phase elements. *Solid State Ionics*, 2009. **180**(14): p. 922-927.
5. Wan, T.H., et al., Influence of the Discretization Methods on the Distribution of Relaxation Times Deconvolution: Implementing Radial Basis Functions with DRTtools. *Electrochimica Acta*, 2015. **184**: p. 483-499.
6. Krivik, P. and S. Vaculik, Impedance Methods for SoC Determination of Lead Acid Battery Cell. *ECS Transactions*, 2017. **81**(1): p. 151-161.

## Electrochemically Deposited Binder-Free MnO<sub>2</sub> Cathode for Aqueous Zinc-Ion Batteries

A. I. Volkov<sup>a</sup>, A. O. Efremova<sup>a</sup>, E. G. Tolstopyatova<sup>a</sup>, and V. V. Kondratiev<sup>a</sup>

<sup>a</sup> Department of Chemistry, Saint Petersburg State University  
Universitetskaya nab. 7/9, Saint Petersburg, 199034, Russia

Recent developments in the field of metal-ion batteries have led to a renewed interest in aqueous zinc-ion batteries (AZIBs) as alternative power sources. Zinc-ion systems are promising research objects for energy storage systems because of their safety, environmental friendliness, and cost effectiveness (1,2).

Various manganese dioxide (MnO<sub>2</sub>) polymorphs are one of the most widely used groups of compounds for cathode materials in AZIBs. Manganese dioxides are promising cathode materials due to environmental friendliness, abundance of resources, high theoretical capacity (308 mA h g<sup>-1</sup>), and relatively wide working voltage. A large and growing body of literature has investigated manganese oxides with various crystal structures as prospective zinc-ion storing materials. Many recent studies have attempted to use  $\alpha$ -,  $\beta$ -,  $\gamma$ -,  $\delta$ -,  $\epsilon$ -,  $\lambda$ -, and todorokite-MnO<sub>2</sub> in zinc-ion systems, and it has been demonstrated that these structures can transform mutually (2). Yet, to date there has been little agreement on what the exact mechanism of charge storage in such systems is. The issue is complicated by the possibility of emergence of compounds like zinc hydroxide sulfate, various hydrates, etc (3).

Electrochemical deposition is a well-known approach to synthesis of MnO<sub>2</sub> compounds. Electrode materials obtained in such a way have been used both in supercapacitors and in Zn-ion batteries (4,5). This method allows to obtain materials without using binders or conductive components, such as carbon black.

This work proposes an electrochemically deposited manganese dioxide-based cathode material. We report on electrochemical performance of binder-free  $\epsilon$ -MnO<sub>2</sub> on graphite foil as a cathode material for AZIBs. Electrodeposition method provides direct contact of  $\epsilon$ -MnO<sub>2</sub> with the current collector, eliminating the need for additional binding and conductive components. The material was deposited in potentiostatic mode at 1.4 V vs Ag/AgCl (sat. NaCl) electrode. Deposition time varied depending on the required mass loading determined via Faraday's law. The materials were calcinated at 300 °C for 3 h prior to the studies.

The morphology, structure, and chemical composition of the product at various stages of its use were analyzed by X-ray diffraction measurements (XRD, Bruker-AXS D8 DISCOVER, Germany) using Cu K $\alpha$  radiation. Morphology of the materials was investigated by scanning electron microscopy (SEM, SUPRA 40VP, Carl Zeiss, Germany). EDX elemental analysis of samples and element mapping was performed.

Electrochemical studies were performed both in standard three-electrode cells and CR2016-type half cells. Mixed aqueous solution of 2 mol dm<sup>-3</sup> ZnSO<sub>4</sub> and 0.1 mol dm<sup>-3</sup> MnSO<sub>4</sub> was used as the electrolyte in all cases. MnSO<sub>4</sub> additive was used, as it is a principal stabilizing agent for MnO<sub>2</sub>-based electrode materials in zinc-ion systems. For three-electrode cells, the obtained MnO<sub>2</sub> material was used as working electrode, and Zn foil was used as both reference and counter electrodes. In half cells, a glass fiber filter paper Whatman® GF/A (pre-soaked in the electrolyte) was sandwiched between  $\epsilon$ -MnO<sub>2</sub> cathode and a zinc foil anode. Cyclic voltammograms and galvanostatic charge-

discharge curves were recorded on Bio-Logic VSP-300 electrochemical workstation and battery testing system Neware BTS-3000.

XRD patterns of the synthesized material show that  $\epsilon$ -MnO<sub>2</sub> was obtained (ICDD no. 00-030-0820).

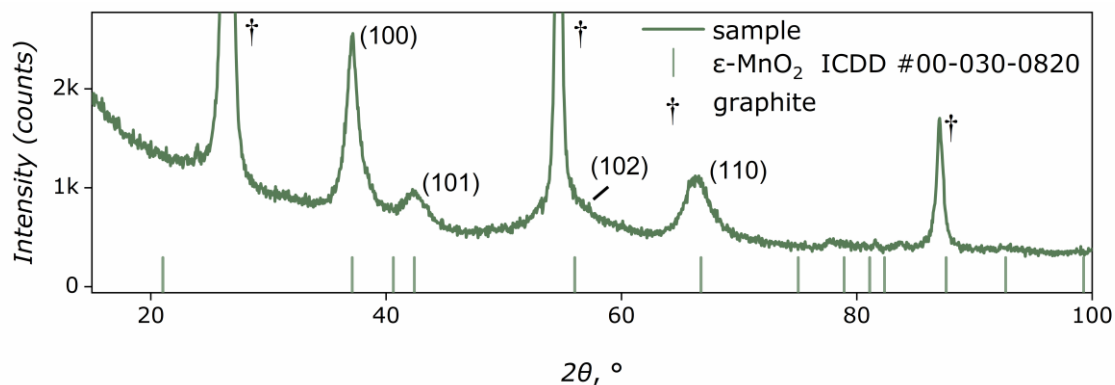


**Figure 1.** XRD pattern of obtained  $\epsilon$ -MnO<sub>2</sub> sample on graphite foil.

Cyclic voltammograms recorded for initial 3 cycles show that redox peaks redistribute to result in a commonly reported curve shape. Reorganization of the material and emergence of new structures, such as zinc hydroxide sulfate, may cause such transformation of voltammograms. In the stabilized form, the oxidation peak at 1.65 V, followed by a shoulder, is opposed by reduction peaks at 1.38 V and 1.22 V. Depending on the prevalence of surface or volumetric processes, MnOOH and Zn<sub>x</sub>MnO<sub>2</sub> both may be the products of cathodic reaction due to Mn<sup>4+</sup> reduction to Mn<sup>3+</sup>.

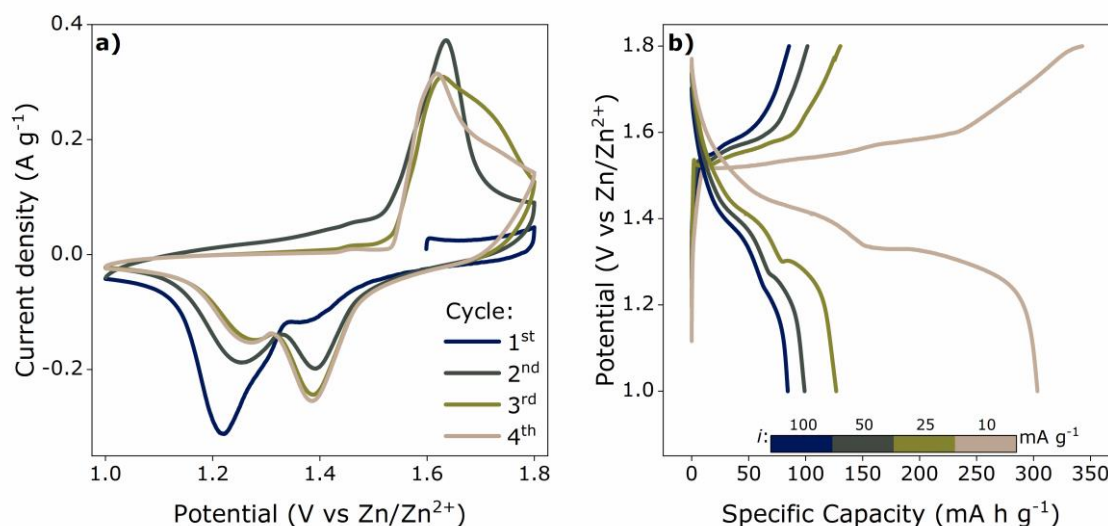


**Figure 2.** a) Cyclic voltammograms of MnO<sub>2</sub> electrodes on initial cycles at 0.1 mV s<sup>-1</sup>, b) galvanostatic charge-discharge curves of MnO<sub>2</sub> electrodes with increased mass loadings in coin cells at various current densities.

Zn/MnO<sub>2</sub> cell with aqueous electrolyte delivers a moderate specific capacity of about 120 mA h g<sup>-1</sup> at 100 mA g<sup>-1</sup> and the cycling stability with 82% capacity retention after 100 cycles. Upon increase of mass loading to 1.3 mg cm<sup>-2</sup> rate capability of electrodes decreased, thus only 84 mA h g<sup>-1</sup> was achieved at 100 mA g<sup>-1</sup>. However, low current density of 10 mA g<sup>-1</sup> allowed to extract up to 303 mA h g<sup>-1</sup>. This high value shows that the processes of Zn intercalation into the

material do not cease due to “stuck”  $\text{Zn}^{2+}$  ions in the crystal lattice. However, it points at necessity to facilitate ionic transport to allow extracting full capacity at higher current densities. Lower current rates also allow to see potential areas requiring more caution for systems with  $\text{MnO}_2$ -based materials. In this case, anodic area above 1.75 V is prone to an irreversible process decreasing total coulombic efficiency, yet this effect only occurs at 10 mA  $\text{g}^{-1}$ .

### Acknowledgments

The financial support from RFBR (grant № 21-53-53012) is gratefully acknowledged. The authors would like to thank the Center for X-ray Diffraction Methods and the Interdisciplinary Center for Nanotechnology of Research Park of Saint Petersburg State University.

### References

1. X. Zhang, L. Wang, H. Fu, *J. Power Sources*, **493**, 229677 (2021).
2. M. Song, H. Tan, D. Chao, and H. J. Fan, *Adv. Funct. Mater.*, **28**, 1 (2018).
3. N. Liu, B. Li, Z. He, L. Dai, H. Wang, and L. Wang, *J. Energy Chem.*, **59**, 134 (2021).
4. A. Huang, J. Chen, W. Zhou, A. Wang, M. Chen, Q. Tian, and J. Xu, *J. Electroanal. Chem.* **873**, 114392 (2020).
5. J. Yang, L. Lian, H. Ruan, F. Xie, and M. Wei, *Electrochim. Acta*, **136**, 189 (2014).

## Study of Negative Electrode for Lead-acid Batteries Using Operando Confocal Laser Microscopy

L. Chladi<sup>a,b</sup> and H. Hálová<sup>a</sup>

<sup>a</sup> Institute of Electrotechnology, Faculty of Electrical Engineering and Communication, BUT, Technická 10, 616 00 Brno, Czech Republic

<sup>b</sup> Centre for Research and Utilization of Renewable Energy, Faculty of Electrical Engineering and Communication, BUT, Technická 10, 616 00 Brno, Czech Republic

Our contribution deals with the laser microscopy observation of the negative electrode for lead-acid batteries during their lifespan. Electrode with pasted negative active mass was optimized for cycling in opto std electrochemical cell by EL-CELL. Crystal growth and changes of electrode surface during cycling were observed using a confocal microscope Olympus Lext OLS4100. We evaluate the surface changes and sulfate crystal growth during deep cycling. The cycling mode leads to fast gradual degradation of the negative electrode – mostly because of irreversible sulfation.

### Introduction

Although lead-acid batteries have been known for more than 150 years, they are constantly evolving due to the emergence of new problems caused by other areas of use and the extension of the overall life of batteries. The current development of lead-acid batteries mainly concerns optimization for hybrid vehicles, where irreversible sulphation occurs due to the long-term persistence of batteries only in a partially charged state (between 40-60% of the total capacity) [1].

Under normal conditions, reversible sulfation occurs in the lead-acid battery - the formed lead sulfate crystals easily decompose into the original active electrode materials and sulfuric acid ions during charging. However, due to the cell remaining only in a partially charged state, the crystals do not disintegrate sufficiently during charging, and thus sulfate is preferentially deposited on the previously formed crystals. The resulting layer of large crystals clogs the pores in the active materials and reduces the effective area of the electrodes - gradually reducing both the battery capacity and increasing the internal resistance and stress on the cells. [2] [3].

The rate of sulfation can be influenced to some extent by additives added to the negative mass – eg the use of BaSO<sub>4</sub>, lignosulfates, or carbon [1]. These additives have a certain positive effect on the size and subsequent growth of crystals, but at the same time, they can lead to more intensive evolution of hydrogen on the electrode during charging and thus affect the gassing of the cell and the loss of water [1] [3].

To be able to reduce the rate of sulfation, it is important to understand deeply the development of sulfate crystals themselves, both in the deep cycle and in the PSoC mode. From the point of view of experimental conditions, the use of a confocal microscope is offered in this direction because of the possibility of continuously monitored the active surface of the electrodes with a resolution up to 10 nm [4]. With the help of successive laser scanning, the relief of the mass surface is gradually scanned with different focus depths and the images are combined in a bright image of the negative electrode surface.

## Experimental

Electrodes were prepared from a lead sheet 0.5 mm thick. A circular disk 1.4 cm in diameter was at first coated with a thin layer of epoxy adhesive on the bottom side - for reducing the active lead surface. Thus, the epoxy layer prevented the reaction on the lead surface outside the area of the pasted mass (Fig. 1 - center). After the glue hardened, the electrode was drilled in the middle, which generate a hole with a diameter of 1.5 mm. The active substance was then prepared from the mixture of lead dust, barium sulfate, borosilicate, and sulfuric acid in a ratio of 10 g of powder mass per 0.5 g of H<sub>2</sub>SO<sub>4</sub>. The homogenized paste was then applied to the lead electrode according to Fig. 1 - center. The weight of active mass was 0.0104 g. The counter-electrode was formed by twisting a 0.5 mm thick lead metal belt with a length of 11 cm and a stripe height of 2 mm, which ensured a sufficiently large active area of the counter-electrode with comparison to the negative pasted electrode (see Fig 1 - left).



**Figure 1.** Counter-electrode (left), Pasted negative electrode (center), assembled in-situ cell for laser confocal microscopy (right)

The formed electrodes were placed in a hermetically sealed cell for optical observations, flooded with 27% sulfuric acid ( $\rho = 1.19 \text{ g/cm}^3$ ), clamped, and placed in a confocal microscope. The cell was contacted and controlled by the Biologic VSP-VMP3 potentiostat.

The initial formation of the lead cell took place for 15 hours at a rate of 0.1 C. Due to the slight gassing of the cell during charging during molding, it was not possible to take a valid series of 3D images from this part with a confocal microscope.

Then the series of the first deep cycles was started, this time with twice the current, ie  $I = 0.208 \text{ A}$  (0.2 C), during which the confocal microscopy was also started. The charging of the cell was limited by potential 0.05 V vs. Cd/Cd<sup>2+</sup> reference electrode and then the limitation potential was held for 30 minutes. Discharging was limited by 0.3 V vs. Cd/Cd<sup>2+</sup>.

Images taken during the first cycles showed changes in the active mass in the charged and discharged state. In the charged state we observed the increase of bright areas and spots that are related to the occurrence of grey lead and at the same time gradual reduction of areas with lead sulfate crystals were observed, while the discharge process was the opposite - there was a gradual decrease in the amount of gray lead at the expense of sulfates formation. Moreover, during the cycling, large sulfate crystals appeared (fig. 2) and because of constructive interference of the reflected laser beam on the surface crystal planes of sulfates, the crystals appeared as striped areas.

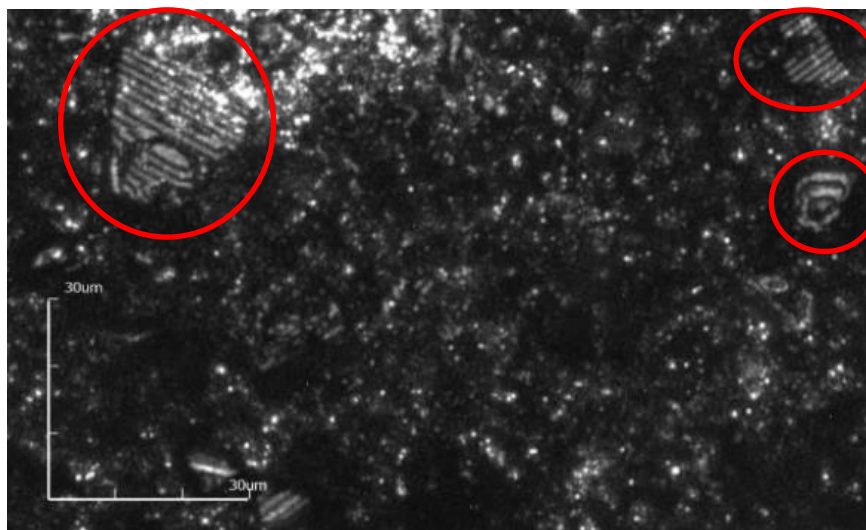


**Figure 2.** Image of negative active mass obtained by confocal scanning microscope with marked sulfate large-sized crystal grown electrode on the surface.

### Conclusions

The use of a confocal microscope in the observation of crystal growth brings new hitherto unrealized possibilities of in-situ monitoring the sulfation process and thus also a more extensive understanding of the issue.

However, for a successful observation, it was necessary to adapt the cell to the corrosive environment of sulfuric acid and to hermetically seal the system also for the corrosive aqueous environment. Since the observation took place only on the upper part of the electrode, it was also necessary to design a suitable geometry of the electrodes and to adapt the cycling mode avoiding excessive polarization of the electrodes and consequently excessive gassing of the cell. A significant reduction in the active mass of the negative electrode turned out to be the right way, with up to 90% of the weight being removed compared to previous proposals.

From the first series of deep cycles, the effect of charging and discharging on the electrode surface was evident. The images showed places with a more significant reduction of emerging crystals compared to other parts of the sample, where there was a more difficult reduction of large crystals. At these less-active sites, it can be expected that faster sulfation will occur during further experiments.

### Acknowledgment

This work was supported by the specific graduate research of the Brno University of Technology No. FEKT-S-20-6206.

### References

1. D. Pavlov, Lead-acid batteries: science and technology: a handbook of lead-acid battery technology and its influence on the product. Elsevier Science, Amsterdam (2011)
2. M. Cenek, Akumulátory od principu k praxi, FCC Public, Prague (2003)
3. P. T. Moseley, J. Energy Storage, **19**, 272-290, (2018)
4. LEXT OLS4100: Industrial Laser Confocal Microscopes, OLYMPUS

## The Electrochemical Performance of $\delta$ -MnO<sub>2</sub> Cathode Material for Aqueous Zinc-Ion Batteries: the Role of Current Collector

M. A. Kamenskii<sup>a</sup>, S. N. Eliseeva<sup>a</sup>, V. V. Kondratiev<sup>a</sup>

<sup>a</sup> Institute of Chemistry, St Petersburg State University, St Petersburg, 199034, Russia

Electrochemical properties of  $\delta$ -MnO<sub>2</sub>-based cathode materials for zinc-ion batteries were studied using various current collectors (stainless steel mesh, carbon paper and titan foil). Among the investigated materials the stainless steel current collector was the most inconvenient for oxide-based electrode materials which was confirmed by galvanostatic charge/discharge measurements and cyclic voltammetry. This phenomenon might be explained by side reactions of electrolyte decomposition and corrosion of steel.

### Introduction

Novel types of energy storage systems are rapidly developed in last decades. Among them, aqueous zinc-ion batteries (AZIBs) have attracted special research attention owing to low cost, high specific capacity of zinc anode (820 mAh·g<sup>-1</sup>), environmental friendliness and safety (1). Many types of cathode materials for AZIBs have been recently investigated (2), among them different types of manganese dioxide MnO<sub>2</sub> are on the top of the study because of its numerous advantages such as environmental friendliness, low cost, abundance, remarkable theoretical capacity (308 mAh·g<sup>-1</sup>) and relative high voltage of redox transformation (1.3 – 1.5 V vs. Zn/Zn<sup>2+</sup>) (3). Among different types of MnO<sub>2</sub> crystal lattice, layered-type MnO<sub>2</sub> (or  $\delta$ -MnO<sub>2</sub>) is promising candidate because of its structure facilitate to reversible process of zinc ion intercalation.

Nevertheless, the main drawbacks of MnO<sub>2</sub> as cathode material for ZIBs are low electronic conductivity of the oxide and manganese dissolution during charge/discharge processes. Addition of Mn<sup>2+</sup>-containing salt helps improving cycling stability by suppressing the dissolution of MnO<sub>x</sub> layer (4). To increase the electronic conductivity, various types of carbon coatings or graphene can be applied.

In accord with reported data different types of current collector were applied for  $\delta$ -MnO<sub>2</sub>-based cathodes: stainless steel mesh or grid, various forms of carbon paper or clothes and titan foil. As it was demonstrated previously for electrode materials for lithium-ion batteries, the nature of current collector can affect on the electrochemical performance of  $\delta$ -MnO<sub>2</sub> cathodes. In the case of AZIBs with aqueous electrolytes also can be supposed that the nature of current collector material can greatly effect on the electrode processes.

### Experimental Details

$\delta$ -MnO<sub>2</sub> was synthesized hydrothermally as it was ascribed in (5). The 0.001 M MnSO<sub>4</sub> aqueous solution was mixed with 0.006 M KMnO<sub>4</sub> aqueous solution under stirring for 30 min, then the solution obtained was transferred in the Teflon autoclave and heated up to 160 °C for 12 h. The product obtained were washed by deionized water for five times and dried under vacuum at 55 °C. The black powder was tested by X-ray diffraction (Cu K <sub>$\alpha$</sub>  radiation).

$\delta$ -MnO<sub>2</sub> electrodes were prepared by mechanically mixing of electroactive grains with carbon black and polyvinylidene fluoride (PVDF) in the ratio 70 wt% of  $\delta$ -MnO<sub>2</sub>, 20 wt% of carbon and 10 wt% of PVDF. The resulting viscous slurry was cast on the stainless steel grid, carbon paper and titan foil (blade gap height – 150  $\mu$ m), dried under vacuum at 60 °C for 12 h. Mass loading of the electrodes was near 5 mg·cm<sup>-2</sup>, 2 mg·cm<sup>-2</sup> and 1 mg·cm<sup>-2</sup> for electrodes on steel, carbon paper and Ti. Electrodes were assembled in CR2032 coin cells vs. Zn anode, Whatman glass fiber soaked in aqueous solution 2 M ZnSO<sub>4</sub> / 0.1 M MnSO<sub>4</sub> was used as separator. Electrochemical tests were performed by galvanostatic charge/discharge (current 0.3 A·g<sup>-1</sup>), cyclic voltammetry (CV) at a scan rate of 0.1 mV·s<sup>-1</sup> in the potential range 1.0 – 1.8 V vs. Zn/Zn<sup>2+</sup> and electrochemical impedance spectroscopy.

## Results and Discussion

X-ray diffraction patterns of powder synthesized and electrode material are shown on Fig. 1. The MnO<sub>2</sub> pattern demonstrated a high-intensive peak at 24.77 ° and several coupled peaks which are usually observed for layered-type material. Thus, it confirmed that layered manganese dioxide MnO<sub>2</sub> with molecular formula K<sub>0.27</sub>MnO<sub>2</sub> · 0.54 H<sub>2</sub>O. The same peaks are observed for electrode material which allow us to conclude that no crystal lattice changes are not occurred.

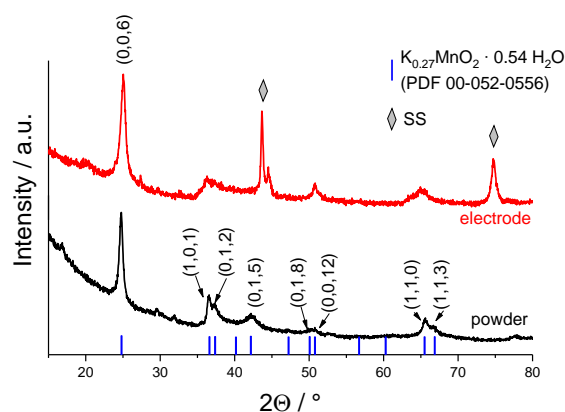


**Figure 1.** XRD patterns of  $\delta$ -MnO<sub>2</sub> powder and electrode material on stainless steel.

Fig. 2,a shows electrochemical performance of  $\delta$ -MnO<sub>2</sub> cathodes vs. Zn anode on two types of current collector: steel and carbon paper, at a current density 0.3 A·g<sup>-1</sup>. It is clearly seen that electrode cast on the carbon paper demonstrated a five-times higher specific capacity values at selected current (near 150 mAh·g<sup>-1</sup>) while electrode material on stainless steel shows only 30 – 40 mAh·g<sup>-1</sup>. In both cases during initial 20 – 25 cycles increasing of specific capacity is observed which correlated with MnO<sub>x</sub> electroactive layer formation, and then the maximum value is stabilized.

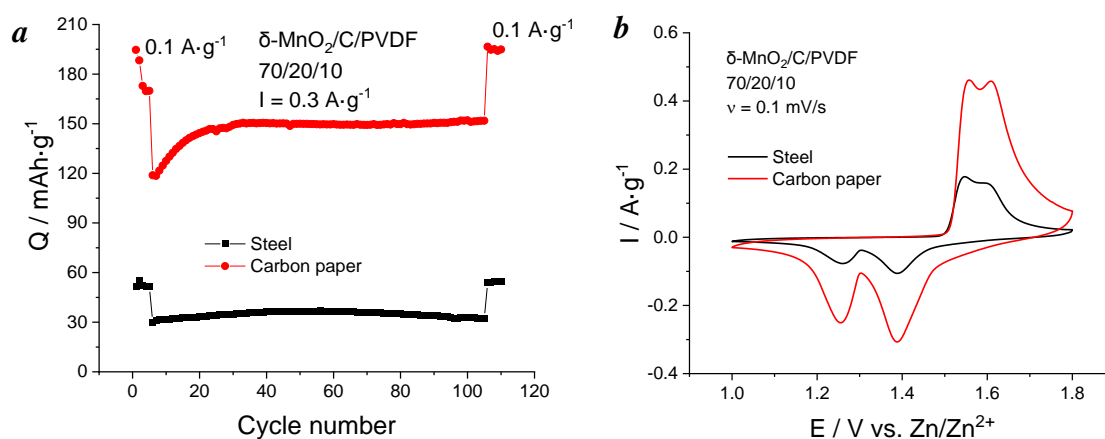


**Figure 2.** a) Cycling stability of  $\delta\text{-MnO}_2$  electrodes on carbon paper and stainless steel at  $0.3 \text{ A}\cdot\text{g}^{-1}$ ; b) cyclic voltammograms of  $\delta\text{-MnO}_2$  electrodes after 100 charge/discharge cycles.

On the cyclic voltammograms of the cells after charge/discharge tests two pairs of peaks are determined. The first pair is connected with zinc intercalation/deintercalation and insoluble salt layer formation and the second one is assigned to proton intercalation. For the  $\delta\text{-MnO}_2$  electrode cast on carbon paper specific current density values were in three times higher than for electrode with steel current collector.

Thus, these results demonstrated that application of stainless steel as current collector is irrelevant than carbon paper or titan foil. This can be associated with corrosion processes on steel and electrolyte decomposition at high anodic potentials.

### Acknowledgments

This work was supported by Russian Foundation for Basic Research (project No 21-53-53012). Scientific research were performed at the Centre for X-ray Diffraction Studies of Research park of St. Petersburg State University.

### References

1. X. Zhang, L. Wang, and H. Fu, *J. Power Sources*, **493**(December 2020), 229677 (2021).
2. N. Liu, B. Li, Z. He, L. Dai, H. Wang, and L. Wang, *J. Energy Chem.*, **59**, 134 (2021).
3. J. Wang, J.-G. Wang, H. Liu, C. Wei, and F. Kang, *J. Mater. Chem. A*, **7**(22), 13727 (2019).
4. C. Qiu, X. Zhu, L. Xue, M. Ni, Y. Zhao, B. Liu, and H. Xia, *Electrochim. Acta*, **351**, 136445 (2020).
5. F. Zhang, C. Wang, J. Pan, F. Tian, S. Zeng, J. Yang, and Y. Qian, *Mater. Today Energy*, **17**, 100443 (2020).

## Ionic liquids as additive modifying electrolyte of lead-acid battery

P. Kędzior<sup>a,b</sup>, W. Rzeszutek<sup>a</sup>, J. Wojciechowski<sup>b</sup>, G. Lota<sup>b</sup>,

<sup>a</sup> PPUH Autopart Jacek Bąk sp. z o.o., Mielec 39-300, POLAND

<sup>b</sup> Institute of Chemistry and Technical Electrochemistry, Poznan University of Technology,  
Berdychowo 4, Poznań 60-965, POLAND

pkedzior@autopart.pl

### Introduction

The lead-acid batteries due to the relatively low energy consumption during production and high efficiency of recycling are still dominating for automotive applications. Currently, a lot of different types of vehicles are characterized by an increase in the degree of hybridization and electrification. Batteries need to improve with the growing demand for reliable energy sources for vehicles and to reduce fuel consumption and carbon dioxide emissions. Growing demand for batteries and developing competing technologies motivate manufacturers of lead-acid battery for continuous improvement, for example grid production methods, alloys composition and additives to active mass or electrolyte (1). The possibility of using Ionic Liquids (ILs) as additive modifying electrolyte is an extremely interesting issue (2-6). Ionic liquids have become the group of the most promising chemical compounds due to their unique properties, like: high conductivity, thermal and chemical stability, low volatility, low toxicity and almost endless possibilities between cations and anions combinations. They found many applications in chemical industry, including electrochemistry (7-8).

### Experimental

All the electrochemical measurements were performed at ambient conditions in 37% H<sub>2</sub>SO<sub>4</sub> aqueous electrolyte (the same electrolyte in a lead acid battery in a charged state) with or without 0.5 mg L<sup>-1</sup> ionic liquid additive. PbCaSn alloy for lead-acid battery grid manufacturing was used as a working electrode, while Pb (purity min. 99,9%) and Hg/Hg<sub>2</sub>SO<sub>4</sub>/1M H<sub>2</sub>SO<sub>4</sub> served as a counter and reference electrode, respectively. At the beginning, hydrogen and oxygen evolution potentials were measured. Then, corrosion potential and corrosion current density values were determined by means of Tafel extrapolation method. All of the electrochemical parameters were assessed using the linear sweep voltammetry. All tests were performed using an electrochemical workstation potentiostat/galvanostat VMP3 (Biologic, France) with impedance module. Ionic liquids used in the research can be divided into two basic groups: alkylammonium sulfates and alkyylimidazolium sulfates. The cations used in the compounds differ in the number of alkyl groups in the structure and the length of the main substituent. The basic long-chain alkyl group in the investigated ionic liquids was the hexadecyl group.

### Results and discussion

The presented results show that the modification of the electrolyte with an ionic liquid increases the overpotential of the hydrogen and oxygen evolution reaction and may have a strong

influence on the corrosion intensity of PbCaSn alloy, even at low concentration. This phenomenon can be explained by the possibility of forming an organic layer at the alloy/sulfuric acid interface.

### Acknowledgments

The authors thank the Polish Ministry of Education and Science for financial support (Applied Doctorate Program, No. DWD/3/20/2019).

### References

1. Pavlov D.: Lead-Acid Batteries Science and Technology, 1 Ed. 2011,
2. B. Rezaei, S. Mallakpour, M. Taki, J. Power Sources, 187 (2009) 605–612,
3. B. Rezaei, E. Havakeshian, A.R. Hajipour, J. Solid State Electrochem., 15 (2011) 421–430
4. M.A. Deyab, J. Power Sources, 390 (2018) 176–180.
5. K. Kopczyński, A. Gabryelczyk, M. Baraniak, B. Łęgosz, J. Pernak, P. Kędzior, G. Lota, Int. J. Electrochem. Sci., 13 (2018) 11058 – 11073,
6. K. Kopczyński, A. Gabryelczyk, M. Baraniak, B. Łęgosz, J. Pernak, P. Kędzior, G. Lota, Int. J. Electrochem. Sci., 13 (2018) 4390 – 4400,
7. D.R. Macfarlane, M. Forsyth, P.C. Howlett, J.M. Pringle, J. Sun, G. Annat, W. Neil and E.I. Izgorodina, Acc. Chem. Res., 40, 1165 (2007).
8. H. Liu, Y. Liu and J. Li, Phys. Chem. Chem. Phys., 12, 1685 (2010).

## Impedance Measurements of AGM Solar Battery for RAPS Systems

Petr Křivík<sup>1</sup>, Petr Bača<sup>1</sup>, Jiří Kazelle<sup>1</sup>

<sup>1</sup> Department of Electrotechnology, Faculty of Electrical Engineering and Communication, Brno University of Technology, Technická 10, 616 00 Brno, Czech Republic

The paper deals with the measurement of the cell impedance parameters during discharging and charging of the AGM 200Ah 6V Sun Power lead acid battery. Re (Z) and Im (Z) of the battery were measured by PEIS method. Results of the impedance changes during discharging and charging were plot to Nyquist diagrams. Important values  $R_s$ ,  $R_{CT}$ ,  $C_{DL}$  and  $\sigma$  were found during discharging and charging of the battery.

### Introduction

Lead acid batteries are an important part of many remote area power supply systems (RAPS). Remote area photovoltaic system (also referred to as an off-grid) is characterized by the fact that it is not connected to the grid and contains a battery. RAPS systems should be used in places where there is no access to the distribution network or where the construction of an electrical connection would involve high costs. An important part of the RAPS systems is the photovoltaic panel, which is connected to the solar controller. It is connected to a battery or a set of several batteries. The controller controls the charging voltage and current from the PV panel to match the recommended battery charging values. Appliances operating on direct current at a voltage level of 12V or 24V are also connected to the controller. Part of the charge controller is monitoring the current capacity of the batteries - in case of risk of overcharging of the battery disconnects the solar panel from it. Conversely, if there is a risk of deep discharge of the battery disconnects all appliances and loads. The controller is the center of the RAPS solar system, to which all other components are connected and controls the supply and output of the energy.

The system voltage determines the voltage of the battery or battery pack. Standard system voltages are 12V, 24V and 48V. The required system voltage can be achieved by appropriate connection of individual battery cells. The system voltage must correspond to the charge controller and the appliances that are connected to the controller. The charging and discharging currents of the battery depend on the system voltage. For the smallest RAPS systems, a voltage of 12V is sufficient, for larger ones it may be more advantageous to choose a voltage of 24V or 48V. Higher system voltages allow you to charge and discharge a battery pack with lower current. To select a suitable power, it is necessary to know at least the daily consumption of the building where the system will be installed - lead batteries must have at least 2 times more capacity in Wh than the daily consumption. Lead-acid batteries are most often used in solar systems. Lead acid solar batteries are usually maintenance-free with electrolyte in the form of a gel or AGM batteries. Recently, lithium-based batteries have been used - eg lithium iron phosphate ( $\text{LiFePO}_4$ ,  $\text{LiFeYPO}_4$ ). Lithium batteries are more expensive, but they have significantly lower weight than lead-acid batteries, it can withstand higher charging / discharging currents, can handle deeper discharges, and have a longer cycle life [1].

Potentiostatic electrochemical impedance spectroscopy (PEIS) may be a suitable method for determination the state of a lead-acid battery used in an RAPS system. This method makes it possible to monitor the impedance of a lead-acid battery over a wide range of frequencies, and the results are displayed by impedance diagrams [2]. The electrochemical impedance of a battery Z is a complex

frequency-dependent number, described either by its real and imaginary parts  $\text{Re}(Z)$  and  $\text{Im}(Z)$ , or by its modulus  $|Z|$  and phase angle  $\phi$ . Different frequencies reflect different lead-acid battery parameters, from ohmic resistance through charge transfer resistance at the electrodes, the double layer capacity to the Warburg impedance associated with ion diffusion in the electrolyte and electrode pores.

The general shape of the Nyquist diagram of the complex electrochemical impedance of a battery is shown in Fig. 1 on the left. This diagram represents the ohmic resistance  $R_S$  in the range  $\text{m}\Omega$ , which is the real part of the impedance at frequencies higher than 100 Hz, the capacitive arc ( $R_{CT}$  size) for frequencies between 0.1 and 100 Hz, the second linear part for frequencies lower than 0.1 Hz. Nyquist diagram contains ohmic resistance due to interconnection, separator, electrolyte resistance and resistance of electrodes, capacitive arc is related to electrode porosity, the second linear part at low frequencies depends on the formation or dissolution reaction of sulphates on electrodes, which rate is controlled by the transport of  $\text{Pb}^{2+}$  ions. The equivalent circuit of the battery cell is shown in Fig. 1 on the right.  $R_S$  [ $\Omega$ ] is the ohmic resistance,  $R_{CT}$  [ $\Omega$ ] is the charge transfer resistance at the electrodes,  $C_{DL}$  [F] is the double layer capacity due to the distribution of the space charge in the electrochemical double layers,  $Z_W$  [ $\Omega$ ] is the Warburg impedance due to ion diffusion in the electrolyte and pores electrodes. Impedance is defined as:

$$Z = R_S + \frac{1}{(R_{ct} + Z_w)^{-1} + j\omega C_{dl}}, \quad \text{kde } Z_w = \frac{\sigma}{\sqrt{\omega}} - j \frac{\sigma}{\sqrt{\omega}} \quad (1)$$

$Z_w$  is the Warburg impedance,  $\sigma$  the Warburg coefficient [ $\Omega\text{s}^{-1/2}$ ] and  $\omega$  the angular frequency [ $\text{s}^{-1}$ ].

After modifying equation (1) we get:

$$Z = R_S + \frac{R_{ct} + \sigma\omega^{-1/2}}{(C_{dl}\sigma\omega^{1/2} + 1)^2 + \omega^2 C_{dl}^2 (R_{ct} + \sigma\omega^{-1/2})^2} + j \frac{\omega C_{dl} (R_{ct} + \sigma\omega^{-1/2})^2 + \sigma\omega^{-1/2} (C_{dl}\sigma\omega^{1/2} + 1)}{(C_{dl}\sigma\omega^{1/2} + 1)^2 + \omega^2 C_{dl}^2 (R_{ct} + \sigma\omega^{-1/2})^2}, \quad (2)$$

$$\text{Re}(Z) = R_S + \frac{R_{ct} + \sigma\omega^{-1/2}}{(C_{dl}\sigma\omega^{1/2} + 1)^2 + \omega^2 C_{dl}^2 (R_{ct} + \sigma\omega^{-1/2})^2} \quad (3)$$

$$\text{Im}(Z) = \frac{\omega C_{dl} (R_{ct} + \sigma\omega^{-1/2})^2 + \sigma\omega^{-1/2} (C_{dl}\sigma\omega^{1/2} + 1)}{(C_{dl}\sigma\omega^{1/2} + 1)^2 + \omega^2 C_{dl}^2 (R_{ct} + \sigma\omega^{-1/2})^2} \quad (4)$$

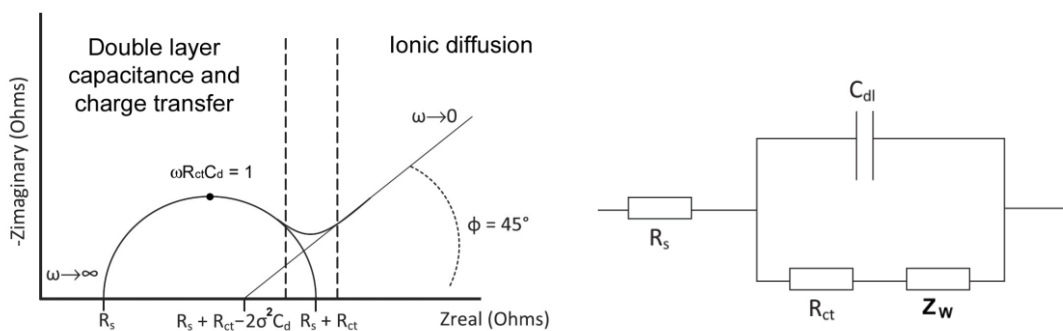


**Figure 1.** Nyquist impedance diagram (left) and equivalent battery circuit (right).

## Experiment

A Hoppecke 200Ah 6V Sun Power VRM lead solar battery was used for impedance measurements. It is an AGM battery from the German manufacturer Hoppecke, which was developed directly for use in solar remote area power systems. The battery is valve regulated with an electrolyte in AGM separator. The main advantages of the battery are absolute maintenance-free throughout the

battery life, a large number of charging cycles, especially in solar applications, long life, high power / low internal resistance. Voltage during float charging 2.25 - 2.27V / cell, recommended ambient temperature 15 - 25 ° C (max. -10 ° C to +40 ° C), any working position of the battery, anti-corrosion design of the poles, design life of the battery 10- 12 years. Capacity: 198.3 Ah - C100 // 183.6 Ah - C48 // 181.2 Ah - C24 // 170 Ah - C10 // 165 Ah - C5. High cyclic resistance - eg 3200 cycles at 40 % of discharge [3]. The measured battery was measured after several years of operation, so it was not new and it was assumed the degradation mechanisms, which resulted in a decrease in capacity.

2 conditioning cycles were performed on the battery: discharging  $I = 20 \text{ A}$ ,  $U = 5 \text{ V} = 1.67 \text{ V / cell}$ , charging  $I = 20 \text{ A}$ ,  $U = 7.25 \text{ V} = 2.42 \text{ V / cell}$ , limiting current  $I = 5 \text{ A}$ . Capacity:  $C1 = 90 \text{ Ah}$ ,  $C2 = 94 \text{ Ah} = 57 \% \text{ of } C5$ . Then the battery was subjected to an intermittent discharge with a discharge current of 20 A at 24 ° C for 1 hour, followed by stand off for 3 hours. Voltage limit at the end of discharge 4.5 V (1.5 V / cell). A total of 6 discharge cycles were performed. The battery was then subjected to intermittent charging with a charging current of 20 A with a voltage limitation of 7.25 V (2.42 V / cell). A total of 12 charging cycles have been performed. During the experiment, the voltage on the battery was measured and the impedance was measured by PEIS method after each discharge or charging interval and the following 2 hours of standing. The amplitude of voltage during PEIS measurement was set at 5 mV, frequency from 6 kHz to 50 mHz, 6 measurements per decade. Fig. 2 are Nyquist diagrams of the battery during intermittent discharging and charging. By means of fitting, for individual Nyquist diagrams we can obtain the changes in the values of the parameters of the equivalent battery circuit during discharging and charging, see Fig. 3.

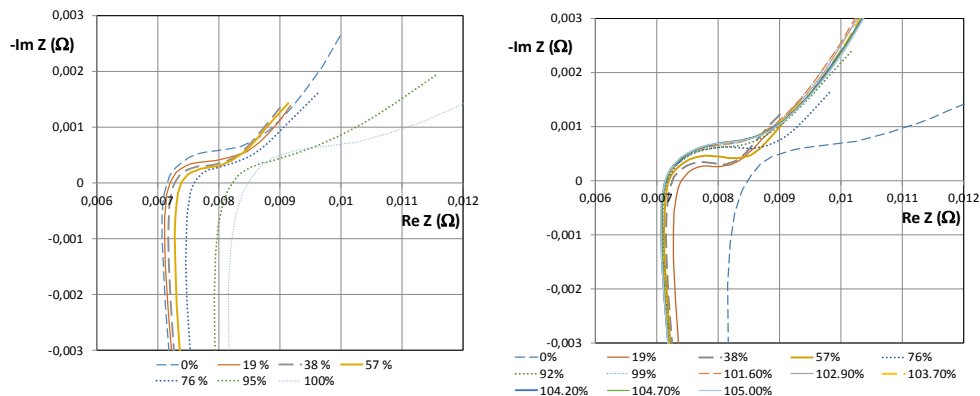


**Figure 2.** Nyquist diagram of the battery during intermittent discharge (left - DoD = 0 % - 100 %) and during intermittent charging (right - SoC = 0 % - 105 %).

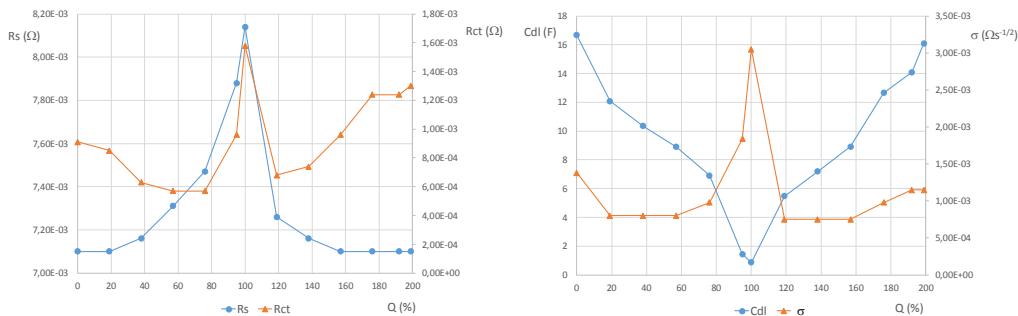


**Figure 3.**  $R_s$  and  $R_{ct}$  (left),  $C_{dl}$  and  $\sigma$  (right) of the battery during intermittent discharge (DoD = 0 % - 100 %) and during intermittent charging (DoD = 0 % - 105 %). 100 % of  $Q$  corresponds to 100 % of DoD.

It can be seen that the ohmic resistance  $R_S$  increases during discharge, which accelerates at the end of discharge. This is related to the increase in the content of non-conductive  $PbSO_4$  in electrodes during discharge. At the beginning of charging, on the other hand, it decreases sharply and in the next part it stabilizes at a value corresponding to the beginning of discharging. The charge transfer resistance  $R_{CT}$  decreases to about 80 % of DoD during discharging. At the end of the discharge, on the other hand, it rises sharply. At the beginning of charging to 20 % of SoC it drops sharply, in the next part of charging, on the contrary, it begins to grow significantly. Its value at the end of charging is higher than at the beginning of discharging. It is clear that at the end of the discharge and charging, the active mass on the electrodes, which could take part in the discharging or charging reactions, decreases and this is reflected in the increase of the charge transfer resistance. The course of  $R_{CT}$  corresponds to the course of  $\sigma$ , which describes the diffusion of ions in the electrolyte and in the pores of the electrodes. The capacity of the  $C_{DL}$  bilayer is constantly decreasing during discharge, and constantly increasing during charging. The decrease in  $C_{DL}$  capacity is related to the increase in the  $PbSO_4$  content in the active mass. During discharge, lead sulphate gradually fills up the pores of the active mass of the electrodes and thus reduces its active area. When charging, the opposite process occurs.

### Conclusions

Nyquist diagrams of a lead acid solar AGM 6V battery during discharging and charging were measured. Important parameters of the battery equivalent circuit were found from the diagrams. These parameters describe the processes that occur in a lead-acid battery during its cycling and it can also be an indicator of the state of charge and the state of health of the battery.

### Acknowledgements

This work was supported by the specific research of the BUT No. FEKT-S-20-6206.

### References

1. <https://www.svp-solar.cz/fotovoltaika/ostrovni-systemy1/>
2. P. Křivík, S. Vaculík, P. Bača, J. Kazelle, Determination of state of charge of lead-acid battery by EIS, *Journal of Energy Storage* 21 581 (2019).
3. <https://ecoproduct.cz/c/vsechno-solarni-baterie-baterie-gel-agm-a-kapalinove-hoppecke-2857>

## Carbon additives effect on lead-acid battery properties

R. Płowens<sup>a, b</sup>, M. Baraniak<sup>a</sup>, M. Bajsert<sup>b</sup> G. Lota<sup>a</sup>

<sup>a</sup> Institute of Chemistry and Technical Electrochemistry, Poznan University of Technology, Berdychowo 4, Poznań 69-965, Poland

<sup>b</sup> Jenox Akumulatory Sp. z o.o, Notecka 33, Chodzież 64-800, Poland

Nowadays, the world is struggling with climate change, so renewable energy sources are inevitable. However, renewable energy sources such as wind turbines or photovoltaic panels are characterised by periodicity production of electricity. Therefore, it is necessary to develop energy storage systems. Lead-acid batteries are a popular form of energy storage due to their relatively low production costs and ease of recycling, but improving their performance is desirable. One way of increasing lead-acid battery properties is to modify the active mass composition and structure. Therefore, carbon additives are an attractive direction in this field. This paper presents the research results concerning the influence of additives of selected carbon materials into the negative electrode on the properties of the Pb/PbO<sub>2</sub> cells, such as capacity, charge acceptance and cycle durability.

### Introduction

Among the important problems of modern civilisation, ensuring sufficient electricity is one of them. Climate change has led to international agreements to reduce the number of greenhouse gases produced by industry, including the energy sector. For this reason, renewable energy sources (RES) such as solar energy, wind energy, geothermal energy, biogas and biomass are becoming more and more popular. Renewable energy installations can work in the off-grid system, using energy storage to accumulate its excess and on-grid, transferring the excess energy directly to the power system. The most popular of RES are wind energy and solar energy. The disadvantage of these systems is the periodicity of the occurrence of the energy source. Wind turbines produce electricity only above a certain wind speed while the sun's rays reach the ground only during the day.

For this reason, one of the biggest problems in systems with renewable energy sources is their storage. Various methods of storing energy are used, both physical: compressed air energy storage, pumped hydroelectric storage, kinetic energy storage, superconducting magnetic energy storage, as well as electrochemical, such as electrochemical battery, supercapacitors (EDLC), fuel cells, flow battery. Electrochemical systems such as Pb/PbO<sub>2</sub> (lead-acid) batteries, Ni-MH batteries or Li-ion batteries are used as a backup power supply (UPS) and as autonomous energy sources [1]. Li-ion batteries have the highest specific power, but their price is a significant disadvantage. On the other hand, lead-acid batteries have lower specific energy. Still, their purchase cost and the possibility of full recycling make them an attractive alternative, especially in small RES installations.

One of the most common undesirable processes in the Pb/PbO<sub>2</sub> cells, resulting in their faster failure, is sulfation, which can occur on both electrodes. It is related to the appearance of coarse-crystalline layers of lead sulfate. The conversion of this type of PbSO<sub>4</sub> to Pb or PbO<sub>2</sub> is ineffective with standard charging methods. The sulfation problem is closely related to the ability of the electrodes to charge acceptance, especially during the initial stages of negative active mass (NAM)

charging. To increase the utilisation of negative active masses, mixtures of lignin, barium sulfate and carbons (generally known as expanders) are added during NAM production [2]. Lignosulfonate is incorporated into the NAM to increase the life cycle, prevent passivation, and increase the active mass utilisation. [3-5]. Barium sulfate ( $\text{BaSO}_4$ ) is a nucleating agent (nucleant) for the formation and growth of small  $\text{PbSO}_4$  crystals. In addition to that, it facilitates the distribution of these crystals across the pore surface of the active mass. This property of  $\text{BaSO}_4$  is based on the isomorphism between  $\text{PbSO}_4$  and  $\text{BaSO}_4$  crystals [2]. Carbon materials are added to the paste mainly to improve the electrical conductivity of the active lead mass at the end of the discharge when the content of  $\text{PbSO}_4$  crystals in the NAM increases significantly [6-8].

This study aimed to examine the influence of the addition of carbon materials on the performance of lead-acid cells, like the ability to charge acceptance and the cyclic durability.

## Experimental

Carbon materials with different physicochemical properties (Tab. I) were added to the negative pastes to create a conductive 3D skeleton in the electrode volume. The expected influence of the modification of the active mass should include improving the electrode conductivity, the increase of the specific surface of the material and the reduction of the sulfation during cyclic operation [6-8].

**TABLE I.** Physical and chemical properties of the used carbon materials.

Product	Contact Water Angle [degree]	BET Surface Area [ $\text{m}^2/\text{g}$ ]	Density [ $\text{g}/\text{cm}^3$ ]
Graphite 1 (G1)	<30	>180	0,33
Graphite 2 (G2)	<30	28	0,03
Carbon black (CB)	95	62	0,06

Lead oxide produced on a ball mill from a large-scale process (approx. 75%  $\text{PbO}$  and 25%  $\text{Pb}$ ), was used for the preparation of the plate. Normal expander and selected carbon additives were added during the paste's manufacturing. They were mixed with demineralised water and sulfuric acid in the amount used during production standard negative electrodes. Negative plates were made with the addition of 0.5% wt. graphite 1 (G1), 0.5% wt. graphite 2 (G2) and 0.4% wt. graphite 1 (G1) + 0.1% wt. carbon black (CB). For comparison, a series of unmodified/standard negative electrodes were also prepared.  $\text{Pb}/\text{PbO}_2$  cells used standard positive electrodes. Batteries systems were designed for a theoretical capacity of 45 Ah. DC formation process, total charge delivered was  $Q = 4,1$  of theoretical capacity. The research included i.a. determination of  $C_{20}$  capacity, charge acceptance test and endurance tests. All tests are based on the EN 50342-1: 2015 standard.

## Results and Discussion

Experimental data showed that the 20-hour capacities  $C_{20}$  in the first three test cycles were repeatable, ranged from 46.5 Ah to 47.5 Ah for all systems. On the other hand, differences were observed during the charge acceptance tests. Modified  $\text{Pb}/\text{PbO}_2$  cells demonstrate significant improvement for the possibility of charging with high currents ( $I_{\text{max}} = 50 \text{ A}$ ,  $E_{\text{max}} = 14.4 \text{ V}$ ). After 10 min. of charging, the average currents decreased to the values of 18.9 A, 13.8 A and 13.5 A for G1, G2 and G1+CB, respectively, compared to 11.6 A for standard cells. A particularly large improvement was observed for the addition of G1 graphite, which was as higher as 64% vs reference system current at the end of the test. In turn, the cyclic test showed that only the G2 graphite improved the properties of NAM. In this case, the increase was at the level of 6%.

The paper presents the effect of selected carbon additives on the operating parameters of a lead-acid battery. It has been shown that carbon additives improve charge acceptance and, to a lesser extent, increase battery lifetime during the cyclic test.

### Acknowledgments

The authors thank the Polish Ministry of Education and Science for financial support (Applied Doctorate Program, No. DWD/3/20/2019).

### References

1. A. Chatzivasileiadi, E. Ampatzi, I. Knight, *Characteristics of electrical energy storage technologies and their applications in buildings*, Cardiff University. Available from: <https://orca.cardiff.ac.uk/47251/1/Chatzivasileiadi%20et%20al.pdf>.
2. D. Pavlov, *Additives to the Pastes for Positive and Negative Battery Plates*, in: *Lead-Acid Batteries: Science and Technology*, Elsevier, Amsterdam, 2 Ed. 2017.
3. D. von Borstel, G. Hoogstraat, W. Ziechmann, *Efficiency of lignosulfonates and humic related substances as expanders in negative electrodes of the lead/acid system*, p. 131, *Journal of Power Sources*, **50** (1994).
4. B.O. Myrvold, *Interactions between lignosulphonates and the components of the lead acid battery Part 2 Interactions with the electrolyte and lead sulphate growth*, p. 573, *Journal of Applied Electrochemistry*, **35** (2005).
5. K. Sawai, T. Funato, M. Watanabe, H. Wada, K. Nakamura, M. Shiomi, S. Osumi, *Development of additives in negative active-material to suppress sulfation during high-rate partial-state-of-charge operation of lead-acid batteries*, p. 1084, *Journal of Power Sources*, **158** (2006).
6. R. Marom, B. Ziv, A. Banerjee, B. Cahana, S. Luski, D. Aurbach, *Enhanced performance of starter lighting ignition type lead-acid batteries with carbon nanotubes as an additive to the active mass*, p. 78, *Journal of Power Sources*, **296** (2015).
7. J. Lach, K. Wróbel, J. Wróbel, P. Podsadni, A. Czerwiński, *Applications of carbon in lead-acid batteries: a review*, p. 693, *Journal of Solid State Electrochemistry*, **23** (2019).
8. X. Zou, Z. Kang, D. Shu, Y. Liao, Y. Gong, C. He, J. Hao, Y. Zhong, *Effects of carbon additives on the performance of negative electrode of lead-carbon battery*, p. 89, *Electrochimica Acta*, **151** (2015).

## Study of Surface Processes Taking Place on the Surface of the Negative Electrode of Lead-acid Batteries Using XRD

J. Smejkal<sup>a</sup> and L. Chladil<sup>a,b</sup>

<sup>a</sup> Institute of Electrotechnology, Faculty of Electrical Engineering and Communication, BUT, Technická 10, 616 00 Brno, Czech Republic

<sup>b</sup> Centre for Research and Utilization of Renewable Energy, Faculty of Electrical Engineering and Communication, BUT, Technická 10, 616 00 Brno, Czech Republic

Our contribution deals with the study of surface processes and chemical composition on the surface of the negative electrode of a lead-acid battery during cycling at different speeds. Thin electrodes were created for the measurements. The negative electrode was analyzed at six SOC states (100 %, 80 %, 60 %, 40 %, 20 % and 0 % SOC). The proportion of individual elements on the surface of the negative electrode during cycling at 0.2 C was evaluated. Chemical changes occurring on the surface of the negative electrode during cycling of the lead-acid battery were studied using an X-ray diffractometer and the presence of individual chemical elements on the surface of the electrode was evaluated using the Rietveld method. An increase in the material was observed, which did not convert during cycling and caused a more significant conversion of material near the negative electrode collector during cycling.

### Introduction

Although the principle of operation of lead-acid batteries has been known for more than 150 years, this type of battery is again intensively studied. Lead-acid batteries are widely used due to the good availability of the materials used, their recyclability, high electrochemical efficiency, the high number of cycles, and high rated voltage of around 2 V. These features and low production cost make them very attractive for use not only in the automotive industry, where they can supply high current for engine starters, but also for storing electricity from renewable sources. More than half of the world's lead production is currently used to make lead-acid batteries [1].

Despite all their positive properties, lead-acid batteries also have several degradation mechanisms. Significant degradation mechanisms are the phenomena referred to as PCL 1, PCL 2, and PCL 3 (PCL-Premature Capacity Loss). In PCL 3, the negative electrode sulfates, forming a fine film of lead sulfate on the surface of the negative electrode, prevent the movement of ions and cause a reduction in battery capacity. This phenomenon is often associated with the selective discharge of the negative electrode [2]. These negative phenomena cause premature loss of capacity and lead to a significant service life-shortening and overall efficiency of lead-acid batteries. One way to suppress these negative phenomena is to add various additives, such as graphite carbon, glass fibers, or titanium dioxide, which helps to suppress the PCL 3 phenomenon [3] [4].

## Experimental

The electrodes were pasted onto a substrate formed of rolled lead sheets. The electrode substrate was circular with a diameter of 13 mm and holes were drilled in it for better adhesion of the active material. The part of the electrode that did not participate in the chemical reactions was insulated with a layer of epoxy adhesive, which was subsequently cured. The detail of the lead substrate can be seen in Figure 1. on the left. The substrate was placed in the formed holder, and the active material was pasted on the substrate. During pasting, it was necessary to achieve high uniformity to avoid erroneous XRD measurements. The electrode was then placed in an environment of 100% humidity, where it matured. The total weight of active material of the negative electrode after maturation was 0.82 g. After maturation, the electrode was placed in a measuring cell with an electrolyte consisting of an aqueous solution of sulfuric acid with a concentration of 27%, where 20 formation cycles were performed at a supplied current of 13.16 mA. Before measurement, the electrodes were dripped with a 33% aqueous sulfuric acid solution and covered with a polyamide film to prevent air from entering the active material. The detail of this electrode can be seen in Figure 1. on the right.

The measurement itself was performed in a three-electrode circuit and the electrode was immersed in a 33% aqueous sulfuric acid solution. Discharge was performed galvanostatically in six steps 100 %, 80 %, 60 %, 40 %, 20 % and 0 % SOC (State of Charge) at a supplied current of 11.35 mA for 1 hour with a potential limit  $E_M = -0.8$  V vs. MSRE. The electrode was discharged at a rate of 0.2 C and subsequently analyzed by XRD. Charging also took place galvanostatically in six steps at a supplied current of -11.35 mA for 1 hour with a potential limitation  $E_M = -1.3$  V vs. MSRE.

Chemical composition on the surface of the negative electrode during cycling was observed using an X-ray diffractometer Rigaku MiniFlex HR 600. Diffractograms were measured at range settings 10-100° at step 0.01, divergence slit 0.625, IHS 5, and  $k\beta$  filter 0.03.



**Figure 1.** On the left, there is a picture of the detail of the lead substrate. On the right, there is a picture of the complete test electrode covered with polyamide foil.

The fully charged electrode contains 8 mol. % lead sulfate. The fully discharged electrode contains almost 32 mol. % metallic lead. The composition on the surface of the electrode in the fully charged and discharged state indicates that at almost 40 mol. % of the used material does not convert during cycling. Between 80 % and 60 % of the SOC, lead was preferentially dissolved. In this range, there was a significant decrease in the proportion of lead on the surface of the negative electrode by 19 mol. %.

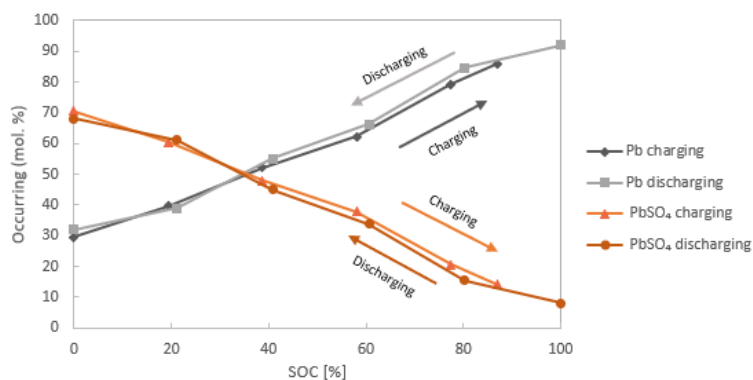


**Figure 2.** Chemical composition on the surface of the active mass of negative electrode at different SOC at a rate of 0.2 C during cycling.

Subsequently, the electrode was charged at a rate of 0.2 C. The charging cycle was also measured for evaluation of expected differences between charging and discharging behavior of the electrode surface. Up to a level of 40% SOC, the electrode was predominantly made of lead sulfate. From the 60% SOC level, the electrode was predominantly made of metallic lead. At 100% SOC, there was 14 mol. % of lead sulfate on the electrode surface, which is about 6 mol. % more than at 100% SOC during discharge.

## Conclusions

From the measured results, it can be observed that at a rate of 0.2 C there was no conversion during cycling of the electrode in almost 40 mol. % of the material used. By adding a carbon additive to the active material of the negative electrode, it could help to reduce the percentage of unused material, and thus contribute to increasing the capacity of the lead-acid battery. During the charging cycle in the state of complete discharge, the surface of the electrode was represented by 30 mol. % lead. This proportion of elements on the electrode surface corresponds to the results of the discharge cycle. An increase in the material was observed, which did not convert during cycling and caused a more significant conversion of material near the negative electrode collector during cycling.

## Acknowledgment

This work was supported by the specific graduate research of the Brno University of Technology No. FEKT-S-20-6206.

## References

1. N. Moubayed, *Parameter identification of the lead-acid battery model*. IEEE (2008)
2. L. T. Lam, *Influence of residual elements in lead on oxygen- and hydrogen-gassing rates of lead-acid batteries*. Journal of Power Sources (2010)
3. D. P. Boden, *Optimization studies of carbon additives to negative active material for the purpose of extending the life of VRLA batteries in high-rate partial-state-of-charge operation*. Journal of Power Sources (2010)
4. K. Micka, *Studies of doped negative valve-regulated lead-acid battery electrodes*. Journal of Power Sources (2009)

## Monitoring The Influence Of The Temperature On The Properties Of Lead-acid Battery

J. Zimáková<sup>a</sup>, P. Bača<sup>a</sup>, M. Langer<sup>a</sup>, T. Binar<sup>a</sup>

<sup>a</sup> Brno University of Technology, Technická 10, 616 00 Brno, Czech Republic

This work deals with lead-acid batteries, their properties and individual types that are available on the market. The temperature dependences of the battery parameters at different ambient temperatures and at different discharging and charging modes are measured. 6 batteries are tested at different charging currents, which provides information about their behavior both during discharge and at the time of charging. During the experiments, testing is not only performed at room temperature, but the batteries are also exposed to high temperatures up to 75 °C.

### Introduction

Accumulators are nowadays an essential element for many devices in daily use. The storage of electrical energy in the form of chemical bond energy is therefore one of the most common ways. They play an important role in portable devices, where Lithium batteries are mainly used. Their suitability lies in the high capacity value, despite their low weight. The use of lead-acid batteries is mainly in the automotive industry, where efforts are being made to adapt the function for hybrid electric vehicles. The main requirement is to maintain a long battery life even with more frequent consumption electric current. Lead-acid batteries have also been used in traction applications, or off-grid systems, where they serve as backup sources to drive stationary device. Different modifications of the internal structure are used for different applications batteries, depending on the number of cycles and the amount of power required to add. Lead-acid batteries generally have larger dimensions and weight, which does not allow them use in portable electronic devices. Their undeniable advantage is quite low price and the possibility of delivering high performance. The main problem of lead-acid batteries is their greater heating, which is manifested mainly by VRLA AGM batteries due to their closed construction [1, 2]. The closed construction provided a number of advantages, but the recombination of oxygen with its subsequent possibility of conversion into water is redeemed by the release of heat.

### Experiment

Pb batteries of prismatic type (square) 12 V, 3 Ah from: BANNER and Varta was used for the experiments proposed below (flooded: Varta YB3L-A, VRLA AGM: Banner Bike Bull AGM YT4L-BS, VRLA GEL: Banner Bike Bull GTR4A-5 )

Number of batteries: For experiments 1-3: 2 sets x 3 batteries = 6 batteries

1. Verification of functional parameters of accumulators - comparison with datasheet, estimated number of accumulators: 3 accumulators (flooded, gel, AGM), 2 sets: a total of 6 batteries

a. Discharge at a constant current of 0.25 C to a final voltage of 10.2 V.

- b. Charge at a constant current of 0.25 C with a voltage limitation of 14.7 V a final state of charge 106 %.
- c. Measure the internal resistance at 1 kHz during cycling with 0.2 A.

2. Cell temperature change (self-heating) when discharging / charging with different currents, estimated number of accumulators: continuation with the same accumulators from experiment 1.

- a. Discharge with a constant current of 0.5 C, 1 C, to a final voltage of 10.2 V.
- b. Charge with a constant current of 0.5 C, 1 C, with a voltage limitation of 14.7 V and a final state of charge of 106 %.

3. Verification of functional parameters of batteries at different temperatures, estimated number of accumulators: continuation with the same accumulators from experiment 1.

- a. Cells placed in the oven, temperature set to: 30, 40, 60, 75 ° C.
- b. Stabilization and temperature tempering for 2 hours.
- c. Charging / discharging characteristics according to 2 a) b) c), but only 0.5 C.

### Measuring workplace

The used measuring workplace (see **Chyba! Nenalezen zdroj odkazů.**) at BUT FEEC is able to automatically measure many quantities for evaluating the current state of up to 16 batteries at one time. The measuring station includes two desktop computers, two Agilent 34980A measuring panels, four Agilent N6700B power supplies, terminal blocks, discharge resistors and wires.



**Figure 1.** a) Measuring control panel; b) Terminal blocks and discharge resistors on the side of the measuring control panel

The measuring workplace is mobile with components stored in a rack-type cabinet. The individual components used to ensure the measurement can be seen from the front, the sides then contain terminals for external connection of batteries and discharge resistors. Batteries were connected to the terminal board on the left side of the cabinet to measure voltage, current and temperatures using temperature sensors attached to the side of the battery.

### Experiment 1 – results

After connecting the measuring control panel with lead batteries, parameters were set in the Agilent VEE program to stop charging or to switch from the discharging part to the charging part. The measurement took place in the voltage range of 10.2 to 14.7 V, switching to the discharging state occurs when 106 % of charge is reached. Each battery was set to a discharge and charging current of 0.25 C. The measurement was performed at room temperature. As it turned out that the capacity of the batteries was gradually decreasing, the end of charging was changed. The original end of charging 106 % of charge was replaced by a time limit when one discharge / charge cycle was set to 24 hours. In this part, a current of 0.2 A was used. Internal resistance was also detected. Charge and discharge curves are shown at Figure 2 and Figure 3.

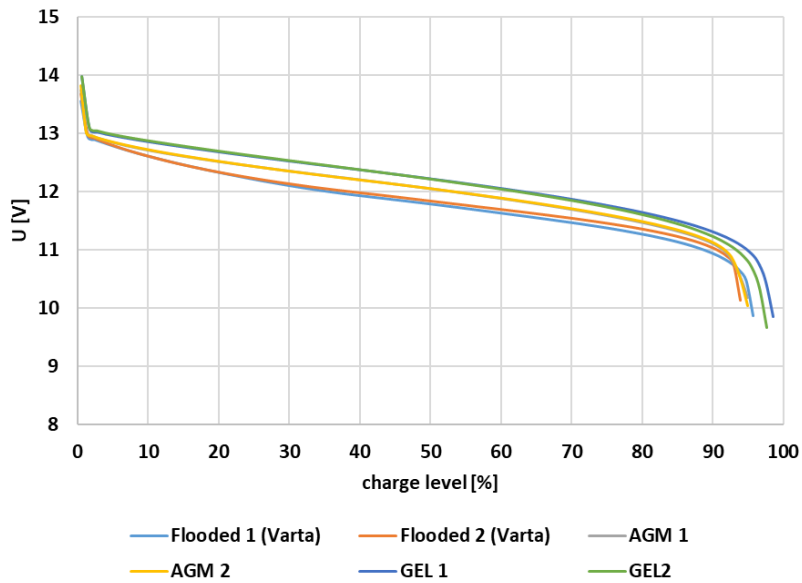


**Figure 2.** Discharge curves of all batteries for 0.25C (4th cycle)

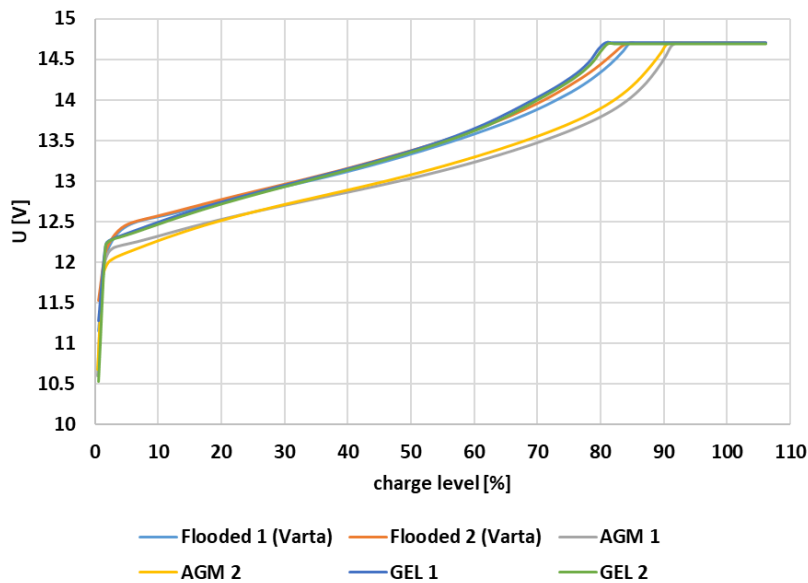


**Figure 3.** Charging curves of all batteries at 0.25C (4th cycle)

## Conclusion

In the first experiment, the batteries were subjected to a relatively low current of 0.25 C, which is to provide us with information about real capacities, their stability and comparability with the values prescribed by the manufacturer. In terms of voltage discharge characteristics, we find that different batteries of the same design behave very similarly. That indicates the similarity of internal resistances. Only for batteries with a flooded structure, a larger drop in the voltage curve can be observed for Flooded1. If we look at the different structures with each other, we observe the smallest losses in gel batteries, which is a sign of the lowest internal resistances. Batteries of flooded construction have the largest voltage drops, and thus the highest internal resistances. From the temperature characteristics, the cooling of the battery with a flooded structure is significantly slower than with the AGM battery. This is due to the large amount of electrolyte in flooded batteries, which gives them a large heat capacity. In contrast, AGM batteries contain significantly less electrolyte, allowing rapid cooling. However, due to the low heat capacity and the actual design of the battery, which allows for an internal oxygen cycle, AGM batteries also experience a greater increase in temperature at the end of charging. Battery capacities for this cycling decreased very quickly. This phenomenon proves that the chosen charging strategy (stop charging at 106 % of the received charge) was not suitable and there was an incomplete charge.

## Acknowledgements

The publication was created within the project of specific research at BUT (No. FEKT-S-20-6206).

## References

1. J. Hu, Y. Guo, X. Zhou, Thermal runaway of valve regulated lead-acid batteries, *Journal of Applied Electrochemistry* 2006, 36(10)
2. H. Catherino, *Complexity in battery systems: Thermal runaway in VRLA batteries* 2006 <https://doi.org/10.1016/j.jpowsour.2005.11.005>

## Organic Multivalent Batteries

Jan Bitenc<sup>a</sup>, Alen Vizintin<sup>a</sup>, Klemen Pirnat<sup>a</sup>, Robert Dominko<sup>a,b,c</sup>

<sup>a</sup> National institute of chemistry, Ljubljana, Slovenia

<sup>b</sup> University of Ljubljana, Ljubljana, Slovenia

<sup>c</sup> Alistore-ERI, Amiens, France

E-mail: [Robert.Dominko@ki.si](mailto:Robert.Dominko@ki.si)

Magnesium, calcium and aluminum are promising elements for future high scale sustainable batteries due to the high gravimetric and volumetric capacities of metals, their abundance and homogenous distribution on the globe. When coupled with redox active organics, they are forming an interesting couple with energy density highly attractive for different large scale applications.

Besides the above-mentioned benefits, there are several challenges connected with stripping and deposition of the metals, with the appropriate electrolyte formulation compatible with the metal anode and potential cathode materials, with current collectors, the housing of the cell and with the choice of appropriate cathode materials.

In this presentation, an overview of recent achievements in our group in the field of multivalent organic batteries will be discussed with a focus on the proper selection of battery components in order to achieve electrochemical properties attractive for commercialization.

### Acknowledgement

This work is supported HONDA R&D Europe and by the Slovenian Research Agency (research core funding No. P2-0393 and research project Z2-1864).

### References:

1. J. Bitenc, K. Pirnat, T. Bančič, M. Gaberšček, B. Genorio, A. Randon-Vitanova and R. Dominko, Anthraquinone-Based Polymer as Cathode in Rechargeable Magnesium Batteries, *ChemSusChem*, 2015, 8, 4128–4132.
2. A. Vizintin, J. Bitenc, A. Kopač Lautar, K. Pirnat, J. Grdadolnik, J. Stare, A. Radon-Vitanova and R. Dominko, Probing electrochemical reactions in organic cathode materials via in operando infrared spectroscopy, *Nat. Commun.*, 2018, 9, 661.
3. Jan Bitenc, Alen Vizintin, Jože Grdadolnik, Robert Dominko, Tracking electrochemical reactions inside organic electrodes by operando IR spectroscopy *Energy Storage Materials* 21 (2019) 347–353
4. A. Robba, A. Vizintin, J. Bitenc, G. Mali, I. Arčon, M. Kavčič, M. Žitnik, K. Bučar, G. Aquilanti, C. Martineau-Corcoss, A. Randon-Vitanova, R. Dominko, *Chem. Mater.*, 2018, 29, 9555-9564.
5. J. Bitenc, N. Lindahl, A. Vizintin, M. Abdelhamid, R. Dominko, P. Johansson, Concept and electrochemical mechanism of an Al metal anode - organic cathode battery. *Energy storage materials*, Jan. 2020, vol. 24, str. 379-383
6. J. Bitenc, A. Scafuri, K. Pirnat, M. Lozinskec, I. Jerman, J. Grdadolnik, B. Fraisse, R. Berthelot, L. Stievano, R. Dominko, Electrochemical performance and mechanism of calcium metal-organic battery. *Batteries & supercaps*, ISSN 2566-6223, [in press] 2020, 14 str.

## Titania Containing Cathodes for Lithium-Sulfur Batteries: Case Studies by Electrochemical Impedance Spectroscopy

L. Kavan, M. Vinarčíková, M. Zlámalová and M. Zukalová

J. Heyrovský Institute of Physical Chemistry, v.v.i., Dolejškova 3, CZ-18223 Prague 8

E-mail: kavan@jh-inst.cas.cz

Sulphur provides attractive specific capacity of 1673 mAh/g, but its insulating nature and complex Li/S cell chemistry, particularly the polysulfide dissolution in electrolyte solution, still present significant technological issues. Titanium dioxide is a promising material for application as a polysulfide reservoir improving the capacity retention and cycle life of lithium-sulfur battery [1]. In our previous work [2], we have shown that coating of the sulfur/carbon composites by TiO<sub>2</sub> made by hydrolysis of titanium isopropoxide can enhance the electrochemical performance of certain cathode materials, depending on the type of carbon component which is present in the cathode. Here, we extended these studies by investigation of new cathode formulations employing commercial TiO<sub>2</sub> materials and nanocarbons. Electrochemical impedance spectroscopy was used to study these cathode materials in coin cells with lithium anode at various stages of galvanostatic cycling. For comparison, also symmetrical coin cells with a pair of positive (S/C/TiO<sub>2</sub>) or negative (Li) electrodes were investigated. In addition to the use of titania as a barrier material impeding the polysulfide diffusion in the electrolyte solution, the inherent Li-insertion activity of TiO<sub>2</sub> at potentials negative to the flatband potential [3] plays a role in this system. To address these questions, we measured the flatband potential by electrochemical impedance spectroscopy of several single-crystal TiO<sub>2</sub> materials (anatase, rutile, brookite) in the Li-containing non-aqueous electrolyte solution [4]. A comparative impedance analysis in aqueous electrolyte solution revealed an important effect of the environment, which can even flip the alignment of Fermi levels of same titania phases.

### Acknowledgement

This work was supported and by the Czech National Science Foundation (contract No. 20-03564S).

### References

1. WEI SEH, Z., LI, W., CHA, J.J., ZHENG, G., YANG, Y., MCDOWELL, M.T., HSU, P.C., CUI, Y., Sulphur-TiO<sub>2</sub> yolk-shell nanoarchitecture with internal void space for long-cycle lithium-sulphur batteries, *Nat Commun*, 4 (2013) 1331.
2. ZUKALOVA, M., VINARCIKOVA, M., BOUSA, M., KAVAN, L., Nanocrystalline TiO<sub>2</sub>/Carbon/Sulfur Composite Cathodes for Lithium-Sulfur Battery, *Nanomaterials*, 11 (2021) 541.
3. KAVAN, L., Lithium Insertion into TiO<sub>2</sub> (Anatase): Electrochemistry, Raman Spectroscopy, and Isotope Labeling, *J. Solid State Electrochem*, 18 (2014) 2297-2306.
4. MANSFELDOVA, V., ZLAMALOVA, M., TARABKOVA, H., JANDA, P., VOROKHTA, M., PILIAI, L., KAVAN, L., Work Function of TiO<sub>2</sub> (Anatase, Rutile, and Brookite) Single Crystals: Effects of the Environment, *J. Phys. Chem. C*, 125 (2021) 1902-1912.

## Printed electrode for sodium ion batteries based on organic compounds

T. Syrový<sup>a</sup>, J. Černý<sup>b</sup>, T. Kazda<sup>c</sup>, L. Kubáč<sup>b</sup>, L. Syrová<sup>a</sup>

<sup>a</sup> Department of Graphic Arts and Photophysics, University of Pardubice, 533 53 Pardubice, Czech Republic

<sup>b</sup> Centre for Organic Chemistry Ltd., 53354 Rybitví, Czech Republic

<sup>c</sup> Department of Electrical and Electronic Technology, Brno University of Technology, 616 00 Brno, Czech Republic

Presented study is focused on the development of printed electrode layers for sodium ion batteries (SIB) made by conventional printing and AM technologies. Hybrid SIB full cells based on cathode (NVP) and organic compound anode PTCNa (tetrasodium perylene-3,4,9,10-tetracarboxylate) as electrodes for SIB batteries were prepared by printing. A screen/stencil printing and micro-dispensing technique were used for fabrication of electrodes. This techniques enabled to print electrode layers with various thickness and specific geometry of electrodes. Fabricated cells made from printed electrodes using water-based PTCNa ink formulation showed specific capacity 89.4 mAh/g at current load 0.3 C and gravimetric energy density 330 Wh/kg.

### Introduction

Nowadays, there is increasing requirement for production of electrical energy production from renewable sources, where for small system photovoltaic or small wind power plants are used together with stationary battery storage systems. These systems help to create partial energy self-sufficiency for their users and also allow to build a decentralized energy grid in the future. Currently, these battery storage systems are mainly implemented through Li-ion batteries (LIB). However, this trend is competing with the rapid development of electric mobility and with huge amount of usage of LIB in common electronic devices. It is sure that lithium resources will not be sufficient to provide required amounts of LIB batteries for stationary applications in the future. From this point of view, it is advantageous to investigate other types of batteries which use electrochemical processes based on other metal ions ( $\text{Na}^+$ ,  $\text{K}^+$ ,  $\text{Mg}^{2+}$ ), despite inferior parameters in terms of specific energy density per unit weight or volume. While these parameters are generally important for stationary energy storage systems, they are not critical in this respect for mobile applications. This fact allows the use of electrochemical systems with lower energy density per volume/weight. On the other hand it must provide sufficient stability and a favorable price per unit of specific energy density. A major advantage of such alternative electrochemical system is the significantly better availability of raw sources of Na, K, Mg, etc.

In the case that SIB reach capacities close to current Li-ion batteries, with sufficient lifetime and at a significantly lower cost, they would accelerate the further development of electricity storage systems in the power sector. Besides the advantage of availability of sodium, SIB provides the possibility of using aluminium as a current collector on both electrodes which generally have an effect to reduce the price and weight of batteries. The main disadvantage of SIB is the low cyclability of the anode materials, which is crucial for applications in stationary energy storage. In present time the

most commonly used materials for anodes are hard carbon, mesoporous soft carbon, MXenes, titanate-based materials such as  $\text{Na}_2\text{Ti}_3\text{O}_7$  or titanate phosphates ( $\text{NaTi}_2(\text{PO}_4)_3$ ), etc. [1-2].  $\text{NaMnO}_2$ ,  $\text{NaFePO}_4$ ,  $\text{NaTi}_2(\text{PO}_4)_3$ ,  $\text{Na}_3\text{V}_2(\text{PO}_4)_3$  (NVP), etc. are mostly used as cathode materials. In the case of high-capacity electrode materials, the capacity of SIB batteries could be around the 300 Wh/kg, whereas for standard ones it is around 150 Wh/kg [3]. However, all these materials suffer from high irreversible capacity associated with SEI formation in the first cycles with low efficiency and low cyclability.

A strong interest about usage of small organic molecules, or polymers as anode, or cathode materials for SIB is observed in the last years. The advantage of organic compound is given by possibility of their structural tailoring towards its enhanced properties as shift of electrochemical redox potential, capacity improvement or low solubility. Various type of small molecules are mentioned in the literature, for example disodium terephthalate [4-5], disodium 4,4-biphenyldicarboxylate [6], croconic acid disodium salt [7] used as electrode in SIB or polymer material like polytriphenylamine [8]. We studied usage of poly(1,5-anthraquinonyl sulphide) [9]. In the presented study the organic compound PTCNa was used as a promising anode material for hybrid SIB. PTCNa based anode was fabricated from two type of ink formulations, The first formulation was based on solvent borne system and the second one on water-based system. In the study we investigated the difference in performance of assembled cells in relation of used type of electrolyte.

## Experimental

The ink formulation for printing of cathode was based on NVP as active material and on PVDF polymer as a binder together with NMP as a solvent. The ratio of NVP to PVDF in ink formulation was set to 8:1. The Super C45 conductive carbon material was used in the same ratio. The anode electrode was based on PTCNa. Ink formulations for water borne and solvent borne (PVDF/NMP) systems were developed for the given electrode material. The electrode layers were printed by stencil/screen printing on Al foil, where thickness of wet layers was varied between 125 and 300  $\mu\text{m}$  according to the printing condition. The printed layers were dried first at 80 °C, than at 120 °C for 1h. Dry layers were cut off to circle electrode with diameter of 16 mm, then was calendared by the pressure of 150  $\text{kg}\cdot\text{cm}^{-2}$ . Prepared electrodes were transferred to Jacomex glovebox with Ar atmosphere. The full cells were assembled in the coin cell CR2025 enclosure. As an electrolyte, three various types of electrolyte was used - 1 M  $\text{NaPF}_6$  in carbonates, 1 M  $\text{NaClO}_4$  in carbonates and 1M  $\text{NaCF}_3\text{SO}_3$  in glymes. The assembled cells were characterized at galvanostatic cycling at current load from 0.1 to 12 C.

## Results

The full cells consisted of NVP cathode and PTCNa-solv (PTCNa with PVDF) anodes were fabricated with three various electrolytes in CR2025 coin cell enclosures. From performed galvanostatic measurements was evaluated, that the highest capacity was obtained for cells with  $\text{NaPF}_6$  electrolyte, where 80.9 mA.h/g was achieved for initial cycle at current load 1 C, 70.6 mA.h/g for  $\text{NaCF}_3\text{SO}_3$  based electrolyte and 63.7 mA.h/g for  $\text{NaClO}_4$  based electrolyte. For the initial cycle, the Coulombic efficiency was low for all electrolyte, what is apparent from figure 1 (A). Low initial Coulombic efficiency is common for given type of organic anode material. In terms of cell cycling stability the order was the same as for obtained specific capacity, where cells with  $\text{NaPF}_6$  based electrolyte exhibit very good cycling stability with capability hundreds of cycles at current load 1 C or 2 C and vice versa to cells with  $\text{NaClO}_4$  based electrolyte, which exhibited by rapid decay in approximately 50 cycles at current load 1 C.

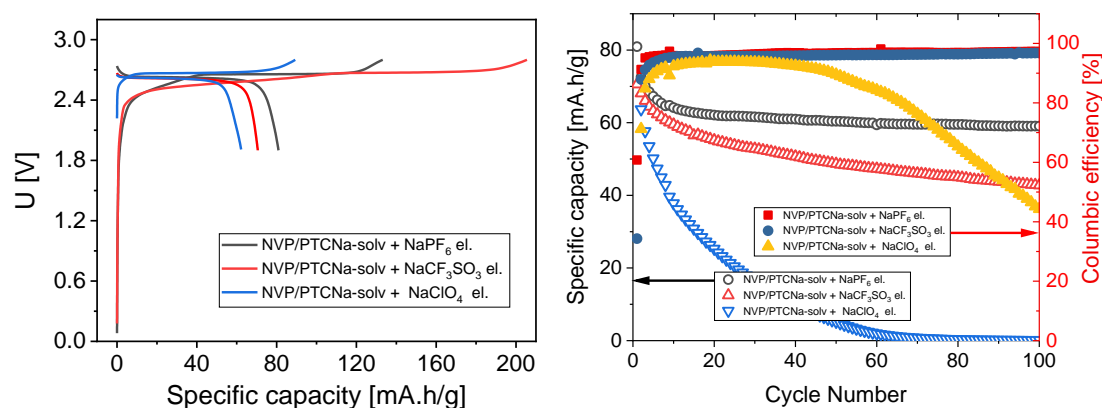


**Figure 1.** (A) Charging/discharging curves for initial cycle for cells with NVP cathode and PTCNa-solv (PTCNa with PVDF) anode and electrolytes based on NaPF<sub>6</sub>, NaCF<sub>3</sub>SO<sub>3</sub> and NaClO<sub>4</sub> (B) Galvanostatic cycling of NVP/PTCNa-solv cells at current rate 1 C and electrolytes based on NaPF<sub>6</sub>, NaCF<sub>3</sub>SO<sub>3</sub> and NaClO<sub>4</sub>.

## Conclusion

By printing technique were prepared electrode layers of cathode (NVP) and organic compound (PTCNa) based anode for full cell SIB. Assembled full cells in CR2025 coin cell enclosure was compared in terms of used electrolyte. From obtained data it is obvious, that cells based on NaPF<sub>6</sub> electrolyte exhibit highest specific capacity related to PTCNa and overall highest stability too.

## Acknowledgments

The work was supported from European Regional development Fund-Project "Organic redox couple based batteries for energetics of traditional and renewable resources (ORGBAT)" No.CZ.02.1.01/0.0/0.0/16\_025/0007445 and by BUT specific research programme (project No. FEKT-S-20-6206).

## References

1. ZHANG, Wanjie, Mouad DAHBI, Shota AMAGASA, Yasuhiro YAMADA a Shinichi KOMABA. Iron phosphide as negative electrode material for Na-ion batteries. *Electrochemistry Communications*. 2016, 69(8), 11-14. ISSN 13882481. doi:10.1016/j.elecom.2016.05.005
2. HWANG, Jang-Yeon, Seung-Taek MYUNG a Yang-Kook SUN. Sodium-ion batteries: present and future. *Chemical Society Reviews*. 2017, 46(12), 3529-3614. ISSN 0306-0012. doi:10.1039/C6CS00776G
3. YABUUCHI, Naoaki, Kei KUBOTA, Mouad DAHBI a Shinichi KOMABA. Research Development on Sodium-Ion Batteries. *Chemical Reviews*. 2014, 114(23), 11636-11682. ISSN 0009-2665. doi:10.1021/cr500192f
4. Zhao, L., Zhao, J., Hu, Y.-S., Li, H., Zhou, Z., Armand, M. and Chen, L. (2012), Disodium Terephthalate (Na<sub>2</sub>C<sub>8</sub>H<sub>4</sub>O<sub>4</sub>) as High Performance Anode Material for Low-Cost Room-Temperature Sodium-Ion Battery. *Adv. Energy Mater.*, 2: 962-965. <https://doi.org/10.1002/aenm.201200166>

5. Wang, Ying & Kretschmer, Katja & Zhang, Jinqiang & Mondal, Anjon & Guo, Xin & Wang, Guoxiu. (2016). Organic Sodium Terephthalate@Graphene Hybrid Anode Materials for Sodium-Ion Batteries. *RSC Adv.* 6. 10.1039/C6RA11809G.
6. Choi, A.; Kim, Y.K.; Kim, T.K.; Kwon, M.-S.; Lee, K.T.; Moon, H.R. 4,4' - Biphenyldicarboxylate Sodium Coordination Compounds as Anodes for Na-ion Batteries. *J. Mater. Chem. A* 2014, 2, 14986-14993. <https://doi.org/10.1039/C4TA02424A>
7. Luo, C.; Zhu, Y.; Xu, Y.; Liu, Y.; Gao, T.; Wang, J.; Wang, C. Graphene Oxide Wrapped Croconic Acid Disodium Salt for Sodium ion Battery Electrodes. *J. Power Sources* 2014, 250, 372–378.
8. Deng, W., Liang, X., Wu, X. et al. A low cost, all-organic Na-ion Battery Based on Polymeric Cathode and Anode. *Sci Rep* 3, 2671 (2013). <https://doi.org/10.1038/srep02671>
9. T. Syrový, T. Kazda, J. Akrman, L. Syrová, Towards roll-to-roll printed batteries based on organic electrodes for printed electronics applications, *Journal of Energy Storage*, Volume 40, 2021. <https://doi.org/10.1016/j.est.2021.102680>

## Perchlorate Based "Water-in-Salt" Electrolyte for Beyond Li-ion Electrochemical Energy Storage Systems

Z. A. Zafar<sup>a</sup>, K. Knizek<sup>a</sup>, G. Abbas<sup>b</sup>, M. Silhavi<sup>a</sup>, and J. Cervenka<sup>a</sup>

<sup>a</sup> FZU-Institute of Physics of the Czech Academy of Science, Czech Republic

<sup>b</sup> J. Heyrovsky Institute of Physical Chemistry, Czech Republic

### Abstract

Electrochemical energy storage systems (EESS) with high energy density, safety, low cost, and low carbon footprint have become indispensable in the modern era of ubiquitous electronics, electric vehicles, and grid storage. Current EESS lack of these characteristics due to the utilization of critical materials which are precious, flammable, and difficult to recycle. Whereas aqueous electrolytes offer higher safety and lower cost. Nevertheless, their biggest bottleneck is the narrow electrochemical window (1.23V) that is preventing from attaining higher energy and power densities in most of the aqueous EESS. For instance, multivalent metal-ion-based aqueous rechargeable batteries promise high energy density due to multivalent redox chemistry of metal ions ( $\text{Al}^{3+}$ ,  $\text{Zn}^{2+}$ ,  $\text{Mg}^{2+}$ , etc.) but they exhibit much lower energy density in real experiments due to the limited electrochemical windows of the aqueous electrolytes. The water-in-salt based electrolytes (WiSE) can potentially eliminate this barrier by offering a larger electrochemical window by reducing the overall electrochemical activity of water on the electrodes. We demonstrate a new concept using aluminum perchlorate based WiSE that is showing a stable and wide electrochemical window of 4 V against Ag/AgCl. The electrochemistry tests of the electrolyte are performed using carbon-based redox-active electrode materials. We employ the new electrochemical system in aqueous rechargeable multivalent metal-ion batteries, revealing superior performance to standard aqueous electrolytes. Our findings provide new possibilities for widening the electrochemical window and enhancing the energy and power density in aqueous EESS.

## Influence of carbonaceous and inorganic additives on electrochemical performance of the sulfur-composite cathode for Li-sulfur batteries

M. Zukalová, M. Vinarčíková and L. Kavan

J. Heyrovský Institute of Physical Chemistry, v.v.i., CAS, Dolejškova 3, Prague 8, Czech Republic

Rapid development of portable electronic devices together with new large-scale applications, such as electrical vehicles and household energy harvesting packages stimulate demand for battery systems providing high capacity and large energy density. Since the classical Li-ion batteries approached their limits, researchers have moved their attention to a Li-sulfur battery with theoretical capacity of 1675 Ah kg<sup>-1</sup> and energy density of 2600 Wh kg<sup>-1</sup>. However, despite indisputable advantages of this system, there are still issues to be solved prior its commercialization. The main problems represent low conductivity of both elemental sulfur and solid sulfides, significant volume expansion on the cathode during lithiation and migration of soluble polysulfides between the cathode and anode, so called shuttle effect. Among the most frequent strategies employed to solve these problems belong introduction of carbonaceous additives with special morphology improving conductivity of sulfur composite cathode and buffering volume expansion. Cycling stability of the system can be further increased by inorganic component with increased adsorption affinity towards polysulfides. This restricts to a certain extent diffusion of lithium polysulfides to the anode.

In our study we evaluated influence of different carbonaceous and inorganic additives on the electrochemical performance of the sulfur-composite cathode in the Li-sulfur battery. The morphology of mesoporous carbon, electrochemical carbon and activated carbon was studied by nitrogen adsorption measurements, the structure of carbonaceous additives with inorganic component by X-ray diffraction and Raman spectroscopy. The sulfur cathode containing electrochemical carbon with the specific surface area of 1606.6 m<sup>2</sup> g<sup>-1</sup> exhibited the best electrochemical performance and provided a charge capacity of almost 650 mAh g<sup>-1</sup> in cyclic voltammetry at a 0.1 mV s<sup>-1</sup> scan rate and up to 1300 mAh g<sup>-1</sup> in galvanostatic chronopotentiometry at a 0.1 C rate<sup>1</sup>. This excellent electrochemical behavior is ascribed to the high dispersity of electrochemical carbon, enabling a perfect encapsulation of sulfur. The surface modification of carbonaceous additives by TiO<sub>2</sub> has a positive effect on the electrochemical performance of sulfur composites with mesoporous and activated carbons, but it causes a loss of dispersity and a consequent decrease of the charge capacity of the sulfur composite with electrochemical carbon. The composite of sulfur with TiO<sub>2</sub>-modified activated carbon exhibited the charge capacity of 393 mAh g<sup>-1</sup> in cyclic voltammetry and up to 493 mAh g<sup>-1</sup> in galvanostatic chronopotentiometry.

### Acknowledgments

This work was supported by the Grant Agency of the Czech Republic (contract No. 20-03564S).

### References

1. Zukalova, M.; Vinarcikova, M.; Bousa, M.; Kavan, L. Nanocrystalline TiO<sub>2</sub>/carbon/sulfur composite cathodes for lithium-sulfur battery. *Nanomaterials* 2021, 11.

## Pyrite as a Low-Cost Additive in Sulfur Cathode Material for Stable Cycle Performance

D. Capková<sup>a</sup>, T. Kazda<sup>b</sup>, J. Macko<sup>a</sup>, O. Petrušc, A. Baskevich<sup>d</sup>, E. Shembel<sup>d</sup>, A. Straková Fedorková<sup>a</sup>

<sup>a</sup> Department of Physical Chemistry, Faculty of Sciences, Pavol Jozef Šafárik University in Košice, Moyzesova 11, 041 54, Košice, Slovak Republic

<sup>b</sup> Department of Electrical and Electronic Technology, Faculty of Electrical Engineering and Communication, Brno University of Technology, Technická 10, 616 00, Brno, Czech Republic

<sup>c</sup> Institute of Materials Research, Slovak Academy of Sciences, Watsonova 47, 040 01 Košice, Slovak Republic

<sup>d</sup> Ukrainian State Chemical Technology University, Haharina Ave 8, 490 00, Dnipro, Ukraine

Various materials have been reported as an efficient host for sulfur to suppress large volume variation and polysulfide shuttle in lithium-sulfur batteries. Carbon materials are widely used as a matrix for sulfur to improve cycle performance and confine sulfur. Addition of transition metal sulfides into cathode material can improve cycle stability due to high efficiency of chemisorption and suppressing the polysulfide diffusion. In this work, various additions of pyrite to carbon and sulfur in the cathode material were investigated. The results show that the amount of pyrite has an affect on capacity and cycle stability of the electrode. Consequently, the lithium-sulfur batteries with the composite cathode materials, containing 10 % of pyrite, exhibits stable discharge capacity of 788 mAh g<sup>-1</sup> after 60 cycles at 0.2 C.

### Introduction

In an effort to reduce our dependence on fossil fuels, the energy storage systems that can be coupled to renewable sources need to be developed and adapt, e.g., solar, wind, wave. Lithium-sulfur (Li-S) batteries are one of the most promising systems that can satisfy requirements for energy storage devices. Their operating process differs from conventional lithium-ion (Li-ion) cells, which operate on intercalation reactions (1, 2). The theoretical energy density of Li-S battery (~2600 Wh kg<sup>-1</sup>) is up to five times greater than that of commercial Li-ion battery (LiFePO<sub>4</sub> - 580 Wh kg<sup>-1</sup>). Furthermore, sulfur is abundant element, environmentally friendly, low-cost material and the theoretical capacity of sulfur is very high (1675 mAh g<sup>-1</sup>) (3, 4).

However, Li-S batteries suffer from several major insufficiencies that restrict their further implementations (5). Octasulfur (cyklo-S<sub>8</sub>) changes during discharge to soluble lithium polysulfides Li<sub>2</sub>S<sub>x</sub> (8 ≤ x ≤ 3) and continuously to insoluble lithium polysulfides Li<sub>2</sub>S<sub>2</sub> and Li<sub>2</sub>S. The structural changes of sulfur and the formed intermediates results in unstable electrochemical contact between components of the cathode material (6). In addition, the constant diffusion of soluble polysulfides between anode and cathode could operate a shuttle effect. Polysulfide shuttle leads to irreversible loss of active material and corrosion of lithium anode (7). Sulfur and Li<sub>2</sub>S are electronically insulating, the electrical conductivity of sulfur is low (~ 5 × 10<sup>-30</sup> S m<sup>-1</sup> at 25 °C) which leads to

weak cycle stability. The long-term cycling stability may be affected by formation of solid electrolyte interphase (SEI) formed by reaction of organic electrolyte and lithium (8).

Herein, we report the application of pyrite  $\text{FeS}_2$  as an additive in the cathode material for lithium-sulfur batteries to improve cycling stability by efficient electrocatalysis. The suitable ratio of carbon and pyrite in the electrode can effectively trap the dissolved polysulfides, improve cycling stability and cycle life presumably due to strong interaction between pyrite and polysulfide species. The composite containing 10 % of pyrite in cathode material maintains stable cycling performance with a reversible discharge capacity of  $788 \text{ mAh g}^{-1}$  after 60 cycles at 0.2 C.

## Experimental

Pyrite  $\text{FeS}_2$  was carefully milled in a ball mill at 500 rpm to a fine powder. The composite material consisting of sulfur, carbon Super P and  $\text{FeS}_2$  in an exact ratio was grounded together in a mortar. The resulting mass ratio of the sulfur cathodes was 60:25:10:10 for sulfur, carbon Super P,  $\text{FeS}_2$  and polyvinylidene fluoride (PVDF) as a binder in the first test sample and the mass ratio of the second cathode material was 60:20:5:10. PVDF was dissolved in N-methyl-2-pyrrolidone (NMP) then the cathode material was added to the binder solution and mixed on magnetic stirrer for 24 hours. The electrode slurry was coated on aluminum current collector with carbon surface modification and dried at  $60^\circ\text{C}$  for 24 h. The cathodes were cut out in the diameter of 18 mm and pressed using a pressure of  $315 \text{ kg cm}^{-2}$ . The weight of sulfur per area was controlled, around  $2.0 \text{ mg cm}^{-2}$ . The electrolyte was made of 1,2-Dimethoxyethane (DME):1,3-Dioxolane (DOL) 2:1 with 0.7 M Lithium bis(trifluoromethanesulfonyl)imide ( $\text{LiTFSI}$ ) + 0.25 M Lithium nitrate ( $\text{LiNO}_3$ ) and saturated in glass fiber separator. Pure lithium in diameter of 18 mm was used as an anode. The electrochemical test cells (El-Cell<sup>®</sup>) were assembled in argon-filled glove box (Jacomex).

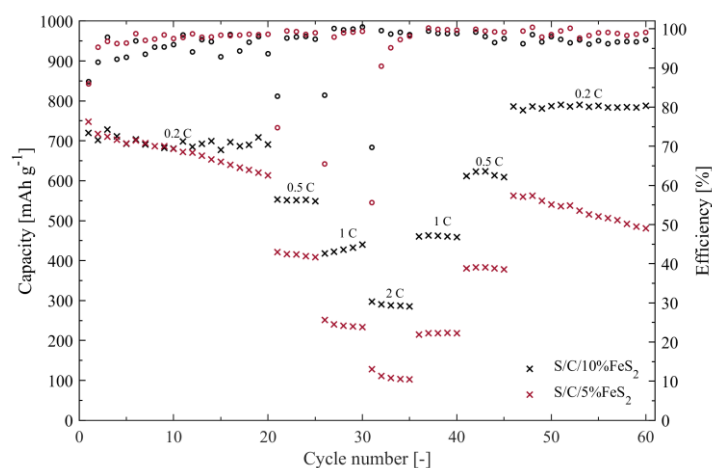


**Figure 1.** The discharge capacities and the efficiency of the S/C/10% $\text{FeS}_2$  and S/C/5% $\text{FeS}_2$  cathodes.

The electrochemical performances of the S/C/10% $\text{FeS}_2$  and S/C/5% $\text{FeS}_2$  electrodes are shown in Figure 1. The discharge capacities of the S/C/10% $\text{FeS}_2$  electrodes are 720.2, 553.0, 418.3 and 297.0  $\text{mAh g}^{-1}$  at the current rate of 0.2, 0.5, 1 and 2 C, respectively. In addition, when the current rate returns to 0.2 C, a stable discharge capacity of 787.9  $\text{mAh g}^{-1}$  is recovered. In comparison, the discharge capacities of the S/C/5% $\text{FeS}_2$  electrodes are 748.3, 421.6, 251.4 and 127.8  $\text{mAh g}^{-1}$  at the current rate of 0.2, 0.5, 1 and 2 C, respectively.

## Conclusions

In summary, the addition of pyrite to the S/C cathode material was demonstrated to boost the transformation of polysulfides. The results suggest that more stable capacities are achieved when 10 % of pyrite is added. The S/C/10%FeS<sub>2</sub> electrode exhibits stable discharge capacity of 788 mAh g<sup>-1</sup> after 60 cycles at 0.2 C. This work provides an insight into the design of low cost and efficient additive to suppress the shuttle effect, increase the stability and capacity of Li-S batteries.

## Acknowledgments

This research was sponsored by the following projects: APVV-20-0138, Development of Novel 3D Materials for Post Lithium Ion Batteries with High Energy Density; APVV-20-0111, Towards Lithium Based Batteries with Improved Lifetime; iCoTS No. 313011V334, Innovative Solutions for Propulsion, Power and Safety Components of Transport Vehicles; vvgp-pf-2021-1756; VEGA 1/0074/17 and specific graduate research of the Brno University of Technology No. FEKT-S-20-6206.

## References

1. Goodenough, J. B., and Kyu-Sung P. "The Li-ion rechargeable battery: a perspective." *Journal of the American Chemical Society*, **135.4** (2013): 1167-1176.
2. Xiulei, J., et al. "A highly ordered nanostructured carbon-sulphur cathode for lithium-sulphur batteries." *Nature materials*, **8.6** (2009): 500-506.
3. Ya-Xia, Y., et al. "Lithium-sulfur batteries: electrochemistry, materials, and prospects." *Angewandte Chemie International Edition*, **52.50** (2013): 13186-13200.
4. Capková, D., et al. "Metal-organic framework MIL-101 (Fe)-NH<sub>2</sub> as an efficient host for sulphur storage in long-cycle Li-S batteries." *Electrochimica Acta*, **354** (2020): 136640.
5. Nazar, L. F., et al. "Lithium-sulfur batteries." *MRS Bulletin*, **39.5** (2014): 436-442.
6. Manthiram, A., et al. "Challenges and prospects of lithium-sulfur batteries." *Accounts of chemical research*, **46.5** (2013): 1125-1134.
7. Chang, Z., et al. "Fabricating better metal-organic frameworks separators for Li-S batteries: Pore sizes effects inspired channel modification strategy." *Energy Storage Materials*, **25** (2020): 164-171.
8. Capková, D., et al. "Carbon Materials as the Matrices for Sulfur in Li-S Batteries." *ECS Transactions*, **95.1** (2019): 19.

## Amorphous Sulfur Copolymer for Li-S Batteries Prepared By Inverse Vulcanization

Ondřej Čech, Tomáš Kazda, Ladislav Chladil, David Kusmič, Guenter Fafilek, Pavel Čudek, Marie Sedlaříková

Department of Electrical and Electronic Technology, Faculty of Electrical Engineering and Communication, BUT, Technická 10, 616 00 Brno, Czech Republic

The work deals with the study of lithium-sulfur batteries, which are promising in terms of their high theoretical capacity and low environmental impact. Instead of elemental sulfur, which is the most common electroactive material of the positive electrode, an inversely vulcanized sulfur with an amorphous structure was used, the preparation process of which was improved and optimized.

### Introduction

Lithium-ion (Li-Ion) batteries currently dominate energy storage. However, their further development is limited by a theoretical energy density of 400 Wh / kg, which is insufficient to meet the growing demands. A potential solution is to use batteries based on a combination of lithium sulfur (Li-S), which can bring a theoretical energy density of up to 2600 Wh / kg [1]. However, the use of sulfur is problematic due to its low specific electrical conductivity of 10-30 S / cm. During the cycle, polysulfides are also formed, which cause morphological and structural changes, further reducing the effective contact and conductivity of the entire electrode [2]. Higher polysulfides are soluble, migrate through the separator electrolyte, and react irreversibly with the lithium anode. This work is focused on the preparation of materials from inversely vulcanized polymer sulfur (IVS). Current research shows that sulfur in amorphous form achieves higher cyclic stability as well as charge efficiency compared to its crystalline form [2]. The inverse vulcanization method, in which polymer sulfur is crosslinked by reaction with a crosslinking agent such as 1,3-diisopropenylbenzene (DIB), stabilizes the polymer sulfur. This prevents recrystallization, which causes problems in the further use of polymeric sulfur materials.

### Experimental

Copolymer material with different ratios of starting materials was prepared by the method of inverse vulcanization (IVS), developed by Griebel, Pyun and colleagues [3]. The temperature of addition of DIB to the sulfur melt proved to be a critical factor in the preparation. If the procedure of the authors of the method was followed, the samples recrystallized sulfur and formed crystalline phases in the sample, which was proved by XRD. Stable results have been achieved by modifying the preparation process, and our preparation method thus produces an amorphous polymeric material which does not recrystallize and precipitate elemental sulfur even after several years.

IVS samples with sulfur, 70, 60, 50 and 40 wt.% Were synthesized. %. In the case of sulfur 70 wt. % was not the resulting solid phase copolymer at room temperature, but was highly viscous. In the case of samples with a sulfur content of 60 wt. % and less the substance was in a glassy state after cooling and in the long run the substance was stable in its properties. As the ratio of the input substances changed, the color shade of the resulting copolymer changed, see Figure. 1

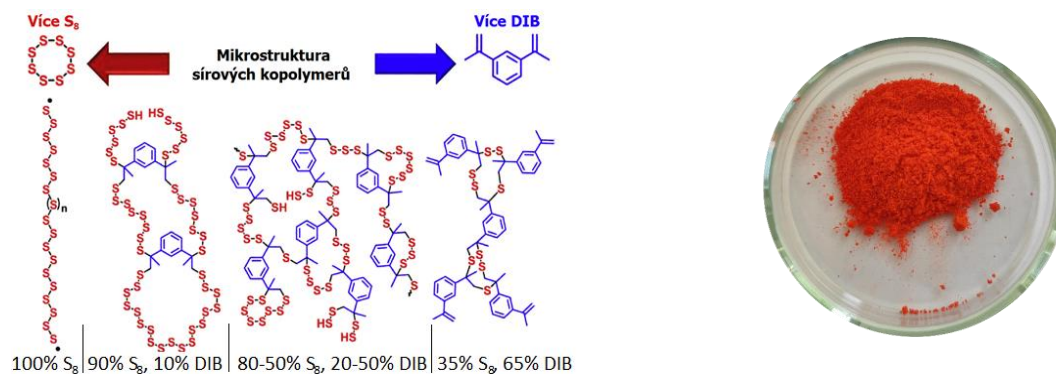


**Figure 1.** Left - IVS structure with different degrees of crosslinking using DIB. Right – grinded IVS with 70 wt% of sulfur.

### Electrochemical characterization of electrode material

Based on the recorded results of the previous sections, a material with a ratio of elemental sulfur and DIB input precursors was chosen for the preparation of the electrode paste in the ratio 70:30 wt. %. This material was chosen for characterization because of all the samples it has the lowest solubility in electrolytes due to the lowest DIB content,

this is related to the largest theoretical capacity for the total weight of the electrode of all prepared samples. The conductivity of the selected material is also the highest of all examined, although this difference is not significant. Electrodes whose material was ground by various methods were examined.

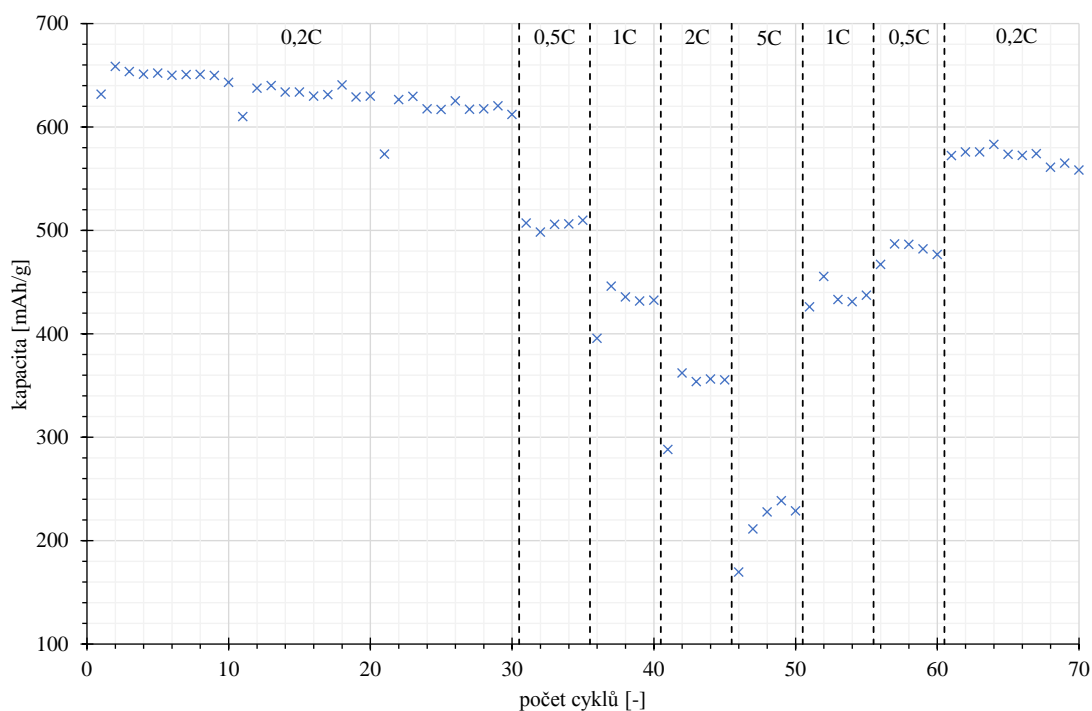


**Figure 2.** Cycling of IVS with 70wt. % of sulfur.

## Conclusion

Based on the study of known methods for the preparation of polymeric sulfur, especially the method of inverse vulcanization of sulfur using 1,3-diisopropenylbenzene, sulfurized polymeric materials with different ratios of input precursors were synthesized. These materials have great potential as electroactive materials for the positive electrodes of lithium-sulfur batteries, but this technology still suffers from a number of unresolved negative aspects, and the study of new high-sulfur polymeric materials could contribute to their solution. An important factor in the inverse vulcanization of sulfur is the temperature at which the components are mixed, in this case the addition of the crosslinker 1,3-diisopropenylbenzene. The crosslinker must be added when the temperature of the sulfur melt reaches 159 °C, otherwise there are problems with the miscibility of the two materials.

## Acknowledgments

This work was supported by the specific graduate research of the Brno University of Technology No. FEKT-S-20-6206. CzechNanoLab project LM2018110 funded by MEYS CR is gratefully acknowledged for the financial support of the measurements at CEITEC Nano Research Infrastructure.

## **Ion-exchange reaction in Li-Na systems as an effective method for the synthesis of sodium-ion battery electrode materials**

N. I. Globa, Yu. V. Shmatok, V. A. Sirosh, S. A. Kirillov

Joint Department of Electrochemical Energy Systems,  
38A Vernadsky Ave., 03680 Kyiv, Ukraine

The work describes electrochemical behavior of  $\text{Na}_x\text{FePO}_4$  and  $\text{Na}_x\text{MnO}_2$  electrode materials obtained by an ion exchange method from industrial samples  $\text{LiFePO}_4$  with the olivine structure and  $\text{LiMn}_2\text{O}_4$  with the spinel structure in limited electrolyte volume conditions.

### **Introduction**

Sodium-ion batteries (NIBs) are considered as alternative systems capable to replace lithium-ion batteries (LIBs), which occupy a significant volume among commercial batteries used in various technology and energy fields [1]. This leads to increased interest in development of effective electrode materials for NIBs.

The synthesis of some electrode materials for sodium-ion batteries is difficult due to their thermodynamic instability.  $\text{LiFePO}_4$  with the olivine structure is a well known electrode material for commercial LIBs [2] and its synthesis is carried out on industrial scale. At the same time, compounds with the structure of maricite are predominantly formed during the synthesis of  $\text{NaFePO}_4$ , but they have low capacity and reversibility during cycling. In this regard, the use of ion exchange method is promising for obtaining olivine-type  $\text{NaFePO}_4$  [3]. The ion exchange reaction can also be used in the case of  $\text{LiMn}_2\text{O}_4$  spinel [4]. One of the factors allowing to consider  $\text{LiMn}_2\text{O}_4$  as a starting material for a positive electrode of NIB is its ability to phase transformations. As a result of sodiation, the spinel structure characteristic of  $\text{LiMn}_2\text{O}_4$  is destroyed with the formation of  $\text{Na}_x\text{MnO}_2$  oxides capable of reversible cycling.

### **Experimental**

Cathodes were made of commercial samples of  $\text{LiFePO}_4$  (Gelon, China) and  $\text{LiMn}_2\text{O}_4$  (Sud-Chemie, Germany). The slurries consisted of an active material, a carbon black additive C-Nergy Super C65 (Imerys Graphite & Carbon, Belgium) and PVDF Solef 6020 (Solvay, Belgium) as a binder taken in mass percentage ratios of 82:10:8 and 80:20:10 for  $\text{LiFePO}_4$  and  $\text{LiMn}_2\text{O}_4$ , respectively. Cathode compositions were casted on an aluminum foil ( $\delta = 20 \mu\text{m}$ ) with a doctor blade. The mass of the cathode material was  $\sim 4 \text{ mg/cm}^2$  and the area of cathodes was  $2 \text{ cm}^2$ . Electrolyte was 1 M solution of sodium perchlorate  $\text{NaClO}_4$  in a mixture of ethylene carbonate (EC, 98 %, Aldrich, Germany), dimethyl carbonate (DMC, 99 %, Aldrich, Germany) and fluoroethylene carbonate (FEC, 98 %, Alfa Aesar, China) taken in a volume ratio of 4:5:1. The volume of electrolyte in cells was  $\sim 40 \mu\text{L}$ .

Electrochemical tests were performed in 2016 coin cells with sodium anode and polypropylene separator (Celgard 2400, China) of  $25 \mu\text{m}$  thickness. Galvanostatic tests were carried out on a Neware battery testing system (China). Cell assembling as well as preparation and storage of electrolyte were made in dry glove boxes.

Before and after cycling cathodes were studied by means of X-ray diffraction (DRON-UM1, LOMO, Russia, Co-K $\alpha$  radiation) and scanning electron microscopy (JEOL JSM 6700F, Japan).

## Results and Discussion

Charge/discharge curves obtained during the cycling of LiFePO<sub>4</sub> in cells with a sodium anode are shown in Figure 1a. Analysis of these dependences showed that the exchange of lithium ions for sodium ions in cells with a limited electrolyte volume occurs during the first few cycles. The presence of two plateaus of the discharge voltage on the first cycle confirms the joint intercalation of lithium and sodium ions. As a reason for this behavior, a sufficiently high concentration of lithium ions in the near-electrode layer can be considered capable of cointercalation into the structure of the electrode during discharge. The changes occurring in an electrochemical process as a result of ion exchange are more clearly demonstrated on the differential capacity curves, presented in Figure 1b. Charge/discharge and differential curves of the 5<sup>th</sup> cycle completely correspond to the dependences known for olivine-type NaFePO<sub>4</sub>. The obtained specific capacity of 112 mAh/g is 73 % of the theoretical value (154 mAh/g) and remains stable during cycling.

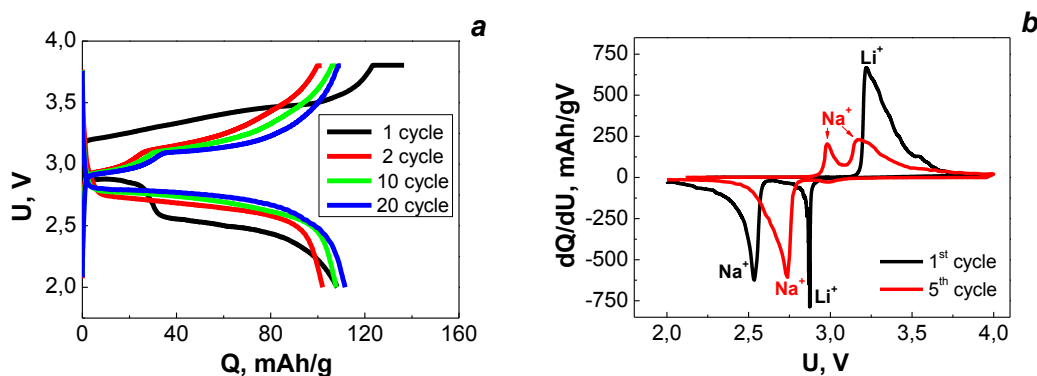


**Figure 1.** Charge/discharge curves (a) and differential capacity curves (b) for Na/LiFePO<sub>4</sub> cells obtained at the cycling charge/discharge currents of 25/50  $\mu\text{A}/\text{cm}^2$ .

Analysis of XRD data after the 1st discharge cycle showed reflections characteristic of both lithium- and sodium-containing phases. After long cycling (100 cycles), the XRD pattern contains peaks characteristic of solely Na<sub>x</sub>FePO<sub>4</sub> and the calculated cell parameters are close to the values known from the literature for Na<sub>x</sub>FePO<sub>4</sub>.

Charge/discharge curves obtained by cycling LiMn<sub>2</sub>O<sub>4</sub> in cells with a sodium anode are shown in Figure 2a. In the case of LiMn<sub>2</sub>O<sub>4</sub> cycling, the process of ion exchange of lithium for sodium occurs gradually, since it is accompanied by a gradual transformation of the initial cubic spinel structure of LiMn<sub>2</sub>O<sub>4</sub> into layered Na<sub>x</sub>MnO<sub>2</sub>. The first charge/discharge cycles are mainly associated with lithium deintercalation and intercalation. This is due to the relatively low phase transformation of spinel into layered oxide. The plateau at the voltage of 3.5 V, which corresponds to the intercalation of lithium, remains to the tenth cycle. At the same time, the plateaus at the discharge voltages below 3.5 V are mainly associated with sodium intercalation and the formation of a layered oxide. The length of the discharge plateaus in the specified voltages increases with the increase in the cycle number. Significant differences in the differential capacity curves obtained on the 1<sup>st</sup>, 5<sup>th</sup> and 18<sup>th</sup> cycles indicate a gradual transformation of LiMn<sub>2</sub>O<sub>4</sub> into layered oxide Na<sub>x</sub>MnO<sub>2</sub> (Figure 2b). The maximum specific capacity of 180 mAh/g sets at about 24 cycles.

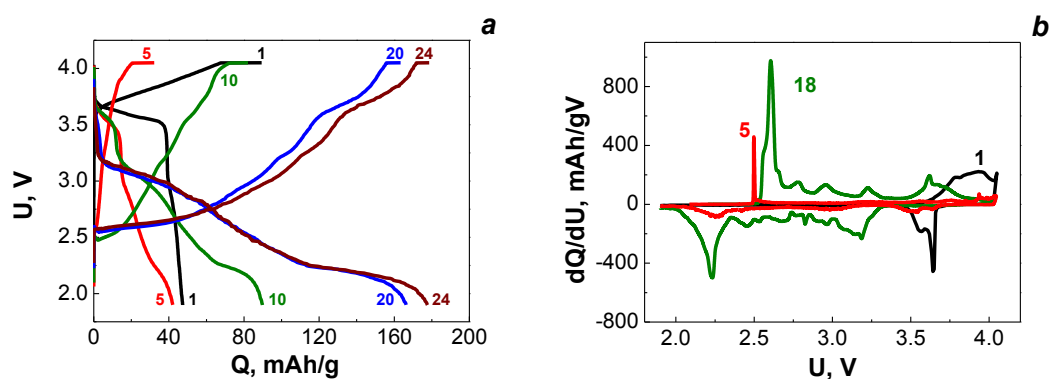


**Figure 2.** Charge/discharge curves (a) and differential capacity curves (b) for Na/LiMn<sub>2</sub>O<sub>4</sub> cells obtained at the cycling current density of 50  $\mu\text{A}/\text{cm}^2$ .

Analysis of XRD patterns obtained after prolonged cycling of the LiMn<sub>2</sub>O<sub>4</sub> electrodes in sodium cell showed changes in the phase composition. The location of the peaks obtained on the X-ray diffraction patterns correspond to the predominant formation of layered oxide Na<sub>x</sub>MnO<sub>2</sub>.

### References

1. J.-Y. Hwang, S.-T. Myung and Y.-K. Sun, *Chem. Soc. Rev.*, **46**(12), 3529 (2017).
2. G. E. Blomgren, *J. Electrochem. Soc.*, **164**(1), A5019 (2017).
3. P. Moreau, D. Guyomard, J. Gaubicher, F. Boucher, *Chem. Mater.*, **22**(14), 4126 (2010).
4. N. Yabuuchi, M. Yano, S. Kuze, S. Komaba, *Electrochim. Acta*, **82**, 296 (2012).

## Determining the Optimal Height of The Active Layer for the Positive Electrode of Lithium-Sulfur Batteries

K. Jaššo<sup>a</sup>, T. Kazda<sup>a</sup>, P. Čudek<sup>a</sup>, and D. Capková<sup>b</sup>

<sup>a</sup> Department Electrical and Electronic Technology, Brno University of Technology, Technická 10, 616 00 Brno, Czech Republic

<sup>b</sup> Department of Physical Chemistry, Faculty of Sciences, Pavol Jozef Šafárik University in Košice, Moyzesova 11, 04154, Košice, Slovak Republic

Increasing the height of the layer of active material and thus increasing the thickness of the electrode is one of the possible methods of producing high-energy density lithium-sulfur batteries. As the height of the layer of active material increases, the energy density often also increases. However, increasing the electrode thickness can also cause many adverse events such as increased internal resistance, increased cell polarization, decreased porosity, or insufficient diffusion. In this study, the impact of the thickness of the positive electrode on the rate capability, energy density, and cycling behavior of the lithium-sulfur cell will be comparatively investigated.

### Introduction

The ever-increasing energy demands of portable electronics and other battery-operated devices (mainly EVs) create a growing demand for high energy density batteries that should simultaneously meet the requirement for low cost and long cycling life. Lithium-sulfur batteries are particularly promising due to the high theoretical capacity of 1672 mAh g<sup>-1</sup>, the volumetric energy density of 2835 Wh L<sup>-1</sup>, and gravimetric energy density as high as 2572 Wh kg<sup>-1</sup> (assuming complete reaction to Li<sub>2</sub>S) (1). Li-S batteries are projected to achieve a practical gravimetric energy density of 400–600 Wh kg<sup>-1</sup> due to their two-electron redox reaction, which is roughly twice that of present Li-ion batteries.

Lithium-sulfur batteries have the potential to replace state-of-the-art lithium-ion batteries in many industries. Their biggest advantage is a higher theoretical energy density and at the same time a low price. However, a few shortcomings, most notably the solubility of polysulfides, need to be addressed before the deployment in the commercial sphere. Dissolution of polysulfides during cycling causes a so-called shuttle effect, which results in capacity fading (2). Other drawbacks include low conductivity ( $\approx 5 \times 10^{-30}$  S cm<sup>-1</sup>) and large volume change (approx. 80%) during cycling due to different densities of sulfur (2.06 g cm<sup>-3</sup>) and lithium sulfide (1.66 g cm<sup>-3</sup>) (3). Many of these problems depend to some extent on the height of the layer of active material.

Increasing the thickness of the electrode and thereby increasing the volume ratio of active material is a promising way to achieve the required sulfur loading on the cathode and thus ensure a high energy density of the Li-S battery. On the other hand, increasing the thickness of the electrode impairs the charge transfer and thus worsens rate capability and power density.

## Experimental

An electrode slurry with a composition of 64 wt% sulfur, 32 wt% Super P carbon black, and 4 wt% CMC binder was prepared in a planetary mill. The slurry was applied to the aluminum foil using an automatic coating machine using 4 different types of coating bars (80, 100, 150 and 200  $\mu\text{m}$ ). The resulting electrodes were dried for 24 hours at 60  $^{\circ}\text{C}$ , and then samples were prepared for analysis under SEM (see Figure 1.). The analysis showed that the height of the resulting dried layer of the active material is only about 8 to 14% of the original height of the coating bar used in the production of the electrode.

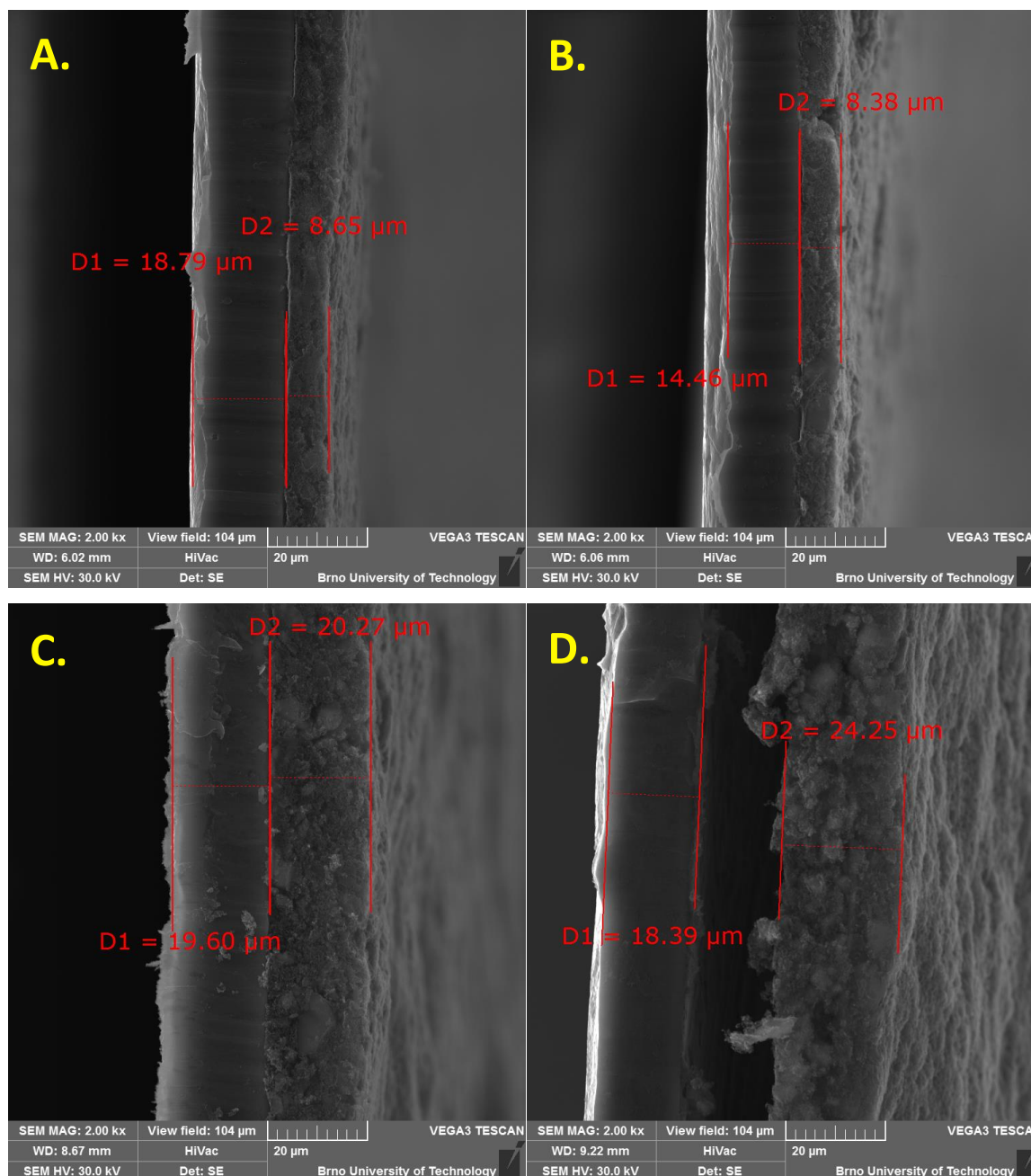


**Figure 1.** Cross-sectional view of positive electrodes made using different coating bar heights with approximate measurement of the height of individual layers: A) 80 $\mu\text{m}$  B) 100 $\mu\text{m}$  C) 150 $\mu\text{m}$  D) 200 $\mu\text{m}$ .

Disc electrodes with a diameter of 18 mm were cut from the rest of the prepared materials. These electrodes were used in the assembly of a lithium-sulfur cell in an electrochemical measuring EI-cell<sup>®</sup> and assembled cells were subjected to electrochemical measurement methods on the Biologic VMP3 potentiostat. One of the measurements was galvanostatic cycling with potential limitation GCPL (see Figure 2.).

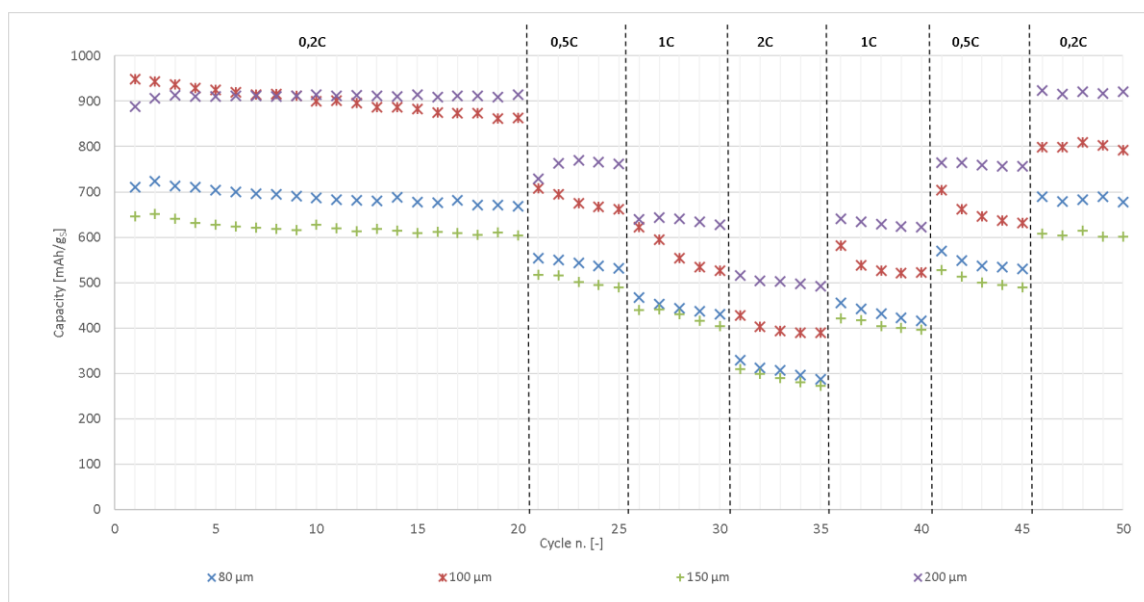


**Figure 2.** Comparison of measured capacities during galvanostatic cycling: 50 GCPL cycles at variable loads.

## Conclusion

From the data measured so far, it is possible to confirm the dependence of energy density and rate capability on the height of the active layer of the positive electrode of Li-S batteries. However, more measurements must be made to determine the optimal height of the active layer, especially with much thicker electrodes than those examined in this experiment.

## Acknowledgments

Authors gratefully acknowledge the financial support from the Ministry of Education, Youth and Sports of the Czech Republic under project No. LTT19001, BUT specific research programme (project No. FEKT-S-20-6206)

## References

1. T. Li et al., *Adv. Funct. Mater.*, **29** (2019).
2. X. Zhang et al., *Mater. Sci. Eng. R.*, **121**, 1-29 (2017).
3. W. Ren, W. Ma, S. Zhang, and B. Tang, *Energy Stor. Mater.*, **23**, 707-732 (2019).

## **Influence of carbonization temperature on morphology and oxygen reduction activity of electrospun Ni/NiO-decorated carbon fibre mats as self-standing cathodes for metal–air batteries**

Tobias Kutsch<sup>ab</sup>, Markus Gehring<sup>ab</sup>, Hermann Tempel<sup>b</sup>, Hans Kungl<sup>b</sup>, Rüdiger-A. Eichel<sup>ab</sup>

<sup>a</sup> Rheinisch-Westfälische Technische Hochschule Aachen, Institute of Physical Chemistry, 52056 Aachen, Germany

<sup>b</sup> Forschungszentrum Jülich GmbH, Institute of Energy and Climate Research – Fundamental Electrochemistry (IEK-9), 52425 Jülich, Germany

E-mail: [tobias.kutsch@rwth-aachen.de](mailto:tobias.kutsch@rwth-aachen.de)

Their high abundance of raw material and high specific theoretical energy density makes alkaline-aqueous metal-air batteries based on iron (9700 Wh/l [1]) or zinc (6220 Wh/l [2]) promising candidates for next generation energy storage. However, in the last decade research has shown that the insufficient performance of the cathodes limits the practical energy density and are the bottleneck of alkaline-aqueous metal-air batteries.[3] The observed high overpotential for “standard” air-cathode architecture (pressed carbon) and diminished cell performance are ascribed to the sluggish kinetics of the oxygen reduction reaction (ORR) at the air-cathode site.[3-4] Most improvements have focused so far on the catalytic active material for enhancing the ORR, but only a few reports take cathode scaffold, architecture, and catalyst-scaffold-interaction into account.[5] Nevertheless, electrospun polyacrylonitrile-based (PAN) carbon nanofibres have been shown to be a purposeful, scalable and cheap way for fibre network- and air cathode-production.[6-8]

In former investigations, our group has constituted that carbonized PAN fibre mats are a mechanically stable and self-standing scaffold for an air-cathode in alkaline-aqueous metal–air batteries.[8-9] It was further shown that the amount of incorporated nitrogen, graphitization degree and therefore the mechanical properties as well as electrochemical activity of such self-standing cathodes is strongly influenced by the carbonization process. However, the overall electrochemical air-cathode performance of pure PAN fibre mats-based cathodes was not remarkably high for both, ORR and long-term investigations. Earlier reports showed that the catalytic activity of such carbon fibre networks can be increased by introducing electrocatalytic active oxygen reduction catalysts, such as Mn-, Co- or Ni-nanoparticles.[10-13]

In this study, Ni-decorated fibres are prepared by electrospinning process and the influence of carbonization temperature ( $T = 600^{\circ}\text{C}–1100^{\circ}\text{C}$ ) is discussed comparing the modified Ni-fibre network with a system without metal additive. In order to receive sufficient information about fibre morphology, graphitization degree and particle decoration, several methods such as scanning electron microscopy, X-ray photoelectron spectroscopy, raman spectroscopy, X-ray diffraction, inductively coupled plasma optical emission spectroscopy and elemental analysis are carried out. For electrochemical studies the fibre mats are directly investigated as air cathode in 6M KOH electrolyte-based half-cell setup used linear sweep voltammetry and chrono-potentiometry.

The results verify that in situ grown Ni-particle-decorated fibres were successfully prepared by electrospinning process followed by thermal treatment. In presence of Ni-decoration the rougher fibre surface, XRD- and Raman-results suggest the formation of turbostratic carbon. A significant influence on the degree of graphitization, nitrogen content and incorporation can be observed through nickel-carbon-interaction. The comparison clearly shows, that partially oxidized Ni-particles enhance

both, ORR activity and long-term stability of the carbon fibre mats with a remarkably performance enhancement for Ni-decorated fibre mats carbonized between  $T = 800^{\circ}\text{C}$ – $900^{\circ}\text{C}$ . In particular, the synergetic effects of nickel additive catalyzing the PAN carbonization as well as the oxygen redox chemistry counteract each other.

In summary the results emphasize the importance of the catalyst framework interaction and cathode scaffold architecture, which is often neglected in studies on air-cathodes for alkaline-aqueous metal–air batteries. By tuning up the optimal carbonization temperature it can be noted that the Ni-decorated fibre networks show appropriate electrochemical activity when directly used as self-standing air cathode for alkaline-aqueous metal-air batteries. Therefore, Ni-decorated carbon fibre mats could be a promising candidate to replace today's state-of-the-art pressed carbon powder-based air cathodes which opens up promising avenues towards the realization of high-capacity metal-air batteries.

### References:

1. H. Weinreich, J. Come, H. Tempel, H. Kungl, R.-A. Eichel, N. Balke, *Nano Energy* 41 (2017) 706–716.
2. M. A. Rahman, X. Wang, C. Wen, *J. Electrochem. Soc.* 160 (2013), 1759–1771.
3. Y. Li, J. Lu, *ACS Energy Lett.*, 26 (2017), 1370–1377.
4. R. O'Hayrea, F. B. Prinz, *J. Electrochem. Soc.* 151, (2004), A756-A762.
5. Z. Ma, X. Yuan, L. Li, Z.-F. Ma, D. P. Wilkinson, L. Zhang, J. Zhang, *Energy and Environmental Science* 8, (2015), 2144–2198.
6. J. Pan, Y. Y. Xu, H. Yang, Z. Dong, H. Liu, B. Y. Xia, *Advanced Science*, 5, 1700691.
7. S. Cheng, Y. Ye, W. Ding, B. Pan, *Journal of Power Sources*, 248 (2014), 931–938.
8. M. Gehring, H. Tempel, A. Merlen, R. Schierholz, R.-A. Eichel, H. Kungl, *RSC Advances* 9 (2019) 27231–27241.
9. M. Gehring, T. Kutsch, H. Tempel, H. Kungl, R.-A. Eichel, *Beilstein Journal of Nanotechnology in progress*.
10. V. Viswanathan, H. A. Hansen, J. Rossmeisl, J. K. Nørskov *ACS Catal.*, 2 (2012), 1654–1660.
11. J. K. Nørskov, J. Rossmeisl, A. Logadottir, L. Lindqvist., J. R. Kitchin, T. Bligaard, H. Jónsson, *The Journal of Physical Chemistry B* 108 (2004) 17886–17892.
12. P. Zhang, Z. P. Guo, Y. Huang, D. Jia, H. K. Liu, *Journal of Power Sources* 196 (2011) 6987–6991.
13. B. Li, S.-W. Chien, X. Ge, J. Chai, X.-Y. Goh, K.-T. Nai, T. S. A. Hor, Z. Liu, Y. Zong, *Mater. Chem. Front.* 1 (2017) 677–682.

## Deposited Layers as Negative Electrodes

J. Maca<sup>1,2</sup>, J. Libich<sup>1,2</sup>, T. Kazda<sup>1,2</sup> and K. Jasso<sup>1,2</sup>

<sup>1</sup>Centre for Research and Utilization of Renewable Energy, Technická 10, Brno, 616 00, Czech Republic

<sup>2</sup>Brno University of Technology, Technická 10, Brno, 616 00, Czech Republic

The battery usage increases every year. The batteries help with development of mobility both from point of view of portable electronic and from view of goods and people transport in electromobility. One of the main parameters is gravimetric and volumetric capacity, which we are trying continually increase. One of the main ways is to change current used material by new ones with better parameters. One of possibilities is to use thin layer and so-called battery conversion principle. Electrodes works on conversion principle have usual higher capacities. The main disadvantage of such system is large volume change of electrode material due charging and discharging. This can be partly solved by special 3D structure which compensate the volume changes. This work focusses on preparing basic thin layer electrode by help of electrodeposition. The electrodes are then cycled against lithium.

### Introduction

Thin layer based on cobalt were prepared by help of electrodeposition. On a copper current collector was truth a suitable mask deposited thin layer. Deposition solution was used 0.01M CoSO<sub>4</sub> heptahydrate and 0.1M ammonium acetate. The pH of the solution was set by 25% solution of ammonia. The electrodeposition was carried out at 1.2V for 15 minutes. Deposited layer was then dried out and assembled in glove box and cycled in EL-cell electrochemical cell. The electrode was tested in potentials corresponding negative electrode from 0.01V – 2.5V. The capacity was determined from this measurement. The average capacity in first ten cycles was 110 mAh/g see figure 1. The measured capacity do not reach theoretical capacity but the experiment was set for first attempt for characterization and understanding of deposited layer. The main goal is to have a suitable surface for growing 3D nanowires structure with should help by compensation of volume change of the conversion electrodes. The deposition process needs to be also optimized for forming uniform flat surfaces without dendrites formation.

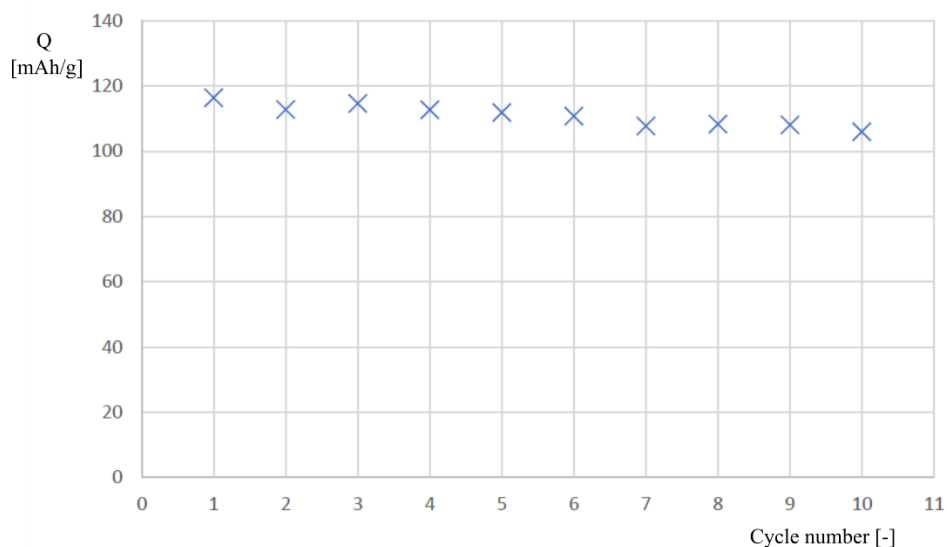


**Figure 1.** Capacity of negative electrode from deposited cobalt layer

### Acknowledgement

Authors gratefully acknowledge the financial support from the Ministry of Education, Youth and Sports of the Czech Republic under project No. LTT19001 and BUT specific research programme (project No. FEKT-S-20-6206)

### References

1. HU, Jiulin, Keyi CHEN, Zhenguo YAO a Chilin LI, 2021. Unlocking solid-state conversion batteries reinforced by hierarchical microsphere stacked polymer electrolyte. *Science Bulletin*. 66(7), 694-707. ISSN 20959273.
2. DI Palma, V., G. Zafeiropoulos, T. Goldsweer, W.M.M. Kessels, M.C.M. Van De Sanden, M. Creatore a M.N. Tsampas, 2019. Atomic layer deposition of cobalt phosphate thin films for the oxygen evolution reaction. *Electrochemistry Communications*. 98, 73-77. ISSN 13882481.
3. Sakita, Alan M.P., Rodrigo Della Noce, Elisa Vallés a Assis V. Benedetti, 2018. Pulse electrodeposition of CoFe thin films covered with layered double hydroxides as a fast route to prepare enhanced catalysts for oxygen evolution reaction. *Applied Surface Science*. 434, 1153-1160. ISSN 01694332.
4. Cui, Can, Rupeng Zhang, Chuankai Fu, et al., 2021. An armor-like artificial solid electrolyte interphase layer for high performance lithium-sulfur batteries. *Applied Materials Today*. 24. ISSN 23529407

## Hollow structure of MnO<sub>2</sub> wrapped sulfur microsphere to suppress the volume changes in lithium-sulfur battery

Marjan Motiei<sup>1</sup>, Haojie Fei<sup>1</sup>, Elif Vargun<sup>1,3</sup>, Constantin Bubulinca<sup>1</sup>, Natalia Kazantseva<sup>1</sup>, Qilin Cheng<sup>1,2</sup>, Gengchao Wang<sup>2</sup>, Hua Bao<sup>2</sup>, Petr Saha<sup>1</sup>

Email: motiei@utb.cz

<sup>1</sup> Centre of polymer systems, Tomas Bata University in Zlin, 76001 Zlin, Czech Republic

<sup>2</sup> School of Materials Science and Engineering, East China University of Science and Technology, Shanghai 200237, China

<sup>3</sup> Department of Chemistry, Mugla Sitki Kocman University, 48000 Mugla, Turkey

**Keywords:** hollow structure, manganese dioxide, volume change, lithium-sulfur battery

Lithium-sulfur batteries are considered as a promising candidate for next-generation energy-storage devices due to their high theoretical energy density of 2600 W h kg<sup>-1</sup> (sulfur cathode coupled with lithium metal anode). The environmentally friendly, low-cost sulfur cathode has a high theoretical specific capacity of 1673 mA h g<sup>-1</sup>. However, there are several challenges in sulfur cathodes before using in practical application such as low conductivity of sulfur and their intermediates, large volumetric expansion during lithiation and “shuttle effect” of soluble polysulfides.

To overcome these challenges, we have prepared sulfur microspheres with hollow structures by adding acid treated MWCNT (a-MWCNT). These hollow structures are able to provide space for the expansion of sulfur during the lithiation. Then, the sulfur microspheres were wrapped by MnO<sub>2</sub> nanosheets, which can strongly absorb the polysulfides to prevent from the “shuttle effect”. The electrochemical performance of assembled lithium-sulfur batteries were measured by cyclic voltammetry (CV) and galvanostatic charge-discharge (GCD) techniques. The effect of hollow structure in the sulfur microspheres on the electrochemical performance especially on cycling life was evaluated.

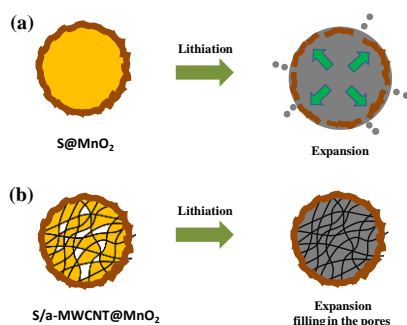


**Figure 1:** Schematic diagram of the mechanism of hollow structure in MnO<sub>2</sub> wrapped sulfur microsphere to suppress the volume changes in lithium-sulfur battery.

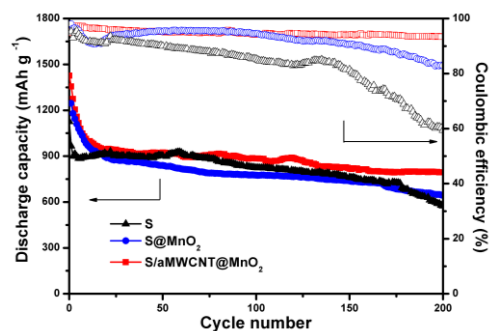


**Figure 2:** Cycling life of MnO<sub>2</sub> wrapped hollow sulfur microspheres (S/a-MWCNT@MnO<sub>2</sub>) compared with other samples.

### **Acknowledgments**

This work is supported by the Ministry of Education, Youth, and Sports, Czech Republic (INTER-EXCELLENCE programme under the grant agreement No. LTT20005. It is also supported by project RP/CPS/2020/005.

## Non-Aqueous Ionic Liquids Based on Quaternary Ammonium Salts for Lithium-Sulfur Batteries

O. Ovchinnikova<sup>a</sup>, Yu. Polishchuk<sup>b</sup>, K. Sukhyi<sup>a</sup>, E. Shembel<sup>bc</sup>

<sup>a</sup> Ukrainian State University of Chemical Technology, Dnipro, 49005, Ukraine

<sup>b</sup> Scientific Research Laboratory of Chemical Power Sources of Ukrainian State University of Chemical Technology, Dnipro, 49005, Ukraine

<sup>c</sup> Enerize Corporation, Coral Springs, FL, 33067, USA

Results of measuring the conductivity of electrolytes with ionic liquids (IL) based on quaternary ammonium salts, promising for innovative lithium-sulfur batteries are presented. The conductivity of IL in a propylene carbonate-dimethylformamide mixture is  $5.2 \cdot 10^{-4}$  Sm/cm depending on the solvent ratio. The presence of lithium salt leads to higher values up to  $8.9 \cdot 10^{-3}$  Sm/cm.

In the modern world increased interest in lithium-sulfur (Li/S) batteries has led to the search for battery systems with a capacity of energy that exceeds the usual lithium-ion battery. The chemical composition of Li/S battery theoretically provides a specific energy of 2567 Wh/kg and an energy density of 2800 Wh/l [1]. Today there are prototypes available which can provide capacity of 350 Wh/kg with an expectation of improvements by a factor 2 [2, 3]. Thus, even now the power capacity of Li/S batteries is much higher than lithium-ion batteries.

Despite the theoretical advantages, there are some practical disadvantages such as: 1) solubility of long-chain polysulfides formed on the cathode as a result of cathode reduction from pure sulfur and/or oxidation of short-chain polysulfides; 2) the lithium metal anode itself is largely metastable with regard to the electrolyte used; 3) the insulating nature of the pure sulfur cathode [4].

By reviewing the literature on Li/S we can determine the predominant use of non-aqueous liquid electrolytes [5-7]. In addition to simply changing the electrolyte components (salts, solvents, additives) and their relative quantities, there is also a choice of a completely different concept, such as ionic liquids.

Ionic liquids (IL) are nonflammable and non-volatile compounds. IL-based electrolytes considered safer in terms of preventing leakage or gassing and all other safety characteristics related to thermal properties compared to the use of conventional liquid-based organic electrolytes.

Propylene carbonate, dimethylformamide, epoxy resin and dimethylaminhydrochloride were used to synthesize ionic liquids.

Synthesis was carried out in a three-neck flask with a thermometer and a stirrer. The mixture was firstly stirred for 3-4 h at the room temperature. Then heated at 50-60 °C for 6-8 h.

A series of solutions of pure IL and with addition of LiClO<sub>4</sub> for conductivity measuring was prepared. Concentration of lithium salt: 0.1, 0.3, 0.5M. Also the values of conductivity IL solution at various ratios of solvent were obtained during the synthesis process of ionic liquids.

A Voltalab-40 analytical radiometer was used to record impedance spectra. The ionic conductivity was measured in a two-electrode glass cell with platinum electrodes. The value of the specific ionic conductivity of the electrolyte used in this work was determined by the formula:

$$\chi = \frac{K}{R}$$

where  $\chi$  is the value of specific ionic conductivity of the electrolyte; K is the cell constant; R is the complex resistance of the electrolyte determined from the impedance spectras.

The values of ionic conductivity of the pure IL are in the range of  $3.33 \cdot 10^{-4} - 5.2 \cdot 10^{-4}$  Sm/cm.

The obtained values of ionic conductivity of the investigated electrolytes with lithium salt are in the range of  $1.79 \cdot 10^{-3} - 8.9 \cdot 10^{-3}$  Sm/cm.

### References

1. X. Ji, L.F. Nazar, *J. Mater. Chem.* **20**, 9821 (2010).
2. Y.V. Mikhaylik, I. Kovalev, R. Schock, K. Kumaresan, J. Xu, J. Affinito, *ECS Trans.*, **25**, 23 (2010).
3. Sion Power, 2012, [www.sionpower.com](http://www.sionpower.com).
4. S.S. Zhang, *J. Power Sources*, **231**, 153 (2013).
5. N.S. Manan, L. Aldous, Y. Alias, P. Murray, L.J. Yellowlees, M.C. Lagunas, C. Hardacre, J. *Phys. Chem.*, **B 115**, 13873 (2011).
6. S. Kim, Y. Jung, S.-J. Park, *J. Power Sources*, **152**, 272 (2005).
7. K. Ueno, J. Park, A. Yamazaki, T. Mandai, N. Tachikawa, K. Dokko, M. Watanabe, *J. Phys. Chem.*, **C 117**, 20509 (2013).

## **Melanin's Semiconductor Nature and his Polymer Structure Successfully Modifies Sulfur Cathode and Increase Efficiency on Li-S batteries.**

Yuliya Polishchuk<sup>a</sup>, Elena Shembel<sup>a,b</sup>, Volodymyr Kyrychenko<sup>c</sup>, Andrea Straková Fedorková<sup>d</sup>  
Vlad Redko<sup>b</sup>, Boris Blyuss<sup>c</sup> and Oleg Girin<sup>a</sup>

<sup>a</sup>Scientific Research Laboratory of Chemical Power Sources of Ukrainian State University of Chemical Technology, Dnipro, 49005, Ukraine

<sup>b</sup>Enerize Corporation, Coral Springs, FL, 33067, USA

<sup>c</sup>Sunoil-Agro, Pavlograd, 51400, Ukraine

<sup>d</sup>Pavol Jozef Safarik University, Košice, SK-04154, Slovak Republic

<sup>e</sup>Prydniprovsky Scientific Centre of the National Academy of Sciences of Ukraine and of the Ministry of Education and Science of Ukraine, Dnipro, 49005, Ukraine

Dynamics of change in impedance spectra and electrochemical parameters of the Li-S rechargeable batteries with non-aqueous liquid electrolyte 0.7 M LiIm, 0.25 M LiNO<sub>3</sub>, DME: DOL (2:1) during storage after assembly and cycling have been shown. For modification of the Sulfur cathode, we used the different types of melanin. Our results confirm that melanin can be used as a promising component of sulfur-based electrodes.

### **Introduction**

Melanins are natural pigments produced found in most organisms in a specialized group of cells – melanocytes, and play an important role in the protection against environmental stresses (1). Due to the presence of unpaired electrons in their structure, they have the properties of stable free radicals and can exist in several red-ox states.

Melanin as a semiconductor, combines the electronic and ionic conductivity, and also has the catalytic properties. These properties on melanin are very attractive for using the melanin for modification the electrodes of Li batteries. We have previously investigated and developed combined innovating cathode system: melanin / LiMn<sub>2</sub>O<sub>4</sub> for Li-ion battery (2)

Our investigation and development using the melanin for modification of the Sulfur cathode of Lithium-Sulfur Batteries are presented in this publication. Sulfur is an among the cathode materials, which have the high level of energy for Li batteries. However, for increasing the stability of the parameters of Li-S batteries during cycling, decreasing the self – discharge and decreasing the impedance / increasing the power of these batteries the modification of the Sulfur cathode using melanin is promising and attractive. These studies are based on our previous experience and research results in the field of Li-S batteries (3 - 5).

Various types of melanin, which have been used during our investigation, are developed and produced by company Sunoil-Agro based on innovative technologies.

## Experimental

The positive electrodes have been fabricated by slurry coating. As the current collector has been used the aluminum foil with modification by fusion of graphite into aluminum (3 - 5). Disk electrodes based on sulfur have the following parameters:  $d = 1.6$  cm, working surface –  $2.0$  cm<sup>2</sup>. Cathode mass has the following composition: Sulfur with polymer structure; Carbon black; Graphite with high conductivity; PVdF (6020/1001, Solef) and various types of melanin, which are synthesized and produced by Sunoil-Agro. The drying of the cathode was under at  $60$  °C for 6 h under vacuum and 2 h at  $120$ °C without vacuum.

The conductivities of various types of melanin powders, which have been used in this development, have been tested by the innovating non-contracted, non-destructive electromagnetic methods (6, 7).

The negative electrodes were made of lithium foil. The microporous polypropylene Celgard®2300 with a thickness of 25 mkm was used as the separator. Electrolyte composition: 0.7M bis(triuroromethanesulfone)imide (LiIm), 0.25M LiNO<sub>3</sub>, DME: DOL (2:1). All procedures were carried out in an Ar-filled glove box.

The following measurements was used: Impedance spectroscopy and galvanostatic cycling Li-S batteries. Impedance spectra were obtained using VoltaLab PGZ 301 analytical radiometer. The frequency range 100 MHz was 100 kHz. Potentiodynamic cycling was performed in the range of potentials from 1.5 – to 2.9 B with 0.5 mV/sec scan rate. The measurements have been conducted at the temperature of  $25$  °C.

## Results

The hodographs of NON modified S-based electrodes have two semicircle (Fig. 1). The resistance values after a day of storage increase slightly.

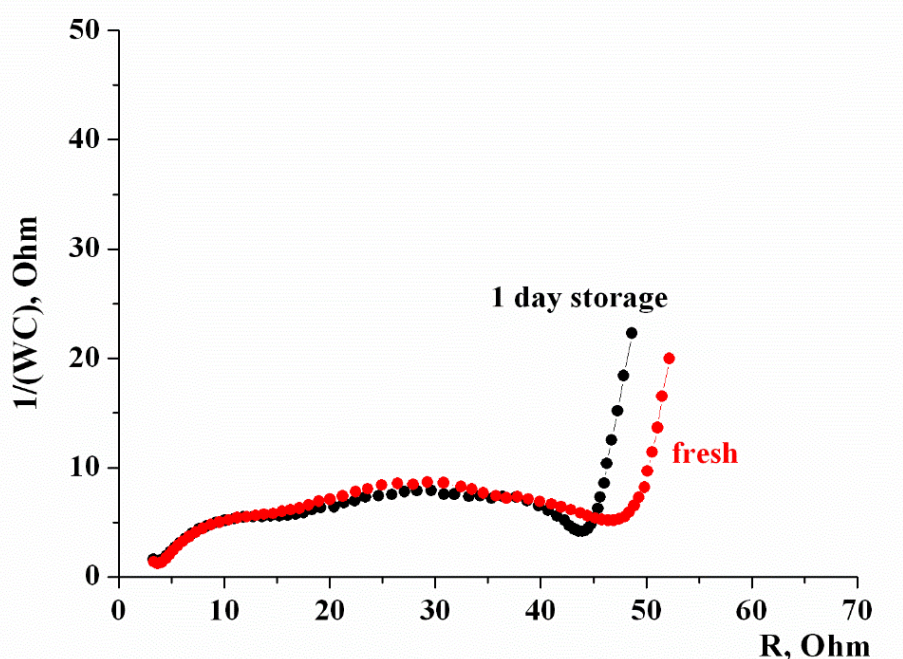


**Figure 1.** Impedance spectra of Li-S-Li cell. The cathode contains 75% sulfur. Electrode area  $2$  cm<sup>2</sup>. Electrolyte: 0,7M LiIm, 0,25M LiNO<sub>3</sub>, DME:DOL (2:1).

The dynamics of changes in the impedance spectra of elements with 5% melanin in cathode mass is shown in Figures 2 – 4.

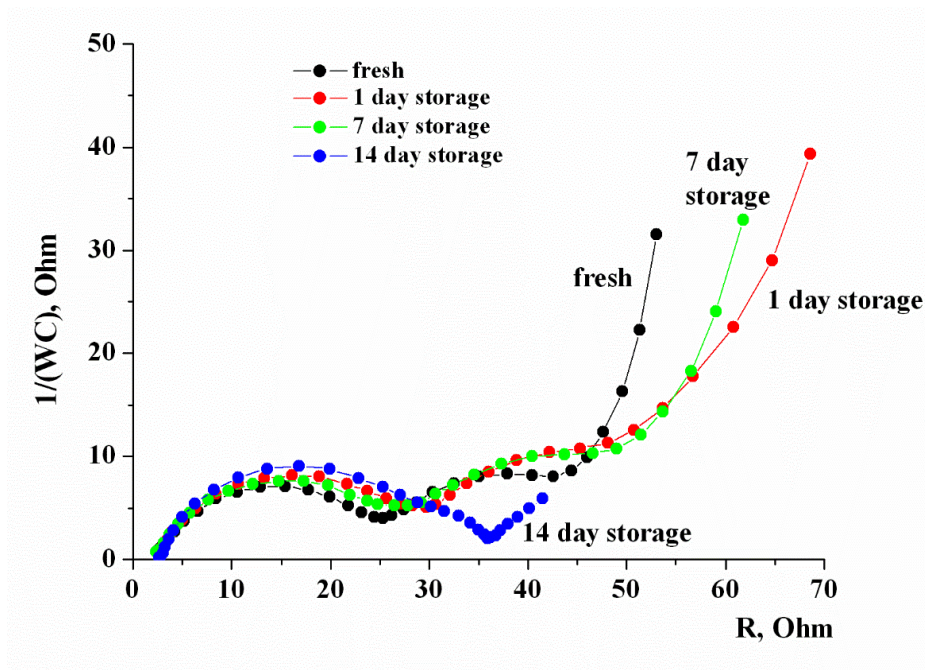


**Figure 2.** Impedance spectra of Li-S-Li cell. The cathode contains 75% sulfur and 5% melanin #1. Electrode area  $2 \text{ cm}^2$ . Electrolyte:  $0,7\text{M LiIm}$ ,  $0,25\text{M LiNO}_3$ , DME:DOL (2:1).

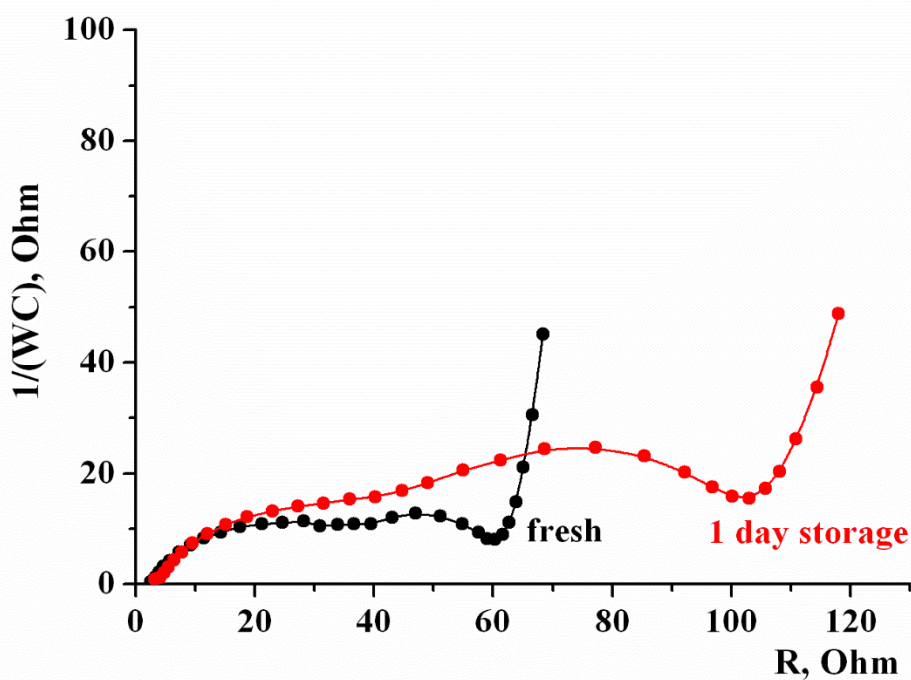


**Figure 3.** Impedance spectra of Li-S-Li cell. The cathode contains 75% sulfur and 5% melanin #2. Electrode area  $2 \text{ cm}^2$ . Electrolyte:  $0,7\text{M LiIm}$ ,  $0,25\text{M LiNO}_3$ , DME:DOL (2:1).

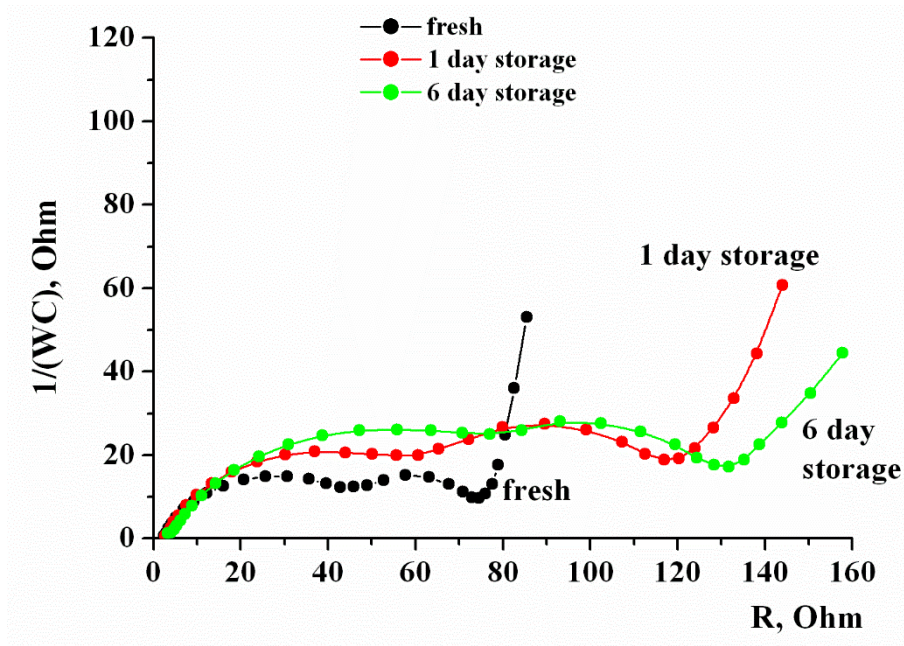


**Figure 4.** Impedance spectra of Li-S-Li cell. The cathode contains 75% sulfur and 5% melanin #3. Electrode area  $2 \text{ cm}^2$ . Electrolyte:  $0,7\text{M LiIm}$ ,  $0,25\text{M LiNO}_3$ , DME:DOL (2:1).

The introduction of melanin in the amount of 5% does not reduce the complex resistance of the system in comparison with electrodes with nonmodified sulfur. However, increasing the melanin content to 20% in the electrode mass significantly reduces the complex resistance of the elements of the disk structure. For example, figure 5 shows the impedance spectra of the elements with 5% melanin #2 (Fig. 5a) and 20% melanin #2 (Fig. 5b). Increasing the content of the modifying additive to 20%, reduces the complex resistance of the element by almost 5 times.

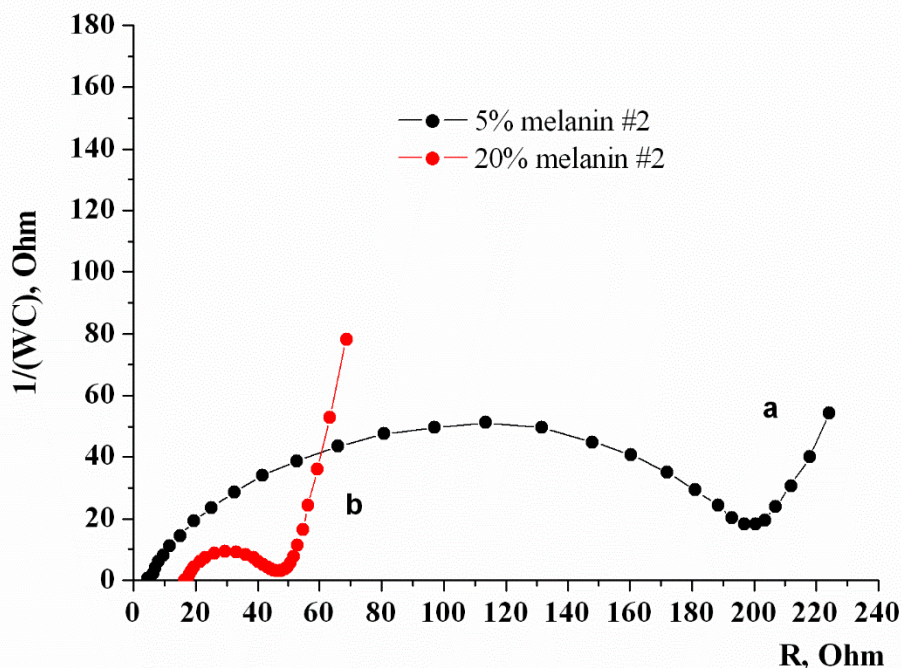


**Figure 5.** Impedance spectra of Li-S 2325 coin cells. The cathode contains 75% sulfur and 5% melanin #2 (a) and 50% sulfur with 20% melanin #2 (b). Electrode area  $2 \text{ cm}^2$ . Electrolyte:  $0,7\text{M LiIm}$ ,  $0,25\text{M LiNO}_3$ , DME:DOL (2:1).

Below the figure 6 shows results of potentiodynamic cycling of Li-S cell with nonmodified sulfur cathode. The storage time after which the elements were put for testing is indicated in the caption below.

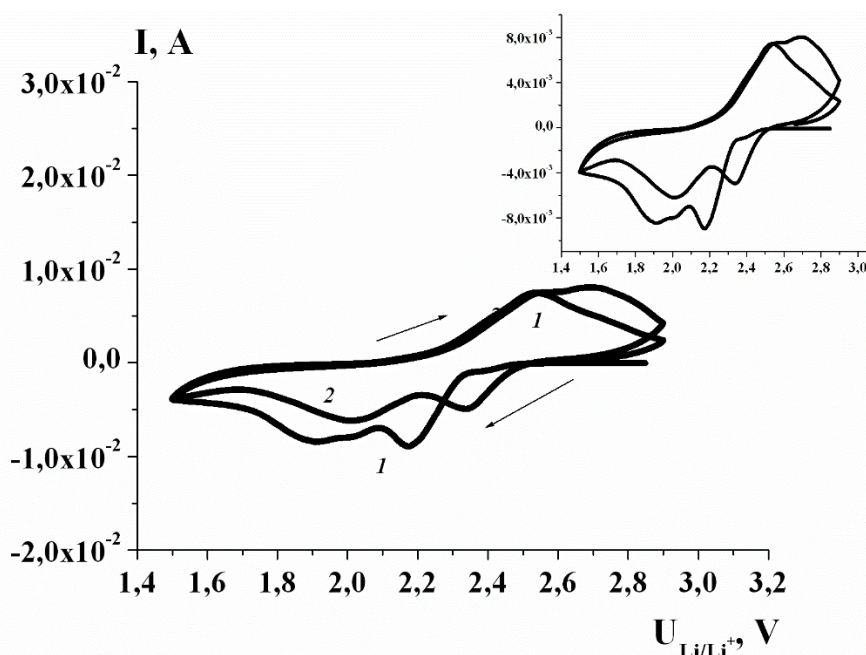


**Figure 6.** Change of Li-S cell volt-ampere curves. The cathode contains 75% sulfur. Electrode area 2 cm<sup>2</sup>. Electrolyte: 0.7M LiIm, 0.25M LiNO<sub>3</sub>, DME: DOL (2:1). Scan rate – 0.5 mV/sec. Cycle range 1.5 - 2.9 V. The numbers at the curves are cycle numbers.

On the first cathode curve of the current-voltage characteristic the electrode shows clear peaks at potentials of 2.2 and 1.9 V. This peak can be associated with the following reactions:



During cycling, there is a small shift of the potential of the first cathode peak to 2.3 V, which may correspond to the reaction:



For the elements with 5% melanin #1 in the cathode mass, the first peak at a potential of 2.2 - 2.3V is shifted to the more positive side and decreases in the second cycle. The second peak at a potential of 1.9 V increases (Fig. 7).

The anode curve has a clear peak at a potential of 2.4-2.5 V. In the second cycle, it does not decrease.

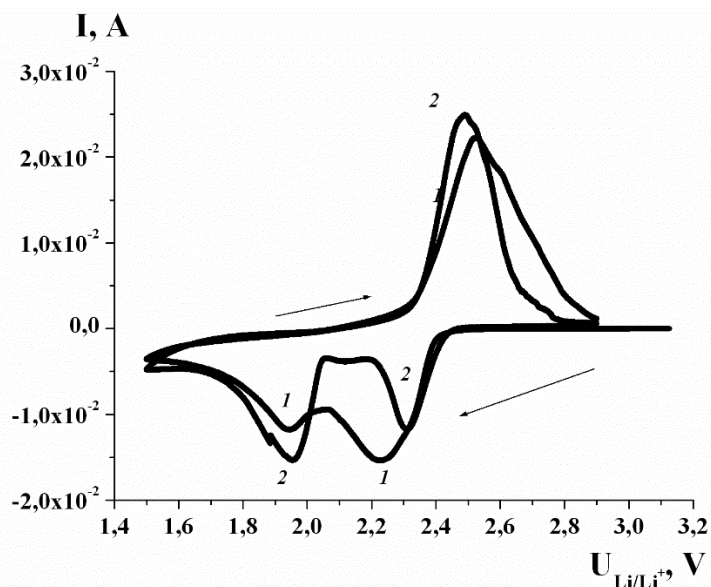


**Figure 7.** Change of Li-S cell volt-ampere curves. The cathode contains 75% sulfur and 5% melanin #1. Electrode area  $2 \text{ cm}^2$ . Electrolyte:  $0.7\text{M LiIm}$ ,  $0.25\text{M LiNO}_3$ , DME: DOL (2:1). Scan rate –  $0.5 \text{ mV/sec}$ . Cycle range  $1.5 - 2.9 \text{ V}$ . Temperature is  $25^\circ\text{C}$ . The numbers at the curves are cycle numbers.

It should be noted that the addition of melanin to the cathode mass leads to an increase of current value in the cathode peaks in 2 times, and the anode peak in 3 times more than for the element without melanin.

Much less effect at  $25^\circ\text{C}$  is observed with the introduction of melanin #2 and #3.

However, the addition of melanin #2 has a positive effect at a temperature of  $40^\circ\text{C}$ . In this case, there is a doubling of the cathode current, compared with nonmodified electrodes (Fig. 8).

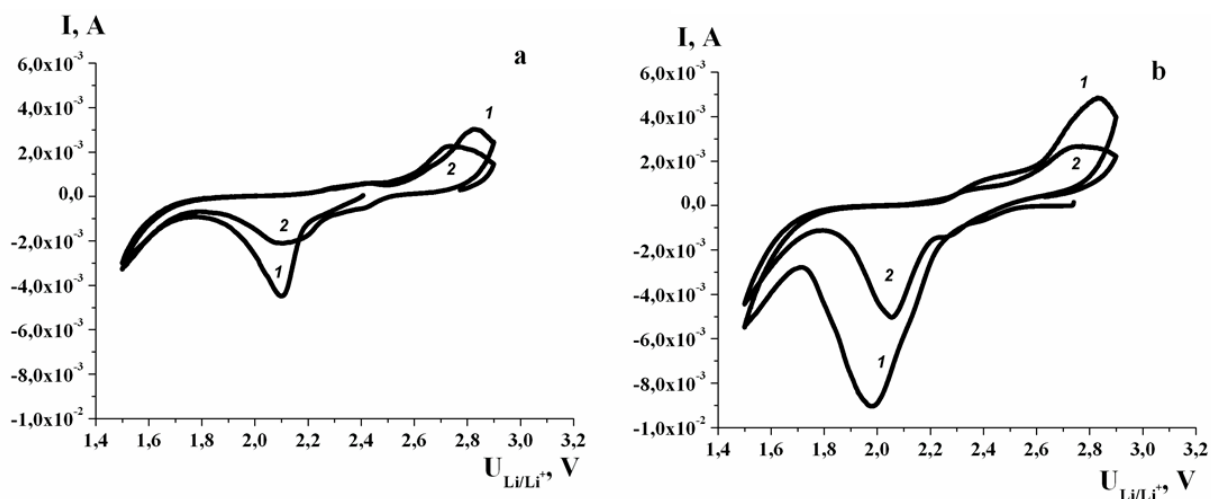


**Figure 8.** Change of Li-S cell volt-ampere curves. The cathode contains 75% sulfur (a); 75% sulfur and 5% melanin #2. Electrode area  $2 \text{ cm}^2$ . Electrolyte:  $0.7\text{M LiIm}$ ,  $0.25\text{M LiNO}_3$ , DME: DOL (2:1). Scan rate –  $0.5 \text{ mV/sec}$ . Cycle range  $1.5 - 2.9 \text{ V}$ . Temperature is  $40^\circ\text{C}$ . The numbers at the curves are cycle numbers.

The area under the curve, which determines the capacitance of the current source, during the modification also increases, which indicates an increase in Faraday efficiency of the process

### Conclusions

1. Modifying additive melanin #2 in the 20% amount in cathode mass reduces the complex impedance of the Sulfur electrode and Li-S cells by almost 5 times compared to impedance of the Sulfur electrode and Li-S cell without melanin.
2. The complex of impedance measurements during storage of cells up to 10 days indicates that a gradual increase in the complex resistance of the system is due to changes in the surface condition of the lithium electrode, rather than modified cathodes. This confirms the stability of sulfur-based electrodes modified with different types of melanin during storage.
3. 5% melanin #2 in the Sulfur electrode and raising the temperature to 40°C significantly increases the efficiency of electrochemical transformations under potentiodynamic cycling. In this case, the value of the cathode current doubles in compare with a parameter under a temperature of 25°C.

### Acknowledgments

These investigations have been carried out in cooperation the Ukrainian State University of Chemical Technology, Scientific Research Laboratory of Chemical Power Sources and company Enerize Corporation, USA. Technologies and materials that are presented in this article are developed also under framework of NATO SPS 985148 project “Development of New Cathodes for Stable and Safer Lithium-Sulfur Batteries”/ Science for Peace and Security Programme. Enerize Corporation is an industrial partner under NATO SPS 985148 project. This investigation has been developed also under project № M/93 -2020 Ministry education and Science of Ukraine in cooperation with “Network thermodynamics as an effective tool for the study of electrode materials; and the subsequent optimization of a high-energy Li batteries” in cooperation with Bar-Ilan University, Israel.

### References

1. M. Naoi, W. Maruyama and P. Riederer. *Encyclopedia of Movement Disorders*, Pages 169, Academic Press, (2010).
2. E. Shembel, V. Kyrychenko, I. Maksyuta, V. Redko, N. Zaderey and M. Tkach, *ECS Transactions*, **99** (1), 47 (2020).
3. Yu. Polishchuk, E. Shembel and Andrea Straková Fedorková. *ECS Transactions*, **99** (1), 133 (2020).
4. . Yu. Polishchuk, E. Shembel, A. Straková Fedorková, V. Redko, N. Zaderey, T. Vergun and E. Zaginayko. *ECS Transactions*, **95** (1), 27 (2019).
5. I. Kirsanova, Yu. Polishchuk, E. Shembel, Andrea Strakova Fedorkova, and V. Redko.. *ECS Transactions*, **95** (1), 149 (2019).
6. V.I. Redko, E.M. Shembel, etc. Method and Apparatus for Measuring Conductivity of Powder Materials Using Eddy Currents. US Patent No. 7,288,941.
7. V.I. Redko, E.M. Shembel, etc. Method and Device for Rapid Non-Destructive Quality Control of Powdered Materials. US Patent No. 8,102,181.

## EIS Analysis of Sulfur Cathodes with Water-Soluble Binder NV-1A for Lithium-Sulfur Batteries

Potapenko A.V.<sup>1,2</sup>, Potapenko O.V.<sup>1,2</sup> Krushevskiy O.V.<sup>1</sup>

<sup>1</sup>Joint Department of Electrochemical Energy Systems,  
38A Vernadsky Ave., 03142 Kyiv, Ukraine

<sup>2</sup>Faculty of Materials Metallurgy and Chemistry, Jiangxi University of Science and Technology,  
Ganzhou, Jiangxi, P.R. China

The growing interest in the Li-S battery system is due to its high energy density ( $\sim 2600 \text{ Wh}\cdot\text{kg}^{-1}$ ), low sulfur cost and increased safety. However, the practical application of Li-S battery technology is hindered by many factors.

One of the methods for modifying the sulfur electrode can be the use of a polymer binder with a large number of polar functional groups, which makes it possible to fix long-chain lithium sulfides and effectively inhibit the shuttle effect in Li-S batteries.

Here, the electrochemical behavior of a Li-S battery with a new water-soluble binder NV-1A has been investigated [1]. Despite a fairly large number of studies showing that the best electrochemical characteristics for Li-S batteries are observed with low sulfur content [2], we share the point of view regarding the percentage of sulfur as part of an electrode [3] and believe that it should not be less than 70 %. The mechanism of electrochemical reactions has been deeply investigated using the electrochemical impedance method (EIS).

As can be seen in the Nyquist diagram (Fig. 1), for our electrodes the resistance  $R_0$ , which characterizes the resistance of the electrolyte in the pores of the separator, increases at the initial stage of the discharge.

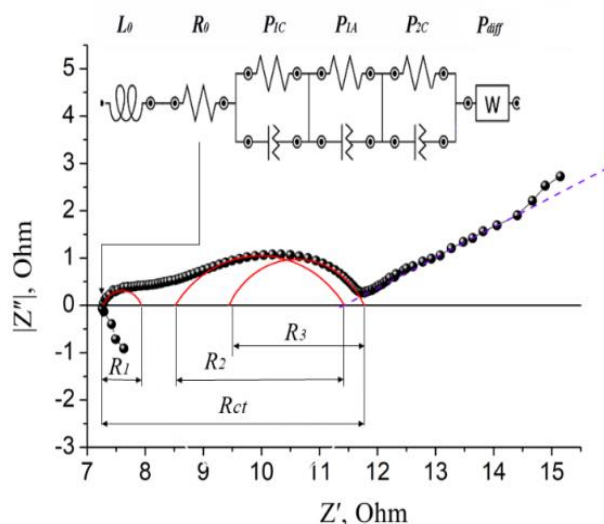


**Figure 1.** Nyquist diagram of sulfur contained electrodes for step 1 in discharge process.

This behavior is associated with a growth the concentration of soluble polysulfides  $S_4^{2-}$  in the electrolyte, while the concentration of  $S_8$  is maintained at the saturation level due to its low solubility

in liquid electrolytes. The increase in resistance  $R_0$  slows down when passing point 3, corresponding to the 2-nd plateau of the Li - S battery discharge process. In some papers, it is assumed that the transition from a high to a low plateau of the discharge voltage occurs simultaneously with the onset of the formation of solid  $Li_2S_2$  and  $Li_2S$ . Since both  $Li_2S_2$  and  $Li_2S$  have extremely low solubility in liquid electrolyte, the concentrations of  $S_2^{2-}$  and  $S^{2-}$  are constant and practically do not affect ion transport in solution, which is reflected in a slight change in  $R_0$  upon further discharge process of the Li - S battery.

An equivalent circuit of a sulfur electrode based on an aqueous binder is proposed. The parameters of this circuit are calculated, including the resistance of the solid electrolyte interface (SEI). It is shown that the main contribution is made by the interface, which is formed on the lithium counter electrode. It is noteworthy that the nonlinear growth of the resistance of SEI layer during the discharge process correlates with the change in the resistance of charge transfer through the interface.

### References

1. O. Potapenko, A. Potapenko, C. Zhou, L. Zhang, J. Xu, Z. Gu. Improved effect of water-soluble binder NV-1A on the electrochemical properties of LFP electrodes, *Russian Journal of Electrochemistry*, 56, 1043 (2020).
2. Y. Li, H. Zhan, S. Liu, K. Huang, Y. Zhou. Electrochemical properties of the soluble reduction products in rechargeable Li/S battery, *Journal of Power Sources*, 195, 2945 (2010).
3. M. Hagen, S. Dörfler, H. Althues, J. Tübke, M.J. Hoffmann, S. Kaskel, K. Pinkwart. Lithium-sulphur batteries - binder free carbon nanotubes electrode examined with various electrolytes, *Journal of Power Sources*, 2135, 239 (2012).

## **Graphene's Correlation of Electrical and Magnetic Properties Manages the Modification and Increasing the Energy of Li Batteries**

Serhii Dubinevych<sup>a</sup>, Vlad Redko<sup>b</sup>, Boris Blyuss<sup>c</sup>, Elena Shembel<sup>b,d</sup>, Oleg Girin<sup>d</sup>,  
and Nellya Zaderey<sup>d</sup>

<sup>a</sup>LLC IMPORTER-K, Kiev, 01001, Ukraine

<sup>b</sup>Enerize Corporation, Coral Springs, FL, 33067, USA

<sup>c</sup>M.S. Polyakov Institute of Geotechnical Mechanics under the National Academy of Sciences of Ukraine, Dnipro, 49005, Ukraine

<sup>d</sup>Ukrainian State University of Chemical Technology, Dnipro, 49005, Ukraine

The importance of lithium power sources is confirmed by the fact that on October 10, 2019, the Nobel Prize in Chemistry in 2019 was awarded for the development of lithium-ion batteries. 10 years earlier, in 2010, physicists Andre Geim and Kostya Novoselov were awarded the Nobel Prize in Physics "for groundbreaking experiments regarding the two-dimensional material graphene". "For groundbreaking experiments on two-dimensional graphene material". A synergistic effect of theory and practicality in the area of lithium batteries, and the theory and practicality in the field of graphene materials creates the unique possibility generate the innovative high-energy Li batteries based on the graphene materials.

The unique results of graphene modification the electrodes of lithium batteries are based on the following properties of graphene:

- High specific surface area, High electronic conductivity, High thermal conductivity,
- Stable chemical properties.

Relatively recently, special attention is paid to the magnetic properties of graphene and the mechanism of the influence of the magnetic properties of graphene on the modification of lithium batteries. We investigate the electrical and magnetic properties of graphene using an innovative non-destructive non-contact electromagnetic method and device. The aim is to increase the energy characteristics of modified lithium power sources based on the synergistic effect of the electrical and magnetic properties of graphene. The results of the parameters of Li batteries are summarized by the parameters of the electrodes modified with graphene. In this case graphene are used for

- Preparation of active materials for Li-ion anodes of batteries.
- Modifications of active materials of Li-ion cathodes of batteries.

Details of the results will be presented during the presentation at the conference and in subsequent publications of the Article.

## Structure, morphology and electrochemical characteristics of $\text{Na}_x\text{MnO}_2$ ( $x = 0.44, 0.67$ and $0.8$ ) as cathode materials for Na-ion batteries

Yu. V. Shmatok, N. I. Globa, S. A. Kirillov

Joint Department of Electrochemical Energy Systems,  
38A Vernadsky Ave., 03680 Kyiv, Ukraine

The paper presents the results of the investigations of structural, morphological and electrochemical characteristics of  $\text{Na}_x\text{MnO}_2$  ( $x = 0.44, 0.67$  and  $0.8$ ) obtained by means of a solid-state synthesis method.

### Introduction

Transition metal oxides of the general formula  $\text{Na}_x\text{MO}_2$  ( $M = \text{Ti}, \text{V}, \text{Cr}, \text{Mn}, \text{Fe}, \text{Co}, \text{Ni}, \text{Cu}$ ) are among the actively studied electrode materials for Na-ion batteries (NIBs) [1, 2]. Among a large number of options, manganese-based oxides  $\text{Na}_x\text{MnO}_2$  have advantages over other metal oxides. This is due to their environmental safety, low cost and the possibility of obtaining high capacities and discharge voltage [3].

One of the factors determining the crystal structure of  $\text{Na}_x\text{MnO}_2$  is the amount of sodium ( $x$ ) in the oxide composition. At small values of  $x$  ( $x = 0-0.44$ ) in  $\text{Na}_x\text{MnO}_2$ , a phase with a three-dimensional tunnel structure is formed [1, 2]. Oxides with high sodium content ( $x > 0.5$ ) have a two-dimensional layered structure. Layered  $\text{Na}_x\text{MnO}_2$  oxides can exist in the form of one of several structural polytypes [4]. Despite a significant number of publications dealing with structural, morphological, and electrochemical characteristics of  $\text{Na}_x\text{MnO}_2$  compounds, the main problems, such as low specific capacity, its stability during cycling, and low discharge rates remain unresolved.

The work presents structural, morphological and electrochemical characteristics of  $\text{Na}_x\text{MnO}_2$  oxides (where  $x = 0.44, 0.67$  and  $0.8$ ) synthesized by a solid-state method from cheap and readily available starting materials, namely chemical manganese dioxide ( $\text{MnO}_2$ ) and sodium hydrogen carbonate ( $\text{NaHCO}_3$ ). The effect of the Na/Mn ratio on the phase composition and morphology of the materials obtained is determined. The electrochemical characteristics of  $\text{Na}_x\text{MnO}_2$  samples of different structures are studied, and the effect of the electrolyte composition on the stability of the specific characteristics of one of the materials is shown.

### Experimental

For the synthesis of  $\text{Na}_x\text{MnO}_2$  oxides, chemical manganese dioxide ( $\text{MnO}_2$ ) without additional chemical and thermal treatment was used as a source of manganese ions. Sodium hydrogen carbonate ( $\text{NaHCO}_3$ ) was used as the sodium source. The  $\text{Na}_x\text{MnO}_2$  samples synthesized were characterized using X-ray diffraction (XRD) method and scanning electron microscopy (SEM).

Electrochemical studies were carried out in CR2016 coin cells. The working electrode consisted of an active material ( $\text{Na}_x\text{MnO}_2$ ), a C-Nergy Super C65 carbon black (Imerys Graphite & Carbon, Belgium) and a Solef 6020 poly(vinylidene difluoride) binder (Solvay, Belgium) taken in a mass ratio of 8:1:1. The cell assembling was carried out in dry glove boxes. Electrochemical tests were performed on a Neware Battery Testing System (China) in a galvanostatic mode in the voltage range of 1.9-3.9 V using a combined CCCV charge mode (residual current – 30  $\mu\text{A}$ ).

## Results and Discussion

According to the results of XRD, the structure of  $\text{Na}_x\text{MnO}_2$  oxides depends on the value of  $x$ . In the case of the minimum sodium content  $\text{Na}_{0.44}\text{MnO}_2$  oxide phase with the tunnel structure was obtained. At higher sodium content, the resulting oxides had a layered structure of P2-type in the case of  $\text{Na}_{0.67}\text{MnO}_2$  and a mixture of P2 and O3-type phases in the case of  $\text{Na}_{0.8}\text{MnO}_2$  sample.

Characteristic differences were also found in particle morphology.  $\text{Na}_{0.44}\text{MnO}_2$  oxide consists of micro-sized rods and rod plates that exist as separate particles or form spherical aggregates. The  $\text{Na}_{0.67}\text{MnO}_2$  and  $\text{Na}_{0.8}\text{MnO}_2$  oxides consist of irregularly shaped particles forming spherical aggregates (similar to the initial  $\text{MnO}_2$ ). At the same time, there are some differences in the morphology of primary particles associated with different phase composition of the samples.

Galvanostatic studies of synthesized oxides in sodium cells showed that their specific capacity and stability during cycling depend on the phase composition and crystal structure. As shown in Figure 1, despite the lowest initial specific capacity (117 mAh/g), the  $\text{Na}_{0.44}\text{MnO}_2$  oxide with the tunnel structure shows better cycling stability compared to layered materials ( $\text{Na}_{0.67}\text{MnO}_2$  and  $\text{Na}_{0.8}\text{MnO}_2$ ) and is characterized by the loss of capacity of ~5% after 50 cycles at the current density of  $50 \mu\text{A}/\text{cm}^2$ . In addition,  $\text{Na}_{0.44}\text{MnO}_2$  oxide has better rate characteristics and with an increase in the discharge current up to  $5 \text{ mA}/\text{cm}^2$  (~11 C) has a specific capacity of 44 mAh/g (Figure 2). In the case of  $\text{Na}_{0.67}\text{MnO}_2$ , a close value of specific capacity (42 mAh/g) was obtained already at the current density of  $1 \text{ mA}/\text{cm}^2$ .

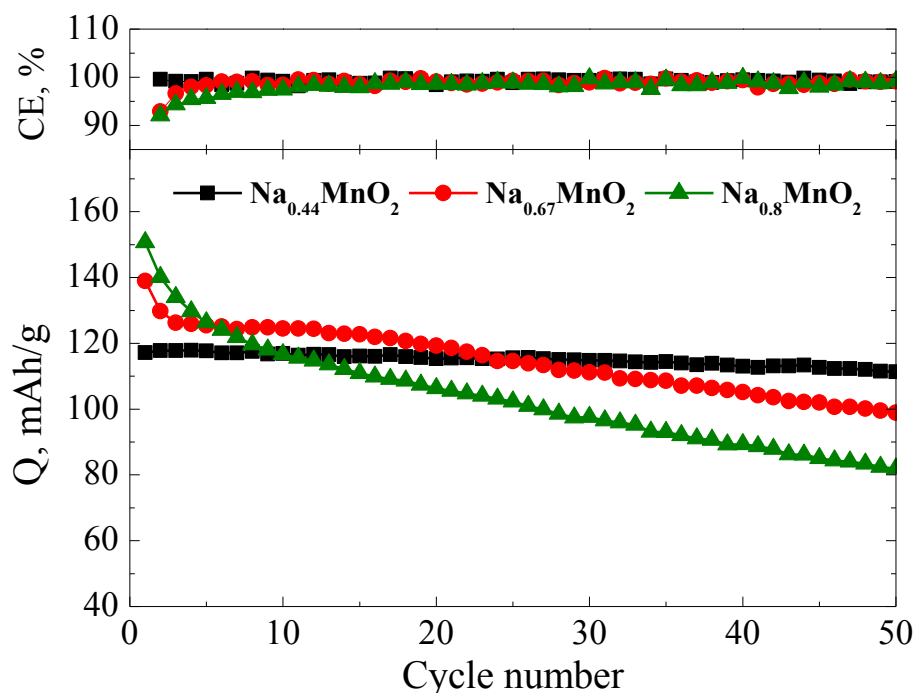


**Figure 1.** Dependences of specific capacity on cycle number for  $\text{Na}_x\text{MnO}_2$  samples at the cycling current density of  $50 \mu\text{A}/\text{cm}^2$ .

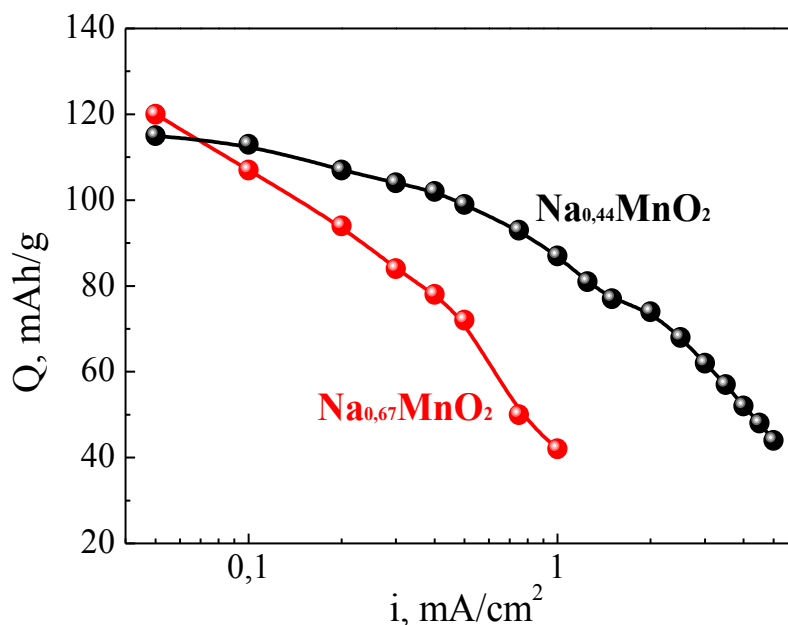


**Figure 2.** Dependences of specific capacity of  $\text{Na}_x\text{MnO}_2$  samples on discharge current density.

Using galvanostatic cycling methods, it was also found that among the used electrolytes containing carbonate solvents, the electrolyte of the composition of 1M  $\text{NaClO}_4$  EC:DMC:FEC (40:50:10) is optimal from the point of view of ensuring the stability of the specific capacity both during long cycling and different current densities discharge as shown for the  $\text{Na}_{0.44}\text{MnO}_2$  sample.

The results obtained testify to the advantages of  $\text{Na}_{0.44}\text{MnO}_2$  oxide with tunnel structure compared to layered materials, which consist in better kinetics of diffusion of sodium ions in the structure of the material and higher stability of the structure during cycling. The latter is the result of a relatively low susceptibility of  $\text{Na}_{0.44}\text{MnO}_2$  to the Jahn-Teller effect, the negative influence of which increases with increasing amount of sodium in the compound.

### References

1. K. Kubota, S. Komaba, *J. Electrochem. Soc.*, **162**(14), A2538 (2015).
2. J.-Y. Hwang, S.-T. Myung and Y.-K. Sun, *Chem. Soc. Rev.*, **46**(12), 3529 (2017).
3. N. Ortiz-Vitoriano, N. E. Drewett, E. Gonzalo, T. Rojo, *Energy Environ. Sci.*, **10**(5), 1051 (2017).
4. C. Delmas, C. Fouassier, P. Hagenmuller, *Physica B+ C*, **99**(1-4), 81 (1980).

## Study of Gel Polymer Electrolytes for Li-S batteries

I. Veselkova<sup>a</sup>, K. Jaško<sup>a</sup>, T. Kazda<sup>a</sup> and M. Sedlaříková<sup>a</sup>

<sup>a</sup> Department of Electrical and Electronic Technology, Brno University of Technology, Technická 10, 616 00 Brno, Czech Republic

Lithium-sulfur batteries are next-generation battery systems with low cost and high specific energy. However, the most popular liquid electrolytes can not solve problems with the growth of lithium dendrites and with safety in lithium metal batteries. Gel polymer electrolytes are perspective materials, which could be used as a replacement.

### Introduction

Lithium-ion batteries are highly popular due to their good electrochemical properties like high energy density, long cycle life, and lightness, but are still not economically attractive for large-scale and transportation applications [1]. The market for electric and electronic devices increases every year. Therefore, the demand for batteries and electrochemical power sources increases too. With this tendency scientists are looking for a battery with the best electrochemical properties, low cost, and high safety, therefore they study different types of battery technologies. Recently, rechargeable Li-S batteries have attracted attention because sulfur has a high theoretical capacity (1675 mAh/g) and high energy density (2600 Wh/g), low cost, and environmental friendliness [2]. But elemental sulfur in the cathode of Li-S battery generates a few problems in comparison with Li-ion batteries: a problem with the „shuttle effect“ of polysulfides and a problem with sulfur utilization or with the volume expansion of sulfur. These problems generate poor cycle life of the cell, low energy efficiency, and low specific capacity [4].

Gel polymer electrolytes (GPEs) are the most promising electrolytes for stable batteries due to their good properties such as flexibility, safety, lightness, and leakage prevention. As liquid electrolytes, GPEs have high ionic conductivity due to the immobilization of a large amount of liquid electrolyte in a polymer host [3]. GPEs are being applied in Li-S batteries to suppress the formation of dendrite on the surface of lithium metal and to improve the safety of the battery [4], [5].

As one of the most studied polymer matrices is PVdF-HFP (poly(vinylidene fluoride-co-hexafluoropropylene)) copolymer, which is being used in gel polymer electrolytes due to high dielectric constant, electrochemical stability and good thermal endurance of flexible polymer matrix [4]. The second polymer, which attracts the attention of scientists, is PMMA (polymethyl methacrylate) with good ionic conductivity. However, gels based only on PMMA, in comparison with gels based on PVdF-HFP, have low mechanical strength, poor structural stability, low lithium migration number and poor performance of depend film forming. Usually, this polymer is being used in combination with other substrates to manifest its effect on lithium-sulfur batteries [4].

### Preparation of Gel Polymer Electrolyte

In order to prepare the gel polymer electrolyte, polymers PVdF-HFP and PMMA were dissolved (in weight ratio 3:2) in DMF (N,N-dimethylformamide) under magnetic stirring for 1 h at 60°C [2]. Afterward, 0.75 M LiTFSI (lithium(trifluoromethane) sulfonamide) and 0.25 LiNO<sub>3</sub>

(lithium nitrate) were added to the homogenized polymer solution and subsequently stirred for 30 min. To obtain a polymer membrane, the homogeneous polymer solution was injected into a Petri dish and allowed to polymerize at ambient temperature overnight.

### Experiment

Prepared GPE was measured in electrochemical testing cell EL-CELL between pure lithium and sulfur-carbon electrode. The composition of the electrode was: 64 wt.% of sulfur + 32 wt.% of Super P + 4 wt.% of a binder CMC (carboxymethyl cellulose). The electrode was dried and pressed.

Electrochemical conductivity of gel electrolyte was measured between two stainless steel electrodes by impedance spectroscopy method with a frequency range from 1 MHz to 0.1 Hz [6]. The conductivity of GPE was 3.2 mS/cm.

The further research will be focused on preparation GPE+sulfur electrode to achieve a good connection with the electrode surface. GPEs with good ionic conductivity could make to adopt high sulfur loadings and improve the performance of Li-S batteries.

### Acknowledgments

This work was supported by the grant FEKT-S-20-6206 "Materiály a technologie pro elektrotechniku IV".

### References

1. Y. Zhao, Y. Zhang and D. Gosselink, *Membranes (Basel)*, **2**(3), (2012).
2. A. Aishova, A. Mentbayeva, B. Isakhov and D. Batyrbekuly, *Materials Today Proceedings*, **5**(11), (2018).
3. J.-K. Kim, *Materials Letters*, **187**, (2017).
4. Q. Yang, N. Deng, J. Chen and B. Cheng, *Chemical Engineering J.*, **413**, (2021).
5. M. Liu, D. Zhou, Y.-B. He and Y. Fu, *Nano Energy*, **22**, (2016).
6. I. Veselkova, M. Sedlářiková, *ECS Transaction*, **99**, (2020).

## Perovskite Single Crystals for Energy Conversion of Solar Radiation

S. Gavranović<sup>a</sup>, J. Pospíšil<sup>a</sup>, V. Novák<sup>b</sup> and P. Vanýsek<sup>b</sup>

<sup>a</sup> Faculty of Chemistry, Brno University of Technology, Purkyňova 464/118, 612 00 Brno, Czech Republic

<sup>b</sup> Department of Electrical and Electronic Technology, FEKT, Brno University of Technology, Technická 3058/10, 616 00 Brno, Czech Republic

Experimental part describes synthesis, structural and optical properties of MAPbBr<sub>3</sub> single crystals and electrical characterization of the Au/MAPbBr<sub>3</sub>/Au light-sensitive assembly. Its parameters (responsivity, external quantum efficiency and specific detectivity) are calculated based on the spectral and switching (on/off) current responses. The material is further discussed as possible active component for photovoltaic panels.

### Single Crystal Perovskite

The single crystals investigated in this part of work were predominantly aimed to serve as material for radiation detectors. However, much of the results, if not all, can be extrapolated and used for design of materials for photovoltaics. The material that was synthesized for this purpose was a compound from the class of perovskites of the type MAPbBr<sub>3</sub>. The desired compound was prepared following the following scheme



The synthetic method was inverse temperature crystallization because the solubility of the solute decreases as the temperature of the solution (dimethylformamide (DMF) as a solvent in this case) increases (1).

Solutions of methylammonium halides (MAX) and lead halides (PbX<sub>2</sub>) in a suitable polar aprotic solvent are used to grow hybrid MAPbX<sub>3</sub> perovskites. Methylammonium halides are organic compounds of the stoichiometric formula MAPbX<sub>3</sub> (CH<sub>3</sub>NH<sub>3</sub>X<sub>3</sub>), where X represents the halide anion Cl<sup>-</sup>, Br<sup>-</sup> or I<sup>-</sup>. In general, these are white substances that are used as precursors in the process of preparation of perovskite materials. MABr and MAI are in the form of a white powder mass, while MACl forms transparent crystals. These precursors can be prepared by mixing methylamine with hydrohalic (HX) acid in an equimolar ratio (2).

The stoichiometric amounts of precursors were dissolved in 1 ml of DMF. The vial containing the prepared solution was placed in a MAPbBr<sub>3</sub> growth apparatus. During the synthesis, the temperature was gradually increased in the range from 40 °C to 80 °C. The initial temperature (40 °C) was chosen based on the solubility curve of this particular perovskite. With the use of this method, a series of MAPbBr<sub>3</sub> single crystals of similar sizes was prepared. The smallest of the prepared crystals had a size of 3 mm x 3 mm x 1 mm and the largest of these was 4 mm x 5 mm x 1 mm. The crystals thus prepared can be contacted by gold collector electrodes, created by vapor deposition. Contacting was performed using a special MB-ProVap-5 thermal evaporator from MBRAUN. Interdigital gold electrodes 100 nm thick were deposited. The distance between the individual electrode fingers was 100 μm. The sample was next mounted using special paste on a prepared glass substrate with

transparent indium tin oxide layer from company Ossila with designation S101. The sample was finally encapsulated by epoxy resin cured by UV radiation.

### Characterization of the Structure and Optical Properties

The diffraction pattern of the grown  $\text{MAPbBr}_3$  single crystal was determined by X-ray powder diffraction (XRD), which was then compared with the theoretical diffractogram of the same single crystal (cubic phase). There is a high agreement between the theoretical and experimentally determined diffractograms. It can be concluded that the prepared single crystals occupy a cubic phase formed by very regular elementary cells.

The cubic elementary cell  $\text{MAPbBr}_3$  also follows from the calculation of the Goldschmit tolerance factor, which is equal to 0.93 for this type of perovskite. The octahedral factor describing the regularity of  $\text{PbBr}_6$  coordination also indicates the regularity of the structure of this perovskite ( $\mu = 0.607$ ).

To define the range of applicability in the field of electromagnetic radiation, it is necessary to determine the absorption spectrum of the grown single crystal. Therefore, the dependence of the absorbance on the EMZ wavelength in the range 300–750 nm was determined using a spectrometer (UV-VIS Varian Cary 100).

The measured spectrum (see Fig. 1) shows a relatively constant absorbance in the range of 350 to 550 nm, which is interrupted by a sharp drop around 550 nm. Thus, in the area of absorbance decrease, a very selective response can be assumed; however, this measurement needs to be supplemented by the measurement of detection parameters, primarily internal quantum efficiency (EQE).

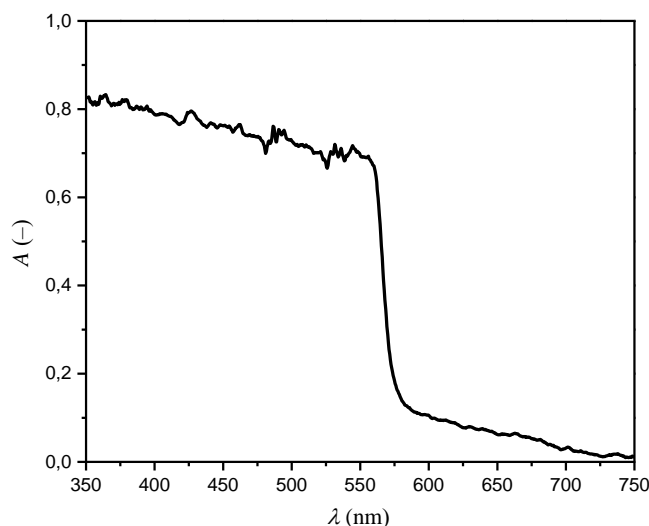


**Figure 1.** VIS spectrum of the  $\text{MAPbBr}_3$  single crystal.

### Electrical Characteristics of the Crystal

The darkness and light current-voltage characteristics of the mounted crystal were measured (see Fig. 2). Based on this measurement, it is possible to evaluate at what potential and at which polarity the measurement of the switching characteristics will take place.

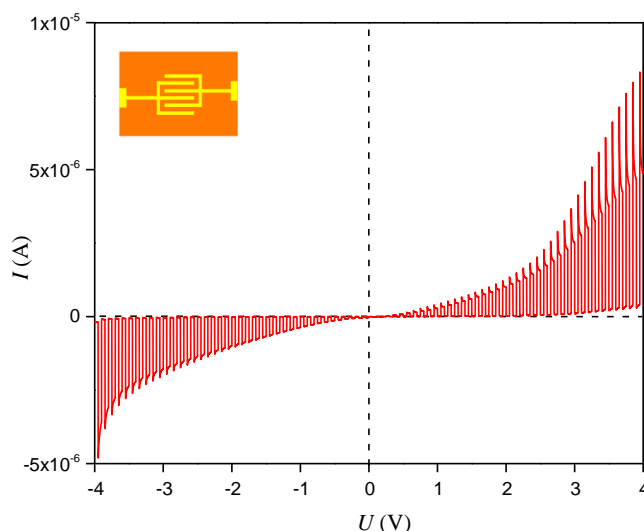


**Figure 2.** Combined dark and illuminated current-voltage characteristics taken at 533 nm light and intensity  $10 \text{ W}\cdot\text{m}^{-2}$ . In the left upper corner is the schematics of the electrode assembly.

The volt-ampere (VA) characteristic of the measured sample shows greater linearity in the negative polarity as compared to the positive polarity. Significant deviations from linearity could be caused by various processes, especially by polarization of the crystal. In order to measure the switching characteristics correctly, it is important to consider not only the linearity and magnitude of the current responses, but also the settling times. It is clear from the measured VA characteristic that the stabilization processes at the positive polarity take considerably longer than in the opposite polarity. However, this polarity was chosen for measuring the switching characteristic (due to higher current responses). For this reason the positive polarity measurement was performed at relatively long pulses of optical signals (60 s, with shorter pulses the stabilization processes predominate). The symmetry of the current responses around the origin indicates the high quality of the contacts between the gold electrodes and the  $\text{MAPbBr}_3$  single crystal.

The switching characteristics of the prepared crystal were measured using a special Zahner CIMPS apparatus.

The measurement of switching characteristics was performed for irradiation intensities of  $5 \text{ W}\cdot\text{m}^{-2}$  to  $0.05 \text{ W}\cdot\text{m}^{-2}$  at 4 V bias potential and an optical signal pulse period equal to 60 s. LEDs with a wavelength of 533 nm were used as the radiation source, which corresponds to the peak of the EQE maximum. The figure (Fig. 3) shows all measured intensities.

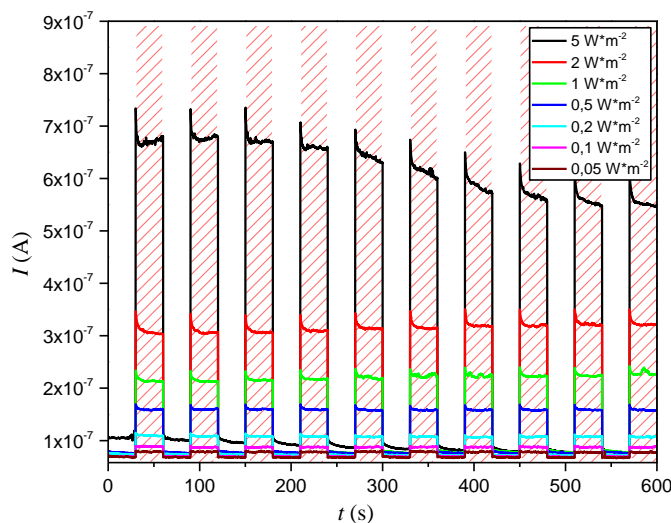


**Figure 3.** Switching characteristics of the prepared mounted perovskite crystal

The prepared device showed much better stability (shorter stabilization processes) at low irradiation intensities. This stability was almost constant after ten cycles (600 s). As the intensity of irradiation increases, so does the magnitude of photon noise. This fact is confirmed by the average values of current at dark: for the irradiation intensity  $1 \text{ W}\cdot\text{m}^{-2}$  ( $1.2\cdot 10^{-7} \text{ A}$ ) and for the intensity  $0.05 \text{ W}\cdot\text{m}^{-2}$  ( $6.7\cdot 10^{-7} \text{ A}$ ). The influence of noise was also reflected on the detection parameters of the optoelectronic system, therefore it was necessary to study the dependence of these parameters on the intensity of irradiation (3).

### Acknowledgement

This study is in part a result of the research funded by the Czech Science Foundation as the project GA ĀR GA19-23718S “Novel Perovskites for Hybrid Photonics Devices” and as the project GA ĀR 20-29499Y “Novel Perovskite Monocrystals for Photosensing.”

### References

1. M. I. Saidaminov, A. L. Abdelhady, G. Maculan and O. M. Bakr, *Chemical Communications.*, **51**, 17658 (2015).
2. H. Li, S. Li, Y. Wang, H. Sarvari, P. Zhang, M. Wang and Z. Chen, *Solar Energy*, **126**, 243 (2016).
3. S. Gavranović, Perovskite Single Crystals for the Detection of Electromagnetic Radiation (In Czech), in Faculty of Chemistry. 2021, Brno University of Technology: Brno.

## Use of Photovoltaic Panels to Power Variable Traffic Signs

T. Binar<sup>a</sup>, J. Zimáková<sup>a</sup>, J. Fridrich<sup>a</sup>, M. Sedlaříková<sup>a</sup>

<sup>a</sup> Brno University of Technology, Technická 10, 616 00 Brno, Czech Republic

The work deals with the possibility of using renewable energy sources to power variable traffic signs. These marks are used for line traffic control. The destination is roads and motorways, where there is a problem with the power supply of signs due to the absence of mains voltage. Currently, lead-acid batteries are used for power supply, which are always replaced with new ones after discharging and taken to a maintenance center for charging. The costs of the whole agenda involved are enormous and it is therefore desirable to reduce them in any way. The aim of this work is to design a photovoltaic panel for the use of solar energy for charging used lead-acid batteries.

### Introduction

Renewable energy sources are those sources that have the ability to be partially or completely renewed during gradual consumption. The main source of energy on earth is the sun, which is the cause of a number of processes from which we can draw energy. An example of such a process can be wind, which is caused by uneven heating of the earth's surface from sunlight. Another example is biomass, which is solar energy converted into chemical bonding in plants by photosynthesis. The main advantage of using renewable sources is their inexhaustibility and low impact on the environment, the main disadvantage is the instability of energy supply and low conversion efficiency. Due to fluctuations in the amount of energy supplied, it is necessary to accumulate it for later use.

Photovoltaic systems are used to convert sunlight directly into electricity. The basis is a photovoltaic cell, working on the principle of photoelectric effect. Since the output of such cell cannot usually be used directly, these cells are connected to various serial-parallel combinations, the output of which is further modified by controllers or inverters to values that we can use.

Photovoltaic cells are made of semiconductor materials. Structurally, the cells are formed by a plate of base material, on which a metal grid forming an electrode is applied. To reduce the reflectivity, an anti-reflective layer is applied, or usually texture created on the surface. [1]

The suitability of a semiconductor material for use in solar cells is determined by the width of the band gap for the material. This value should be in the range of 1.1 eV to 1.7 eV. It is also required that the materials used be characterized by high mobility and long life of minority charge carriers. There are many semiconductor materials that meet these requirements. These are mainly Si, GaAs, CdTe, InP, AlSb and others, but for price reasons silicon is mainly used [2] [3].

### Design of the PV panel location

The photovoltaic panel used has dimensions of 1559 mm × 1046 mm × 46 mm [4]. It is mounted on a frame welded from L 30 mm × 30 mm × 3 mm profiles. In the center of the weld is a flange that allows the panel to rotate 90 °, the inclination of the panel is fixed at an angle of 35 °. The panel must always be oriented so that it does not exceed the vertical projection barriers. The construction allows

the panel to rotate around the vertical axis by  $360^\circ$  thanks to the web formed by a tube  $70 \text{ mm} \times 3 \text{ mm} \times 1700 \text{ mm}$ , which is attached to the base.

For safety reasons, a breakable coupling is added between the base and the web so that in the event of a car accident, the structure does not form a solid obstacle.

The base is ready for mounting a load against overturning and shifting. The load is realized using concrete tiles, due to their easy availability and low price. When the solar panel is oriented vertically, the battery box can also be used as a load. The base includes adjustable legs for partial leveling of uneven terrain. The design of the base is shown in Figure 1.

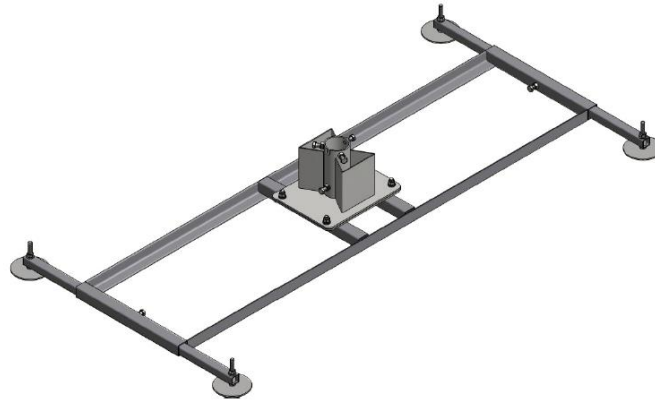


**Figure 1.** The base of the panel mounting structure

Visualization of the panel installed between the ArcelorMittal OSNH4 / H2 barriers is shown in Figure 2. The figure illustrates the horizontal and vertical orientation of the panel.

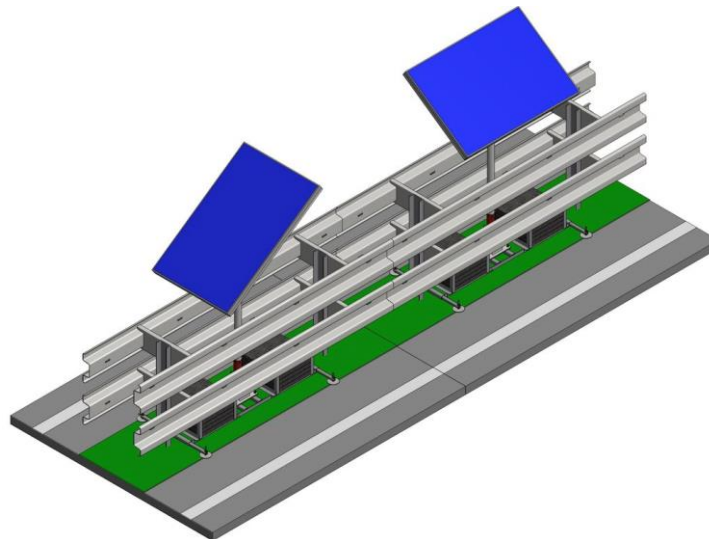


**Figure 2.** PV panels between barriers

### Static calculation

The calculation of wind load is based on the requirement of the Directorate of Roads and Motorways of the Czech Republic, which is specified in the design and quality requirements guidelines [5]. The device must withstand a wind load of at least  $p = 0,8 \text{ kN} \cdot \text{m}^{-2}$ . Position the panel horizontally is less advantageous from the point of view of stability and will be require more load because the force tilts the stand over the shorter arm.

## Conclusion

It was designed a set, which will be used to power mobile variable traffic signs using renewable energy sources. Due to the target, attention was paid mainly to the use of energy from photovoltaics. The way in which brands are currently powered is unsatisfactory and solar power supply is directly offered as a suitable alternative. The proposed kit consists of three parts, namely a photovoltaic panel, a battery box and a fuel cell box. The photovoltaic panel includes a mounting structure that has been structurally adapted for use in the center lane of the highway between the barriers, as there are the biggest space restrictions at this point. The design took into account the requirements of the authorities approving the use of equipment in road transport. Based on these requirements, static calculations were performed to ensure stability under wind loads, from which the dimensions of the equipment are based. Detailed calculations and distribution of acting forces on the panel will be given in the following works.

## Acknowledgements

The publication was created within the project of specific research at BUT (No. FEKT-S-20-6206).

## References

1. A. LUQUE, S. HEGEDUS, *Handbook of Photovoltaic Science and Engineering*. Wiley, 2003. 1179 s. ISBN 0-471-49196-9.
2. R. SATPATHY, V. PAMURU, *Solar PV Power*. 1st edition. Academic Press, 2020. 520 s. ISBN 978-0-12-817626-9.
3. A. McEVOY, T. MARKVART, L. CASTANER. *Practical Handbook of photovoltaics*. 2nd edition. Academic Press, 2011. 1268 s. ISBN 978-0-12-385934-1.
4. *Datasheet SunForte PM096B00*. [online]. AU Optronics corp., ©2018, [cit. 17. 4. 2021].
5. Directorate of Roads and Motorways of the Czech Republic. *PPK-PRE*. [online]. 3.2019 [cit. 11. 12. 2020]. available at: <[https://www.rsd.cz/wps/wcm/connect/0c99ac31-0e87-4e79-b43d-7920a69f29b7/PPK\\_PRE\\_03-19.pdf?MOD=AJPERES](https://www.rsd.cz/wps/wcm/connect/0c99ac31-0e87-4e79-b43d-7920a69f29b7/PPK_PRE_03-19.pdf?MOD=AJPERES)>.

## Solar-Powered Irrigation System

K. Jandova<sup>a</sup>, M. Janda<sup>b</sup>

<sup>a</sup> Department of Electrotechnology, Brno University of Technology, Faculty of Electrical Engineering and Communication Technologies, Technicka 10, 616 00 Brno, Czech Republic

<sup>b</sup> Department of Power Electrical and Electronic Engineering, Brno University of Technology, Faculty of Electrical Engineering and Communication, Technicka 12, 616 00 Brno, Czech Republic

This article deals with the issue of solar-powered irrigation, specifically, by connecting a solar power source to a drip irrigation system. Thanks to an independent energy source the irrigation system is able to work anywhere. In addition to energy independence, thanks to the drip mode of irrigation, another benefit is water saving, which is up to 70% compared to conventional irrigation. The simplicity of this system allows use both in small gardens and in agriculture. Another advantage of the system is its expandability with various sensors (e.g. soil moisture monitoring), which will help with more efficient management of watering.

### Introduction

The main requirements for an irrigation system are minimum water consumption and minimum energy consumption. For this reason, photovoltaic-powered drip or trickle irrigation systems are coming to the fore. Due to their principle of operation, which is based on the transfer of relatively small quantities of water, their demands on the energy sources that power them are relatively minimal.

### Solar irrigation system

The solar-powered irrigation system was chosen because there is no electrical outlet connection available at the irrigation site and also because the system is fully automated. The experiment was conducted from 13 July 2020 to 26 July 2020, with daytime temperatures ranging from 21 to 26°C, nighttime temperatures not dropping below 10°C and winds not exceeding 10 m/s. The system responded flexibly to daytime cloud cover.

Due to the impossibility of connecting to the electricity grid, a self-contained irrigation system was purchased, manufactured by Irrigatia. The irrigation part of the system was placed on a bed area of 6m x 4m. This system was chosen based on affordability and suitable parameters for irrigating the defined area. The experiment was conducted based on the experience of previous years when the selected land was irrigated in the conventional way, i.e. by a watering can or a sprinkler system. Under conventional watering, some areas had an excess of moisture and others deficiency. Another disadvantage of conventional irrigation was that, with increased sunshine and wind, it was necessary to irrigate several times a day.

The irrigation system itself is equipped with a master control unit and a pump. This is then connected to a system of backbone hoses that distribute the water to the individual irrigated areas. Parallel branches are then connected to the backbone lines, which are terminated either by a drip line at each plant or by a soakaway hose. In this way, the water is brought directly to the plants and no water is wasted on the surrounding soil, where in most cases it evaporates without benefit. To ensure

efficient watering, the pump switches on at certain intervals (according to the controller settings) and runs for a predefined period of time. Ideally, these two parameters are regulated depending on the intensity of the sunlight, which influences the rate of soil drying.

The photovoltaic panel, which is used to charge the battery, is connected to the control unit and can also serve as a sensor of the solar intensity of the irrigated area. The panel itself is designed in such a way that the batteries are recharged to full capacity when the pump is idle. The batteries then serve as a power source when the sunlight is not sufficient to switch on the control unit and the pump. The system under test (IrrigatiaSOL-C160) has the following parameters: Solar panel: 20 W; Battery: 12 V Ni-MH 4400 mAh, lifetime min. 1000 charging cycles; System capacity up to 260 l/day.

### Water consumption

In both cases the water used was from a rainwater tank. In conventional watering, the water consumption was about 110 litres per day per defined area of watered land. For the period under review (13.7.2020 - 26.7.2020), this represents a consumption of 1540 litres of water for watering. In contrast, the solar irrigation system had during this period consumption of approximately 435 litres per the defined area of land watered. This calculation therefore shows a water saving of around 70%. Advertising sources claim water savings of up to 90%. Compared to the theoretical assumption, this is almost 20% less than the claim, but still a greater water saving compared to conventional irrigation.

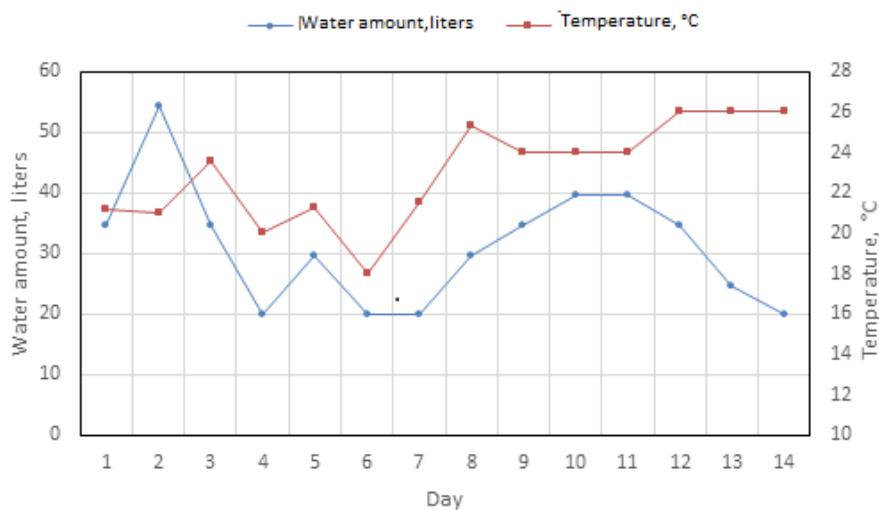


**Figure 1.** Graph of water consumption of the irrigation system and ambient temperature for the monitoring period

In order to be able to comprehensively assess the savings in water required for irrigation, the effect of wind, which dries out the soil, must also be taken into account.

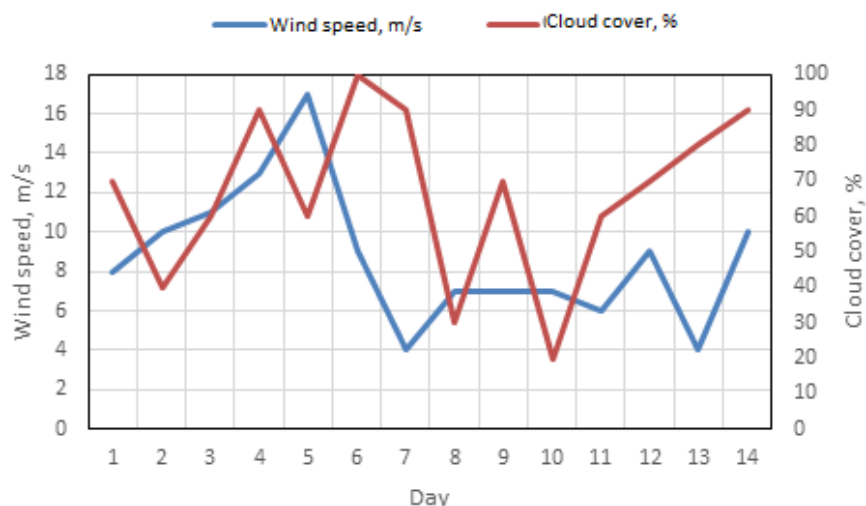


**Figure 2.** Graph of weather conditions (cloud cover and wind speed) for the period under study

### Conclusion

The aim of this article was to spread awareness of the use of renewable energy in a less traditional sector. The combination of a photovoltaic module and irrigation has proven to be suitable for use on smaller areas of land without the need for a connection to the electricity grid or a connection to a running water supply. The big bonus of this combination is the environmental friendliness of the system, the saving of utility water and the automated operation that ensures a regular supply of water to the plants, unlike conventional irrigation. Due to the water savings achieved, this system can also be used in locations where pressurised water cannot be used.

### Acknowledgments

This work was supported by the specific graduate research of the Brno University of Technology No. FEKT-S-20-6206.

### References

1. H. CHEN ET AL.: *Progress in electrical energy storage system: A critical review*, Progress in Natural Science 19 (2009) 291–312
2. *Solární zavlažování* [online]. [cit. 2021-5-9]. Available from: [https://ecoproduct.cz/c/vsechno-solarni-zavlazovani-1880?gclid=CjwKCAjwkN6EBhBNEiwADVfyawnaR3AwnD8bx3I\\_I7AZlhqytmz-NzKudAAGT2SO68ZSXYBvLO-DhoCqA0QAvD\\_BwE](https://ecoproduct.cz/c/vsechno-solarni-zavlazovani-1880?gclid=CjwKCAjwkN6EBhBNEiwADVfyawnaR3AwnD8bx3I_I7AZlhqytmz-NzKudAAGT2SO68ZSXYBvLO-DhoCqA0QAvD_BwE)
3. Meteorological information [online]. [cit. 2021-5-9]. Available from: <https://www.ventusky.com/cs/49.172979;16.358169#>

## The influence of environmental conditions of the recycling of solar modules

F. Langer, J. Vanek, K. Jandova, P. Maule

Fakulta elektrotechniky a komunikačních technologií, Vysoké učení technické v Brně,  
Technická 10, 612 00 Brno

The work describes experiments conducted on ethylene vinyl acetate layer in samples of photovoltaic module, where it functions as insulation and binder. The degradation was achieved by thermal vacuum oven, in which degradation by heat in common air and nitrogen atmosphere was conducted.

### Introduction

While solar energy is described as clean source of electrical power, the photovoltaic modules used to harvest this energy represent a problem, which we should focus our attention on. It is expected that the world leaders in solar energy (China, United States of America, Japan, India and Germany) will produce by year 2050 up to approximately 80 tons of photovoltaic panel waste alone. The solution to this prevailing problem could be recycling. The main focus of recycling of photovoltaic module are module frame, protective glass and silicon wafers. While the module frame is easily removed, the protective glass and silicon wafer must be mechanically and thermally processed. This process is notorious for its high energy and temperature requirements. As a result, it is desirable to look for cheaper and less energy intensive procedures.

The ethylene vinyl acetate foil encapsulates silicon wafer, in addition to attaching it to protective glass and back sheet of module. It is being attached by process of lamination in temperatures reaching 150 °C. It was theorized, that explosion of the ethylene vinyl acetate layer in solar module to high temperatures could lead to high enough degradation of this binding layer, so that removal of glass with minimal physical strength was required.



*Figure 1. One of samples of solar module used for experiments.*

## Experiment

A series of experiments was conducted on samples of thin layer solar module, which were all cut by water jet. Firstly, it was necessary to find out temperature, in which laminated ethylene vinyl acetate starts to noticeably degrade. The measuring was conducted in vacuum thermal oven, in which the sample was placed. After being heated to set temperature, the sample continued to be exposed for two hours, after which it was set to cool down. After cooling down enough, ethylene vinyl acetate layer was observed and mechanically tested for degradation. By repeated measuring, the temperature was determined to be approximately 340 °C. When sample of solar module was exposed to this temperature, the ethylene vinyl acetate thawed enough to remove protective glass from rest of sample by use of minimal physical strength. The process is accompanied by fire destruction of back sheet TEDLAR® layer and creation of exhaust gases. This experiment was repeated with difference of air in vacuum oven chamber being replaced with gas nitrogen. Exposing sample to temperature of 340 °C in nitrogen environment prevented fire and achieved same level of thawing of ethylene vinyl acetate while creating less exhaust gases. Even though the fire was prevented, TEDLAR® layer was still destroyed by the high temperature. Regrettably, apart from one instance in which the protective glass was extracted in one piece at the end of experiment, the cracks of protective glass caused by water jet cutting resulted in protective glass breaking up into pieces.

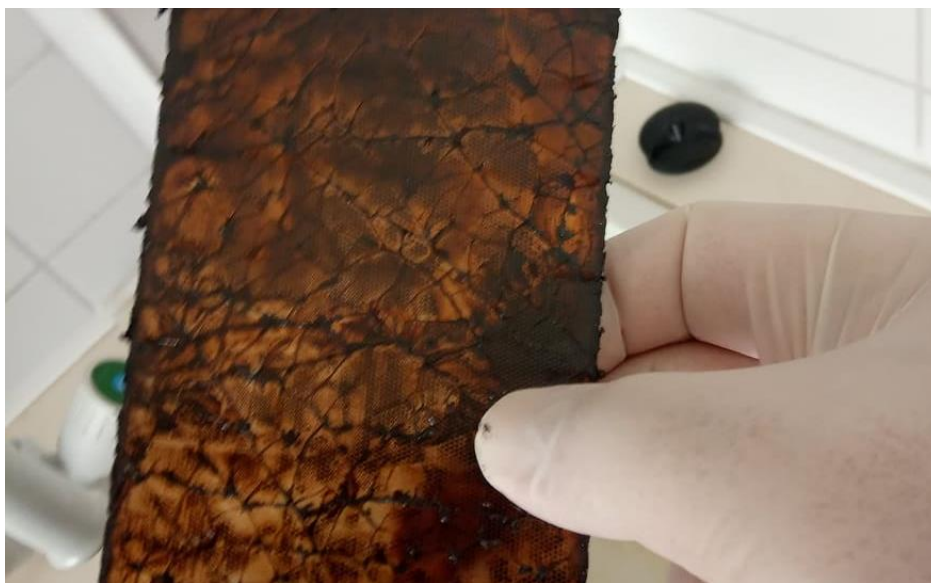


*Figure 2. Protective glass of solar module sample separated by degradation of ethylene vinyl acetate as a whole*

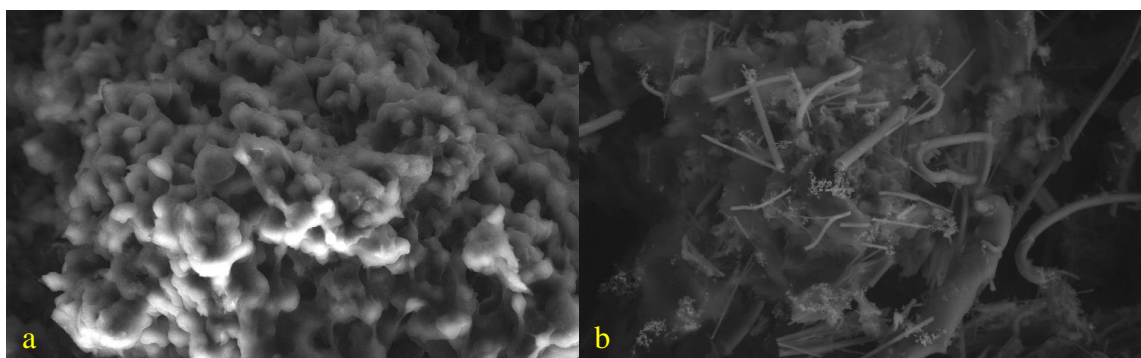


**Figure 3.** a) Detail of ethylene vinyl acetate melted during experiment under electron microscope b) Detail of ethylene vinyl acetate sublimated and condensated on the surface of module sample during experiment with nitrogen under electron microscope

### Conclusion

Our experiment confirmed that it is possible to utilize environmental degradation of ethylene vinyl acetate in process of solar module recycling. By exposition of this insulation layer, we are able to separate protective glass from the rest of the module. This reduces heating temperature applied from over 500 °C to 340 °C. Furthermore, this could lead to redundancy of mechanical processing of solar modules. In addition, by exposing solar module to ethylene vinyl acetate degrading temperature in nitrogen atmosphere can be used to reach same result with less exhaust fumes created. However, due to amount of nitrogen used to fill out space in which recycling takes place combined with high price of nitrogen gas, this proves to be costly alternative.

### Acknowledgments

This work financial support for a specific research project at the Brno University of Technology. FEKT-S-20-6206

### References

1. VANĚK, J.; MAULE, P.; JANDOVÁ, K. Development of Recycling of Photovoltaic Systems from the Point of View of Prolonging the Total Service Life of Photovoltaic Modules and Circular Energetic. In 21st International Conference on Advanced Batteries, Accumulators and Fuel Cells (ABAF 2020). ECS Transaction. 21. USA: ECS – The Electrochemical Society, 2020. s. 211-219. ISSN: 1938-6737.
2. STRACHALA, D.; HYLKÝ, J.; JANDOVÁ, K.; VANĚK, J. Mechanical Recycling of Photovoltaic Modules. In ECS Transaction. ECS Transactions. USA: ECS Transaction, 2017. s. 199-208. ISSN: 1938-5862.
3. STRACHALA, D.; HYLKÝ, J.; VANĚK, J.; FAFILEK, G.; JANDOVÁ, K. Methods for recycling photovoltaic modules and their impact on environment and raw material extraction. Acta Montanistica Slovaca, 2017, roč. 22, č. 3, s. 257-269. ISSN: 1335-1788.

## Numerical Simulation of Cathode Structure Influence on Lithium-Sulphur Battery Behaviour

M. Mačák<sup>a</sup>, K. Jaššo<sup>a</sup>, P. Vyroubal<sup>a</sup>, T. Kazda<sup>a</sup>, P. Čudek<sup>a</sup>

<sup>a</sup> Department of Electrical and Electronic Technology, Brno University of Technology, Brno 616 00, Czech Republic

This article investigates the influence of the size of sulphur clusters present in the cathode on the battery overall electrochemical behaviour. The properties of the cathode are studied by cyclic voltammetry simulations using a custom numerical model implemented into Ansys Fluent. The simulation is supplemented by experimental cyclic voltammetry measurements and images from a scanning electron microscope.

### Introduction

Lithium-sulphur (Li-S) batteries are one of the most favourable next generation technologies for energy storage systems. Classic lithium-ion batteries can only offer a specific capacity of around  $0.3 \text{ Ah}\cdot\text{g}^{-1}$ . Sulphur, which is one of the most abundant environmentally friendly elements on earth has a theoretical capacity of  $1.672 \text{ Ah}\cdot\text{g}^{-1}$  [1]. Additionally, it has a theoretical specific energy density of  $2600 \text{ Wh}\cdot\text{kg}^{-1}$  [2]. To supplement the profound experimental research, it is necessary to develop accurate numerical models. In contrast to the simple chemistry of intercalation reactions in Li-Ion batteries, the governing electrochemical reactions of Li-S batteries are very complex [3]. Voltametric investigation of the electrochemical behaviour of Li-S batteries is slightly complicated as there is a considerable difference between fundamental and application-oriented setups. Fundamental research usually uses inert planar electrodes and studies the influence of different electrolytes on the electrochemical mechanism [4]. On the other hand, the application-oriented research focuses on the behaviour of a real battery. In this case, the lithium electrode operates as a reference and counter electrode simultaneously [5]. This article presents a custom numerical model implemented into Ansys Fluent, which is used to investigate the influence of the sulphur clusters size on the electrochemical behaviour of the battery. Voltametric simulations were carried out to study the change of the response with a changing size and to find which sulphur clusters significantly influence the battery behaviour.

### Numerical model

The reaction mechanism used in this article is based on the widely accepted work of Kumaresan et al. [6], which consists of five step chain reactions accompanied by dissolution and precipitation. The main assumption for the geometry description was based on the work of Barnes et al. [7], which showed that a response of one hollow pore can represent the response of the whole porous electrode. The numerical model was made in a commercially available CFD software Ansys Fluent. The transport of species is defined by Nernst-Planck equations [6], which can be subsequently simplified to a diffusion equation [7]. The reaction kinetics are described by the Butler-Volmer reaction [6].

## Results

Presented simulations investigated the influence of sulphur cluster size on the electrode's electrochemical behaviour. To study the effects, series of voltametric simulations were carried out. To determine the dimensions of sulphur clusters and to create a reference point for the numerical results a test Li-S battery was assembled. Its properties were examined by a scanning electron microscope and a voltammetry measurement.

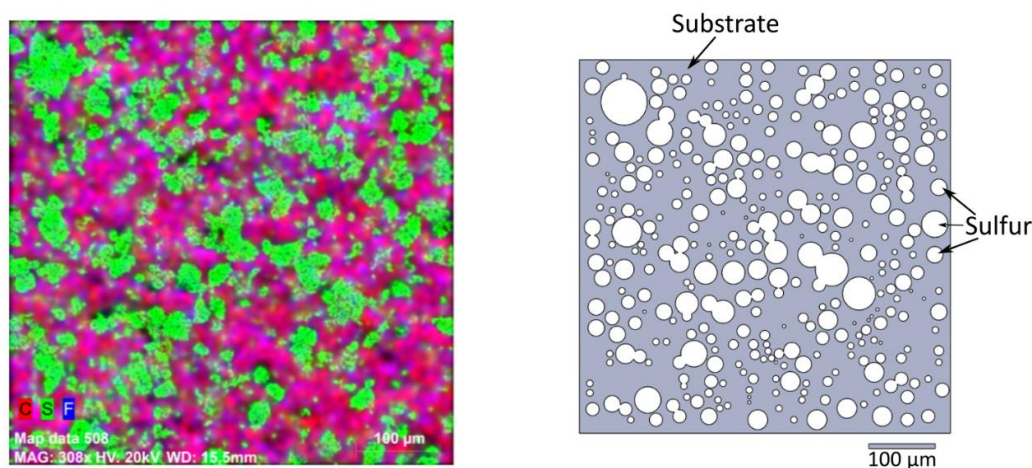


**Figure 1.** Surface of the electrode. Element distribution from X-Ray spectroscopy (left). Approximated surface for numerical simulations (right).

From the electron microscope images, a simplified geometry has been generated, in which the sulphur clusters were approximated with spheres of various diameters  $d$  ranging from 5  $\mu\text{m}$  to 70  $\mu\text{m}$ . The reaction parameters were initially assumed as in [6]. The scan rate was set to 0.1  $\text{mV}\cdot\text{s}^{-1}$ . The resulting voltammograms are shown in Figure 2.

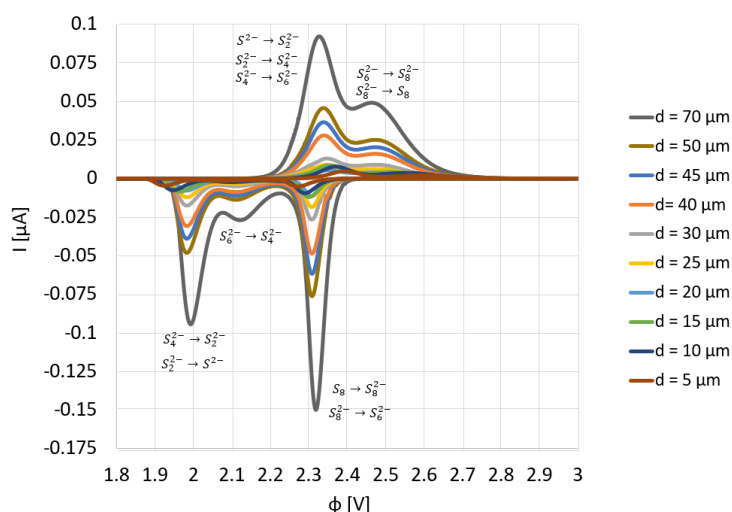


**Figure 2.** Simulated voltammograms for different particle sizes.

## Conclusions

The results presented in this work show that the custom numerical model is able to describe sulphur redox reactions in a Li-S battery. The obtained numerical results suggest that even a small change in a sulphur cluster size changes the voltametric response. The numerically obtained voltammogram was generally in agreement with the experimental measurement as it matched the general shape. However few differences emerged, such as visible reduction peak at 2.1 V, or shift of the peaks during the anodic scan towards more positive potentials. These differences can be caused by the reaction kinetic parameters, which were only assumed. Additionally, the diffusion of polysulfides outside of their initial cluster can be the reason for the differences. It would be then necessary to consider the diffusion between individual spheres in the numerical model.

## Acknowledgments

This work was supported by the BUT specific research program (project No. FEKT-S-20-6206).

## References

1. C. Arneson, Z. D. Wawrzyniakowski, J. T. Postlewaite, and Y. Ma. *The Journal of Physical Chemistry C*, **122**(16), pp. 8769-8779 (2018).
2. M. M. Islam, A. Ostadhossein, O. Borodin, A. T. Yeates, W. W. Tipton, R. G. Hennig, N. Kumar, and A. C. T. van Duin, *Physical Chemistry Chemical Physics*, **17**(5), pp. 3383-3393 (2015).
3. M. Cuisinier, C. Hart, M. Balasubramanian, A. Garsuch, and L. F. Nazar, *Advanced Energy Materials*, **5**(16) (2015).
4. M. Wild, L. O'Neill, T. Zhang, R. Purkayastha, G. Minton, M. Marinescu, and G. J. Offer, *Energy & Environmental Science*, **8**(12), pp. 3477-3494 (2015).
5. X. Huang, Z. Wang, R. Knibbe, B. Luo, S. A. Ahad, D. Sun, and L. Wang, *Energy Technology* (2019).
6. K. Kumaresan, Y. Mikhaylik, and R. E. White, *Journal of The Electrochemical Society*, **155**(8) (2008).
7. E. O. Barnes, X. Chen, P. Li, and R. G. Compton, *Journal of Electroanalytical Chemistry*, **720-721**, pp. 92-100 (2014).

## Photoassisted Electrodeposition of Cuprous Oxide Thin Films

Katharina Mairhofer<sup>1</sup>, Betina Kipper-Pires<sup>2</sup>, Günter Fafilek<sup>2</sup>

<sup>1</sup>KAI GmbH, Europastraße 8, AT-9524 Villach

<sup>2</sup>Vienna University of Technology, Institute of Chemical Technologies and Analytics,  
Getreidemarkt 9, AT-1060 Vienna

Well-defined cuprous oxide (Cu<sub>2</sub>O) thin films can be electrodeposited from an electrolyte containing copper (II) sulfate, lactic acid and sodium hydroxide [1] [2].

As Cu<sub>2</sub>O is a p-type semiconductor, due to Cu<sup>+</sup> vacancies in the material [3], the process can be accelerated through illumination with light of sufficient energy (> 2eV). The electrons created in the conduction band are driven to the electrode – electrolyte interface through external polarization, where they lead to the reduction of Cu<sup>2+</sup> ions in the solution. The resulting Cu<sup>+</sup> ions react with OH<sup>-</sup> ions according to [1]:



Cyclic voltammetry and transient potentiostatic measurements were performed in a three-electrode set-up with copper metalized wafers as a working electrode. Illumination was performed through the electrolyte, therefore absorption by the electrolyte also had to be taken into consideration.

Potentiostatic measurements with an LED as a light source with  $\lambda = 465$  nm have shown an increase in layer thickness of 3 times in comparison to depositions without additional illumination. The deposited films were investigated with SEM analysis.

### References

1. I. S. Brandt, M. A. Tumelero, S. Peligrini, G. Zangari und A. A. Pasa, „Electrodeposition of Cu<sub>2</sub>O: growth, properties, and applications,“ Journal of Solid State Electrochemistry, 2017.
2. K. Mairhofer und F. Günter , „Conditioning of Copper by Deposition of Cu<sub>2</sub>O Thin Films,“ Vienna, 2018.
3. Gmelin Handbuch der anorganischen Chemie, Kupfer. Teil D: Elektrische Eigenschaften der Kupferoxide., 8 Hrsg., Weinheim, Verlag Chemie, 1963.

## **Mathematical and Physical Analysis of the effect of conical and detached shock waves at the tip of a static probe in an experimental chamber**

P. Šabacká<sup>a</sup>, J. Maxa<sup>a</sup>, A. Maxová<sup>b</sup>,

<sup>a</sup> Department of Electrical and Electronic Technology, Brno University of Technology, Technická 10, 616 00 Brno, Czech Republic

<sup>b</sup> The St. Cyril and Methodius Comprehensive School and Pedagogical High School Brno

As part of the research in the field of pumping vacuum chambers in the Environmental Electron Microscope, research on supersonic flow through apertures is being carried out at the Department of Electrical and Electronic Technology of the Brno University of Technology in cooperation with the Institute of Scientific Instruments of the CAS. This paper deals with the influence of the shape of the static probe cone design for static pressure measurements in the supersonic flow regime in the Experimental Chamber. The cone of the probe has an effect on the shape of the shock wave, which significantly influences the detected static pressure value.

### **Introduction**

At the Department of Electrical and Electronic Technology of Brno University of Technology, in cooperation with ISI Brno, research on supersonic flow at low pressures is underway (1, 2, 3). The results are used in the design of vacuum chambers of the Environmental Electron Microscope (4, 5, 6). Within the research in the field of gas flow during the pumping of the chambers of the vacuum system, the principle of Pitot tube is used to measure the flow velocity. In Pitot tube, the total pressure is probed from the front of the tube and the static pressure is probed from the side. Since it is a supersonic flow velocity probing, a shock wave is generated at the probe head, which can form in two shapes, the detached shockwave or the cone wave, depending on the Mach number and the angle of the probe tip that is inserted into the flow (7). As a part of the preparatory work for the design of the Experimental chamber, the effect of shock waves on the values of the sensed pressure given by the probe for static pressure was analyzed.

### **Experimental chamber**

The current Experimental Chamber consists of two chambers separated by a small opening that simulates the condition created by differential pumping in an electron microscope.

Figure 1 shows a schematic of the given chambers P1 and P2 separated by the nozzle as it will be used for the calculation in Ansys Fluent. This calculation will be performed as 2D axisymmetric.

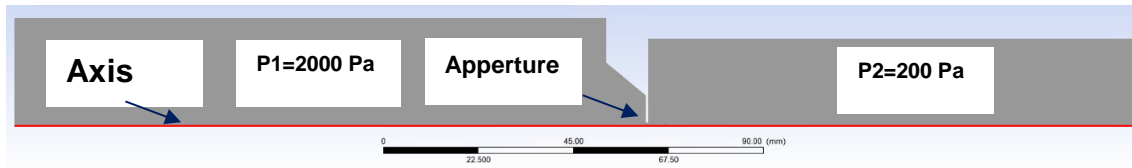


**Figure 1.** 2D axisymmetric model

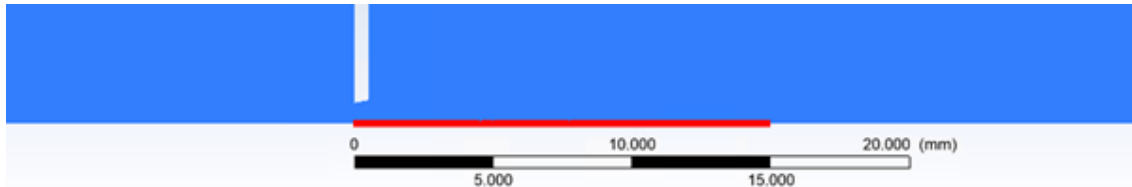


**Figure 2.** Path for Free variant

For the Free variant with no probe inserted (Figure 2), the pressure and Mach numbers were also plotted (Figure 3).

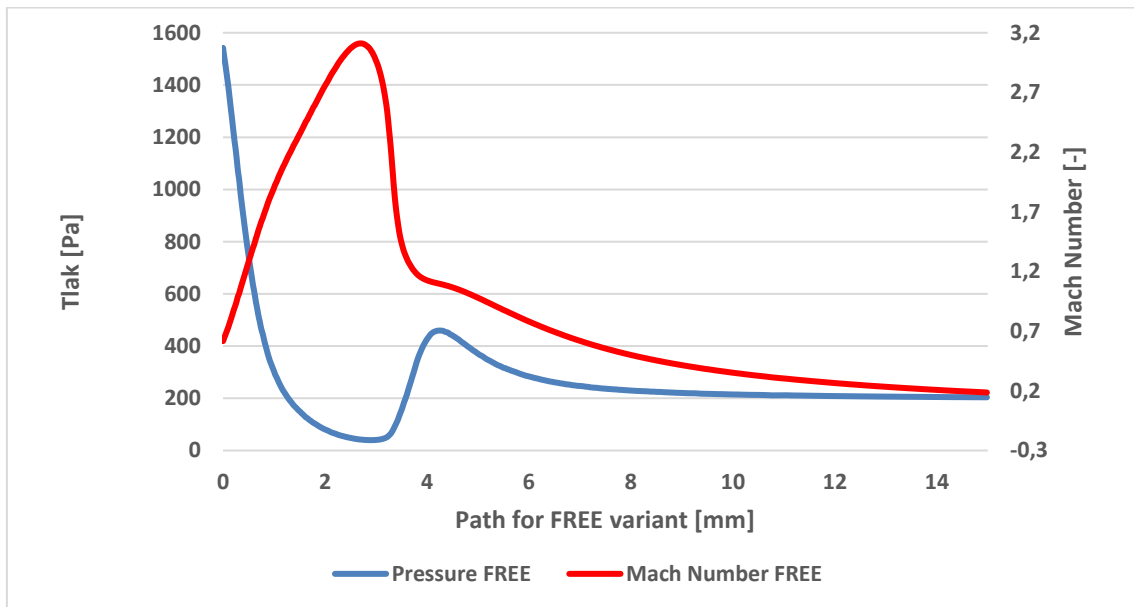


**Figure 3.** Pressure and Mach Number – Free variant

Subsequently, two variants were simulated where probes were inserted into the stream behind the nozzle, both within 1 mm of the narrowest point of the nozzle. At that point in the free stream the flow conditions are - Mach Number 1.9 and pressure 300 Pa.

## Results and Discussions

Under such conditions, the cylindrical shape is subject to shock wave detachment. The condition for ensuring a conical shock wave forming is to mount a cylindrical probe with a cone angle of maximum 39°. At a higher angle, the detached shock wave occurs (Figure 4).

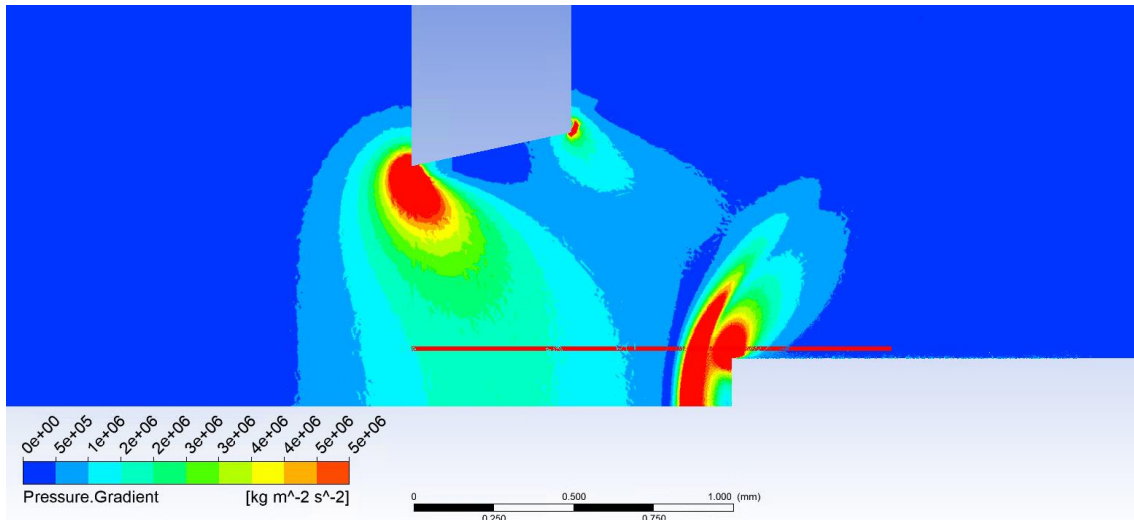


**Figure 4.** Cylinder variant – detached shockwave - Path

Figure 5 shows an example of a retracted cone probe with an angle of 8°, where the conical shock wave is forming at the tip.

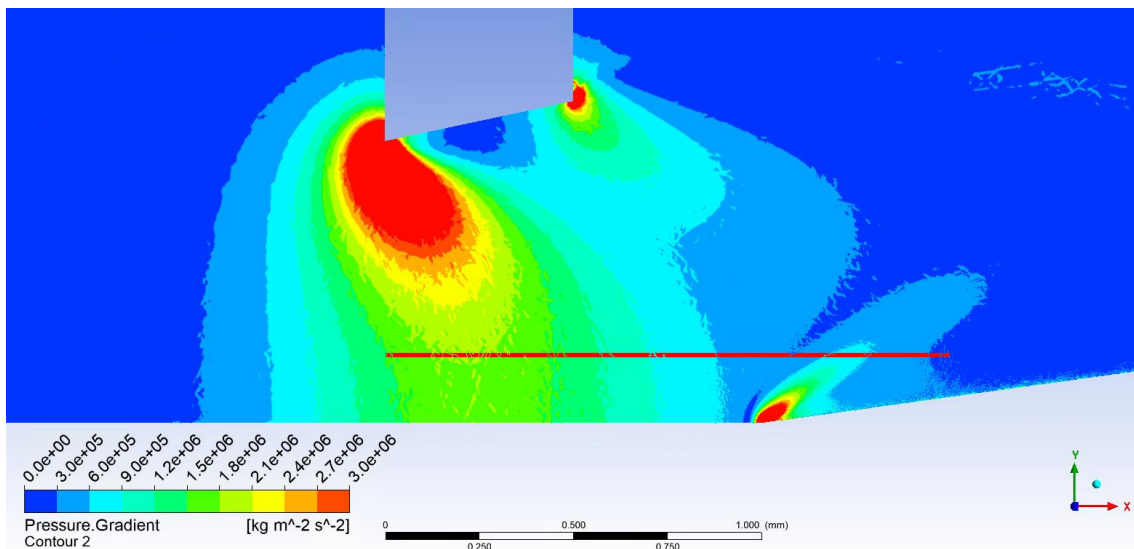


**Figure 5.** Cone variant – cone shockwave - Path

Fig. 6 shows a significant effect of the shape of the probe face. For the cylinder probe, the detached shock wave results in a significant pressure spike up to a threefold increase. Behind this shock wave, the state variables are affected.

A mathematical and physical analysis of the probe fitted with a cone of a size that ensures a conical shock wave shows that there is only a very slight increase in pressure at the point of the shock wave without any effect on the state variables behind the shock wave.

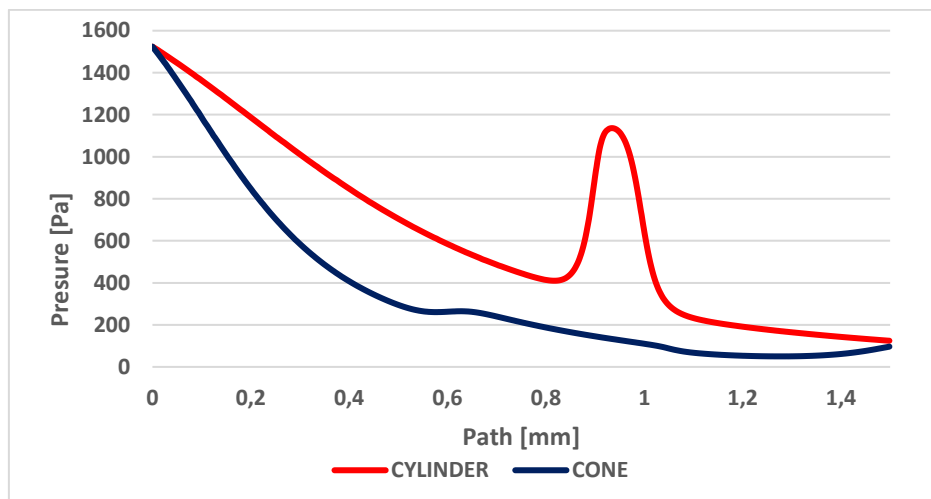


**Figure 6.** Pressure response during the shock wave penetration for both variants

### Acknowledgments

This research was supported by Brno University of Technology specific research program: Materials and technology for electrotechnics IV, reg. no. FEKT-S-20-6206.

### References

1. E. Tihlaříková, V. Neděla, and B. Dordevic, in In-situ preparation of plant samples in ESEM for energy dispersive x-ray microanalysis and repetitive observation in SEM and ESEM, *Scientific Reports*, 9(FEB), 2300. ISSN 2045-2322. doi: 10.1038/s41598-019-38835-w, (2019).
2. J. Maxa, V. Neděla, J. Jiráček, P. Vyroubal, and K. Hladká, in Analysis of gas flow in a secondary electron scintillation detector for ESEM with a new system of pressure limiting apertures, *Advances in Military Technology*, roč. 7, č. 2, s. 111-116. ISSN 1802-2308, (2012).
3. J. Maxa, M. Bílek, P. Hlavatá, P. Vyroubal, and K. Leptlová, in Comparisons Using Methods of Continuum Mechanics and Monte Carlo at Differentially Pumped Chamber, *Advances in Military Technology*, 11, n. 2, p. 143-150. ISSN: 1802-2308, (2016).
4. M. Bílek, J. Maxa, P. Hlavatá, and R. Bayer, in Modelling and simulation of a velocity field within supersonic flows in low-pressure areas, *ECS Transactions*, 81(1), pp. 311–316, (2017).
5. P. Hlavatá, J. Maxa, M. Bílek, and V. Neděla, in Impact of the shape of the differentially pumped chamber on critical flow character, *ECS Transactions*, 81(1), pp. 317–322, (2017).
6. P. Hlavatá, J. Maxa, M. Bílek, P. Vyroubal, and R. Bayer, in Influence of critical flow in the differentially pumped chamber AQUASEM, *Advances in Military Technology*, 12(2), pp. 301–310, (2017).
7. M. Daněk, in *Aerodynamika a mechanika letu*, VVLŠ SNP: Košice, Slovak republic, pp. 83, (1990).
8. A. Maxová, P. Šabacká, and J. MAXA, in Comparison of the Ansys Fluent system solvers for the possibility of supersonic flow solving at the low pressures, *ECS Transactions*, pp. 32-37, ISBN: 978-80-214-5109-4, (2019).
9. A. Maxová, J. Maxa, and P. Šabacká, in The Impact of Pumping Velocity on Temperature Running in Chambers of Experimental System, *ECS Transactions*, pp. 317-323, ISBN: 978-80-214-5109-4, ISSN: 1938-5862, (2021).

## Mathematical-physical analysis of Drag Force of a .223 REM caliber projectile

P. Šabacká<sup>a</sup>, J. Maxa<sup>a</sup>, F. Maxa<sup>b</sup>,

<sup>a</sup> Department of Electrical and Electronic Technology, Brno University of Technology, Technická 10, 616 00 Brno, Czech Republic

<sup>b</sup> The St. Cyril and Methodius Comprehensive School and Pedagogical High School Brno

This article deals with the mathematical and physical analysis of the drag force affecting a .223 REM projectile as a basis for further modification of the aerodynamic shape of the projectile by changing the perpendicular shock wave at the projectile tip into a conical one. For the analyses, the Institute's experience from the analysis of the supersonic flow generated during the pumping of the vacuum chambers of the electron microscope was used [1, 2, 3].

### Introduction

Because at the Institute of Electrical Engineering of the Brno University of Technology research is conducted in the field of gas flow during the pumping of the chambers of the vacuum system, part of which is the wrapping of the tips of the static probe of the Pitot tube at supersonic speed, the research has been extended to the field of external ballistics.

### External ballistics

The ballistic curve calculation is based on the total force acting on the projectile. This consists of two components:

$$F = F_g + F_{od} \quad (1)$$

; where  $F_g$  is the gravitational force vector and  $F_{od}$  is the vector of air resistance (Drag Force).

The following applies to the magnitude of these forces:

$$F_g = m \cdot g \quad (2)$$

$$F_{od} = \frac{1}{2} \cdot C \cdot S \cdot \rho \cdot v^2 \quad (3)$$

; where:  $m$  is the mass of the projectile,  $C$  is the drag coefficient,  $S$  is the cross-sectional area of the projectile,  $\rho$  is the air density and  $v$  is the velocity of the projectile.

The drag force of the air has a much greater effect on the projectile than the gravitational force. The drag force is not directly proportional to the velocity, but it does increase rapidly with the transition to supersonic velocity.

The first step was to compare the drag force for the 7.62 x 39 caliber (Figure 1) published in [4] with the results of the mathematical and physical analysis in Ansys Fluent [5].

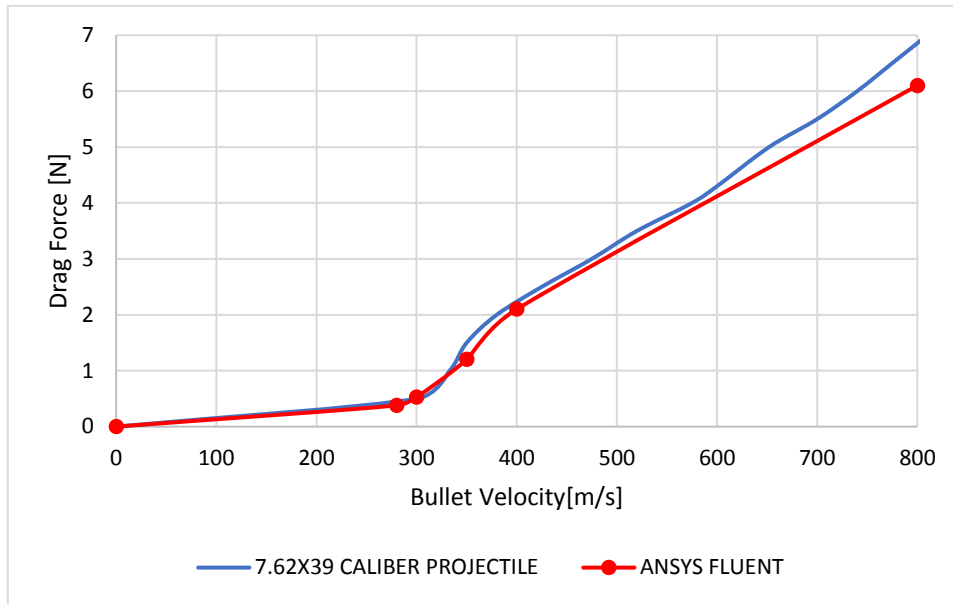


Figure 1. Drag Force  $F_{od}$  for 7.62 x 39

Table 1. Evaluation of the results of the dependence of the velocity on the drag force

Projectile velocity [m.s <sup>-1</sup> ]	Drag force [N]	
	Theoretical value	Ansys value
280	0.4	0.38
300	0.5	0.53
350	1.5	1.2
400	2.3	2.1
800	6.85	6.1

For the analyses, the shape of the bullet was modelled based on the data from Practical Thoughts About Transonic Bullet Stability and Accuracy [6] and subsequent analyses were performed in Ansys Fluent. A Density Based solver setup with an implicit formulation of the solution equations was chosen to handle the assumed high pressure gradients associated with supersonic flow.

Also, the Advection Upstream Splitting Method (AUSM) calculation scheme was used, which is more convenient for solving supersonic flow. A second-order discretization scheme was used for discretization.

The calculations were performed for the following projectile velocities: 280, 300, 350, 400, 800 m.s<sup>-1</sup>. The values were deliberately chosen mostly in the vicinity of the supersonic flow interface. The values came out very similar, or just slightly lower, which may indicate an idealized state.

### Caliber .223 Rem

Due to the agreement between the results obtained by Ansys Fluent and the experimental results, it was possible to use the debugged system settings for mathematical and physical analyses for other calibers. The chosen caliber was .223 Rem. The .223 Remington cartridge was developed in 1957 as an experimental military cartridge for the newly developed AR-15 assault rifle. The cartridge was designed by R. Hutton, and the rifle's designer was Eugene M. Stoner (1922-1997). The rifle was

tested with the new cartridge in 1960-61 in the US Air Force. As a result of the trials, it was adopted into the Army's armament in 1964 under the designation M 16 [8].

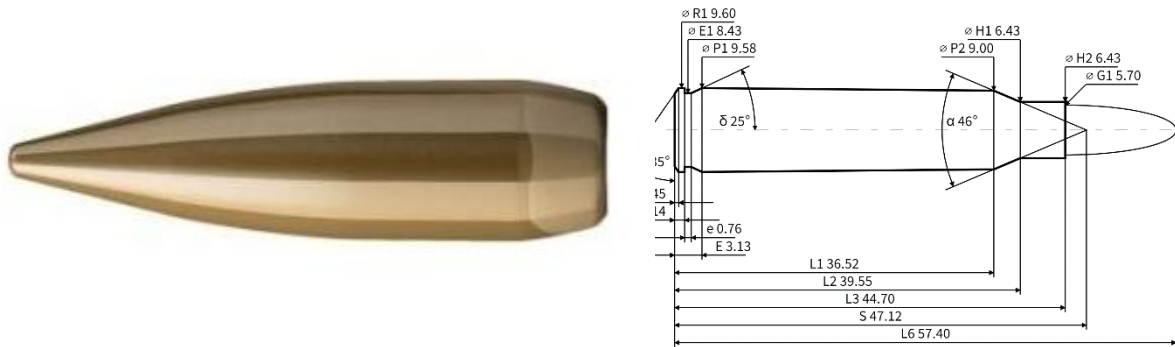


Figure 2. 223 REM caliber projectile [6, 7]

The same velocity range was chosen again for the analyses, taking into account the assumed increase in the drag force due to the exceeding of the speed of sound and the occurrence of a shock wave.

### Results and discussions

Comparison of the drag force for both calibers fulfilled the assumption that the .223 Rem caliber has a lower drag force due to its smaller cross-section. The cross-section of the 7.62x39 caliber bullet is 45.6 mm<sup>2</sup>, while that of the .223 Rem is 25.5 mm<sup>2</sup>. In this ratio, the drag force is proportionally lower.

Table 2. Evaluation of the results of velocity versus drag force for both calibers

Caliber velocity [m.s <sup>-1</sup> ]	Drag force [N]	
	Ansys value .223 Rem	Ansys value 7.62 x 39
280	0.1	0.38
300	0.12	0.53
350	0.76	1.2
400	1.1	2.1
800	3.3	6.1

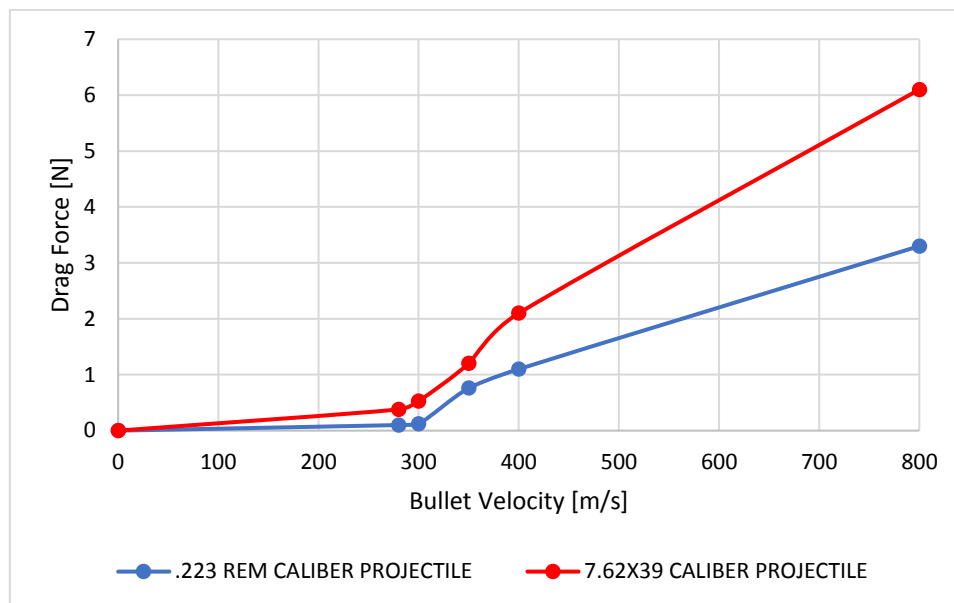


**Figure 3.** Comparison of drag force of 7.62x39 and 223 REM caliber projectile.

The graph in Fig. 3 shows, similarly to the 7.62x39 caliber, the .223 Rem has a dramatic increase in drag force in the area of supersonic velocity exceedance. Its increase is not as steep as that of the previous caliber of larger cross-section.

### Acknowledgments

This research was supported by Brno University of Technology specific research programme: Materials and technology pro electrotechnics IV, reg. no. FEKT-S-20-6206.

### References

1. Tihlaříková, Eva; Neděla, Vilém; Dordevic, B. In-situ preparation of plant samples in ESEM for energy dispersive x-ray microanalysis and repetitive observation in SEM and ESEM. *Scientific Reports*. 2019, 9(FEB), 2300. ISSN 2045-2322. doi: 10.1038/s41598-019-38835-w.
2. Maxa, Jiří; Neděla, Vilém; Jiráček, Josef.; Vyroubal, P.; Hladká, K. Analysis of gas flow in a secondary electron scintillation detector for ESEM with a new system of pressure limiting apertures. *Advances in Military Technology*. 2012, roč. 7, č. 2, s. 111-116. ISSN 1802-2308.
3. Maxa, J.; Bílek, M.; Hlavatá, P.; Vyroubal, P.; Lepltová, K. Comparisons Using Methods of Continuum Mechanics and Monte Carlo at Differentially Pumped Chamber. *Advances in Military Technology*, **2016**, 11, n. 2, p. 143-150. ISSN: 1802-2308.
4. Balistika. *Vnější balistika* [online]. Dostupné z: [http://www.balistika.cz/vnejsi\\_teorie.html](http://www.balistika.cz/vnejsi_teorie.html)
5. Maxa, F. ; *Tuning of the Ansys Fluent system for the analysis of supersonic flight of a 7.62x39 caliber projectile*, EECT 2021
6. Practical Thoughts About Transonic Bullet Stability and Accuracy. *Accurate Shooter* [online]. Dostupné z: <http://bulletin accurateshooter.com/tag/m118lr/?fbclid=IwAR1Bdiq6Uh7Vw760dFtOAFknyZkwz1PU4QOhrc9olRU6JDlu9FxBnbHRZWo>
7. *Zbraně Tobiášek* [online]. Dostupné také z: <https://zbranetobiasek.cz/strely-pro-prebijeni/2771-strela-223-rem-sb-fmj-36g-2903-8590690338221.html>
8. <https://www.zbrane.cz/strelivo/raze/223-remington>

## **A critical review of recent development of novel Li-ion battery cooling methods using phase change materials for fast charging application**

Amrit Kumar Thakur, Ravishankar Sathyamurthy

Department of Mechanical Engineering, KPR Institute of Engineering and Technology, Arasur, Coimbatore, Tamil Nadu 641407, India

With increasing population, tremendous industrial growth and escalating energy demands, there is excessive exploitation of fossil fuels resources. However, the usage of fossil fuels are adversely affecting the environment with increasing pollution and green house emission. In the view of reducing pollution and achieving net zero emissions, the electric vehicles (EVs) and hybrid electric vehicles (HEVs) are high energy efficient and environmental-friendly alternative, compared to the conventional internal combustion engine based vehicles. With the growing global demand of EVs, a growth rate of around 15 – 30 % in the market-share has been predicted from 2020 to 2030. In internal combustion engine based vehicles, the energy requisite to drive is achieved from burning of oils, however in the EVs, battery stored energy using power supplied in the idle conditions and later, this energy is used for powering the vehicle during normal working condition. EVs can save can save remarkable amount of the fossil fuel alongwith significant reducing in the emissions, leading to better environmental conditions. However the major concerns of the electric vehicle in further commercialization of this mode of transportations is long charging time for efficient operation and long-run. Therefore, battery must be designed in such a way to rapidly charge and make it more convenient for operation. The major limitations of battery during fast-charging is significant rise in battery temperature, leading to several adverse effect such as lithium plating, thermal runaway and may cause fire during the operation. In this view, the present work present a detailed analysis of battery thermal performance during fast charging conditions and summarize the suitable battery thermal management system (BTMS) for fast charging application.

Several cooling approaches such as air-cooling, liquid cooling and heat-pipes based cooling are widely used for BTMS, however every methods have merits and demerits. Air-based cooling are widely used by various automotive companies owing to their advantage regarding compact design and space, reliability during operational and lower maintenance and fabrication cost. However, due to poor thermal conductivity of air, this BTMS cooling capacity is limited and it is inadequate under high temperature working conditions and fast-charging mode. Phase change materials (PCMs) based cooling provide excellent temperature uniformity and limit the maximum temperature, however the absorber heat in PCM must be dissipated properly to the surrounding ambient for efficient battery operation for continuous long-term charging and discharging. Therefore, PCM cooling should be combined with other cooling mode such as air-cooling and liquid cooling using heat pipe to solve the aforementioned concerns without increasing the system weight and complexity. It is concluded from the critical review work that hybrid cooling methods including PCM with heat pipes are potential solution for maintaining the battery temperature during fast charging and provides the most optimal solutions for effective cooling under the severe ambient conditions such as extreme hot or cold climatic conditions.

## **Mathematical and Physical Analysis of Pressure Gradient in the Experimental Chamber for Subsequent Comparison with Optical Methods**

R. Bayer<sup>a</sup>

<sup>a</sup> Department of Electrical and Electronic Technology, Brno University of Technology, Technická 10, 616 00 Brno, Czech Republic

As a part of the research in the field of pumping vacuum chambers in the Environmental Electron Microscope, a research on supersonic flow through the Apertures is being carried out at the Department of Electrical and Electronic Technology of the Brno University of Technology in cooperation with the Institute of Scientific Instruments of the Czech Academy of Science. This paper deals with the possibility of investigating shock waves using the slit optical method, which allows to observe pressure gradients as the first derivation of pressure.

### **Introduction**

The paper describes the pumping process in the experimental chamber from atmospheric pressure to the operating ranges used in the Environmental Electron Microscope. During this pumping, the value of the pressure gradient, which is very significant during the development of supersonic flow over the aperture, was monitored. The results obtained from this mathematical and physical analysis will be compared with the experimental data obtained from the Experimental Chamber using the Schlieren method. The results are used in the design of the vacuum chambers of the Environmental Electron Microscope (1, 2, 3).

### **Schlieren Optical Method**

The Schlieren method is based on the bending of the light beam trajectory when passing through an inhomogeneous transparent object. Unlike the Shadowgraph method, a filter (optical knife) is used, which is implemented by inserting an aperture into the focal length of the imaging lens (Figure 1).

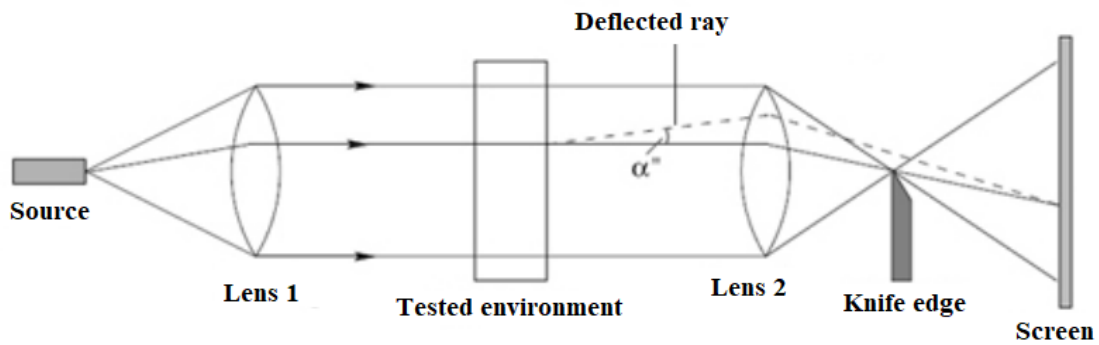


**Figure 1.** Schematic drawing of the Schlieren method

The resulting image of the Schlieren method represents the first derivation of the density of the screened medium.

Due to its simplicity and clarity, the Schlieren method is used to visualize heat transfer, momentum or flow of matter and will be used for experimental verification of the results of mathematical and physical analyses from Ansys Fluent.

### Experimental Chamber

The current experimental chamber consists of two chambers separated by a small aperture, as seen in Figure 2, which simulates the condition created by differential pumping in an electron microscope (4, 5, 6).

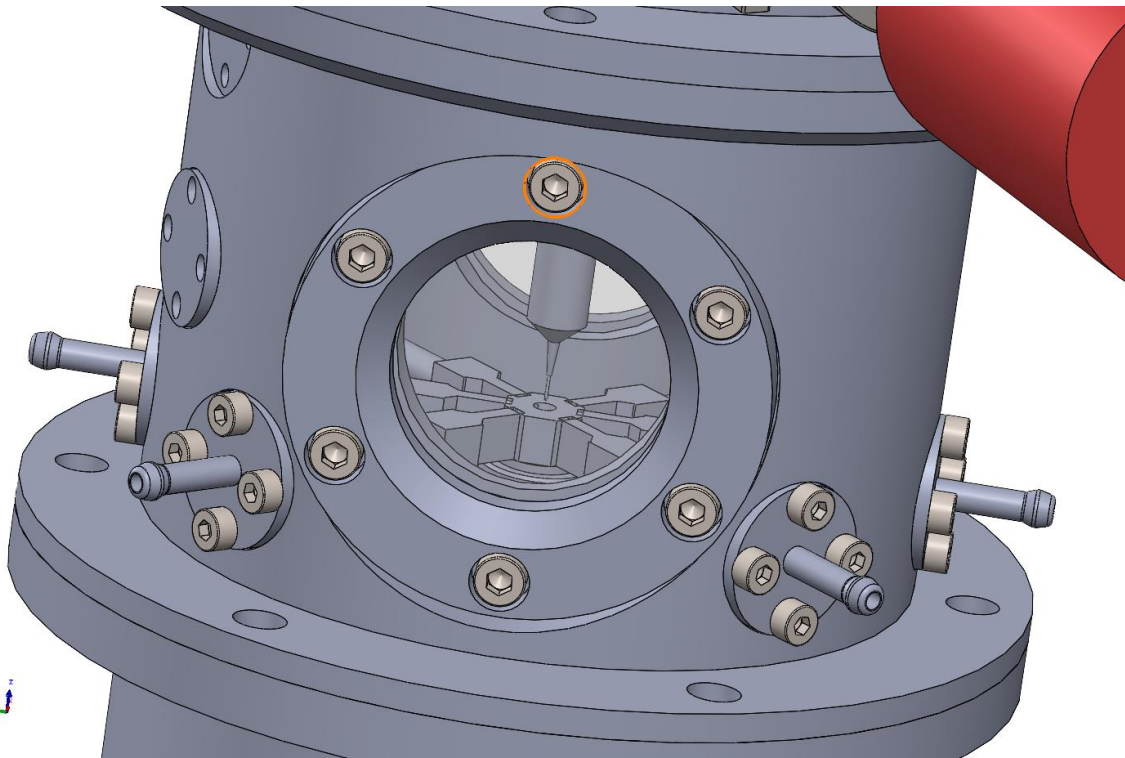


**Figure 2.** Experimental chamber concept

Figure 3 shows a schematic of the given chambers V1 with a volume of  $1.25 \times 10^6 \text{ mm}^3$  and V2 with a volume of  $1 \times 10^6 \text{ mm}^3$  separated by an Apperture with 2 mm diameter as used for the calculation in Ansys Fluent. This calculation was performed in Ansys Fluent as a time-varying 2D axisymmetric calculation (7, 8).

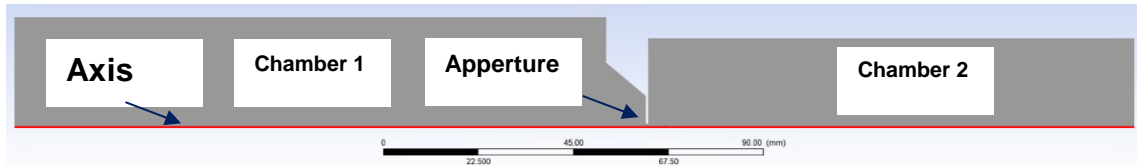
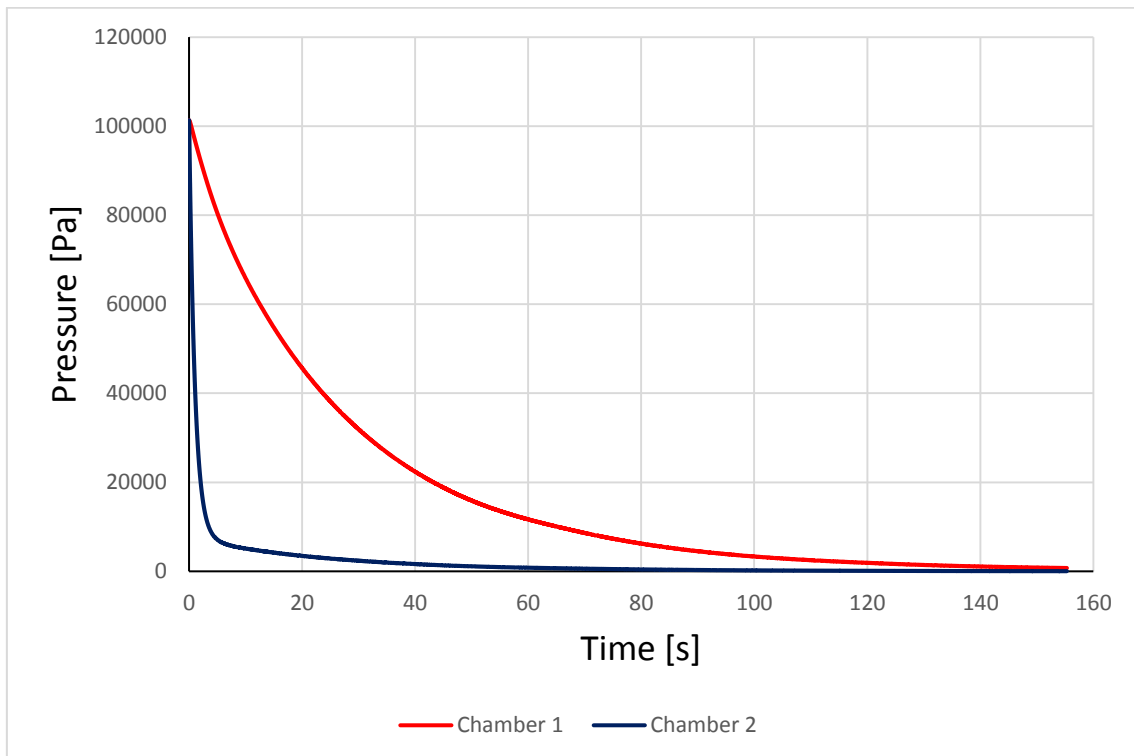


**Figure 3.** 2D axisymmetric model

The performance of the assumed Lavat RV 40/21 pump with a pumping rate of  $0.01 \text{ m}^3 \cdot \text{s}^{-1}$  was taken into account in the pumping simulation.

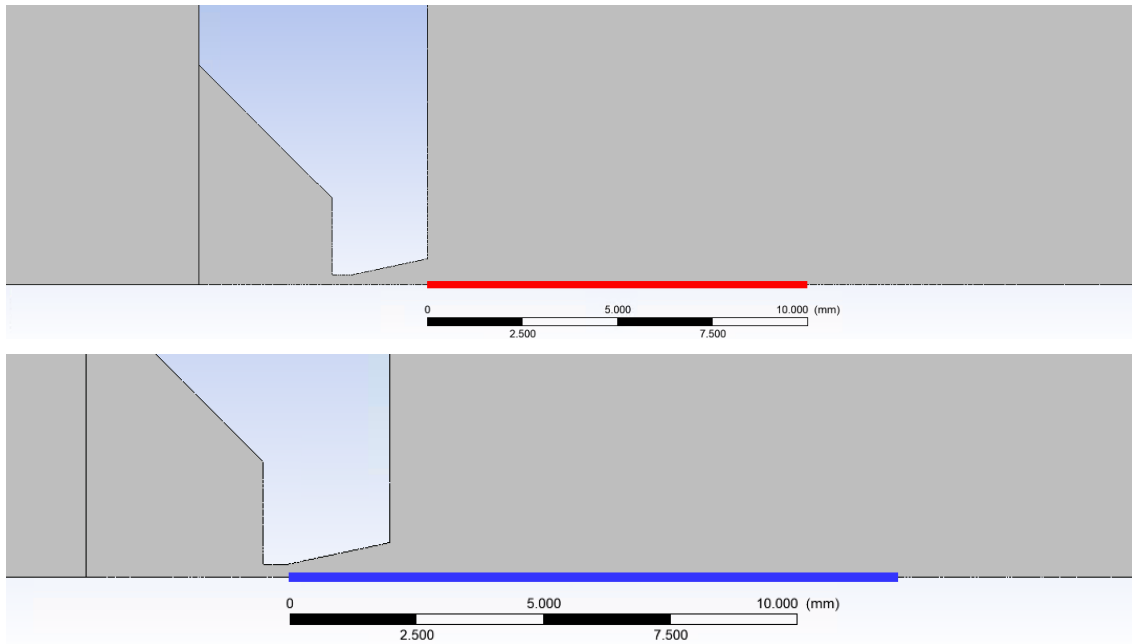
### Results and Discussions

Figure 4 shows the pressure development in both chambers during pumping. The assumed ratio of 2000 Pa in Chamber 1 and 70 Pa in Chamber 2, which is one of the possible scenarios for the ESEM operation and which will be investigated in the first step of the experiment, should be reached at 120 seconds of pumping. During the pumping, the behavior of the shock waves will be investigated using the Schlieren method.



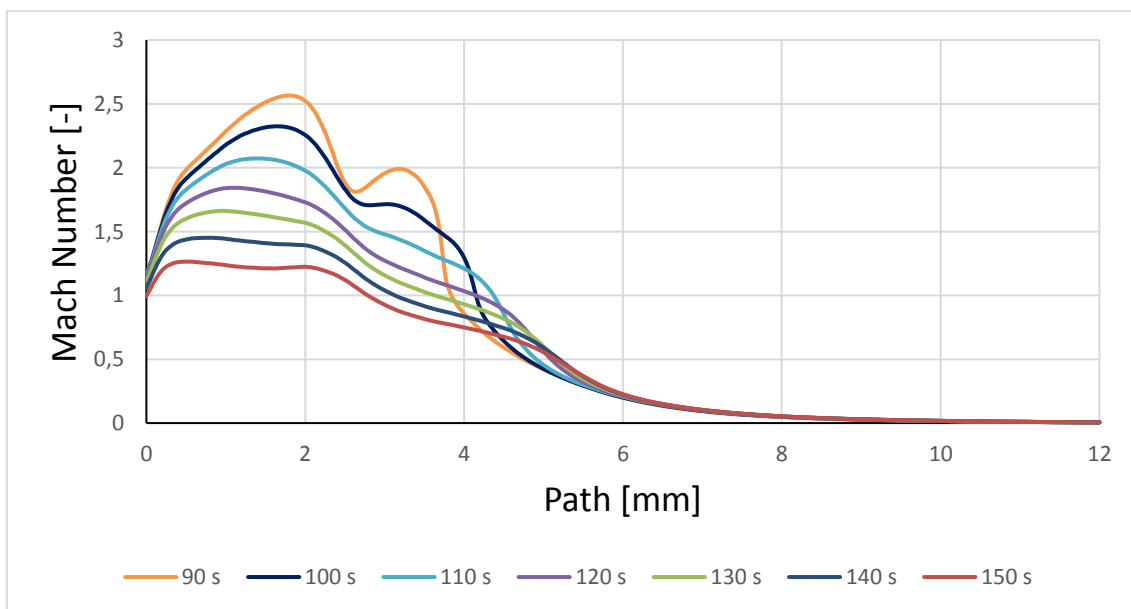
**Figure 4.** Pumping progress of vacuum chambers

Figure 5 shows the paths on the flow axis on which the pressure gradient and Mach number profiles were calculated.



**Figure 5.** Calculation paths for pressure gradient (red) and Mach Number (blue)

Mathematical and physical analyses show that due to the strong pumping power, high pressure ratios between the two chambers and supersonic flow in the aperture occur after only 0.2 s from the start of pumping. The highest velocity occurs at around 40 s, when it reaches a value of slightly over Mach 3. Thereafter, the pressure difference between the two chambers decreases due to pumping, and thus the Mach number gradually decreases (Figure 6).



**Figure 6.** Mach number evolution in selected times of pumping

The fluctuations in the values show the influence of the change in the position of the Mach disk and the second region of the supersonic flow, where pulsations occur during the Mach number drop in the time from 90 to 150 seconds.

The results obtained from this mathematical and physical analysis will be compared with the experimental data obtained from the Experimental Chamber using the Schlieren method.

### Acknowledgments

This research was supported by Brno University of Technology specific research program: Materials and technology for electrotechnics IV, reg. no. FEKT-S-20-6206.

### References

1. E. Tihlaříková, V. Neděla, and B. Dordevic, in *In-situ preparation of plant samples in ESEM for energy dispersive x-ray microanalysis and repetitive observation in SEM and ESEM*, Scientific Reports, 9(FEB), 2300. ISSN 2045-2322. doi: 10.1038/s41598-019-38835-w, (2019).
2. J. Maxa, V. Neděla, J. Jiráček, P. Vyroubal, and K. Hladká, in *Analysis of gas flow in a secondary electron scintillation detector for ESEM with a new system of pressure limiting apertures*, Advances in Military Technology, roč. 7, č. 2, s. 111-116. ISSN 1802-2308, (2012).
3. J. Maxa, M. Bílek, P. Hlavatá, P. Vyroubal, and K. Leptová, in *Comparisons Using Methods of Continuum Mechanics and Monte Carlo at Differentially Pumped Chamber*, Advances in Military Technology, 11, n. 2, p. 143-150. ISSN: 1802-2308, (2016).
4. M. Bílek, J. Maxa, P. Hlavatá, and R. Bayer, in *Modelling and simulation of a velocity field within supersonic flows in low-pressure areas*, ECS Transactions, 81(1), pp. 311–316, (2017).
5. P. Hlavatá, J. Maxa, M. Bílek, and V. Neděla, in *Impact of the shape of the differentially pumped chamber on critical flow character*, ECS Transactions, 81(1), pp. 317–322, (2017).
6. P. Hlavatá, J. Maxa, M. Bílek, P. Vyroubal, and R. Bayer, in *Influence of critical flow in the differentially pumped chamber AQUASEM*, Advances in Military Technology, 12(2), pp. 301–310, (2017).
7. A. Maxová, P. Šabacká, and J. MAXA, in *Comparison of the Ansys Fluent system solvers for the possibility of supersonic flow solving at the low pressures*, ECS Transactions, pp. 32-37, ISBN: 978-80-214-5109-4, (2019).
8. A. Maxová, J. Maxa, and P. Šabacká, in *The Impact of Pumping Velocity on Temperature Running in Chambers of Experimental System*, ECS Transactions, pp. 317-323, ISBN: 978-80-214-5109-4, ISSN: 1938-5862, (2021).

## Use of Cold Kinetic Deposition Technology on Materials Used in Electrical Engineering

T. Binar<sup>a</sup>, J. Zimáková<sup>a</sup>, M. Šustr<sup>b</sup>, L. Řehořek<sup>c</sup>, M. Sámel<sup>a</sup>, M. Sedlaříková<sup>a</sup>

<sup>a</sup> Brno University of Technology, Technická 10, 616 00 Brno, Czech Republic

<sup>b</sup> Mendel University in Brno, Zemědělská 1, 613 00 Brno, Czech Republic

<sup>c</sup> Brno University of Technology, Faculty of Mechanical Engineering, Technická 2896/2, Brno 616 69

For the experiment described in this work, a sample with a coating of copper was created on an aluminum substrate by the cold spray method. Subsequently, this sample was split for corrosion tests, where the split samples were exposed to a corrosive environment for different exposure times. The extent of corrosion degradation of the samples was evaluated by acoustic emission and metallographic analysis for corrosion-loaded samples for 100, 200 and 300 hours. Finally, an illustrative design of the application of cold spray technology was created.

### Introduction

The progressive method of cold kinetic coating (from English for short "cold spray") has become a topic of increased interest in recent years, especially in the electrical and mechanical engineering industries. This is a method of applying coatings by accelerating particles of a deposited powder to a substrate material, wherein the temperature of the gas by which the powder particles are accelerated does not exceed the melting point of the particles and thus the particles do not undergo a phase change. The particles are adhered to the surface of the substrate due to high plastic deformation, which together with the invariability of the phase phase offers a number of advantages over conventional thermal coating methods. Thanks to the cold spray method, the microstructure of the applied coating is minimally modified, the coating achieves a high density and low porosity, low oxidation of the coating occurs and this results in high corrosion resistance. The resulting coating also has excellent electrical and thermal conductivity.

Acoustic emission is a non-destructive passive method that uses a physical phenomenon to observe acoustic signals emitted by a mechanically or thermally stressed body, and it is also a diagnostic method based on this phenomenon. Already in the past, the so-called tapping on this body (for example, brick, ceramic, wood, etc ...) and based on the body's response to this strike, we were able to detect a possible change in the body's own frequency, thanks to which we were able to determine a hidden problem in the body. Today's acoustic testing methods are no longer subjectively evaluated, but are based on precise measurement procedures (in terms of signal excitation and detection). [1], [2], [3]

In a study by P. Dostál and his team, acoustic emission was used to investigate the corrosion and fatigue parameters of aluminum alloys and the formation of corrosion cracks under cyclic loading in a salt chamber for 21 days. Corrosion degradation was visualized and studied in real time by acoustic emission, and the results of this research pointed to the formation of pitting and intergranular corrosion in aluminum alloys, which led to cracks in the material. These microcracks lead to a

deterioration of the properties of the materials and can even lead to the complete destruction of the material and deterioration, when the material can break. Thanks to the use of this method in real time, it is possible to predict the behavior of the material in a corrosive environment (in relation to real conditions), it is possible to prevent corrosive degradation of the material and thus increase its life cycle. This fact helps to increase the safety of machines and processes where these materials are used, and thanks to this method it is possible to prevent accidents and incidents. [4]

### Production of experimental samples

An aluminum plate measuring 120 x 100 mm (width x height) and 3 mm in diameter was used as the substrate material. Subsequently, we deposited a layer of copper using this method of cold spray on this substrate. The cold spray device used is from Impact Innovations GmbH, in particular the Impact Cold Spray System 5/11 (shown in Figure 1). This device works with a maximum operating temperature in the gas heater up to 1100 ° C, the maximum operating pressure of this device is 5 MPa and the heating power reaches up to 40kW.



**Figure 1.** Impact Cold spray system 5/11

The powder selected for coating the aluminum substrate is from Safina a.s. and is 99.9% copper batches Cu5760517 and Cu3530916 (mixture of two identical powders), with a powder particle size in the range of 38-75  $\mu\text{m}$ . Nitrogen was chosen as the accelerating gas, which is more commonly used commercially, mainly due to its cost relative to helium. In the gas heater, this gas reached a temperature of up to 450 ° C and operated in the system under a pressure of 2.5 MPa. The powder particles accelerated by this gas reached a velocity of about 350 m / s, which leads to plastic deformation of these particles on the substrate surface and their excellent bonding to the substrate interface, because the critical velocity of copper with oxygen content 0.01% of total weight is about 327 m / s. s (also depends on particle size). The estimated deposition efficiency is therefore very high, also due to the fact that the angle of incidence of the particles was close to 80 °. The layer of copper coating thus applied by cold spray has a diameter of 0.5 mm. [5], [6]

Due to further experiments, it was necessary to divide the sample into 4 smaller samples. Since the sample was 120 x 100 mm (width x height), we decided to divide the samples into 4 smaller ones, each measuring 50 x 50 mm. The LECO MSX250A2 was used to divide the sample. It is a dividing device ideal for obtaining medium-sized profiles.

## Corrosion tests

Corrosion tests were performed in accordance with ČSN ISO 9227. For the given tests we used samples marked with numbers 1, 3 and 4. Sample 1 was exposed to the corrosive environment in this chamber for 100 hours, sample 3 for 200 hours and sample 4 for 300 hours. A salt-like corrosion medium (NaCl atmosphere) with a concentration of  $50 \pm 5$  g / l of distilled water was used for the accelerated corrosion tests. The density of the solution at this concentration and temperature of 25 ° C is 1.0225 to 1.0400 g / cm<sup>3</sup>. Corrosion tests were performed at 35 ° C

### Analysis of corrosion attack by acoustic emission

The diagnostic acoustic emission (AE) method was used to analyze the samples made by us exposed to accelerated corrosion conditions. The aim of this method was to monitor and subsequently analyze the degradation effect of corrosion on the application of a layer of copper by cold spray on an aluminum substrate. Piezoelectric sensors MTR-15 were used to measure AE.

The set of used AE system consisted of:

- 3x piezoelectric sensor
- 3x 35 dB preamplifier
- Sensor extension wiring
- 6-channel DAKEL Xedo Diagnostic System
- Notebook (connection to Xedo device with LAN cable)

The universal measuring and diagnostic device DAKEL XEDO from the company ZD Rpety-Dakel is widely used in the measurement of physical quantities. Up to several dozen measuring modules can be connected to this device via a computer and thus centrally monitor the status of the measured samples and is ideal for data processing during AE measurement. After connecting a piezoelectric AE sensor, we are able to measure basic parameters such as Counts. The Count value is an expression of the number of detected signals (overshoots) that have exceeded the specified detection threshold during corrosion attack analysis. With this device it is possible to process emission events with the possibility of their localization and direct digital sampling of emission signals. [7]

The Figure 2 shows the course of recording the acoustic emission during the experiment.

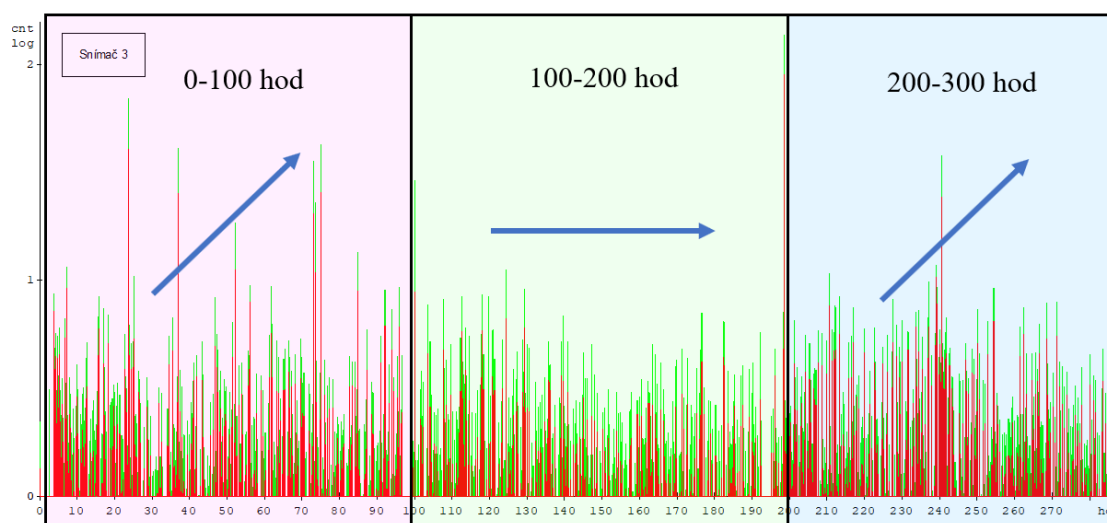


**Figure 2.** Graph representing the course of corrosion attack of test sample 4 over a period of 300 hours. Arrows represent an increase or stagnation of corrosion degradation.

## Conclusion

After exposing the samples to a corrosive environment, we monitored the progress of corrosion degradation using acoustic emission.

- After exposing the sample to a corrosive environment for 100 hours, it is possible to observe the rapid onset of galvanic corrosion. In this sample, initial cavitation occurs in the form of pitting corrosion. Furthermore, this sample is passivated by a copper coating.
- When the sample is corroded for 200 hours in a salt chamber, the corrosion course is less acoustically pronounced and is in the attenuation phase.
- The most acoustically significant is the exposure time to the corrosive environment of 200 - 300 hours, and this time appears to be the most critical for the studied material of copper spray coating on aluminum substrate, there is expansion and new formation of pitting corrosion, which leads to cracking in the materials.

## Acknowledgements

The publication was created within the project of specific research at BUT (No. FEKT-S-20-6206).

## References

1. SUSTR, Michal, Jaroslav ZACAL, Peter DOSTAL, Oldrich CERNY, Miroslav PRISTAVKA, David DOBROCKY, Stefan GASPAR a Jan PASKO. Acoustic Emission of Corroded Weldments During Tensile Test. *Management Systems in Production Engineering* [online]. 2019, 27(4), 211-216 [cit. 2021-04-30]. ISSN 2450-5781. Available at: doi:10.1515/mspe-2019-0033
2. ZAČAL, Jaroslav, Petr DOSTÁL, Michal ŠUSTR a David DOBROCKÝ. Acoustic Emission During Tensile Testing of Composite Materials. *Acta Universitatis Agriculturae et Silviculturae Mendelianae Brunensis* [online]. 2017, 65(4), 1309-1315 [cit. 2021-04-26]. ISSN 12118516. Available at: doi:10.11118/actaun201765041309
3. ZAČAL, Jaroslav, Petr DOSTÁL a Michal ŠUSTR. Acoustic Emission with Testing the Pressure Resistance and Structural Integrity in Mineral Feeds. *Acta Technologica Agriculturae* [online]. 2015, 18(4), 122-125 [cit. 2021-04-26]. ISSN 1338-5267. Available at: doi:10.1515/ata-2015-0024
4. DOSTÁL, Petr, Michal ČERNÝ, Jaroslav LEV a David VARNER. Proportional monitoring of the acoustic emission in crypto-conditions. *Acta Universitatis Agriculturae et Silviculturae Mendelianae Brunensis* [online]. 2014, 59(5), 31-38 [cit. 2021-04-26]. ISSN 12118516. Available at: doi:10.11118/actaun201159050031
5. Cold Spraying. In: *Impact-innovations.com*. [online]. [cit. 2021-05-20]. Available at: <https://impact-innovations.com/en/portfolio-item/impact-spray-system-5-11/>
6. LI, Chang-Jiu, Wen-Ya LI a Hanlin LIAO. Examination of the Critical Velocity for Deposition of Particles in Cold Spraying. *Journal of Thermal Spray Technology* [online]. 2006, 15(2), 212-222 [cit. 2021-5-1]. ISSN 10599630. Available at: doi:10.1361/105996306X108093
7. KEKYRAS, S., C., WILCOX, S., J., BORTHWICK, W., D., K., REUBEN, R., L. Acoustic Emission monitoring of Turning Operations using PVdF Film and PZT Sensors. AEWG 35. Boston 1991, p. 72 – 79

## Power Supplies For Variable Traffic Signs

T. Binar<sup>a</sup>, J. Zimáková<sup>a</sup>, P. Bača<sup>a</sup>, J. Fridrich<sup>a</sup>, M. Sedlaříková<sup>a</sup>

<sup>a</sup> Brno University of Technology, Technická 10, 616 00 Brno, Czech Republic

This paper describes the design of mobile power sets for variable traffic signs for the use of energy storage in lead-acid battery. The supply point is intended primarily for use in powering traffic lights and mobile variable traffic signs for line traffic control. At the same time, it should allow the short-term connection of other devices, such as electric hand tools, with a maximum power input of several hundred watts.

### Introduction

Mobile line traffic control is used on traffic closures as part of road repairs, mainly on motorway sections. It serves to increase the flow of traffic with the restrictions necessary to make repairs. To inform drivers, variable traffic signs (VTS) are used with an LED display matrix measuring approximately 1 m × 1 m, on which traffic signs and information texts are displayed according to current needs. Each controlled restriction consists of several sections, spaced approximately one kilometer apart, in which the VTS are located on both sides of the road. On motorways, 8-10 VTSs are usually used within one restriction. Due to the unavailability of mains power, VTS are powered by lead-acid batteries with a voltage of 12 VDC. The used accumulators are in the VRLA design and their capacity is mostly 200 Ah, while 1-2 pieces of these accumulators are used for each VTS [1]. Each battery is housed in a sheet steel case with bushings for supply cables. The embodiment of the housing is illustrated in Figure 1

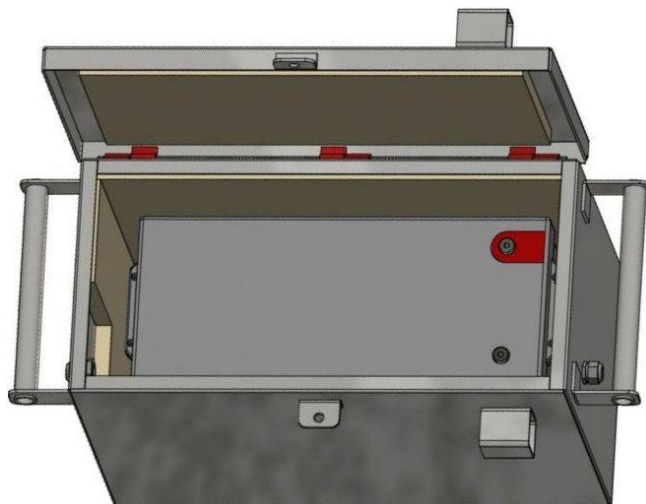


**Figure 1.** Current battery container

The power consumption of the VTS depends on the specific displayed symbol, and due to the used automatic brightness control also on the level of ambient light, usually in the range of about 10-100 W. This means that one battery will be completely discharged in the range of 1-10 days, in reality it is a maximum of 2-3 days, because the mark shines for much of the day at maximum brightness.

Before battery discharging, a service intervention is required, during which a charged battery is transported to the site, replaced and the discharged piece is removed for recharging. The depth of discharge affects the service life of the accumulators [1], therefore their replacement is carried out in practice before complete discharge, which further increases the frequency of necessary trips. In reality, the depth of discharge reaches a value of approximately 80%, so the batteries can handle a maximum of several hundred charging cycles. Then there is a decrease in their capacity and thus also the time for which they are able to supply the connected equipment, which results in a further increase in the frequency of service trips.

For economic reasons, the batteries of all VTS are always changed on departure, regardless of the current state of charge. Due to the relatively long driving distances, which are often over 100 km, the operation of the equipment is financially very expensive, and for the customer, renting such equipment is a significant impact on the budget.

Another problem is the construction of the battery containers themselves, into which the cabling opens through the cable glands and is firmly connected to the batteries.

The replacement of the battery itself thus has a significant effect on the time required and increases the operating costs of the device.

Another problem is the whole agenda with charging the batteries, and with their constant transport to the place of need and back. To ensure continuous operation of the VTS, two sets of batteries are needed, one of which is always in operation and the other is charged.

Last but not least, it is necessary to mention the ecological aspects of the operation of the facility in the current regime. It creates a relatively large amount of worn-out batteries, which are no longer sufficient for their capacity to reasonably economically operate VTS, however, they are not yet completely functional. Although the recycling of lead-acid batteries is now very well managed, a certain proportion of non-recyclable residues is necessarily generated. Other environmental impacts result from the operation of vehicles, which are used to ensure the logistics of battery replacement. The operation of the facility in the current regime is economically and ecologically unbearable for a long time and it is necessary to start solving the situation. For optimal design, it is necessary to know the real consumption of VTS. Without this information, it is not possible to properly dimension the alternative method of power supply and optimize the costs of acquisition and operation.

Within this work it was performed long-term measurement of VTS consumption, including the time distribution of consumption.

### **Proposed solutions**

The use of renewable energy sources is directly offered to reduce service interventions to the necessary extent. With regard to the field of application, the only possibility seems to be the use of solar radiation and its direct conversion into electricity using photovoltaic panels. The following requirements have been set for the proposal:

- mobile devices, easy to transport,
- installation without special landscaping,
- light but stable construction that withstands weather conditions and dynamic shocks of air pressure from passing vehicles,
- dimensionally allow to be installed between the barriers in the center lane on the highway,
- maximum usability of existing technology.

The accumulators will use the existing lead, the used constructions will have a hot-dip galvanized surface treatment, or a paint with the color RAL 7042 - traffic gray.

### Power required

As already mentioned, the current consumption of the VTS varies depending on the ambient conditions and the type of symbol displayed, so that an accurate calculation of consumption is practically impossible. However, long-term operational experience shows that the average daily consumption is around 1 kWh. Currently, the aim is not to ensure completely autonomous operation only with the use of sunlight. To maintain a reasonably small built-up area, only two monocrystalline panels, each with a power of 325Wp, were used for initial testing.

### Backup power

In order to ensure a certain autonomy of operation, the set was supplemented with a backup energy source, which consists of a DMFC fuel cell. The aim was to test the possibilities and properties of the fuel cell and to gain experience from operation. An EFOY Pro 2400 fuel cell weighing 9 kg and measuring 433 mm × 188 mm × 278 mm was used for testing. The cell manufacturer promises the least life 4500 hours of operation, power 110 W and fuel consumption approximately 0.9 l / kWh, operating temperature range -20 °C to +50 °C. During the guaranteed period of operation, the power should not fall below 80 W [2]. At the end of its service life, the cell can be refurbished and operated again.

### Mobile set design

The overall assembly consists of the following parts:

- photovoltaic panel including mounting structure,
- battery container with electrical equipment,
- fuel cell container.

Figure 2 shows a block diagram of the connection of the assembly.

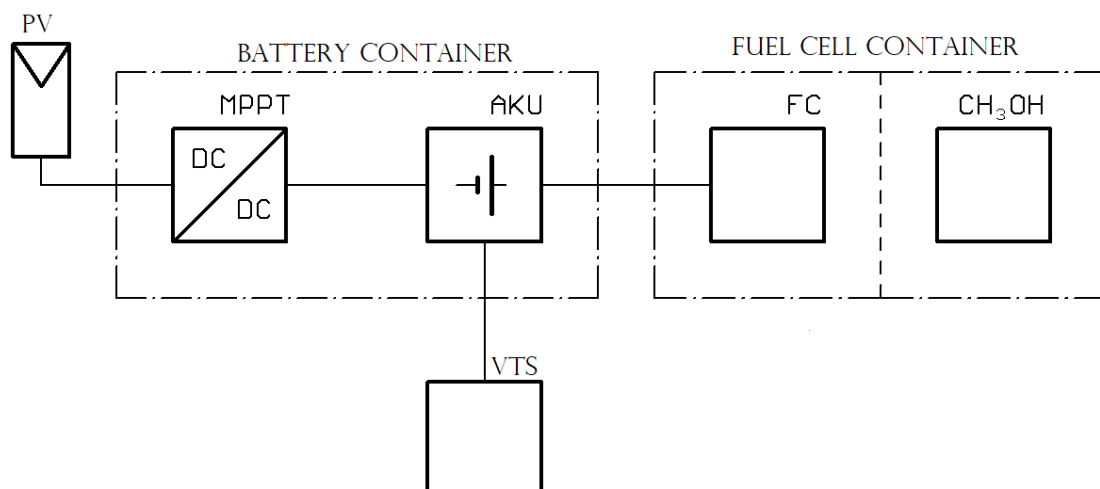


**Figure 2.** Block diagram of a mobile set; PV – photovoltaic panel, MPPT - solar charge controller, AKU – accumulator, VTS – variable traffic light, FC – fuel cell, CH<sub>3</sub>OH – methanol

To secure against theft, eyelets for welding the hardened chain are welded on all parts of the assembly. The whole assembly is locked with a security padlock.

### Conclusion

In this work, it was designed a mobile set to be used to power variable traffic signs using renewable energy sources. Due to the target, attention was paid mainly to the use of energy from photovoltaics. The way in which VTS are currently powered is unsatisfactory and solar power supply is directly offered as a suitable alternative.

The proposed set consists of three parts, namely photovoltaic panel, battery and fuel cell containers.

Complete production documentation was created for all parts of the set, numbering more than a hundred drawings. According to this documentation, a test sample was produced, which verified that the documentation was usable for introduction into production.

Measurements on the test set continue in order to compile sampling diagrams for the entire year. For now, data are only available from January to May. Further attempts will also be made to use a polycrystalline PV panel instead of an existing monocrystalline one.

### Acknowledgements

The publication was created within the project of specific research at BUT (No. FEKT-S-20-6206).

### References

1. *Reserve Power. SPB Batteries*. [online]. Systems Sunlight S.A., [b.r.], [cit. 15. 4. 2021]. Available at URL: <[https://www.systems-sunlight.com/wp-content/uploads/2019/09/sunlight\\_spb\\_12pages\\_210x295\\_final\\_web\\_mones.pdf](https://www.systems-sunlight.com/wp-content/uploads/2019/09/sunlight_spb_12pages_210x295_final_web_mones.pdf)>.
2. *EFOY Pro - Operation and installation Manual*. [online]. SFC Energy A.G., ©2019, [cit. 17. 4. 2021]. Available at URL: <<https://www.efoy-pro.com/wp-content/uploads/sites/10/usermanual-efoy-pro-800-2400-2nd-generation-en.pdf>>.

## Example of Application of Cold Spray Technology in Electrical Engineering

T. Binar<sup>a</sup>, J. Zimáková<sup>a</sup>, M. Šustr<sup>b</sup>, M. Sámel<sup>a</sup>, M. Sedlaříková<sup>a</sup>

<sup>a</sup> Brno University of Technology, Technická 10, 616 00 Brno, Czech Republic

<sup>b</sup> Mendel University in Brno, Zemědělská 1, 613 00 Brno, Czech Republic

This work presents a possible illustrative design of the application of cold spray technology, with a presentation of the advantages of this application on a selected electrical component - contactors.

### Introduction

The cold spray method is a technique of coating coatings on the surfaces of materials using solid particles (contained in powder) with a diameter of 1 - 100  $\mu\text{m}$ , which are rapidly sprayed using a suitable gas on the surface of the substrate at a speed of approximately 1500 m / s supersonic nozzle. These particles fall on the surface of the substrate and a bond is formed at the interface between the substrate and the powder, or a bond of the powder particle with the substrate particles, respectively. [1]

As can be seen in Figure 1, the cold spray technique is not complicated at all. Initially, nitrogen gas, helium, or mixtures thereof, is compressed in a gas reservoir, at a pressure of 1-4 MPa. This gas then flows into the system through two distribution paths. One pipe blows gas into the powder container, where this gas serves the purpose of introducing the powder into the spray gun. By means of the second pipe, the gas from the storage tank is blown into an electric gas heater, which is preheated to a temperature of 100 - 800 ° C, in some cases even up to 1100 ° C. This preheating contributes to further acceleration of the gas and consequently of the powder particles. The two pipes meet in the opening of the spray gun. The conventional spray gun is equipped with a convergent-divergent Laval nozzle (referred to as a supersonic nozzle in Figure 1), which has the task of accelerating the warm compressed gas in which the powder particles are contained to supersonic speed. Finally, particles fly out of this nozzle at supersonic speed and impinge on the surface of the substrate to form a coating. Even if the gas in the heater is heated to relatively high temperatures, the particles leaving the nozzle remain in a solid state due to the relatively short exposure of the particles to this gas. It should also be noted that this gas is heated to a temperature which is usually well below the melting point of the powdered particles. In addition, the gas temperature is significantly reduced due to the passage through the divergent part of the gun nozzle. [1]

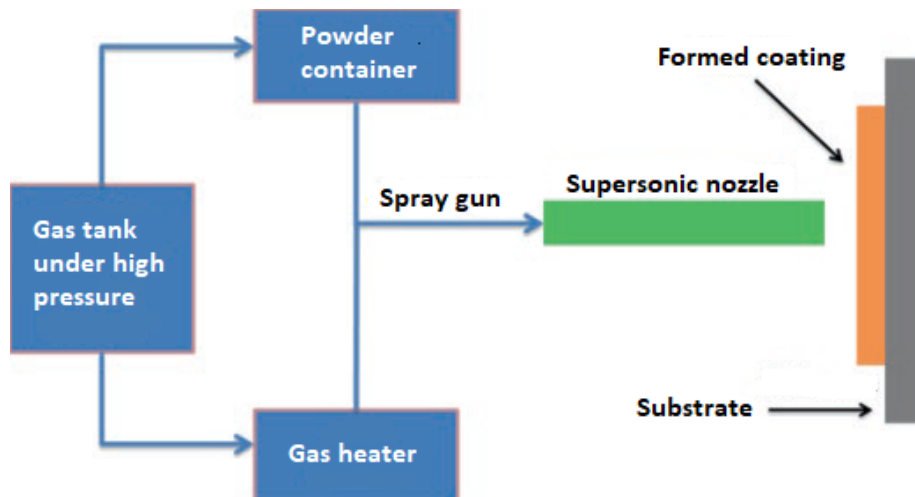


**Figure 1.** Schematic representation of the cold spray process.

Material deposition by cold spray is created by several successive impacts of accelerated microparticles in the solid state on the substrate. The impact of the particle on the substrate surface is associated with viscoelastic deformation of the interacting powder particles and the substrate surface, which leads to a gradual compaction of the powder raw material into the substrate deposits. Upon impact of the powder particles, the kinetic energy of the particles is converted into mechanical deformation and heat. Approximately 10% of the total kinetic energy of the particles is stored in them in the form of elastic energy. Thus, upon impact of the powder particles on the substrate, a metallurgical particle-particle interface is formed. [2]

The diameter of the powder particles is usually 10 - 50  $\mu\text{m}$  and the time interval from the beginning of the firing of the powder particles from the gun to the impact on the surface of the substrate is approximately 100 ns. This time span is so small that experimental monitoring of this phenomenon is very difficult, even impossible. Numerical simulations serve as an alternative for obtaining a preview of the phenomenon of the impact of particles on the surface of the substrate and their individual interactions. These are based on quantitative models of basic physics. The given simulations and models are primarily built in such a way that they represent an ideal case of a perpendicular impact of a spherical powder particle on a flat surface of a substrate. [2]

Cold spray coating appears, for electrical applications, as a possible replacement for conventional thermal coating methods in cases where we require the resulting coating to have specific properties. The coating applied by the cold spray method primarily differs from the thermal methods, in particular in that the resulting coating is without a change in the phase and this offers a number of advantages. The cold spray coating has excellent mechanical properties such as higher hardness and tensile strength, high density and low porosity. Oxidation in the resulting coating is minimal and the coating has a high resistance to corrosion. All these factors prolong the life cycle of a given coating compared to thermal methods. The cold spray coating also has high electrical and thermal conductivity. As part of the research, we offer a possible illustration of the future use of the cold spray method in electrical engineering on the component of a three-phase contactor.

### Three-phase contactor

A contactor is an electromagnetic device that is used to switch electrical circuits on and off. Contactors are used for switching circuits with high or medium current carrying capacity and are often used mainly for the control of electric motors. The three-phase contactor is simple in construction and consists primarily of a coil with a core, a spring around the coil, an armature on a metal core, fixed contacts and power switching contacts attached to the armature (shown in Figure 2).

The contactor works in such a way that a voltage is applied to the coil terminals to switch the electrical circuit, which creates a magnetic field around the coil, which attracts an armature of a metal (most often iron) core, on which the main (power) switching contacts are located. These are connected to the fixed contacts and thus the contactor closes the given electrical circuit (Figure 2 will help for visualization).

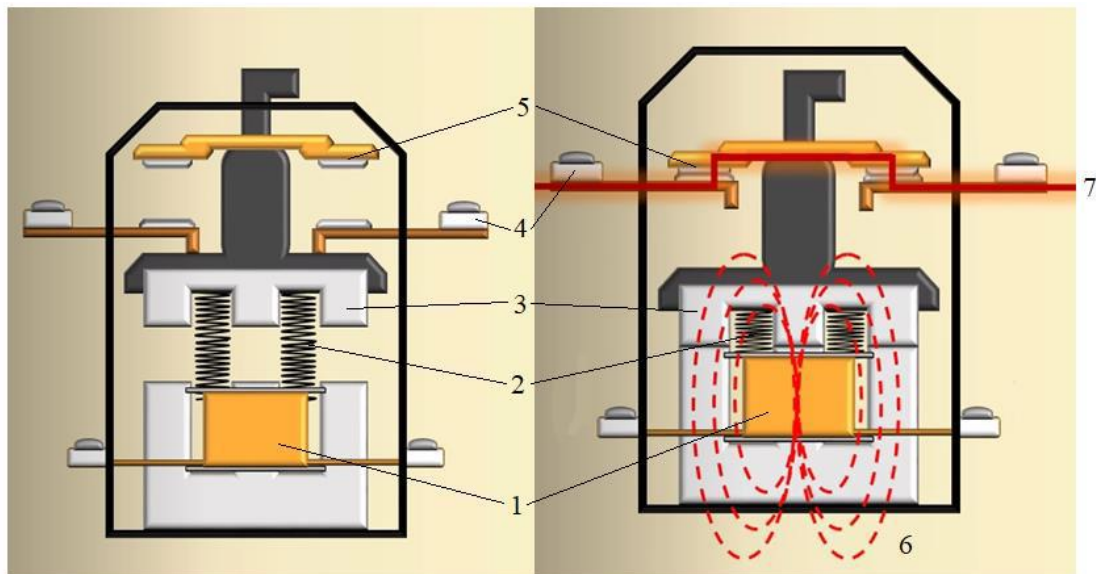


**Figure 2.** Contactor before switching on (left), after switching on (right). Coil with core (1), spring (2), metal core anchor (3), fixed contacts (4), main (power) switching contacts (5), generated magnetic field (6), closing with electrical circuit (7). Taken from [3].

### Contactor model - design of the place of application of the coating by the cold spray method

To visualize the possible application of the cold spray method, we first modeled the device - contactor, in the SolidWorks 2020 program. This assembly contained 152 components and is used for simple visualization of the place where it would be possible to use the coating by cold spray method. This model is shown in Figure 3.

Figure 4 then shows the possible application of cold spray.

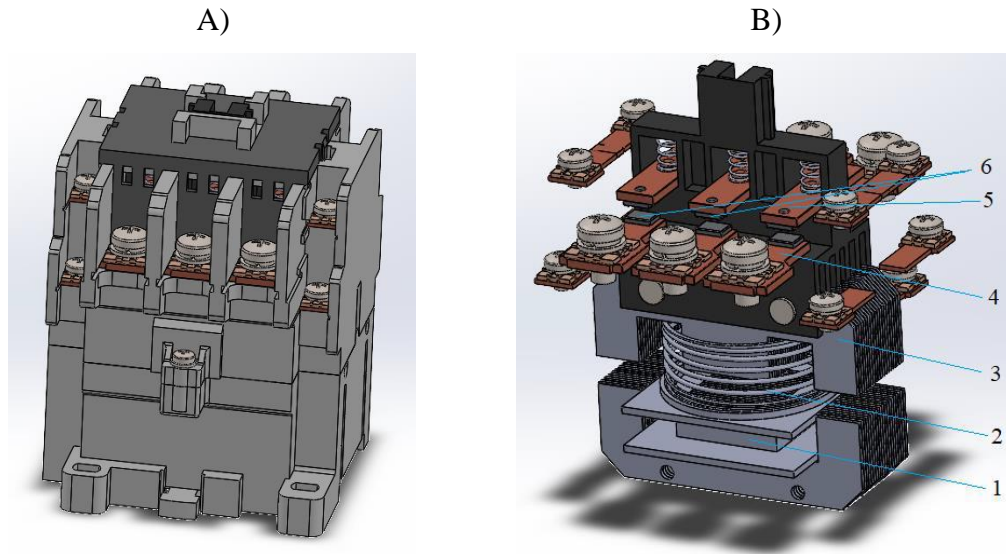


**Figure 3.** Contactor modeled in SolidWorks with plastic cover (A) and without cover (B) with coil with core (1), spring (2), metal core anchor (3), fixed contacts (4), main (power) switching contacts (5) and contact surfaces of switching and fixed contacts (6).

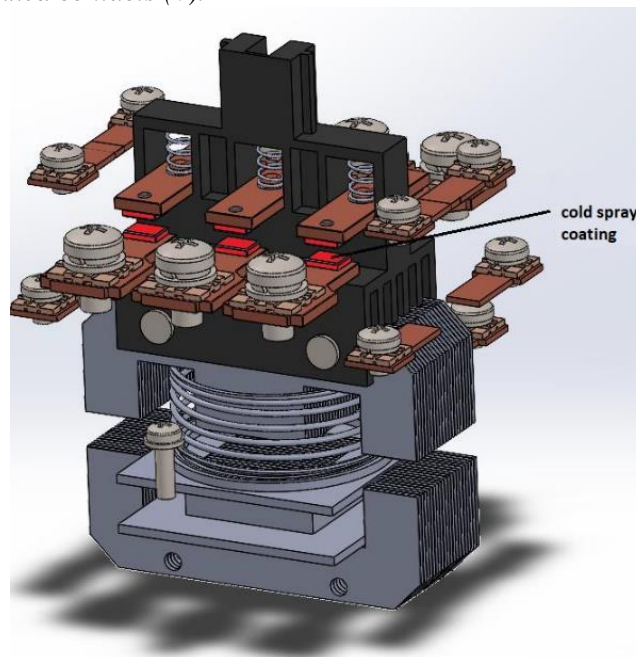


**Figure 4.** Visualization of the coating by cold spray method marked in red.

### Conclusion

The main switching contacts, as well as the fixed ones, are made of pure copper. However, their contact surface must be very durable in order to withstand the high starting current and switching temperature, and therefore this surface is usually covered with a thicker layer of silver.

The first reason to apply a layer of cold spray to the contact surfaces is to replace the material - silver. This metal is relatively expensive and rare. Silver is characterized by excellent electrical and thermal conductivity, which are needed in the contactor component at this point due to the high starting load. By using another cheaper material and applying this material instead of the silver

coating, we could achieve comparable electrical and thermal conductivity, as the method of applying coatings using cold spray technology is characterized by the improvement of these parameters.

### Acknowledgements

The publication was created within the project of specific research at BUT (No. FEKT-S-20-6206).

### References

1. *Cold-spray coatings: recent trends and future perspectives*. Editor Pasquale CAVALIERE. Cham: Springer, [2018]. ISBN 978-3-319-67182-6.
2. ASSADI, H., H. KREYE, F. GÄRTNER a T. KLASSEN. Cold spraying – A materials perspective. *Acta Materialia* [online]. 2016, 116, 382-407 [cit. 2020-11-24]. ISSN 13596454. Available at: doi:10.1016/j.actamat.2016.06.034
3. In: *Electrical4u.net*. [online], 2020 [cit. 2021-5-20]. Available at: <https://www.electrical4u.net/contactors/what-is-contactors-construction-working-operation/>

## Evaluation of the Use of Cold Kinetic Deposition Technology on Materials Used in Electrical Engineering

T. Binar<sup>a</sup>, J. Zimáková<sup>a</sup>, J. Šteiniger<sup>a</sup>, L. Řehořek<sup>b</sup>, P. Křivík<sup>a</sup>, P. Čudek<sup>a</sup>, M. Sedlaříková<sup>a</sup>

<sup>a</sup> Brno University of Technology, Technická 10, 616 00 Brno, Czech Republic

<sup>b</sup>Brno University of Technology, Faculty of Mechanical Engineering, Technická 2896/2, Brno 616 69

The work deals with a process called cold kinetic deposition. Using this technology, a copper layer was formed on a sample with an aluminum substrate by high-pressure spraying at a pressure of 25 bar. In the experimental part, the influence of corrosion degradation in the salt chamber was assessed at time cycles of 100 h, 200 h and 300 h, where changes in internal resistances before and after corrosion were measured. Subsequently, the analysis of corrosion products was performed, where the extent of corrosion attack was determined using an electron microscope. These methods led to a targeted evaluation of the boundary limits of the applied coating layer by cold kinetic deposition, after the action of corrosion.

### Introduction

Cold kinetic deposition is one of many names that describe a coating process in which a metal or dielectric substrate is exposed to a high velocity current at a speed of 300 to 1200 m / s for small particles with a diameter of 5 - 40  $\mu\text{m}$ . The particles are accelerated by a high-velocity stream of compressed gas and spread in a de Laval nozzle. This process is based on selecting a combination of particle temperature, velocity and size that allows spraying at the lowest possible temperature. [1]

In the process of cold kinetic deposition, the powder particles are accelerated by a high-velocity gas stream at a temperature which is always lower than the melting point of the material, which leads to the formation of a coating of solid particles. Upon leaving the nozzle and upon impact with the substrate, the solid particles plastically deform to form a combination of metallurgical and mechanical bonding with the surrounding material. This leads to the formation of a coating, but the application of the material only takes place if the impact velocity of the particles exceeds a specified material- and temperature-dependent threshold, the so-called critical velocity. [1]

During application, the sprayed materials experience only slight changes in the microstructure and with little oxidation or decomposition. Most metals such as copper, aluminum, nickel, titanium and nickel-based alloys can be applied by cold spraying. [2]

As a result, the detrimental effects of high temperature oxidation, evaporation, crystallization, residual stress, gas release, surface separation, and other common problems are reduced or eliminated for traditional thermal spraying methods. The removal of detrimental effects at high temperatures on coatings and substrates offers significant benefits and new possibilities that make cold kinetic deposition promising for many industrial applications. [2] [3]

The aim of this work is to evaluate the technology of cold kinetic deposition on the proposed application. The influence of corrosion on the change of electrical quantities, namely internal resistance, was assessed. These facts are pointed out by methods such as the use of a corrosion

chamber and analysis using an electron microscope. It was necessary to determine by electron microscopy how the corrosion spreaded, thus examining the surface of the material, the edge of the material and the interface between the deposited copper by cold kinetic deposition and the aluminum substrate.

### Production of experimental samples

In the experimental part, it was used aluminum substrate on which copper layer was sprayed. The spraying was performed with an Impact Cold Spray System 5/11 (see Figure 1) and the powder required for spraying was supplied by Safina a.s., the copper content was approximately 99.9%. It was a mixture of two identical Cu powders. The particle size ranged from 38 - 75  $\mu\text{m}$ . Nitrogen was used as the carrier gas, at a pressure of 25 bar and a temperature of 450 ° C. The name of the nozzle sprayed is OUT1, its distance from the sample was 30 mm and the nozzle feed speed was 450 mm/s.



**Figure 1.** Impact Cold spray system 5/11

The plate with aluminum base and copper injection was divided and 4 smaller samples were formed. The plate was divided on a Leco MSX-250 using a 54A25 cutting disc. The sample separation rate was 0.5 mm / s. The cut-out parameter was determined according to the required sample length +5 mm margin. Since the size of the sample was 50 x 50mm and there were two samples next to each other, the first cut was 100 mm + 5mm margin, determining the total length of the cut 105 mm.

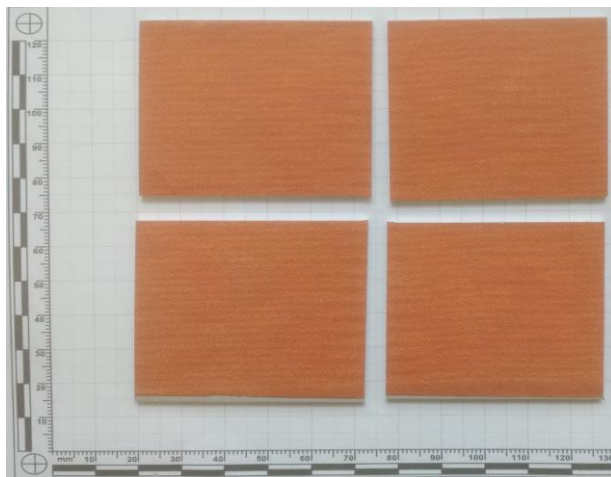


**Figure 2.** *experimental samples after splitting*

### **Internal resistance measurement**

Resistance measurements were performed using three samples that had been previously divided. The aim was to determine the percentage difference of internal resistances of samples measured without corrosion and after corrosion at different temperatures. An electrode system was used for the measurement, in particular no protective electrode is connected when the internal resistance is connected. The Stericell hot air sterilizer was used to measure the internal resistance of the samples, from which the wires were led to a measuring device called the LCR-meter HP 4284A. This instrument was needed to read temperatures selected in the range of 20 ° C to 80 ° C. The results were stored in Microsoft Excel, where various resistance values were measured at frequencies ranging from 20 Hz to 10000 Hz. Samples No. 1, No. 3 and No. 4 were selected for comparison of resistances. Internal resistance was measured on these samples at temperatures of approximately 20 ° C, 40 ° C, 60 ° C, 80 ° C.

### **Corrosion chamber**

Subsequently, the samples were transferred to a corrosion chamber. It is a degradation chamber from the company Liebisch type S 1000 M-TR. Sample No. 1 was left in the corrosion chamber for 100 hours, sample No. 3 - 200 hours, sample No. 4 - 300 hours. Sample No. 2 was not placed in the corrosion chamber, so it was omitted from the experiment.

### **Measurement of resistance after corrosion**

Following the completion of the cycles in the corrosion chamber, it was necessary to re-measure the internal and surface resistance of the samples at specified temperatures ranging from 20 ° C to 80 ° C. Samples after corrosion were found to have increased resistance in contrast to samples measured before corrosion. Subsequently, for all three samples, we compare and describe the percentage differences of individual resistances at given temperatures and specifically determined frequencies. Selected patterns of tables and graphical dependencies will be documented. An example of the measured results is shown in Figure 3

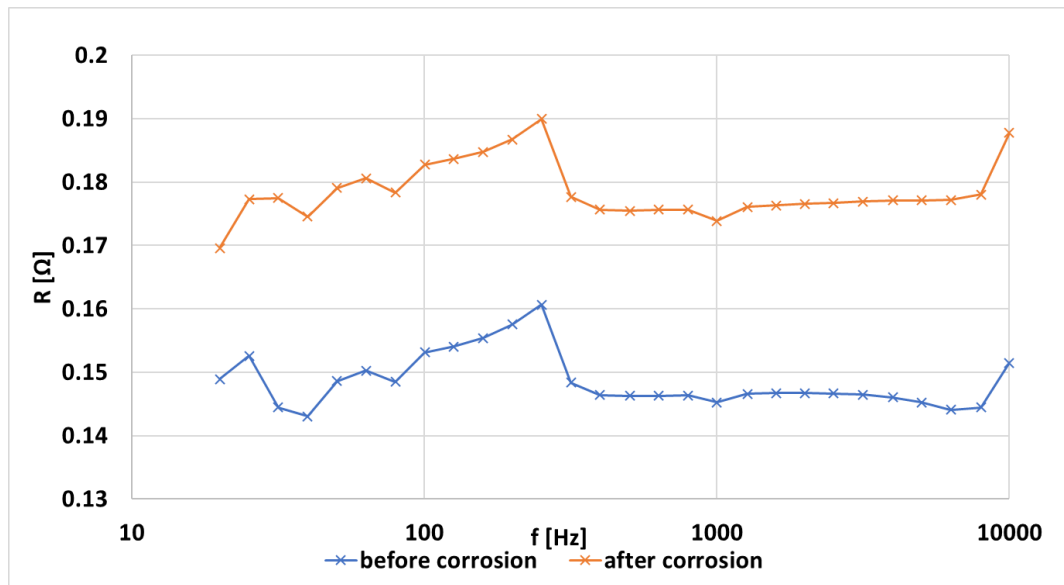


Figure 3. Sample No. 3 for internal resistance at 40 °C

### Conclusion

A plate with an aluminum base was used for the experimental part, on which copper was sprayed by means of the mentioned cold kinetic deposition. The sample was divided into smaller parts due to the use of different time cycles in the corrosion chamber.

The first test was to measure the internal resistance before and after corrosion, at different temperatures from 20 to 80 °C, to determine the percentage difference in resistance. The samples were placed in a corrosion chamber to determine the limit of the formed coating layer.

It was found that the samples after corrosion showed a percentage increase in resistance, which increased with the time of the sample left in the corrosion chamber. The smallest increase was recorded in sample No. 1 (100 hours in corrosion chamber), which ranged from 8.6% to 10.9%. Sample No. 3, which spent 200 hours in the corrosion chamber, recorded a significant increase in resistance by 26%. Sample No. 4 was left in the corrosion chamber for 300 hours. A time of 300 hours is considered crucial, as the increase in internal resistance reached a maximum of 34.6 %.

### Acknowledgements

The publication was created within the project of specific research at BUT (No. FEKT-S-20-6206).

### References

- VILLAFUERTE, Julio, ed. Modern cold spray: materials, process, and applications. Cham (Switzerland): Springer International Publishing, 2015. ISBN 978-3-319-16771-8.
- MAEV, R. G. a Volf LESHCHYNSKY. Introduction to Low Pressure Gas Dynamic Spray: Physics & Technology. Weinheim: WILEY-VCH Verlag GmbH & Co., 2008. ISBN 978-3-527-40659-3.
- PAPYRIN, A. N. Cold spray technology. London: Elsevier, 2007. ISBN 0080451551.

## **A tool for effective management of the logistics process with a direct link to the material life cycle**

J. Zimáková<sup>a</sup>, T.Binar<sup>a</sup>, Pavel Šafl<sup>a</sup>, M. Sedlaříková<sup>a</sup>

<sup>a</sup> Brno University of Technology, Technická 10, 616 00 Brno, Czech Republic

The aim of this work was to create a program that will be used to calculate the price for military vehicles storing using a new system. The program is able to calculate the prices for storing one to x vehicles using its own resources. The prices for each item are defined directly but can be changed according to current needs. The program allows to export the results in the form of a graph and a text file. The program includes the calculation of the total storage time and the corresponding number of days. The application was created using Visual C# as "Windows FormsApplication" in Microsoft Visual Studio. Windows Forms is a framework (a structure used to support programming) that uses .NET technology. Generally speaking, this is a type of object-oriented programming.

### **Introduction**

Due to changing climatic conditions depending on the season, military equipment is constantly exposed to different temperature effects, humidity, weather conditions and UV radiation. Therefore, a decreasing service life of materials can be expected with an impact on shortening the life cycle of military equipment. Aging is either operational, which is caused by operation and operational wear of individual parts of the equipment, or caused by age, where the effects of climate cause the changes of the original properties of materials. Degradation of the materials leads to depreciation and malfunction of equipment. While losses and degradation caused by operation can be replaced by profits from its own operating, aging while the equipment is not used is always only loss-making without the possibility of creating financial value. The largest financial losses in military equipment, which is earmarked for deployment in crisis situations, arise due to the long-term standstill of this equipment and its non-operating. The value of this equipment lies in its ability to act, which is required by state obligations in the event of a crisis. The funds are divided into individual areas of everyday life of organizational units, as well as in the case of commercial companies, but in case that the funds are not exhausted, they cannot be carried over to the following calendar year. In case of a deficit of funds in the area of expenditure on operation and maintenance of equipment, which are part of logistics, the funds cannot be increased. As a result, the quality of the life cycle of equipment is reduced.

### **Description**

The program consists of several windows in which it is possible to set the necessary values to determine the resulting costs of storing vehicles. The costs are divided into material and labor costs. Material costs are divided into several tables in which are listed the necessary materials for storage and their prices. The individual tables contain the names of the materials, their number, the price per piece and finally the total price. Each item also has its use stated. If necessary, it is possible to change the number of used pieces and the price for one piece. (Figure 2, 3) Labor price tables describe the

calculation of labor costs. The program contains the "Price" button, which can be used to adjust individual prices of hourly wages of employees, the value of the standard hour and fixed and variable administrative costs. The final price (the price of work for 4 hours, which includes storage and, if necessary, removal of the vehicle + administrative costs) is shown in the adjacent text field. There is also the possibility to use two teams. By pressing the appropriate button, the program reconsider that a team of 4 people is working on storing thus the storing time will reduce from 3 hours to 1.5 hours. After the program is started, the main window opens and then it is possible to switch to other windows, where the prices for individual items can be changed. The program also includes the option of displaying a graph that plots the values obtained in the "Results" ("Main window"). This chart can be saved as an image in .Png format.

### Main menu

Figure 1 shows the "Main window" table, which contains several blocks, which are divided according to their context. By clicking on the individual buttons opens new windows in which it is possible to set prices for individual materials and work. It is also possible to set the number of vehicles that will be stored. The text box in which the results are displayed is marked in **yellow** (1 vehicle) and **green** (several vehicles).

**Figure 1.** Main window

### Procedure

The program control is very simple. When there is no need to adjust any prices, it is possible to press the "Calculation" button in the "Main window" and all values will be calculated. In this case, prices are rounded. If the parameters are changed, the calculation will be performed with exact values.

Procedure I:

(Without adjusting the prices)

1. Turning on the program
2. Setting the number of vehicles ("Number of vehicles button")
3. Setting the number of teams that will work (1 team is set automatically but it is possible to set two teams)
4. Pressing the "Calculation" button. In this step, all values are calculated.
5. Graph displays and the values are exported. If necessary, by clicking on the "Graph" button, a graph is displayed and can be saved with the "Save" button. The "Export" button saves the values to a text file.

Procedure II:

(With adjusting the prices)

1. Turning on the program
2. Setting the number of vehicles ("Number of vehicles button")
3. It is possible to change a certain price by pressing the button, either in the block of tables ("Conservation, Storage, Funds") or by pressing the "Prices" button in the block "Prices for work".
4. In the new window it is possible to make a change and then confirm it in the window with the "Calculation" button.
5. The adjusted values are calculated by pressing the "Calculation" button in the main window.
6. Graph displays and the values are exported. If necessary, by clicking on the "Graph" button, a graph is displayed and can be saved with the "Save" button. The "Export" button saves the values to a text file.

List of materials for preservation

	Material	Consumption [pcs]	Price per piece [K€]	Total price [K€]	Use
▶	CORTEC ElectrCorVpCI 238 Multi-Metal	1	760	760	For protection and conservation of electrical wiring
	CORTEC EcoTire Duragloss	4	363	1452	To protect rubber parts and tires
	CORTEC Foam Pads VpCI 132	6	89	534	To protect the free indoor environment
	CORTECDehydrosil	12	50	600	To protect the free interior environment of the cab and body of the vehicle

Calculation

**Figure 2.** List of used materials

List of materials to store

	Material	Consumption [pcs]	Price per piece [Kč]	Total price [Kč]	Use
▶	Milcor 123 VpCl White	1	6100	6100	Heat-shrinkable film releasing corrosion inhibitors with UV filter
	Non-woven fabric white Cor-Pak	1	720	720	Layers between the vehicle surface and the foil
	Scapa tape	4	200	800	For attaching the fabric to the vehicle and wrapping sharp edges
	HDPE Penefol	1	2032	2032	For underlaying vehicle wheels
	Nopafoam	2	200	400	For wrapping sharp edges
	Safety gloves	2	100	200	Hand skin protection
	Glasses	2	100	200	Eye protection when using spray preservatives

Calculation

Figure 3. List of materials used for storing

### Acknowledgements

The publication was created as part of a specific research project at Brno University of Technology (No. FEKT- S- 20- 6206).

### References

1. Binar, T., Švarc, J., Šilinger, K., Foltin, P., *The Impact of Corrosion on the Life Cycle of Military Vehicles*, (2016)
2. Binar, T., Švarc, J., Dostál, P., Šustr, M., Tippner, J., *The spread of corrosion in cast iron and its effect on the life cycle of transportation vehicles*, vol. 65, no. 2, p. 383-389 (2017)
3. Švarc, J., Binar, T., Dostál, P., Černý, M., Tippner, J., *The influence of corrosion attack on grey cast iron brittle-fracture behaviour & its impact on the material life cycle*, vol. 65, no. 4, p. 1295-1301 (2017)
4. ČSN EN ISO 14556 (420380) Steel - Charpy V-notch pendulum impact test - Instrumented test method. (European Standard EN ISO 14556:2015)
5. ČSN EN 10045-1 (420381) Metallic materials - Charpy impact test - Part 1: Test method. (European Standard EN ISO 148-1:2016)
6. ČSN 42 0382 (420382) Metal testing. Charpy impact test at low temperature.
7. ČSN 42 0383 (420383) Metal testing. Charpy impact test at elevated temperatures.
8. ČSN 038131 (038131) Corrosion test in the condensation chamber.
9. ČSN 03 8205 (038205) Corrosion protection. General requirements for temporary protection of metals.

## Impacts of Simulated Climate Change on Vehicle Engine Function Parts

Tomáš Binar<sup>1</sup>, Jana Zimáková<sup>2\*</sup>, Pavel Šafel<sup>2</sup>, M. Sedlaříková<sup>2</sup>

<sup>1</sup>Faculty of Military Leadership, University of Defence, Brno, Czech Republic

<sup>2</sup>Brno University of Technology, Technická 3058/10, 616 00 Brno, Czech Republic

\*Corresponding author

This work describes the influence of climatic conditions, temperature and relative humidity on the life span of the cylinder forming the functional part of the vehicle TATRA 815 6x6 VVN. The corrosion effect on specimens with or without corrosion protection was evaluated based on measured notch-toughness values. A condensation chamber was used to simulate corrosion conditions which can cause corrosion and degradation process in the material leading to lifetime reduction and limit state development. There were three sets of samples for simulations with different number of cycles (9, 18 and 27 cycles).

### Introduction

Machinery failure can be caused by overloading, material failure, failure to comply with manufacturing process, external influences on the machine part which is a functional unit of the device or due to other influences. As a result of changing climatic conditions, depending on the season, military technology is permanently exposed to different temperature effects, air humidity, weather conditions, UV radiation, and it is possible to assume the effects of reducing life of materials with impact on shortening the life cycle of military technology. The experiment consisted of measurements of parameters influencing the military equipment life cycle and estimating how the parameter characterizing the behaviour of the material to brittle failure is influenced by climatic changes that can cause irreversible damage (material corrosion). The aim of the climate tests was to verify the new short-term storage system, which was carried out simultaneously with the physical storage of the vehicle TATRA 815 6x6 VVN for one year.

### Experimental program

The test bodies were made from functional parts of the engine cylinder insert. Simulated climatic tests in the condensing chamber were carried out according to (ČSN 03 813) and (ČSN 03 8205) for subsequent evaluation of the parameter influencing the material life by impact bending test.

The tests were carried out on test sample sets which were packed in a special foil with corrosion inhibitors and other sets without corrosion protection to demonstrate degradation effects and changes in material life-reducing properties that cause external influences. A corrosion inhibitor-based foil the MilCorr VpCI 126 White, designed for outdoor protection for one to two years, and the second MilCorr VpCI Shrink Film for 5-year protection, were used to perform the experiment. Both foils comply with MIL-PRF-22019D and MIL-B-22020D standards.

The conditions for performing the simulated corrosion tests, specifying the cycle times and the designation of the samples for the appropriate test set are shown in Table 1. The test mode was the same for all simulated tests.

**Table 1.** Simulated corrosion tests conditions

<b>Simulation for 1-2 years</b>				
Set name	Number of cycles	Sample numbers	Corrosion protection	Note
A Set	9	1 - 21	NO	
		22 - 28	YES	MilCorr VpCI 126 White
<b>Simulation for 3 years</b>				
B Set	18	29 - 49	NO	
		50 - 56	YES	MilCorr VpCI Shrink Film
<b>Simulation for 5 years</b>				
C Set	27	57 - 77	NO	
		78 - 84	YES	MilCorr VpCI Shrink Film
Test mode: 1 cycle = 24 hours – 8 hours in the chamber, at temperature $43 \pm 2$ °C a 100% relative humidity; – 16 hours outside the test chamber at temperature $23 \pm 2$ °C and maximal 75 % relative humidity in a room with a clean atmosphere.				

Photographic documentation (Fig. 1a, 1b, 1c), after corrosion tests, detects the degradation effect of corrosion on the test bodies.

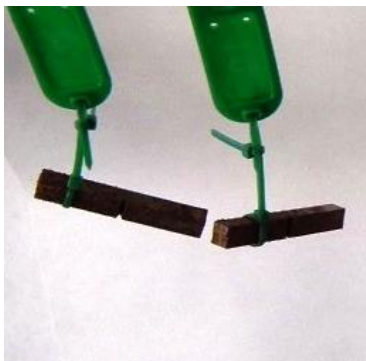


**Figure 1a.** Set A samples after 9 cycles of corrosion test

**Figure 1b.** Set B samples after 18 cycles of corrosion test

**Figure 1c.** Set C samples after 27 cycles of corrosion test

The samples with corrosion protection were not affected by corrosion unlike the samples without protection. It can be assumed that military technology will be affected by accelerated aging of military technology materials and lead to the forced spending of unplanned funds to restore the original properties. In the case of non-applying the newly designed short-term storage system, the damage can be predicted to state property as a result of non-compliance with internal regulations and will result in ineffective and inefficient spending of funds in logistics. The reduction of the reliability and combat ability of military technology can be expected. To assess the impact of the environment on the parameter influencing material lifetime, a bending impact test was performed on the A, B and

C sets of test bodies in accordance with (EN ISO 14556), (ČSN EN 10045-1), (ČSN 42 0382), (ČSN 42 0383) standards, and the results from the bending impact tests carried out in professional publications (Binar et al. 2016), (Švarc et al. 2017 pp. 1295-1301), (Binar et al. 2016, pp. 123). The tests were carried out in a temperature range of -80 °C to +100 °C. Impact bending tests allow the material assessment to be susceptible to brittle fracture, which is one of the most dangerous damage to the material and provides valuable information on the impact of the external environment on the material life due to possible damage to state property on military technology.

In order to process the results of the observed parameter influencing the durability of the military material, susceptible to fragile material fracture, regression was used from the above test using a suitable regression function.

A regression function of the hyperbolic tangens type was used to regress the temperature dependence of the notch toughness.

$$KCV = \frac{L+H}{2} + \frac{H-L}{2} \operatorname{tgh} \frac{2(t-t_{tr})}{\Delta t} \quad (1)$$

With parameters whose significance is closely related to the characteristics of the transit curve: L is the lower and the H is the peak toughness level,  $t_{tr}$  is the transit temperature, and  $\Delta t$  is the width of the transit area. The resulting regression for 9, 18 and 27 cycles are shown in the Fig. 2.

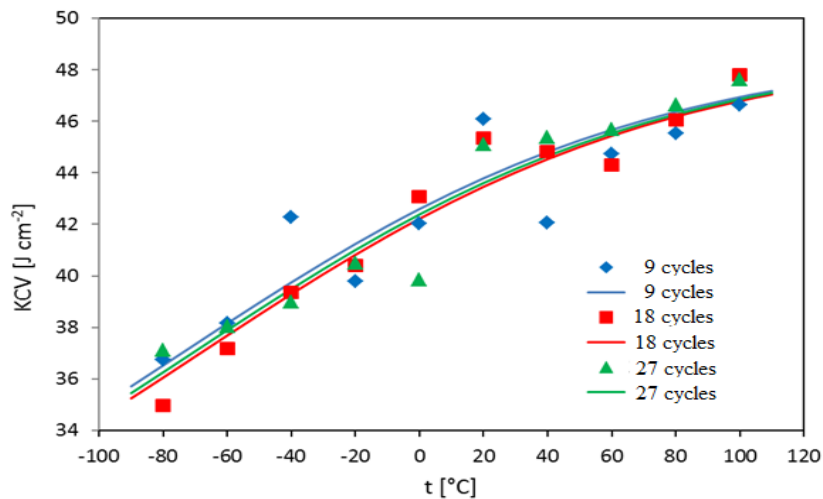


**Figure 2.** The resulting regression of the temperature dependence of the notch toughness for 9, 18, 27 cycles

The lower toughness value for all three curves was fixed at 25 J\*cm<sup>-2</sup>. The upper-level value was counted as a mutual value again for all three curves with a result of 49.0 J\*cm<sup>-2</sup>. The common transit width is 293 °C and the transit temperatures are for 9 cycles -74 °C, for 18 cycles -69 °C and for 27 cycles -71 °C. The minimum differences in transit temperatures and their non-monotonic dependence on the number of corrosion cycles are just another proof of the fact that the variance of the measured toughness values is greater than the influence of the number of corrosion cycles.

Answer to the issue of corrosion effect is a new short-term storage system with a corrosion inhibitor film that will protect the technology from climate change including UV radiation and will not reduce its reliability by degradation processes in the material caused by changes in the external environment.

Realization of short-term storage into foil containing corrosion inhibitors:

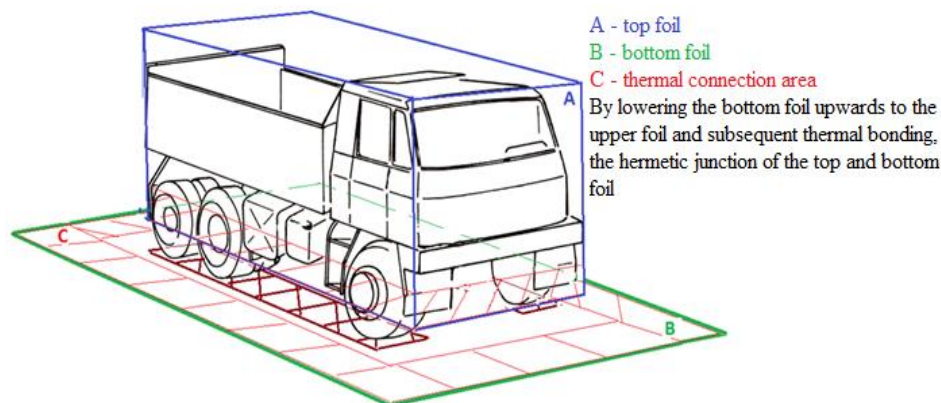


**Figure 3.** Place the top and bottom of the MilCorr VpCI 126 White foil before heat shrinking

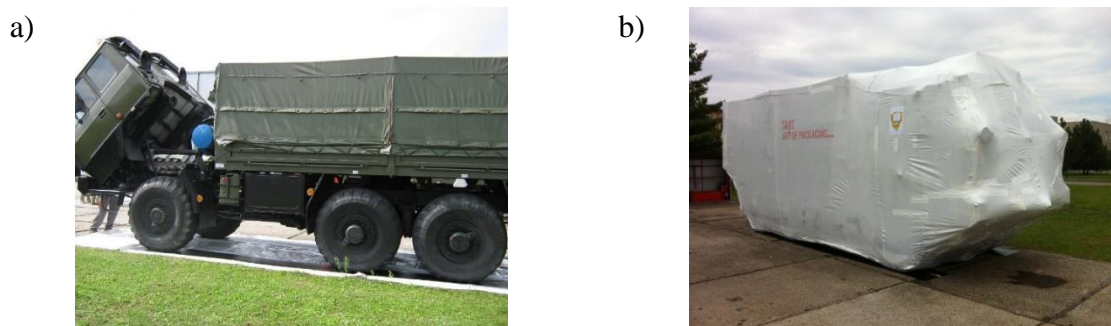


**Figure 4.** a) TATRA 815 6x6 VVN, b) TATRA 815 6x6 VVN covered by foil

### Acknowledgements

The publication was created as part of a specific research project at Brno University of Technology (No. FEKT- S- 20- 6206) and by Ministry of Defence of the Czech Republic, grant ROZVOLOG: Development of Capabilities and Sustainability of Logistics Support.

### References

1. Binar, T., Švarc, J., Šilinger, K., Foltin, P., *The Impact of Corrosion on the Life Cycle of Military Vehicles*, (2016)
2. Binar, T., Švarc, J., Dostál, P., Šustr, M., Tippner, J., *The spread of corrosion in cast iron and its effect on the life cycle of transportation vehicles*, vol. 65, no. 2, p. 383-389 (2017)
3. Švarc, J., Binar, T., Dostál, P., Černý, M., Tippner, J., *The influence of corrosion attack on grey cast iron brittle-fracture behaviour & its impact on the material life cycle*, vol. 65, no. 4, p. 1295-1301 (2017)
4. ČSN EN ISO 14556 (420380) Steel - Charpy V-notch pendulum impact test - Instrumented test method. (European Standard EN ISO 14556:2015)
5. ČSN EN 10045-1 (420381) Metallic materials - Charpy impact test - Part 1: Test method. (European Standard EN ISO 148-1:2016)
6. ČSN 42 0382 (420382) Metal testing. Charpy impact test at low temperature.
7. ČSN 42 0383 (420383) Metal testing. Charpy impact test at elevated temperatures.
8. ČSN 038131 (038131) Corrosion test in the condensation chamber.
9. ČSN 03 8205 (038205) Corrosion protection. General requirements for temporary protection of metals.

## Using Neural Network for Estimation of Li-ion Battery Depth of Discharge

R. Cipin<sup>a</sup>, M. Toman<sup>a</sup>, P. Prochazka<sup>a</sup>, and I. Pazdera<sup>a</sup>

<sup>a</sup>Department of Power Electrical and Electronic Engineering, Brno University of Technology, Brno, Technicka 12, 6161 00, Czech Republic

This paper deals with the estimation of depth of discharge for Li-ion batteries. Estimation is based on the knowledge of discharging curves measured for discrete values of loading currents. The estimator of the depth of discharge is a form of feedforward neural network which is trained with the measured data of discharge curves.

### Introduction

At present, it is highly desirable to know the instantaneous values of Li-ion battery states, i.e., state of charge (SOC), state of health (SOH), or depth of discharge (DoD). For the estimation of instantaneous state, it is used a large variety of methods, i.e., lookup tables, Kalman filters, and applied machine learning, see (1). Dependence between SOC, SOH, and DoD can be easily expressed in the form

$$SOC = SOH - DoD. \quad [1]$$

The purpose of this paper is to investigate the possibility of estimating DoD using a feedforward neural network based on the measured instantaneous values of battery terminal voltage and battery current.

### Measurements

For our study, the battery Panasonic 18650 was chosen. Main battery parameters are: minimal voltage 2.5 V, maximal voltage 4.2 V, nominal voltage 3.6 V, and nominal capacity 3.2 A·h. All battery tests were conducted at 40 °C in a climate chamber. The battery was charged with a constant current of 0.5 A, and the charging was terminated when the current dropped below 20 mA.

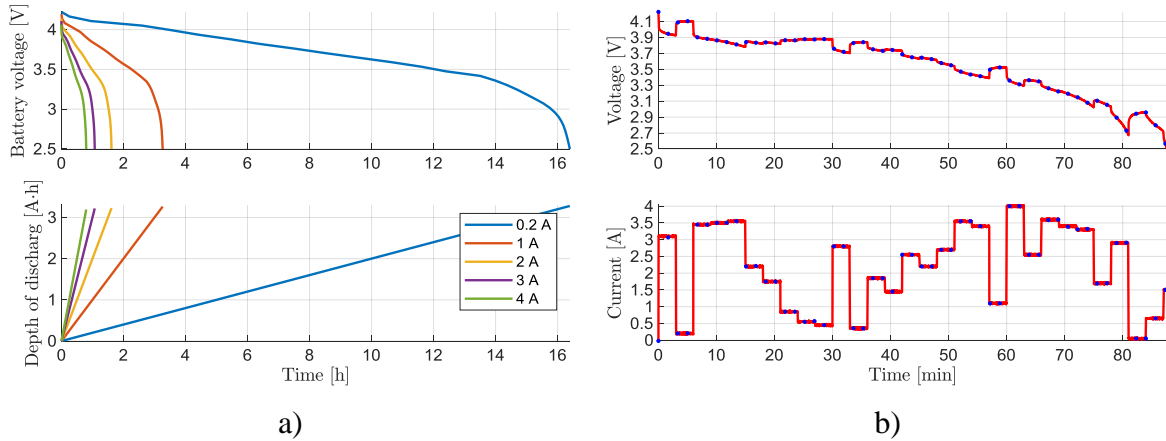
The first series of measurements consist of battery loading with a constant current of 0.2, 1, 2, 3, and 4 A from a fully charged state with cut-off voltage 2.5 V, see Figure 1 a). Depth of discharge (DoD) is calculated based on these measured discharging characteristics. DoD is the total amount of energy that is discharged from a battery

$$DoD(t) = DoD(t_0) + \int_{t_0}^t i_{bat}(\tau) d\tau, \quad [2]$$

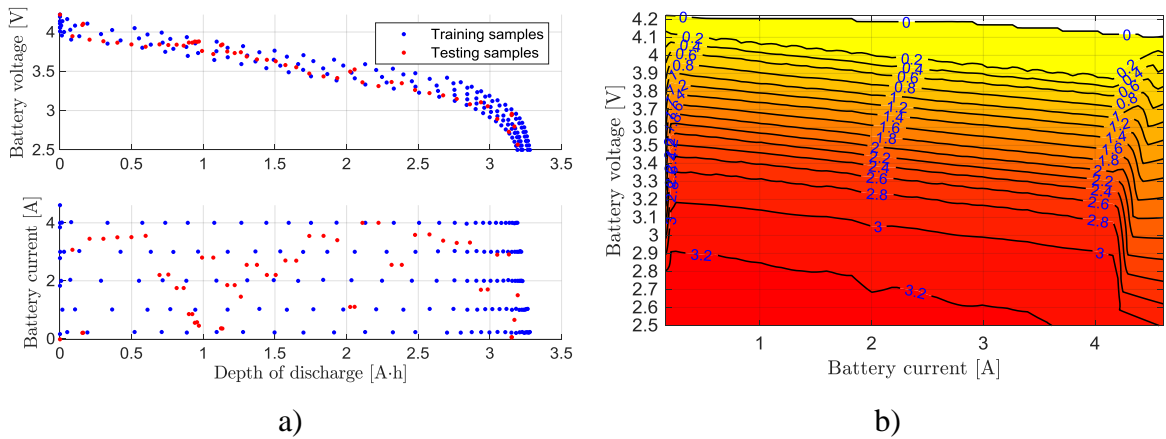
where  $i_{bat}$  is the battery current,  $t$  is the time, and  $\tau$  is general integration variable.

Figure 2 a) shows dependencies of battery voltage and battery current on the actual value of DoD. Blue dots are measured and calculated samples from Figure 1 a). These samples are further used for training designed neural network. Red dots are samples used for testing designed neural network and they are taken from data shown in Figure 1 b).

The second measurement is used for testing the accuracy of the designed and trained neural network (NN). During this test, the battery was loaded with a constant current, which was every three minutes randomly changed in the range from 0 to 4 A, see Figure 1 b).



**Figure 1.** a) Course of battery voltage and depth of discharge during battery discharging with a constant loading current. b) Courses of battery voltage and discharging current with shown samples (blue dots) used for testing the designed NN.



**Figure 2.** a) Measured points (blue dots) used for training of NN, and a testing point (red dots) used for testing of NN. b) Contour map of measured depth of discharge [A·h] in dependence on battery voltage and current.

### Feedforward Neural Network

The main idea of the estimation of DoD using neural network is that the current state of the battery is possible to get from instantaneous battery parameters, i.e., the instantaneous values of battery current, voltage, temperature, etc., see Figure 2).

The first step is constructing a map, in our case a contour map shown in Figure 2 b), which maps the dependencies of instantaneous parameters, i.e., current, voltage, on wanted parameters, i.e., the depth of discharge. Then, it is very easy based on this map to estimate the instantaneous value of battery DoD from the instantaneous value of battery loading current and battery terminal voltage.

The second step is to design a neural network. In our case, the structure of the neural network is shown in Figure 3. NN consists of two linear neurons in the input layer, five neurons in two hidden layers, and one linear neuron in the output layer.

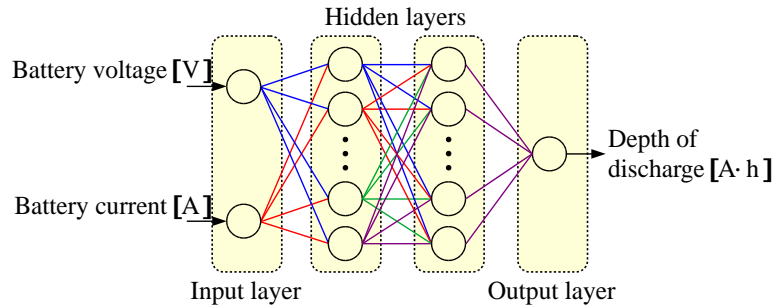


**Figure 3.** Schema of neural network.

The activation function of individual neurons in hidden layers is the parametric rectified linear unit (PReLU), which is defined as follows

$$\text{PReLU}(x) = \max(0, x) + \alpha \min(0, x), \quad [3]$$

where  $\alpha$  is a learnable parameter.

### Conclusions

The paper presents a possibility to use the neural network with two input neurons and one output neuron to estimate the depth of discharge of li-ion batteries within broad working limits.

### Acknowledgments

This research work has been carried out in the Centre for Research and Utilization of Renewable Energy (CVVOZE). Authors gratefully acknowledge financial support from the Ministry of Education, Youth and Sports under institutional support and BUT specific research programme (project No. FEKT-S-20-6379).

### References

1. C. Vidal, P. Malysz, P. Kollmeyer, and A. Emadi, IEEE Access, **8**, 52796 (2020), DOI: 10.1109/ACCESS.2020.2980961

## **Influence of Machining Parameters on the Surface Quality of Technical Plastics**

D. Dobrocky<sup>a</sup>, J. Sedlak<sup>b</sup>, A. Polzer<sup>b</sup>, Z. Joska<sup>a</sup>, J. Prochazka<sup>a</sup>, Z. Studeny<sup>a</sup> and E. Svoboda<sup>a</sup>

<sup>a</sup> Department of Mechanical Engineering, Faculty of Military Technology, University of Defence, Kounicova 65, 662 10 Brno, Czech Republic

<sup>b</sup> Institute of Manufacturing Technology, Faculty of Mechanical Engineering, Brno University of Technology, Antonínská 548/1, 601 90 Brno, Czech Republic

The article deals with the evaluation of the influence of conventional methods of machining on the surface quality of selected technical plastics. The thermoplastic polymer polyoximethylene (POM-C) Ertacel C and polyamide (PA 6) Ertalon 6SA were selected for machining. Both materials are suitable for machining and are used for the production of precision mechanical components (e.g. gears, plain bearings, guides, etc.), but also in electronics and electrical engineering. In all these applications, the quality of machined surfaces is important, especially for functional surfaces that interact with other surfaces. Test specimens from these materials were turned and milled. The technological conditions of machining (speed  $n$ , cutting speed  $v_c$ , feed  $f$ , depth of cut  $a_p$ ) were adapted to achieve approximately the same surface roughness values. The milled samples were machined with and without cooling medium (for drought). Turning was performed only dry. As the cutting speed  $v_c$  increased, the surface roughness of the turned Ertacel C material decreased, while milling led to a deterioration in the roughness as the cutting speed  $v_c$  increased. Similar behavior was observed for Ertalon 6SA. The process fluid led to a deterioration in the roughness of the milled surfaces of both plastics. Turned surfaces showed worse roughness than milled surfaces.

## Effect of temperature cycling on IMC growth and solder joint strength of SAC305 solder alloy and REL61 low silver alloy

Jakub Dokoupil a Jiří Starý

Faculty of Electrical Engineering and Communication, Brno University of Technology, Brno, Czech Republic

### Extended abstract

Directive 2002/95/EU of the European Parliament and of the Council on the restriction of the use of certain hazardous substances in electrical and electronic equipment in force since 1 July 2006 has had a major impact on the solder alloy market. Until then, the most common SnPb solder alloys had to be replaced by lead-free alloys. One of the most widespread lead-free replacements became the alloy SAC305 ((Sn 96.5%; Ag 3%; Cu 0.5%). However, lead-free alloys have several major disadvantages compared to lead alloys. One of them is the higher melting temperature, which is in the range of 217-220 °C for the SAC305 alloy. The increased melting temperature affects the growth of intermetallic compounds (IMC) at the substrate-solder and solder joint-pin interfacial. A thin IMC layer is essential for proper metallurgical bonding of dissimilar metals of the substrate and solder joint. However, the IMC layer is brittle and if its thickness is too large, it can significantly affect the strength of the soldered joint and thus its overall reliability. This feature of the IMC layer is particularly dangerous when the solder joint is exposed to thermal stress. This thermal stress can take the form of thermal aging or thermal cycling. The thickness of the IMC layer is also influenced by the surface finish used on the substrate, which provides protection of the mainly copper conductive connections from oxidation and contamination, and at the same time ensures the solderability of the surface. The metals contained in these surface finishes also react at the interfacial area and influence the composition and behavior of the IMC layer. Nickel-based surface finishes such as ENIG (electroless nickel immersion gold) have been shown to limit the growth of the IMC layer, as the nickel acts as a diffusion barrier.

As the price of silver has increased several times since 2006 and electronics manufacturers are under constant pressure to reduce the cost of production, they are switching to lower silver content solder alloys. This work focuses on the comparison between the standard SAC305 solder alloy and an alternative alloy REL61 (SnBiAgCu) with lower silver content and a melting temperature in the range of 208-215 °C in terms of IMC layer growth during thermal cycling and its effect on the shear strength of the solder joint.

PCBs with FR-4 base material, 18 µm thick copper foil and with ENIG surface finish, were used for testing. These PCBs were double-sided assembled with 0 ohm SMD resistors in an 0805 package and soldered in a reflow oven. PCBs were soldered using two different temperature profiles. Subsequently, the samples were temperature cycled according to two temperature profiles - TC1 (25-100 °C, dwell time on  $T_{max}$  and  $T_{min}$  7 minutes) and TC2 (-40 - +125 °C, dwell time on  $T_{max}$  and  $T_{min}$  5 minutes). Then micro-sections were made, which were evaluated using an environmental scanning electron microscope.

The results show that the growth of the IMC layer is lower for the REL61 solder alloy than for the SAC305 solder alloy. This corresponds to the shear strength of the solder joint for SAC305 alloy, where the joint strength decreases with increasing thickness of the IMC layer. The situation is different for REL61 alloy, where for cycling at temperatures above freezing, the strength of the joint increased with increasing IMC layer. For cycling involving sub-zero temperatures, the growth of the

IMC layer was less than in the previous case, but the strength of the solder joint decreased. The reason for this behavior will be further investigated. In terms of replacing the SAC305 solder alloy in the scope of this work, the REL61 solder alloy appears to be a suitable.

## Thermodynamics of Moist Air for Vacuum Technology

V. Horák, B. T. Phan, and L. Dobšáková

Department of Mechanical Engineering, University of Defence, Brno, Czech Republic

The paper is focused on the developing a predictive mathematical model for describing thermodynamic processes connected with the moist air depressurization in vacuum chambers. Equations of the mathematical description are based on principles of the energy and mass conservation, which are complemented by the moist air thermodynamics, the state behavior of water and vapor, including principles of the critical flow. The problem has been solved using the MATLAB software. In the paper, two cases are applied and discussed: the vacuum drying and the specimen chamber of an environmental scanning electron microscope. The specific requirements are especially important for environmental scanning electron microscopes, where it is possible to observe samples, which contain water, in their natural condition. If the air pressure, temperature and humidity do not have suitable values, observed sample may be dried or damaged.

### Thermodynamic Model of Moist Air for Vacuum System

The moisture contained in the air within vacuum systems play a substantial role during ongoing thermodynamic processes. These processes have an impact mainly in vacuum batch drying systems and in the specimen chamber of an environmental scanning electron microscope. In both cases, it is important to find and ensure the suitable relation among the air pressure, temperature and humidity. The prediction of state quantities during depressurization and the ensuring of the precisely defined pressure and temperature are important tasks for the design and operation of these low-vacuum systems. The model is based on the first law of thermodynamics. This principle is supplemented by the water phase changes, state behavior, and thermodynamic functions of the moist air. The system of differential equations has been solved numerically with the MATLAB using the fourth-order Runge-Kutta integration. The mathematical model requires a set of input data and boundary conditions (i.e. the vacuum chamber volume, the orifice diameter, the pumping speed, the initial temperature, the heat transfer coefficient, the heat transfer area, the flow coefficient, thermodynamic properties, and the ambient air pressure, temperature and relative humidity).

### Results and Validation

Results of the solution are validated by experiment for three cases of the orifice (aperture) diameters, namely:  $d = 1.044$ ,  $1.524$ , and  $2.157$  mm. Other input parameters are: the vacuum chamber volume  $V_1 = 0.045$  m<sup>3</sup>, the chamber surface area  $A = 0.7188$  m<sup>2</sup>, the pumping speed  $V_p = 0.001389$  m<sup>3</sup>s<sup>-1</sup>, the atmospheric pressure  $p_2 = 100525$  Pa, the ambient temperature  $T_2 = 294.65$  K and the ambient air relative humidity  $\varphi_2 = 20$  %.

Results of the solution provide us with the evolutions of pressure, temperature, and humidity for various opening orifice's diameters. Here, two cases are applied and discussed: the vacuum drying and the specimen chamber of an environmental scanning electron microscope.

## Results for the vacuum drying

Time courses of the pressure, the temperature, the moisture mass flow rate due to drying and the relative humidity in the vacuum chamber during the vacuum drying are shown in Fig. 1.

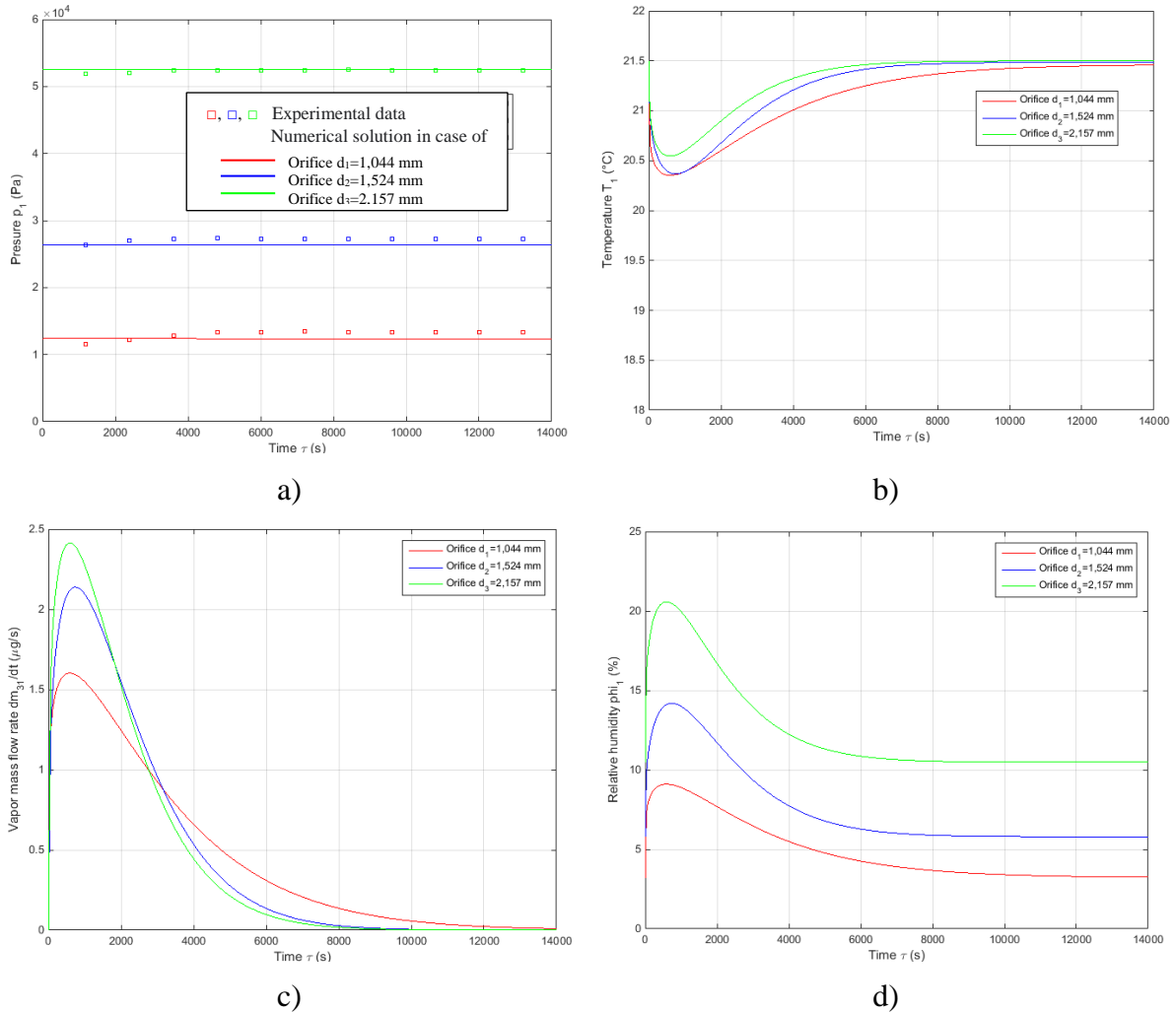


**Figure 1.** Time courses of drying process for various orifice diameters: a) pressure in vacuum chamber, b) temperature in vacuum chamber, c) moisture mass flow rate due to drying, d) relative humidity in vacuum chamber.

## Results for the specimen chamber of environmental scanning electron microscope

The specific requirements for the pressure, temperature and humidity control in the specimen chamber are especially important for environmental scanning electron microscopes, where it is possible to observe samples, which contain water. In particular, the pressure in the chamber must not drop below the saturated water vapor pressure for a given temperature of sample, so as not to be damaged. Concurrently, the saturated humidity in the specimen chamber must be kept, by the controlled injection of water, so that the sample is not dried. The model provides us with various results for the state of equilibrium, which is reached after some time from the depressurization beginning. The relation between the orifice diameter and the air pressure and humidity in the specimen chamber for various rates of water injected from a hydration system is shown in Fig. 2.

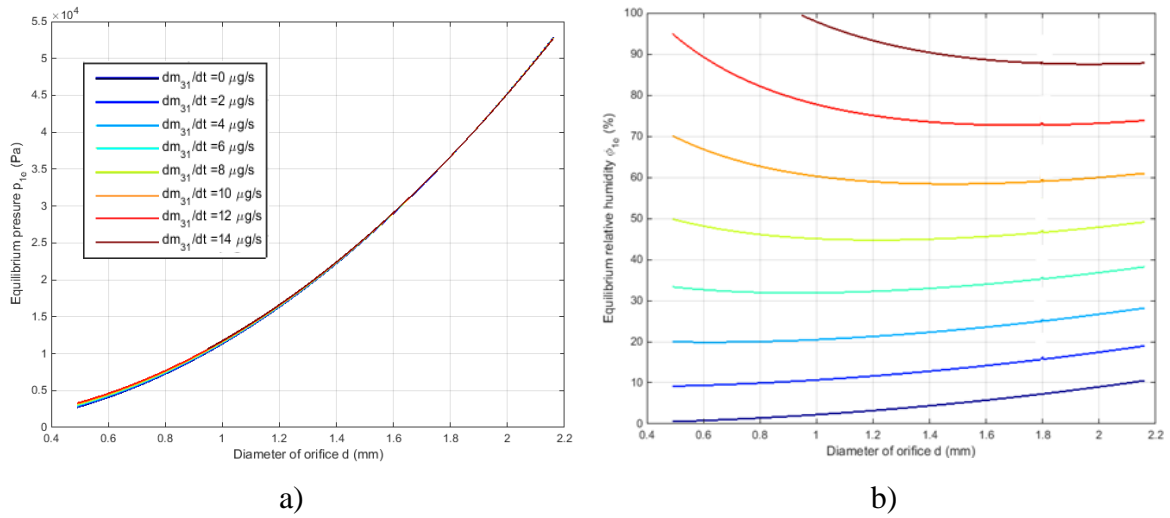


**Figure 2.** Influence of orifice diameter on a) pressure and b) humidity in the specimen chamber for various rates of hydration.

The control of the rate of hydration to ensure the saturated humidity in the specimen chamber is another task of calculation. Rates of hydration as the flow rate of injected water vapor are given in Fig. 3.

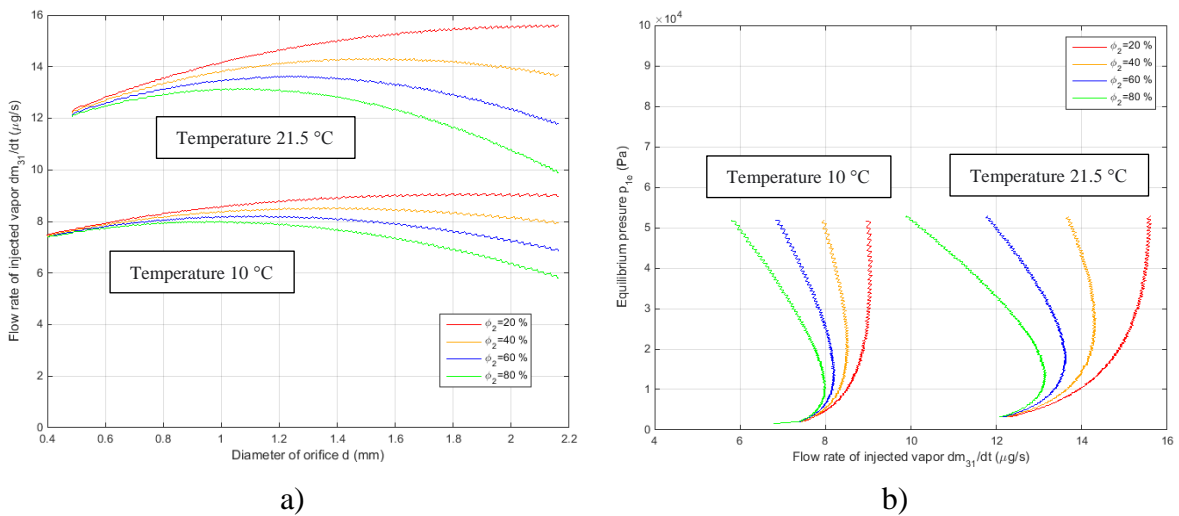


**Figure 3.** Rates of injected water vapor for full hydration versus a) orifice diameter and b) pressure in specimen chamber for various ambient air temperatures and humidity.

### Conclusion

The predictive model describing thermodynamic processes connected with the moist air depressurization in vacuum chambers has been developed. The problem is solved numerically by MATLAB. Two cases are applied and discussed: the vacuum drying and the specimen chamber of an environmental scanning electron microscope. It is obvious that the presented model is capable to solve various unsteady-state and equilibrium problems connected with moist air thermodynamic processes in the vacuum chambers.

### **Acknowledgment**

The support by the research project of the Faculty of Military Technology SV20-216 and by the institutional funding of the University of Defence DZRO FVT 3 is acknowledged.

## Ecological Epoxy Casting Systems for Electrical Engineering Applications

L. Horák<sup>a</sup>, J. Kazelle<sup>a</sup>

<sup>a</sup> Department of Electrotechnology, Faculty of Electrical Engineering and Communication, Brno University of Technology, 616 00 Brno, Czech Republic

Presented thesis is focused on studying of electro-insulating casting systems based on epoxy resin. The aim of the article is to acquaint the reader with the development of this systems – epoxy resin with ecological hardeners without toxic components. The temperature and frequency dependence of complex permittivity, complex electrical modulus, loss factor and inner and surface resistivity of the given samples are investigated.

### Introduction

Civilization has gone through several periods in its development. Each of them can be named according to the material that prevailed in the period - the Stone Age, Bronze Age, Iron Age. Today it is possible to speak of the "polymer" or "composite" period. Epoxy resins are relatively young plastics, the first mentions are recorded in the second half of the 19th century, but their production did not develop until after World War II. [1][2]

Epoxy resins are polymeric materials of synthetic origin, which belong to the group of thermosets. They are colorless to yellowish and can be stored almost indefinitely under normal conditions. Epoxy resins acquire significant properties only after curing, which most often occurs by a chemical polyaddition reaction. Cured products have good electrical insulating and dielectric properties, mechanical strength, especially shear strength, chemical resistance to water, acids and some solvents. They also excel in very good adhesion to metal, glass, ceramic, wood and other materials. Furthermore, epoxies are characterized by high toughness, low shrinkage and some of them even good elasticity. [1][2]

Epoxies are widely used in the preparation of adhesives, laminates, potting, coating, molding and impregnating materials. They are used in almost all industries, from mechanical engineering, construction industry, electrical engineering, aerospace, food industry, to healthcare.

The current goal of applied research is to develop new pre-filled casting systems based on epoxy resins with hardeners that comply with REACH authorization. These are environmentally friendly hardeners without toxic components. The European Union emphasizes the ecology of the production of these systems and restricts the use of certain substances. One of the much-discussed components is methylhexahydrophthalic anhydride, which is being replaced by environmentally friendly anhydrides that are not on the list of prohibited substances.

### Samples for measurement

The samples were made in cooperation with company SYNPO a.s. Pardubice. The article is focused on epoxy casting systems designed for outdoor use. The original system with the trade name Sadurit 560-1987/1 is still in use and needs to be modified according to current legislation. It is a two-component system. Component A is based on cycloaliphatic epoxy resin and it is filled with special fillers (amount of filler is 64.7 %). Component B (hardener) is based on anhydride and contains the

much-discussed and prohibited methylhexahydrophthalic anhydride. This component is also filled with special fillers (amount of filler is 68.7 %). Different types of micro-ground quartz sand are most often used as filler. The mixing ratio of component A and component B is 100:100.

The original epoxy system Sadurit 560-1987/1 should replace the newly designed system called Sadurit 560-1667, which does not contain discussed anhydrides. It is also a two-component system for outdoor use. Component A remained practically the same. It is based on cycloaliphatic epoxy resin and it is filled with special fillers (amount of filler is 64.7 %). Component B has been reformulated newly using an anhydride that is not on the list of prohibited substances. Component B is also filled with special fillers (amount of filler is 69.4 %). Different types of micro-ground quartz sand are used as filler. The mixing ratio of component A and component B is 100:100. The glass transition temperature  $T_g$  of this system is between 85 - 100 °C.

### Results and discussion

The measurement of relative permittivity and loss factor as a function of temperature was performed at an operating voltage of 500 V, a frequency of 50 Hz and electrode pressure of 5 N/cm<sup>2</sup> on an impedance analyzer Tettex 2830/2831 in conjunction with a three-electrode system Tettex 2914 according to ČSN IEC 250 [3].

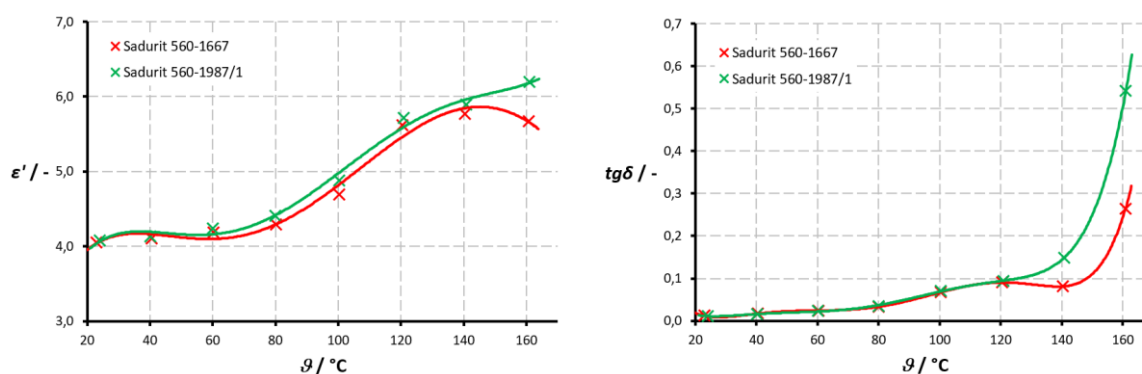


**Figure 1.** Dependence of relative permittivity (left) and loss factor (right) on temperature

Inner and surface resistivity were measured on Agilent 4339B High Resistance Meter in conjunction with a three-electrode measurement system Agilent 16008B Resistivity Cell. The measurement was performed according to standard ČSN IEC 93 [4]. The temperature dependences were determined at a DC voltage of 1 kV.

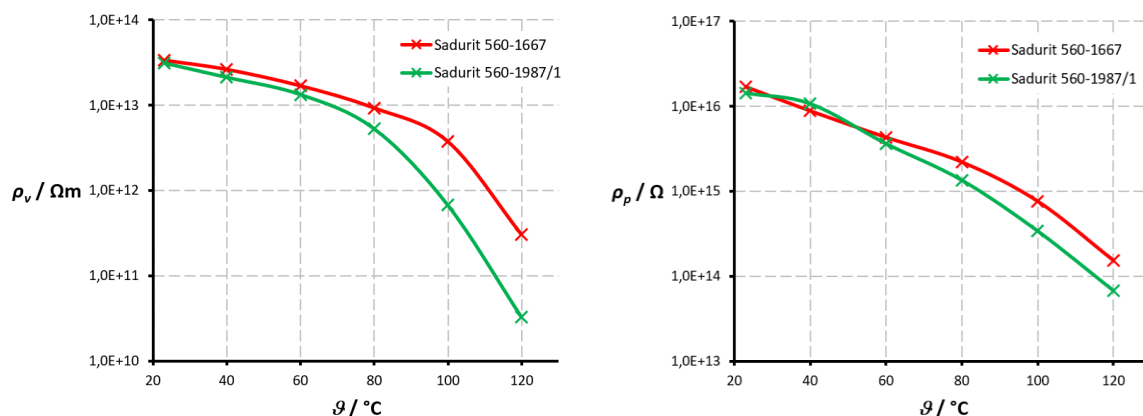


**Figure 2.** Dependence of inner (left) and surface resistivity (right) on temperature

The performed experimental activity shows that the analyzed epoxy materials for outdoor use show almost identical results in the temperature range of 25 - 120 °C. The newly designed system called Sadurit 560-1667, which contains environmentally friendly hardeners compliant with the REACH authorization, achieves slightly better results (lower loss factor, higher resistivity).

### Acknowledgments

This work was supported by the specific graduate research of the Brno University of Technology No. FEKT-S-20-6206.

### References

1. LIDAŘÍK, M. *Epoxidové pryskyřice*. Praha: Státní nakladatelství technické literatury, 1983. Makromolekulární látky. 729 s.
2. MLEZIVA, J. a ŠŇUPÁREK, J. *Polymery - výroba, struktura, vlastnosti a použití*. Praha: Sobotáles, 2000. 544 s. ISBN 80-85920-72-7.
3. ČSN IEC 250. Doporučené postupy ke stanovení permitivity a ztrátového činitele elektroizolačních materiálů při průmyslových, akustických a rozhlasových kmitočtech včetně metrových vlnových délek. Praha: Český normalizační institut, 1997. 30 s.
4. ČSN IEC 93 Metody měření vnitřní rezistivity a povrchové rezistivity tuhých elektroizolačních materiálů. Praha: Český normalizační institut, 1993. 17 s.

## Preparation of an electrochemical cell inside a scanning electron microscope

O. Klvač<sup>a</sup>, T. Kazda<sup>a</sup>, Y. Fam<sup>b</sup>, L. Novák<sup>b</sup>

<sup>a</sup> Department of Electrical and Electronic Technology, Faculty of Electrical Engineering and Communication, BUT, Technická 10, 616 00 Brno, Czech Republic

<sup>b</sup> Thermo Fisher Scientific Brno, Vlastimila Pecha 12, 627 00, Brno, Česká Republika

Preparation of electrochemical cell inside scanning electron microscope. The aim of this work is to design an experimental setup for the in-situ characterization of electrode materials of electrochemical power sources by scanning electron microscopy. The first part describes the process of preparation of a lithium-lithium titanate electrochemical system using the FIB-SEM technology. The following is a report on the course of individual experiments and the results of electrochemical measurements. Finally, there is a discussion of the results and the next steps.

### Introduction

Lithium-ion batteries (LIBs) are currently the most commonly used cells for high-performance applications and they are considered a suitable candidate for future applications such as energy storage for renewable electricity sources or electric vehicle propulsion [1]. However, there are still some issues that need to be solved before they can be spread on a massive scale. Obtaining electrode materials is still relatively expensive and represents a burden on the environment. Moreover, today's materials reach their capacity limits. Although there are other promising materials (sulfur, silicon), which could theoretically solve the problems, they are not very widespread due to technological problems (solubility, poor conductivity, particle cracking, delamination, ...) [2]. These problems are well observable by scanning electron microscopy (SEM) [3].

In this work, the whole battery is created inside the SEM chamber from active electrode materials only. This will allow us to see phenomena responsible for the capacity fade directly, in-situ. In the first steps, well known, stable lithium-lithium titanate system is created for tuning the parameters of the preparation processes. If the system will work, the LTO can easily be replaced by another material.

### Experimental

The half-cell is assembled on the surface of the MEMS chip [4], initially designed for in-situ heating and biasing experiments in Thermo Fisher Scientific tools [5]. For the experiment, only one pair of biasing contacts is used (Figure 1 left). MEMS chip is fixed in a holder and biasing contacts are electrically directly connected with 25 pin CANON connector at the air side of the vacuum feedthrough installed on the SEM chamber.

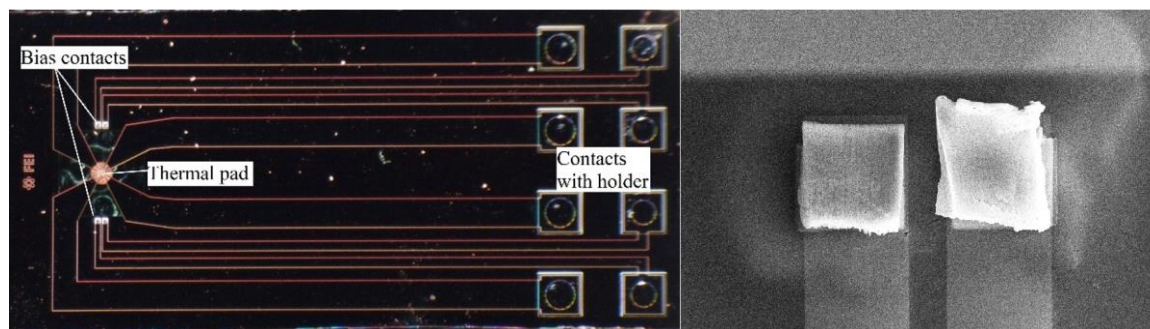


**Figure 1.** Used MEMS chip (left); voltage contrast imaging of redeposited material between electrodes of created system (right)

LTO electroactive material is cut from commercially available electrode sheet (CUSTOMCELLS<sup>®</sup>) using xenon plasma focused ion beam (PFIB) system Helios Hydra 5 UX DualBeam (Thermo Fisher Scientific). A chunk of approx. 50x50x20  $\mu\text{m}$  is attached on EasyLift micromanipulation needle by carbon deposition using MultiChem Gas Delivery System, transferred, aligned with appropriate MEMS pad and contacted with carbon deposition as well. For lithium chunk preparation, Helios 5 UC DualBeam (Thermo Fisher Scientific) with gallium FIB is used similarly.

As an electrolyte, 1-Ethyl-3-methylimidazolium tetrafluoroborate (EMIMBF  $\geq 98\%$ , SigmaAldrich) ionic-liquid (IL) in a mixture with  $\text{LiBF}_6$  salt in 0.5M concentration is used.

The IL was chosen because it cannot be evaporated under vacuum conditions. The liquid is applied to the MEMS chip surface near the LTO in a small amount with a pipette. At the required moment, IL is moved toward electrodes using stage tilt.

The calculated capacity of the created cell is approximately 16 nAh. For electrochemical characterization, BioLogic SP-150 potentiostat is connected with a shared reference electrode (RE) and the counter electrode (CE) to lithium, LTO is on the working electrode (WE).

## Results

In the first case, the open-circuit voltage was measured during the soaking of electrodes by the electrolyte. The voltage increased to 302.3 mV within 4.5 s, but it was not stable, after 2 min, there were only units of millivolts. In galvanostatic mode, at 2.5 nA, the voltage fluctuated around 5 mV. At higher currents, there was higher voltage, but the battery was not charged.

In the second case, the current of 100 nA was tried to pass through the cell without electrolyte. The current flowed here and a voltage drop of 1.5 V was measured. It turned out that a very thin layer of tungsten was redeposited between the contacts during ion milling of the EasyLift needle, which forms a parallel resistance. The material could be seen using voltage contrast imaging (Figure 1, right). This area was cleaned by FIB. Then, the electrolyte was moved between electrodes and there was a stable voltage of about 0,65 V. During imaging, there was a high electron beam current which reversed the polarity. This step damages the cell completely.

In the last case, only LTO was contacted on the MEMS chip and dived in the electrolyte. Lithium was glued on the EasyLift needle which is connected on the ground of SEM, where was attached shared RE and CE electrode. When the lithium touched the electrolyte, there was a voltage of about 2V. The electrode was dived and emerged several times, in dived state, the voltage was stable. Cycling failed because the ground is a source of strong noise and the potentiostat was not able to work in galvanostatic mode.

## Discussion

In all cases, there was a problem with the connection. In the first case, the cell was short-circuited with a layer of redeposited material. In the second case, it was removed, but the system was destroyed by an electron beam. The problem of local charging is described in the literature [6]. As the solution, in the third case, lithium was placed on a grounded EasyLift needle, which should allow fast charge dissipation. The system was stable but cycling failed because the ground is a source of strong noise.

In the next steps, we will use insulated EasyLift needle as a current collector for lithium and insulated sample stub for LTO. It is the simplest connection where we can test if cycling works. In the near future, LTO will be replaced with another material. After tuning the necessary parameters, a special MEMS chip for four-point measurement will be designed.

## Acknowledgments

This work was supported by the specific graduate research of the Brno University of Technology No. FEKT-S-20-6206. The work was developed in cooperation with Thermo Fisher scientific Brno.

## References

1. Y. Liang et al., *InfoMat*, 1, 6-32 (2019).
2. H. -J. Kim et al., *Electronics*, 9 (2020)
3. H. Liu et al., *Journal of Power Sources*, 306, 300-308 (2016)
4. L. Mele et al., *Microscopy Research and Technique*, 79, 239-250 (2016)
5. L. Novák, J. Stárek, T. Vystavěl, and L. Mele, *Microscopy and Microanalysis*, 22, 184-185 (2016)
6. D. Chen, S. Indris, M. Schulz, B. Gamer, and R. Mönig, *Journal of Power Sources*, 196, 6382-6387 (2011)

## The Corrosion Resistance of anodized EN AW 7075 T6 Alloy

D. Kusmič<sup>a</sup>, L. Klakurková<sup>b</sup>, M. Juliš<sup>b</sup>, P. Gejdoš<sup>a</sup>, J. Viliš<sup>a</sup>, O. Čech<sup>c</sup>

<sup>a</sup> Department of Mechanical Engineering, University of Defence, Brno, Czech Rep.

<sup>b</sup> Research Group RG 1-06, CEITEC Brno University of Technology, Brno, Czech Rep.

<sup>c</sup> Department of Electrical and Electronic Technology, Brno University of Technology, Brno, Czech Rep.

In this paper, commercially cold-rolled and artificial aged EN AW 7075 T6 alloy has been used. To ensure increased corrosion resistance, surface hardness, scratching resistance, and aesthetic features were this aluminium alloy subsequently hard anodized and hot-water sealed (AC-A). The hard anodizing and sealing process increased surface hardness up to  $304 \pm 13$  HV1, from an initial surface hardness of  $194 \pm 3$  HV1. Also, the microhardness of the anodized layer and bulk material has been documented. Scanning electron microscopy (SEM) was used for microstructure and trapped  $\eta$  precipitates investigation in the  $42.9 \pm 1.4$  thick formed anodized layer investigation. The corrosion properties of the T6 treated (AC) and hard anodized and sealed (AC-A) EN AW 7075 alloy were evaluated using the anodic potentiodynamic polarization tests (PPT) in a neutral 2.5% NaCl deaerated solution. The corrosion rate CR (mm/y) decreased approx. 39-times for the hard anodized and sealed EN AW 7075 alloy (AC-A), associated with the shift of the  $E_{\text{corr}}$  (mV) to more positive values, decreased  $I_{\text{corr}}$  ( $\mu\text{A}$ ) and increased  $R_p$  (Ohm) values compared to the artificial aged (AC) alloy. Additionally using the laser confocal microscopy, the pitting was evaluated, and the pitting coefficient was calculated as well.

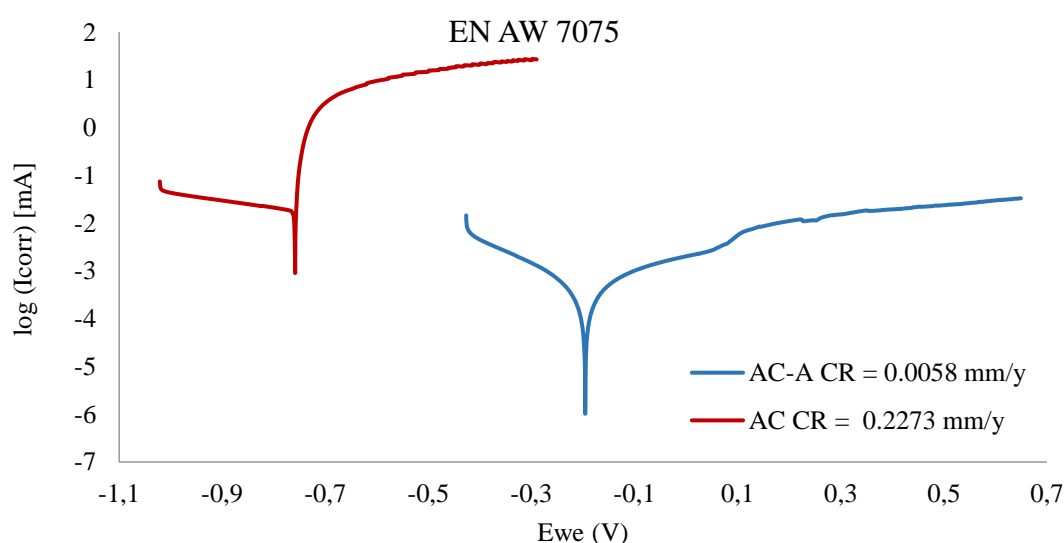


**Figure 1.** PPT curves of artificial aged (AC) and hard-anodized and sealed (AC-A) EN AW 7075 alloy (Biologic SP 150 device, EC-Lab V11.10. software)

## Equivalent Circuit Modelling of Li-S Batteries

M. Mačák<sup>a</sup>, T. Kazda<sup>a</sup>, K. Jaško<sup>a</sup>, P. Vyroubal<sup>a</sup>

<sup>a</sup> Department of Electrical and Electronic Technology, Brno University of Technology, Brno 616 00, Czech Republic

The presented article describes a Multi-Scale Multi-Domain model of a Li-S battery using an equivalent circuit model consisting of R-C pairs. The parameters of the equivalent circuit model were obtained by fitting experimentally measured results from electrochemical impedance spectroscopy at various states of charge. The presented model is able to capture characteristic behaviour of Li-S batteries.

### Introduction

Lithium-sulphur batteries seem to be an interesting candidate for the next generation energy storage. Their main advantage lies in the high energy density and capacity. Sulphur is also environmentally friendly and abundant material (1). To accelerate the practical implementation of these batteries, it is necessary to develop accurate numerical models. While the experimental research is quite profound, the development of new computational models is relatively limited (2, 3). Currently there are two main approaches: physics-based models and 0D equivalent circuit models (4). Current physics-based models are using simplified reactions mechanism, which do not represent the reality closely, while still using a considerable number of parameters (3). In the application-oriented studies, it is not necessary to resolve internal processes and so the equivalent circuit models pose as an ideal alternative (5). This article presents a Multi-Scale Multi-Domain model of Li-S battery implemented into Ansys Fluent software, which can study macroscopic effects.

### Numerical model

The presented numerical model is based on a classic 0D approach integrated to a 3D geometry of a battery. The equivalent circuit model consists of a voltage source, series resistor and two parallel R-C elements.

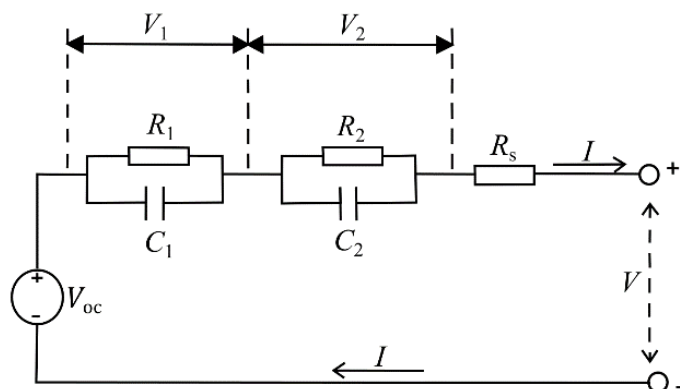


**Figure 1.** 2 R-C model used in the study (6)

In this case, the resulting battery voltage can be simply solved analytically as:

$$V = V_{oc} - R_1 I \left(1 - e^{\frac{-t}{R_1 C_1}}\right) - R_2 I \left(1 - e^{\frac{-t}{R_2 C_2}}\right) - R_s \cdot I \quad [1]$$

The change of state of charge (SoC) is calculated as:

$$\frac{dSoC}{dt} = \frac{I}{3600 Q_{Ah}} \quad [2]$$

This circuit is then solved in the first iteration of a timestep for every computational cell of the battery geometry. In the 3D geometry an equation is solved for positive  $\varphi_+$  and negative potential  $\varphi_-$  (5):

$$\nabla \cdot (\sigma \nabla \varphi) = J \quad [3]$$

Where the current density source term  $J$  is solved as (5):

$$J = \frac{V_{oc} - V_1 - V_2 - (\varphi_+ - \varphi_-)}{R_s \cdot Vol} \quad [4]$$

The model parameters were obtained from an electrochemical impedance spectroscopy measurement at different SoC.

## Results

The circuit parameters were estimated from impedance spectra measured every 20% SoC during a discharge of a 0.1 C. The average error of the fit was 2.7%. A significant change is visible between the characteristics at 100% and 0% and the spectra at 20% - 80 %.

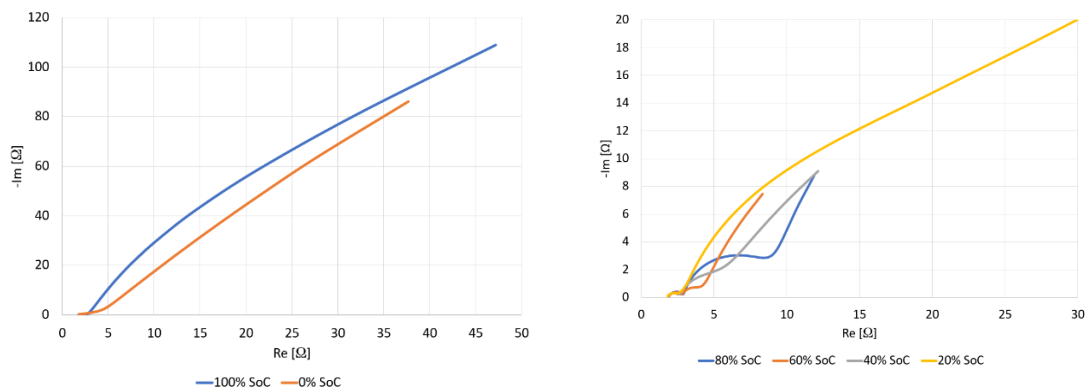


**Figure 2.** Measured impedance spectra at 100 % and 0% SoC (left) and from 20% to 80% SoC (right).

Figure 3 shows the experimental 0.1 C discharge curve and simulated discharge curves for 0.1 C, 0.2 C and 0.5 C. The measured specific capacity of the battery was 866 mAh/g for 0.1 C, while the specific capacity of the simulated battery was 846 mAh/g. The difference between the position of inflection point was quite small (276 mAh/g for the experimental vs 258 mAh/g for the simulation). The positions of plateaus were also in a good agreement.

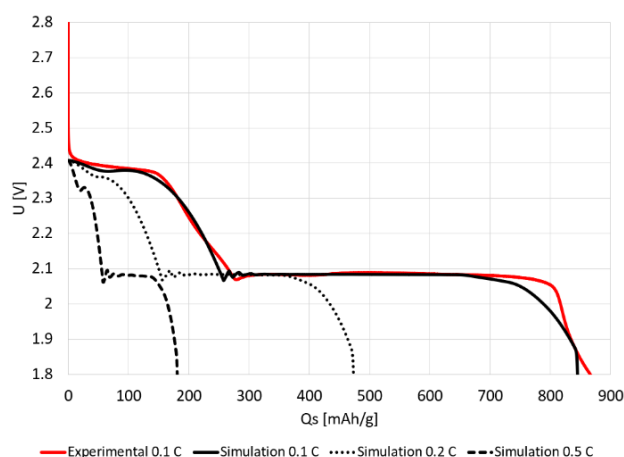


**Figure 3.** Experimental (0.1 C) and simulated discharge curves (0.1 C, 0.2 C and 0.5 C).

### Conclusions

Equivalent circuit modelling is a simple and accurate way to model behaviour of Li-S batteries without knowing their complicated physical nature. The presented model couples the 0D ECM with a 3D macroscopic model while keeping the complexity of the whole model low. The 2 R-C circuit used in this study was able to capture characteristic behaviour of a Li-S battery. The main differences, such as oscillations near the inflection point or slower voltage drop near the end of the discharge were caused by a small amount of measurement points for impedance spectra and by the circuit itself. For a more precise simulation a circuit consisting of more R-C elements should be used.

### Acknowledgments

This work was supported by the BUT specific research program (project No. FEKT-S-20-6206).

### References

1. A. F. Hofmann, D. N. Fronczek, and W. G. Bessler. *Journal of Power Sources*, **259**, pp. 300-310 (2014).
2. Z. Deng, Z. Zhang, Y. Lai, J. Liu, J. Li, and Y. Liu. *Journal of The Electrochemical Society*, **160**(4), pp. A553-A558 (2013).
3. K. Kumaresan, Y. Mikhaylik, and R. E. White. *Journal of The Electrochemical Society*, **155**(8) (2008).
4. A. Fotouhi, D. J. Auger, K. Propp, and S. Longo. *IET Power Electronics*, **10**(11), pp. 1289-1297 (2017).
5. S. Jung and D. Kang. *Journal of Power Sources*, **248**, pp. 498-509 (2014).
6. P. Vyroubal and T. Kazda. *Journal of Energy Storage*, **15**, pp. 23-31 (2018).

## Modelling of Electrochemical Magnetohydrodynamics in Ansys Fluent

M. Mačák<sup>a</sup>, P. Vyrubal<sup>a</sup>

<sup>a</sup> Department of Electrical and Electronic Technology, Brno University of Technology, Brno 616 00, Czech Republic

The presented article describes a simulation of a magnetohydrodynamically enhanced electrochemical reaction using a custom model implemented into Ansys Fluent. The applied magnetic field can increase the mixing of fluids, which also accelerates the transport of species towards the electrode surface.

### Introduction

Electrochemical magnetohydrodynamics (MHD) is an important area in the field of microfluidics or lab-on-chip applications. By introducing a magnetic field into the domain, it is possible to control the flow of weakly conducting fluids, which are commonly used in biomedical applications (1). The main advantage of MHD is that it does not require any moving mechanical parts and is not limited by dimensions of microfluidic devices (2). The application of CFD simulation can bring more insight into the overall process as it is difficult to study individual parts separately. The presented article presents a custom electrochemical and MHD model implemented into a CFD software Ansys Fluent. The model is used to simulate a cyclic voltammetry in the presence of a magnetic field.

### Numerical model

The presented numerical model consists of three parts: species transport (3), electrochemistry (4) and MHD (5). The fluid flow is described by single phase Navier-Stokes equations, which use a mixture approximation (3). The transport of individual species is governed by diffusion and convection. Electrochemistry and MHD were implemented into Ansys Fluent using User Defined Scalars and User Defined Functions. Kinetics of electrochemical reactions are described by a Butler-Volmer reaction (4), which was implemented into wall surface reactions, while the electric field is described by Poisson's equation. The magnetic field is described by Maxwell equations (5). As User Defined Scalars are governed by a general transport equation, the governing equation for magnetic flux density was described through the magnetic vector potential. The effect of electromagnetic field on the fluid flow was described through the Lorentz force (2). The current density in the computational domain is solved as (1):

$$\mathbf{j} = nFD\nabla c \quad [1]$$

### Results

A simulation of cyclic voltammetry in the presence of a magnetic field was carried out. The length of the electrode was 1 mm. A simple one electron electrochemical reaction was considered, in which both the product and reactant had same properties ( $D = 1e^{-9} \text{ m}^2\text{s}^{-1}$ ). The standard reduction potential of the reaction was set to 0 V and the speed of the scan was set to  $0.01 \text{ Vs}^{-1}$ . The magnetic

flux density was set to 2 T. Figure 1. shows the resulting voltammogram. It is possible to see the change from the classic shape towards the response of a micro-electrode.

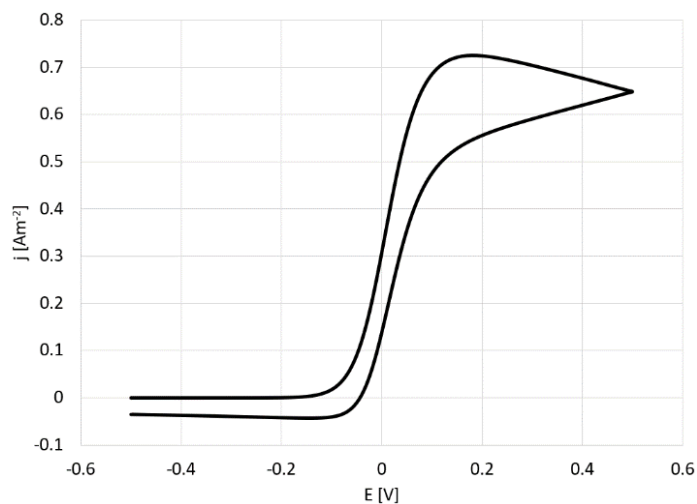


**Figure 1.** Resulting voltammogram in the presence of a magnetic field

The influence of the magnetic field on the species transport is shown in Figure 2. Due to the concentration gradient a current is formed, which is then used in the momentum source term. Based on the direction of the magnetic field, it is possible to control the fluid flow.

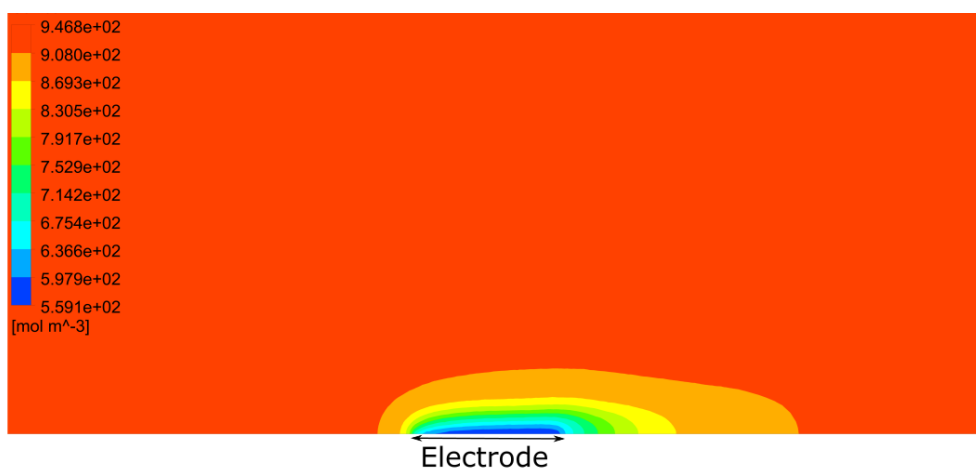


**Figure 2.** Concentration distribution in the presence of a magnetic field at time  $t = 1500$  s.

Vortices, which are formed are shown in Figure 3. The maximum velocity was around  $20 \mu\text{m}\cdot\text{s}^{-1}$ . As the concentration gradient became more asymmetric, the position and intensity of vortices changed.

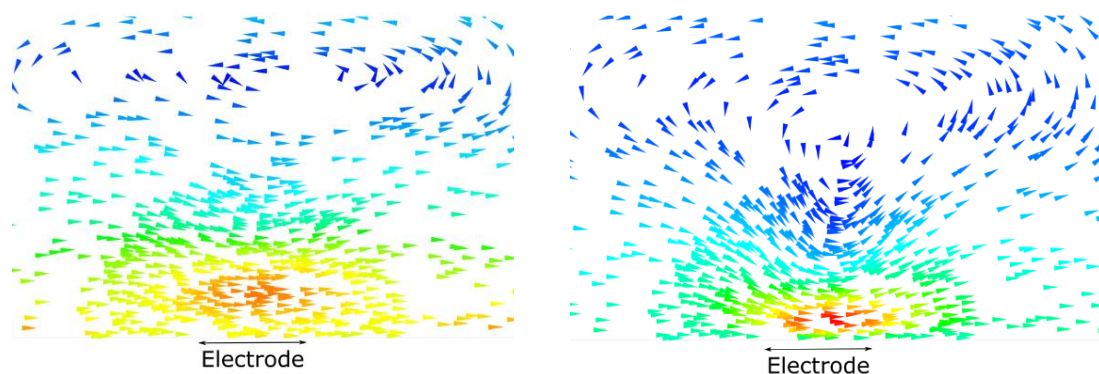


**Figure 3.** Velocity vectors at times  $t = 500$  s (left) and  $t = 1500$  s (right).

### Conclusions

The presented model is able to describe electrochemical phenomena coupled with MHD effects. With the application of magnetic field, it is possible to control the flow or increase the mixing of fluids. As a result, it is possible to increase the transport of species towards the electrode, which will accelerate the electrochemical reaction. In this case, the current density is dependent only on the number of electrons exchanged, diffusion coefficient and the concentration gradient. To increase the mixing of a defined solution it would be necessary to increase the magnetic flux density.

### Acknowledgments

This work was supported by the BUT specific research program (project No. FEKT-S-20-6206).

### References

1. D. Sen, K. M. Isaac, N. Leventis, and I. Fritsch, *International Journal of Heat and Mass Transfer*, **54**(25-26), pp. 5368-5378 (2011).
2. M. I. Hasan, A. J. F. Ali, and R. S. Tufah, *Engineering Science and Technology, an International Journal*, **20**(3), pp. 982-989 (2017).
3. A. L. Whitworth, D. Mandler, and P. R. Unwin, *Phys. Chem. Chem. Phys.*, **7**(2), pp. 356-365 (2005).
4. P. Vyroubal, J. Maxa, T. Kazda, and J. Vondrak, *ECS Transactions*, **48**(1), pp. 289-296 (2014).
5. P. Fiala, R. Kadlec, and J. Zukal, *2019 12th International Conference on Measurement*, pp. 295-298 (2019).

## Effects of Hybrid Surface Treatment Composed of Plasma Nitriding and CrN Coating on Friction-Wear Properties and Adhesion Strength of Stainless Steel

Huu Chien Nguyen, Emil Svoboda, Jiří Prochazka

UNOB - University of Defence in Brno, Brno, Czech Republic, EU, [huuchien.nguyen@unob.cz](mailto:huuchien.nguyen@unob.cz)

This study was conducted to investigate the effect of hybrid surface treatment composed of plasma nitriding (PN) and chromium nitride (CrN) coating on the friction-wear properties, adhesion strength of AISI 316L stainless steel. The CrN coatings with the thickness of 1.0  $\mu\text{m}$  and 2.1  $\mu\text{m}$  were formed on the surfaces of both substrates with plasma nitriding (PN/CrN coating) and without plasma nitriding (CrN coating). The plasma nitriding, CrN coating, and the hybrid treatment combining them improved markedly the friction-wear properties of the stainless steel. The plasma nitriding generated a hardened layer between the soft substrate and the thin hard coatings and improved markedly friction-wear properties of the CrN-coated stainless steel and the adhesion of the CrN coatings.

**Keywords:** Stainless steel, plasma nitriding, CrN coating, adhesion, friction-wear properties

## Battery Monitoring System using Microcontroller ESP32 and Internet of Things

P. N. Nam<sup>a</sup>, J. Leuchter<sup>b</sup>, P. K. Lam<sup>b</sup>, R. Bystřický<sup>b</sup>, and D. Q. Huy<sup>c</sup>

<sup>a</sup> Department of Communication Technologies, Electronic Warfare and Radiolocation, University of Defence, Brno, Czech Republic

<sup>b</sup> Department of Aviation Technology, University of Defence, Brno, Czech Republic

<sup>c</sup> Viettel Group, VIETNAM

This paper deals with designing and implementing a battery management system (BMS) for autonomous devices, using batteries as the power source. BMSs are now available in packaged form as an integrated chip. However, these chips are often expensive and not available in the Czech market. Besides, their ability to integrate custom functions, especially function wireless communicating between BMS and work station, is limited. In practice, monitoring the state of the battery during the device operation is very important to devise a suitable operating tactic. This work is aiming to design a module that can measure and estimate the parameters of the several batteries in an autonomous device and wirelessly send the measured data to the workstation for monitoring and analysis during the device's operation.

### Introduction

Since the late 19th century, unmanned devices have been used in wars to minimize human casualties. Since then, this field has not stopped growing and becoming popular, not only in the military. Today, we can be exposed to unmanned devices right in our homes. The development trends of unmanned devices are the decrease in size, mass as well as noise, and the increase in range of operation. Closely related to this trend is the issue of source parts. Combustion engines are too noisy, heavy and polluted, so nowadays people mainly use electric drivers. These drivers used to be powered by lead-acid batteries; however, these batteries were too heavy and their life cycles were too short. Therefore, they are gradually replaced by Nickel batteries and the most modern ones, Lithium batteries. Tab. 1 shows the outstanding advantages of Lithium batteries compared to other types of batteries.

A lithium battery is usually a combination of many similar battery cells connected in series and parallel. Therefore, during usage, Lithium batteries require BMS to ensure safety. The BMS has the function of managing batteries' state of charge (SOC), as well as battery protection. Battery protection function, especially against disbalance (voltage difference between cells), is not mentioned in this paper. This paper focuses helping a workstation or control station monitor the status of the several batteries in an autonomous device during the device's operation. Communication between the workstation and the device is ensured by the Internet of Things technology. For this purpose, the main part of the system is the microcontroller ESP32, which is low-cost, low-power, popular in the market. ESP32 has integrated the function of wireless communication and the ability to transfer data wirelessly via Bluetooth, Wi-Fi, or ESP-NOW. ESP-NOW is a protocol for wireless communication using bandwidth 2,4GHz, similar to Wi-Fi, with lower consumption.

**TABLE 1.** Typical types of batteries

Type of Battery	Voltage per cell [V]	Self-discharge [%/month]	Life cycle [cycle]	Energy density [Wh/kg]	Energy density [Wh/L]
Lead-Acid	1.80 – 2.10	4 – 8	500 – 700	< 40	< 90
Ni-Cd	0.85 – 1.35	10 – 15	500 – 1000	< 40	< 100
Ni-MH	0.85 – 1.35	15 – 30	500 – 1000	≈ 100	≈ 400
Li-Ion	3,00 – 4.20	≈ 2	> 1000	> 200	> 550

### Model of Battery and Estimate the battery’s SOC

This part deals with methods of estimating the battery’s SOC. Currently, there is no exact method to measure the battery's SOC, so we can only estimate it according to 3 main methods. The first is Open Circuit Voltage Method (OCV). This method is the simplest but not suitable for our system because it requires the battery to be disconnected from an electrical circuit and not under any load. The next is Battery Internal Resistance Method (BIR). This method is complex that requires accurate and complex gauging devices; therefore, it is not suitable for our system. The third is the Coulomb Counting Method - CCM. This method estimates the SOC of the battery base on measuring current. The amount of electric charge flowing in (out) battery is the product of current and time.

### Hardware design

The device consists of 3 main blocks: control block, power block, and sensor block. The control block is the microcontroller ESP32 that controls the operation of the whole system and sends data to the workstation. The sensor block can measure the current, voltage, and temperature of the battery, as well as measure the voltage of each cell. From the measured data, the system will estimate the battery's SOC according to the CCM method. The power block converts battery voltage to 5V and 3.3V for microcontrollers and sensors.

### User interface

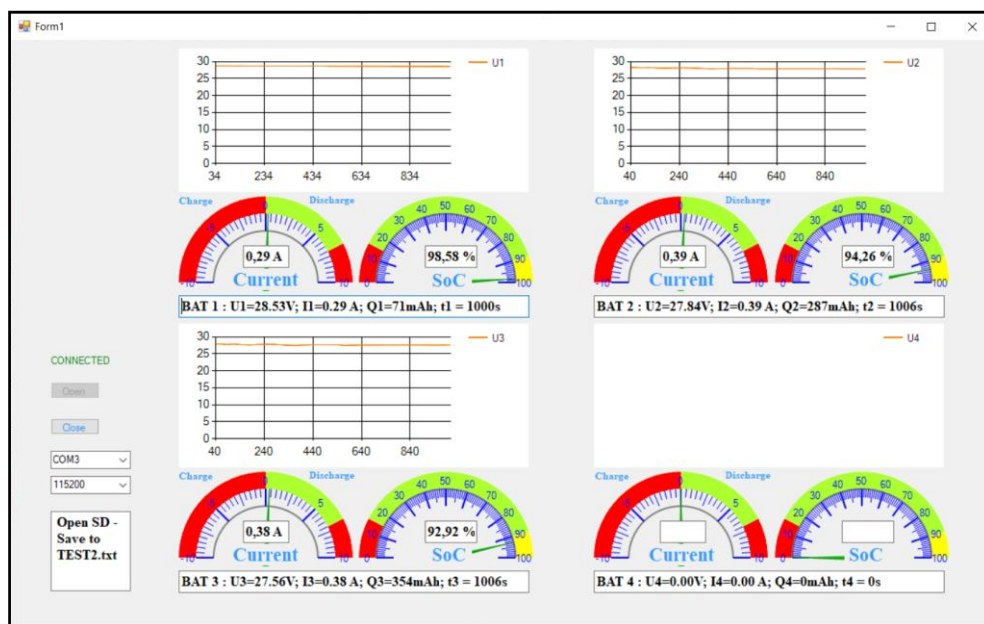


**Figure 1.** User interface in C#.

## Experiments and result

The system after calibration is implemented in autonomous devices in the University of Defence. The measured data show that the error of the system is smaller than 0.03 V (measuring voltage in range 0 – 35 V), 0.2 A (measuring current in range 0 – 20 A) and 0.1 °C (measuring temperature in range -20 – 100 °C). The system has ability to estimate the battery's SOC with the error smaller than 5 % when the battery is in the cycle charge–discharge (see Fig. 3).



*Figure 2. Implementation system in device.*

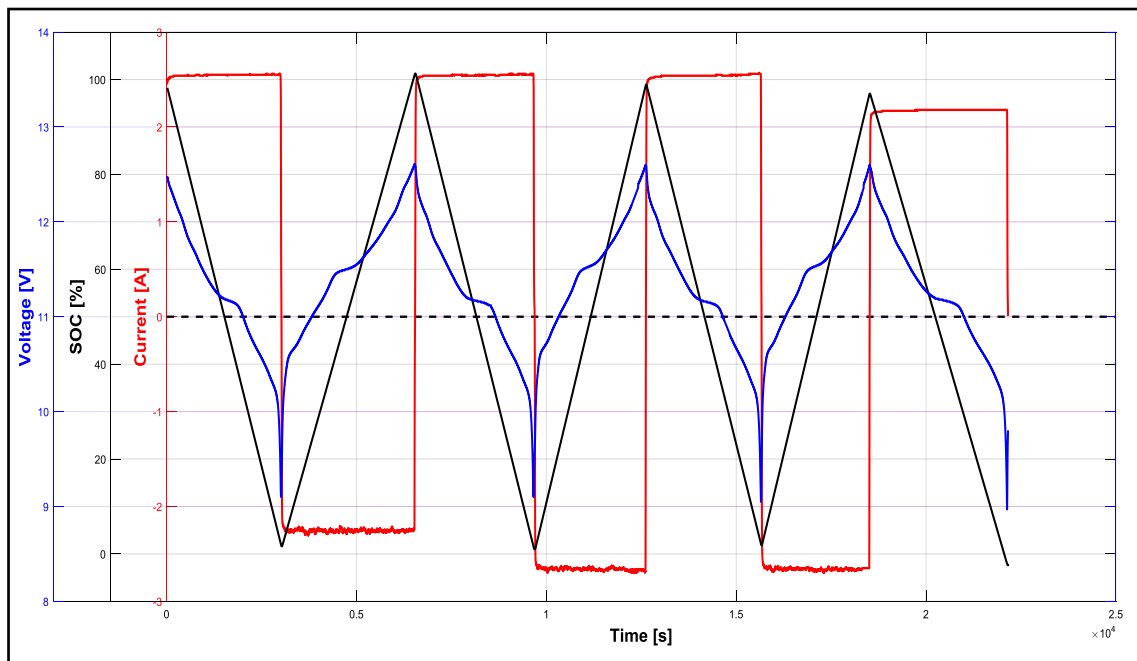


*Figure 3. The result of measurement in 6 hours (process of 4 discharging, 3 charging).*

## Acknowledgments

The work presented in this paper has been supported by the specific research project of the Faculty of Military Technology SV20-206/2, the University of Defence in Brno.

## Dielectric properties of nanocomposites based on epoxy resin

H. Polsterová

Ústav elektrotechnologie, VUT v Brně, Technická 10, Brno, CZ  
E-mail: polstera@feec.vutbr.cz

Nanocomposites are subject of research in many fields of science. Electrical technology focused on the study of electrical properties of nanocomposites including breakdown strength, relative permittivity, resistivity and other. This paper describes the results of measurement of electrical parameters of a nanocomposite at various temperatures. The nanocomposite matrix was casting epoxy resin and nanoparticles were made of TiO<sub>2</sub> powder at different concentrations.

### Preface

Nanotechnologies is one of the most rapidly developing scientific discipline. They are applied both in communication technologies and in power electrical engineering in the field of electrical engineering. In power electrical engineering, attention is focused primarily at nanocomposite materials, which are expected to improve mechanical and electrical properties. The mechanisms of electrical conductivity of nanocomposites in the presence of an electric field have not been fully elucidated yet. They are the subject of a number of studies, some of which are trying to explain the phenomena taking place at the interface around the nanoparticles (1), others investigate the electrical or mechanical properties of nanocomposites. (2), (3), (4).

This paper purpose with studying of the electrical properties of a nanocomposite whose matrix was casting epoxy resin and titanium dioxide (TiO<sub>2</sub>) nanoparticles were used as filler.

### Theoretical basis

In an ideal nanocomposite are filler particles, with dimensions ranging in nanometres, uniformly dispersed in a homogeneous matrix. The distance  $d$  between the particles decreases with increasing concentration and if the particle diameter  $r$  is small, very rapidly even at low concentrations as well. However, the distance  $d$  depends not only on the concentration of the particles but also on the relative densities of the filler and the matrix:

$$d = r \left\{ \left[ \frac{4\pi}{3} \left( 1 + \frac{1-F}{F} \frac{\rho_f}{\rho_m} \right) \right]^{\frac{1}{3}} - 2 \right\} \quad [1]$$

where:  $F$  percentage by mass of filler,  
 $\rho_f$  filler density,  
 $\rho_m$  density of the base material (1).

At the contact places between the matrix and the particles, an interface is formed in which the properties of the nanocomposite change gradually from those of the particle to those of the surrounding matrix. The interface surrounds the particle to a distance of a few nanometres. The

contact of the particle with the underlying matrix can lead to the formation of a new phase with properties different from both the matrix and the filler properties. These could have a decisive influence on the properties of the nanocomposite.

### Experimental procedure

The experimental specimens were made of four-component casting epoxy resin. Titanium dioxide (TiO<sub>2</sub>) nanoparticles made by firm Sigma-Aldrich were chosen as filler. The maximum diameter of the nanoparticles was 25 nm and their nominal diameter was 5 nm. A spherical shape of the nanoparticles was assumed.

The purity of the TiO<sub>2</sub> powder is reported by the manufacturer to be 99.7 % and the surface area from 200 to 220 m<sup>2</sup>g<sup>-1</sup>. The particles are prepared by calcination at the temperature of 300 °C. For the experiment a filling range from 0.5 to 8 weight percentage of filler was chosen based on information from the literature (2).

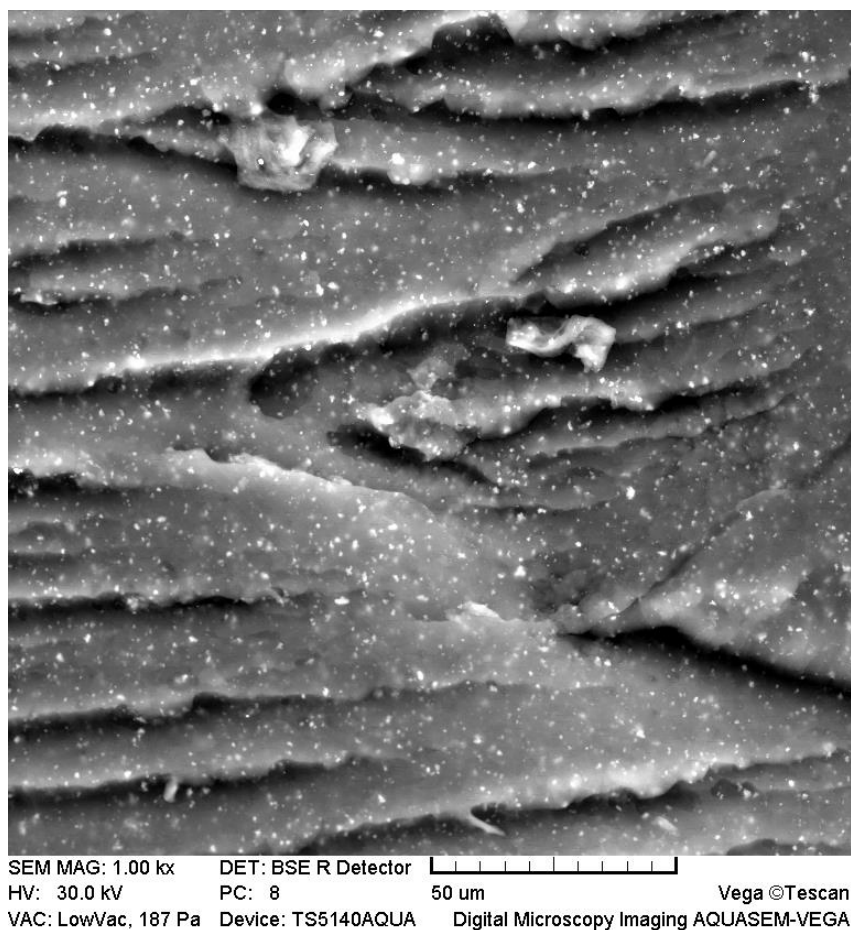


**Figure 1.** Image of a sample containing 5 % of TiO<sub>2</sub> filler – internal structure of the sample multiplied by 1000×.

The preparation of the experimental samples in the form of planar plates was very difficult. The mould walls had to be very carefully coated with a silicone vaseline separator. In order to successfully cast the samples into the mould, the resin had to be heated to 65 °C to reduce its viscosity. In the prepared container, a selected amount of filler nanoparticles was mixed into the resin. The mixture was mixed mechanically in the first stage, followed by mixing the mixture in a water bath using

ultrasonication, again at 65 °C. During the mixing of the epoxy resin components as well as the addition of the nanofiller, a large amount of air was introduced into the mixture on the samples, therefore the prepared mixture had to be vacuumed very carefully. Vacuuming had to be done again at elevated temperature to reduce the viscosity of the prepared mixture and to facilitate vacuuming. Especially for the mixtures for the production of samples with a higher nanofiller content, i.e., 5 % and 8 %, the mixture had to be vacuumed for quite a long time, up to several hours.

After removing the air from the mixture, the mixture was poured into a prepared, pre-heated mould. This was followed by further vacuuming of the mixture to remove any air that may have entered the mixture during the pouring of the mixture into the mould. The curing process was carried out in two stages: first, pre-curing at 90 °C for 3 hours, removing the samples from the mould, and then post-curing at 140 °C for 10 hours.

The dispersion of nanoparticles in the epoxy matrix was observed using a VEGA TESCAN environmental scanning electron microscope (REM). Figure 1 shows an image of a sample containing 5 weight percentage filler. Despite efforts to perfectly mix the filler in the mixture, it is evident that the nanoparticles form small clumps in the sample material. The samples were placed in a desiccator in which zero relative humidity was maintained.

Measurements of the electrical parameters of the samples were always performed on a set of ten samples with identical nanoparticle loading in the chamber at zero relative humidity to ensure stable measurement conditions.

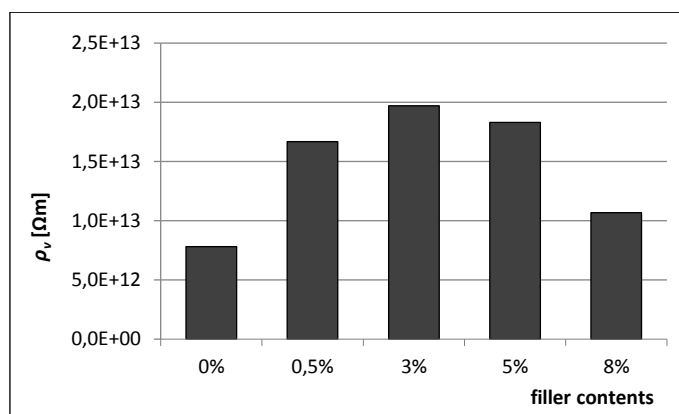


**Figure 2.** Dependence of internal resistivity on filler content for 60 °C

In the experiment, the temperature dependences of internal resistivity, relative permittivity and loss factor were measured in the temperature range from 20 °C to 120 °C. At temperatures of 20 °C and 40 °C, the differences in the measured values of the monitored quantities were inconclusive; the effect of filling the samples with nanoparticles was more pronounced at higher temperatures.

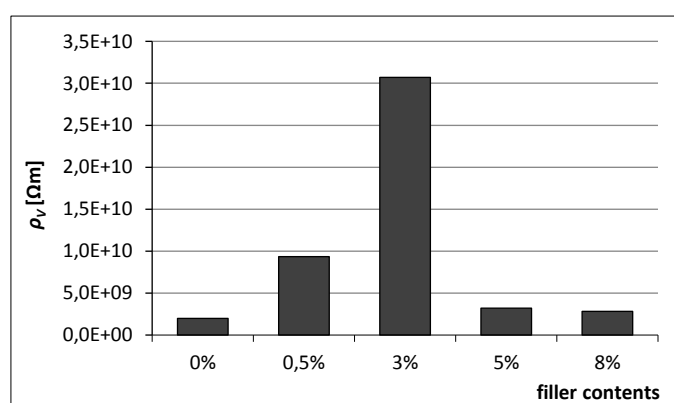


**Figure 3.** Dependence of internal resistivity on filler content for 100 °C

The internal resistivity of samples with different weight percentages of nanoparticle filling at 60 °C is shown at Figure 2, while Figure 3 shows the same dependence for 100 °C. As the temperature increases, the predicted values of internal resistivity decrease. However, an increase in values of internal resistivity for 3 % nanoparticle loading can be observed in both plots.

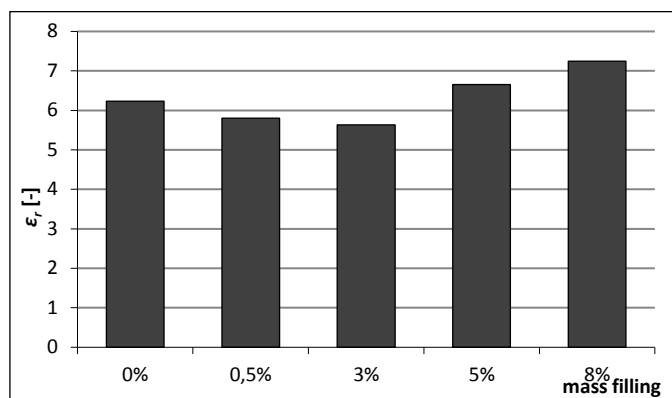


**Figure 4.** Dependence of relative permittivity on filler content for 60 °C

The dependence of the relative permittivity on the filler content at 60 °C and 100 °C is shown in Figure 4 and Figure 5. At 60 °C, the relative permittivity values for the unfilled sample and the samples filled with 0.5 % and 3 % filler are approximately the same, the increase in relative permittivity values is noticeable for 5 % and 8 % filling. At 100 °C, the trend of the relative permittivity values is similar, again the sample with 3 % nanoparticle filling shows the lowest value.

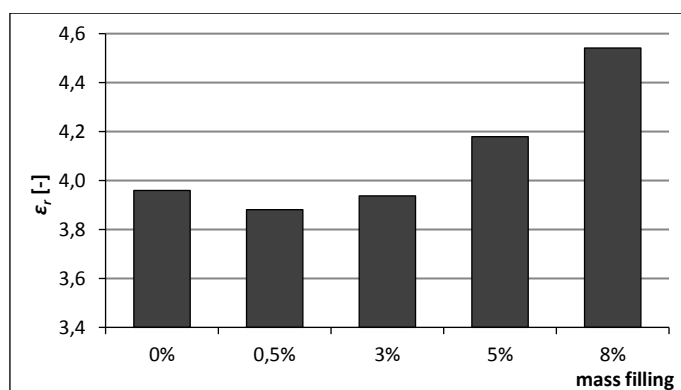


**Figure 5.** Dependence of relative permittivity on filler content for 100 °C

The dependence of the loss factor on the filler content for temperatures of 60 °C and 100 °C are shown in Figure 6 and Figure 7.

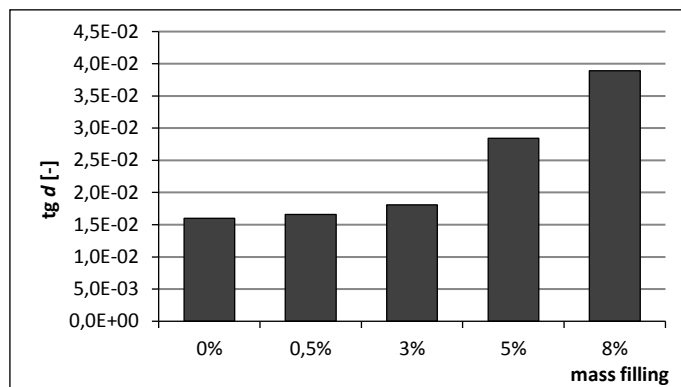


**Figure 6.** Dependence of loss factor on filler content for 60 °C

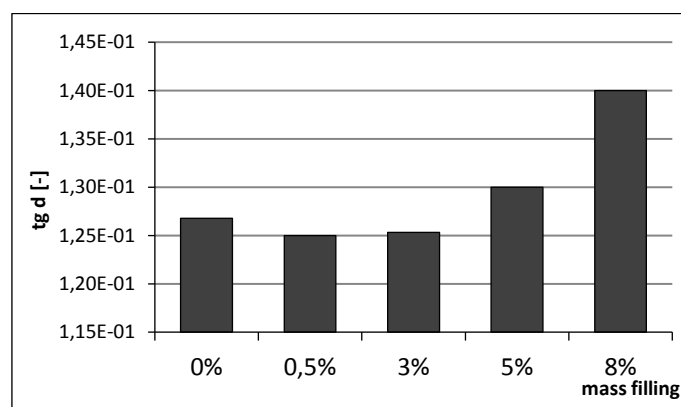


**Figure 7.** Dependence of loss factor on filler content for 100 °C

A noticeable increase in loss factor values can be observed for the 5 % and 8 % fillings at 60 °C. In contrast, samples with 0,5 % and 3 % filler content at 100 °C show approximately the same loss factor values. A slight increase in values is again observed for samples with higher nanoparticle fillings.

## Conclusion

The electron microscope images show that the desired dispersion of TiO<sub>2</sub> nanoparticles in the epoxy matrix could not be achieved. Nevertheless, the influence of the nanofiller was evident in the experiment. By filling with nanoparticles, the material increased its density and thus its strength, but its elasticity decreased.

The electrical properties of the epoxy resin itself, from which the samples were made, are very good. Nevertheless, at elevated temperatures, an increase in internal resistivity values and a decrease in relative permittivity can be observed for the samples with filler contents of 0,5 % and 3 % by weight. The values of the loss factor do not differ much from each other for the samples with lower filler content, but they increase for the samples with 5 and 8 % filler content. At higher filler content, the percolation threshold is probably already exceeded, the material is oversaturated with nanoparticles. This fact is also reflected in the values of the observed electrical properties.

### Acknowledgments

This work was created with financial support for a specific research project at the Brno University of Technology FEKT-S-20-6206.

### References

1. J. T. Lewis, Nano-Composite Dielectrics. *The Dielectric Nature of the Nano-Particle Environment*, IEEE Trans. FM, vol. **126**, no.11 pp. 1020–1030 (2006).
2. S. Singha, M.J. Thomas, *Dielectric Properties of Epoxy Nanocomposites*. IEEE Trans. on Dielectrics and Electrical Insulation, vol. **15**, no.1, pp. 12–23 (2008).
3. P. Maity, P. K. Poovamma, S. Basu, V. Parameswaran, N. Gupta, *Dielectric Spectroscopy of Epoxy Resin with and without Nanometric Alumina Fillers* IEEE Trans. on Dielectrics and Electrical Insulation, Bangalore, India, pp.1481-1488 (2009).
4. A. Chatterjee, M. S. Islam, Fabrication and Characterization of TiO<sub>2</sub> -Epoxy Nanocomposite. *Materials Science and Engineering A* 487, IEEE, pp. 574-585 (2008).

## **Electrical circuit model of Lithium-ion batteries and revisiting of its parametrization procedures**

Anna Pražanová<sup>a</sup>, Václav Knap<sup>a,b,c</sup>

<sup>a</sup> Faculty of Electrical Engineering, Czech Technical University in Prague, Czech Republic

<sup>b</sup> GomSpace A/S, Aalborg Denmark

<sup>c</sup> Department of Energy Technology, Aalborg University, Aalborg, Denmark

Lithium-ion (Li-ion) batteries found their way into a wide range of applications. Nowadays, they are the key technology for electric vehicles. They participate in the integration of renewable energy sources via stationary energy storage systems, and they have even enabled the miniaturization of satellites into currently popular CubeSats. When Li-ion batteries are used, there is a great demand for knowing their State-of-Charge (SOC), as it brings customers' comfort, allows planning, which leads to more efficient use, and it is a base for many State-of-Health (SOH) estimation methods. Popular SOC estimation methods require a battery model, and it applies that better the model, better the estimation. Thus, a well-established electrical circuit model (ECM) is used, and by revisiting the steps leading to its parameters, it is an intention to improve its accuracy.

Therefore, the model is methodologically developed from multiple steps to accurately capture a battery behavior (e.g., SOC, hysteresis, impedance). The selected steps respect the essential characteristics of Li-ion batteries and are formed by a suitable combination of measurements and parametrization algorithms. Parameters dependence on SOC was monitored during the analysis of the parametrization procedure. The temperature dependence of the parameters was considered as well, and the experiments were performed for various temperature levels.

After revisiting parametrization procedures, the ECM is validated to obtain its resulting accuracy by using different measurement profiles. It is obvious that changes in selected parameterization/ testing steps of the model affected its resulting accuracy. The developed ECM combines the requirements for accuracy with consideration of changes in regular measurement procedures.

This work describes the effects of individual parametrization steps on the accuracy of ECM by revisiting applied parametrization procedures leading to its improvement and provides a basis for change of perspective to the measurement routines. In the future, the ECM will be extended by more measurement profiles, which will enable a deeper insight into determining the accuracy of the models and behavior of Li-ion batteries.

## Modification of surface structure by diffusion processes

J. Prochazka<sup>a</sup>, D. Dobrocky<sup>a</sup>, Z. Joska<sup>a</sup>, H. Ch. Nguyen<sup>a</sup>, J. Sedláček<sup>b</sup>, J. Sedlák<sup>c</sup>, A. Polzer<sup>c</sup>,  
and P. Sliwková<sup>c</sup>

<sup>a</sup> Department of Mechanical Engineering, Faculty of Military Technology, University of Defence,  
Brno 662 10, Czech Republic

<sup>b</sup> MORAVIA CANS a. s., Tovární 532, 687 71 Bojkovice, Czech Republic

<sup>c</sup> Brno University of Technology, Faculty of Mechanical Engineering, Institute of Manufacturing  
Technology, 616 69 Brno, Czech Republic

**Key words:** Diffusion technology, gaseous ferritic nitrocarburizing, case-hardening steel, microhardness, nitriding hardness depth, wear resistance

Surface technologies are currently considered as an integral part of engineering. Theirs utilizing provides possibilities of surface parameters modifications that includes e.g. hardness, wear resistance or corrosion resistance. Therefore, lower requirements on material's properties but not on its quality can be placed and thus manufacturing costs can be reduced. The most common technological procedures are based on a creation of surface layers or coatings. The quality of such treated resulting surfaces especially of components with highly exposed surfaces depends on machining as well as on the quality of the material (1). Hence, a chemical composition and a presence of undesired inclusions is also necessary to verify in steels as well as in other Fe and Al based alloys.

In cases of mechanically highly exposed components different parameters of surface and core microstructure are demanded. Whereas, in the case of such components, the surfaces to high pressure, abrasion or to corrosive environment must be resistive, in the core high toughness is required. Such combination of the properties we are able to obtain, among others, by heat treatment i.e. surface hardening or by chemical-heat treatments which also include the most frequently utilized carburizing as well as low temperature technologies such as nitriding and ferritic nitrocarburizing (2). The chemical heat-treatments are diffusion based technologies which utilize a saturation of treated components surfaces by chemical elements from an atmospheres rich in these elements. In case of the carburizing, the surfaces of a low carbon steels by carbon from solid, liquid or gaseous atmospheres are saturated. Due to a higher carbon solubility in  $\gamma$ -Fe lattice, the carburizing taking place at temperatures in range from 850 °C to 950 °C (2, 3, 4).

The interstitial element diffuse further into the microstructure inwardly to the component's core. Hence, a chemical composition of the microstructure alter gradually in the surface vicinity. An increase of the carbon content in the surface microstructure cause an increase of its hardenability by quenching which always follows the carburizing. By a rapid cooling within quenching atoms are confined in the lattice with restricted possibility to diffuse (3). An internal stress in the microstructure is accumulated and led into a martensitic transformation. The martensite is hard and brittle structure, hence tempering should be performed subsequently. During the tempering a residual stress contained in the microstructure is decreased. By this procedure, the brittleness as well as hardness are reduced. The product of the procedure described above is a deep, hard and wear resistive surface layer which mostly provide enhancement of a service life of the components. Unfortunately, the manufacturing to some problems relating to the carburizing must face. A component distortion and thus dimensional inaccuracy could be caused by quenching. Occurrence of cracks after quenching is not rare too (5).

Therefore, in case of components of heavy duty vehicles, power plants or mill plants and especially military vehicles and weapons systems, where high requirements on components quality are placed, different surface treatments are being looked for.

Hence, one such technology providing a better dimensional precision of treated components is gaseous ferritic nitrocarburizing. The ferritic nitrocarburizing as well as nitriding is a low temperature chemical heat-treatment. Such treatments are taking place at temperatures around 550 °C and hence no structural transformation occurs during cooling of the treated components (3, 4). Contrary to the carburizing, where martensitic structure is responsible for the hardness increase, in case of the low temperature chemical heat-treatments alloying elements present in the microstructure and their ability to create hard compounds is utilized (6). During the gaseous ferritic nitrocarburizing the interstitial elements carbon and nitrogen by the component's surface from gaseous atmosphere are adsorbed. The elements dissolve in the microstructure and a creation of compounds is started. In cases of the ferritic nitrocarburizing and the nitriding, three different areas of the microstructure it is possible to distinguish. On the top of the surface a white layer composed of  $\epsilon - (\text{Fe}_{2-3}\text{N})$  or  $\epsilon$  and  $\gamma' - (\text{Fe}_4\text{N})$  is created (7, 8). The second area is called a diffusion layer (9). It consists of a dispersion of nitrides and carbides in the origin microstructure. The last one is a transition area between the diffusion layer and the original microstructure.

As well as carburizing an application of the mentioned low temperature chemical-heat treatments also provide an increase of the hardness, fatigue and the wear resistance and moreover, contrary to carburizing, a surface corrosion resistance is also enhanced (10, 11, 12).

Therefore, in the paper the selected case-hardening steel 18CrNiMo7-6, primarily predetermined for carburizing, frequently utilized in manufacturing of gears, helical gears, pins, shafts, bearings etc. (13), was ferritic nitrocarburized and subsequently subjected to the experimental measurements.

For a verification of the chemical composition the spark discharge based optical emission spectrometer Tasman Q4 was used by utilizing Fe110 method. The microstructure observation and the determination of the white layer thickness was performed on the Opto-digital microscope Olympus DSX500i. The nitriding hardness depth of the surface layer from the microhardness profiles obtained by the microhardness tester LM247 AT LECO was deduced according to ISO 18203:2016(E) (14, 15). The wear resistance was assessed by utilizing the Scratch test method performed on the tribometer Bruker UMT-3 TriboLab.

Results of the measurements present an effect of gaseous ferritic nitrocarburizing on the surface properties of the steel 18CrNiMo7-6 and provide a perception of possibility to substitute the frequently utilized carburizing by the gaseous ferritic nitrocarburizing.

### Acknowledgments

This work was supported by the specific research project 2020 "SV20-216" at the Department of Mechanical Engineering, University of Defence in Brno and the Project for the Development of the Organization "DZRO Military autonomous and robotic systems" and by the grant „Application of the New Surface Treatment Technologies in Metal Packaging Industry“, PID: FV40313, Ministry of Industry and Trade, The Czech Republic.

### References

1. I. Barenýi, J. Majerik, Z. Pokorný, J. Sedlak, J. Bezečný, D. Dobrocký, A. Jaros, M. Eckert, J. Jambor and R. Kusenda. *Material and technological investigation of machined surfaces of the OCHN3MFA steel*, vol. 57(2), pp. 131-142, Metallic Materials, (2019).
2. J. L. Dossett and H. E. Boyer, *Practical Heat Treating*, 2<sup>nd</sup> ed., p. 301, ASM International, OH (2006). ISBN: 0-87170-829-9
3. L. Ptáček, *Nauka o materiálu II*, CERM, p. 350, Brno (1999), ISBN 80-7204-130-4.
4. J. R. Davis, *Surface Engineering for corrosion and wear resistance*, p. 279, ASM International, USA (2001).
5. P. Hiremath, Sharma S, M.C. Gowrishankar, Shettar M, B.M. Gurumurthy. *Effect of post carburizing treatments on residual stress distribution in plain carbon and alloy steels – a numerical analysis*, vol. 9(4), pp. 8439-8450, Journal of Materials Research and Technology (2020). Doi: 10.1016/j.jmrt.2020.05.104
6. M. Pospichal, R. Dvorakova, Z. Studený, Z. Pokorný, *Influence of initial carbon concentration on nitride layers*, vol. 15(5), pp. 889-893, Manufacturing technology (2015).
7. D. Pye. *Practical Nitriding and Ferritic Nitrocarburizing*, p. 256, ASM International, USA (2003).
8. Z. Pokorný, V. Hruby, *Plasma Nitriding of Deep Narrow Cavities*, vol. 465, pp. 267-270, Key Engineering Materials (2011).
9. Z. Pokorný, J. Kadlec, V. Hruby, Z. Joska, D. Q. Tran, D. Beran, *Plasma nitriding of bored barrels*, vol. 6(1), pp. 69-76, Advances in Military Technology (2011).
10. D. Kusmic, T. V. Doan, O. Pilch, M. Krbata, *Corrosion resistance and tribological properties of plasma nitrided and tenifered 42CrMo4 steel*, pp. 1103-1108, METAL (2016). ISBN 978-80-87294-67-3.
11. Z. Studený, Z. Pokorný, D. Dobrocký, *Fatigue properties of steel after plasma nitriding process*, pp. 1175-1180, METAL (2016), ISBN 978-80-87294-67-3.
12. Z. Studený, D. Kusmič, *Influence Of Inclusions Size On The Nitrided Components Fatigue Life*, 23rd International Conference on Metallurgy and Materials. Brno: TANGER Ltd., Ostrava (2014). ISBN 978-80-87294-52-9.
13. N. Samroeng and P. Srichandr, *Failure of a Helical Gear in a Power Plant*, vol. 32, pp. 81–90, Engineering Failure Analysis (2013). Doi:10.1016/j.engfailanal.2013.03.002.
14. O. Pilch, F. Šňahničan, V. Hrubý, Z. Studený, *The Effect of Plasma Nitriding Parameters on the Thickness of Nitrided Layers*. *Manufacturing Technology*, vol. 15(5), pp. 881-889, (2015). ISSN 1213-2489.
15. ISO 18203:2016(E). Steel – *Determination of the thickness of surface-hardened layer*. (2016).

## Corrosion Processes of Sintered Materials Based on Fe-Mg

M. Sedlaříková<sup>a</sup>, M. Zatloukal<sup>a</sup>, J. Hrabovský<sup>a</sup>, P. Čudek<sup>a</sup>

<sup>a</sup> Department of Electrical and Electronic Technology, FEEC, Brno University of Technology, Technická 10, 616 00 Brno, Czech Republic

This work deals with a current topic, which are biodegradable sintered Fe-based materials and their corrosion. These materials may be suitable for applications where gradual decomposition is required. An important parameter is not only the mechanical properties so that the material can withstand the load, but above all the corrosion properties and the degradation process. In this work, sintered materials based on Fe-Mg are tested. The introductory part is an introduction to the corrosion processes of the basic components of the tested systems, i.e. Fe. The practical part is focused on the preparation of samples based on Fe with the doping element Mg.

### Corrosion Processes

Corrosion can be defined as the action of the external environment on a material, whereby the material degraded and corrosion products are formed. Corrosion is a very important process in implants that needs to be monitored, and implants are subjected to various corrosion tests so that they do not corrode and are not dangerous in the body. While bioinert materials are corrosion resistant, with biodegradable implants we want to control their rate of corrosion so that there is an even, reasonably rapid degradation and no release of hazardous corrosion products. The main factors influencing the rate of corrosion include environmental influences, such as temperature, humidity, pH, as well as material properties, such as structure, composition.

### Corrosion Mechanism of Iron

In most cases, iron corrosion is undesirable, for biodegradable materials it is required. The aim is to ensure the most uniform long-term corrosion that will allow gradual degradation of the material at the desired time. There is a lot of expert work that deals with corrosion processes in these materials, however, the determination of ideal parameters is a complex matter, which in addition to the composition of samples depends on its structure, size, oxygen concentration, corrosive environment properties and other parameters. To determine the dependence of corrosion on the environment, resp. its pH uses E-pH diagrams, also known as Pourbaix. These diagrams contain three basic areas:

- area of immunity - the metal is stable and resistant to attack,
- corrosion area - thermodynamic conditions are met for this area, soluble ions are stable,
- passivity area - insoluble components protecting the material against corrosion are stable.

During anodic dissolution of metals, electrons are released and iron is transferred to Fe<sup>2+</sup>. This reaction is balanced by the reaction at the cathode, where oxygen depolarization and the formation of hydroxide anions occur, leading to an increase in pH. Due to the presence of hydroxide anions, iron hydroxide may form. Iron cations can also be further oxidized to Fe<sup>3+</sup> and together with hydroxide anions can form iron hydroxide. These reactions are summarized by Equations [1.1] – [1.4].



In the case of body fluids, various inorganic and organic substances are also present, which significantly influence the corrosion process. Particularly important are chloride ions  $Cl^{-}$ , the content of which in the blood plasma is about 100 mmol·l<sup>-1</sup> and significantly disrupt the passive layers and facilitate the course of corrosion.



### Sample Preparation

The method of replication was chosen for the preparation, in which a matrix is used, which serves as a basis for the created sample. For this case, a polyurethane foam matrix, commercially referred to as Bulpren S 28089, with a pore count of 60 PPI was used. Samples were prepared in two sets. Samples were prepared from a suspension of distilled water and a 10% solution of PVA and a mixture of powdered metals. A polyurethane sponge (dimensions approx. 10 · 5 · 5 mm) was then placed in this prepared suspension, which was removed after sufficient absorption of the suspension and placed in a dryer at 37 ° C for 24 hours. In this way, samples with magnesium percentages of 0.5%, 1%, 2.5% and 5% were prepared.

The samples were heat treated to form a solid structure and remove the polyurethane matrix. The temperature profile for the samples in the first set was chosen - increase to 450 ° C and stagnation for 2 hours, then increase to 1120 ° C and stagnation for 1 hour in a nitrogen atmosphere. The annealing of the second set of samples was performed in cooperation with the University of Chemical Technology in Prague and, depending on the content of powder metals, the most suitable temperature profile was chosen. In the first step, the polymer matrix is removed and in the second step, at a higher temperature, the powdered metal is sintered. The temperature rise was set at 5 ° C / minute and the annealing was performed under a nitrogen atmosphere.

The measurements were performed on an AUTOLAB TYPE II device from Metrohm, using a three-electrode connection consisting of a working electrode (PIGE), an auxiliary electrode (platinum) and a reference electrode (fully saturated calomel). The measurement was performed in 0.9% NaCl solution and a potentiodynamic method was chosen, for which a step of 0.001 V and a scan rate of 0.01 V · s<sup>-1</sup> were set. The samples were thoroughly cleaned with isopropyl alcohol and distilled water before measurement, then dried for 4 hours, and then a metal powder was formed from the sample, which was applied to a working electrode. The test results are shown in the following graphs, where for simplicity only the classic saline solution -0.9% NaCl is used. The effect of SBL solutions means (based on initial tests) more complex corrosion processes.

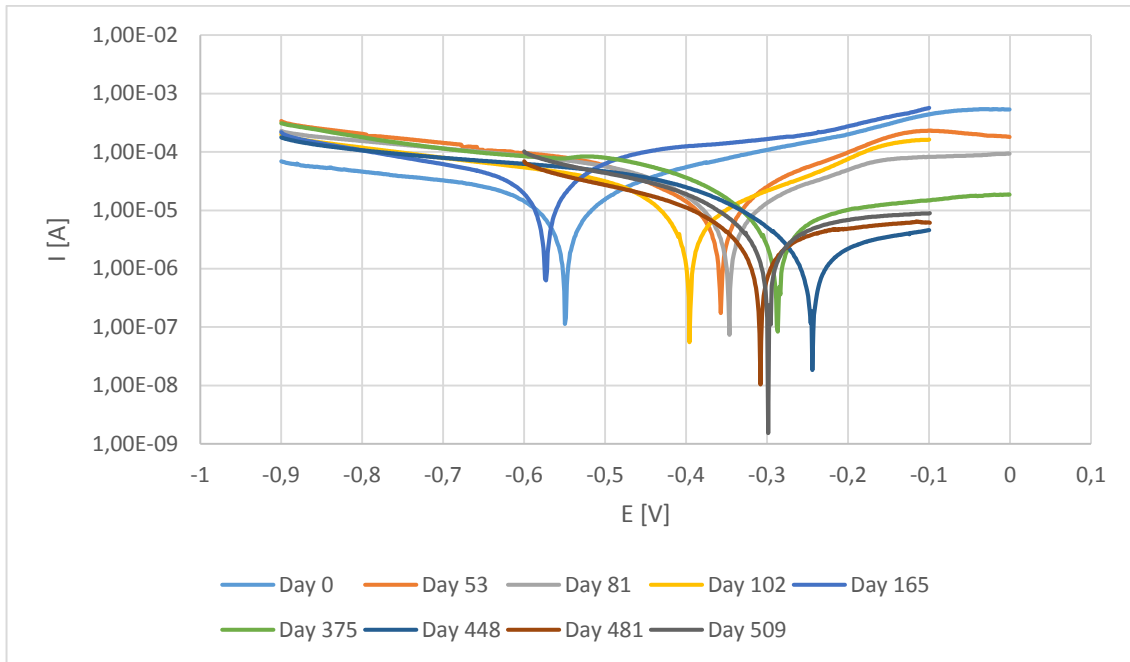


**Figure 1.** Fe Sample in 0.9% NaCl

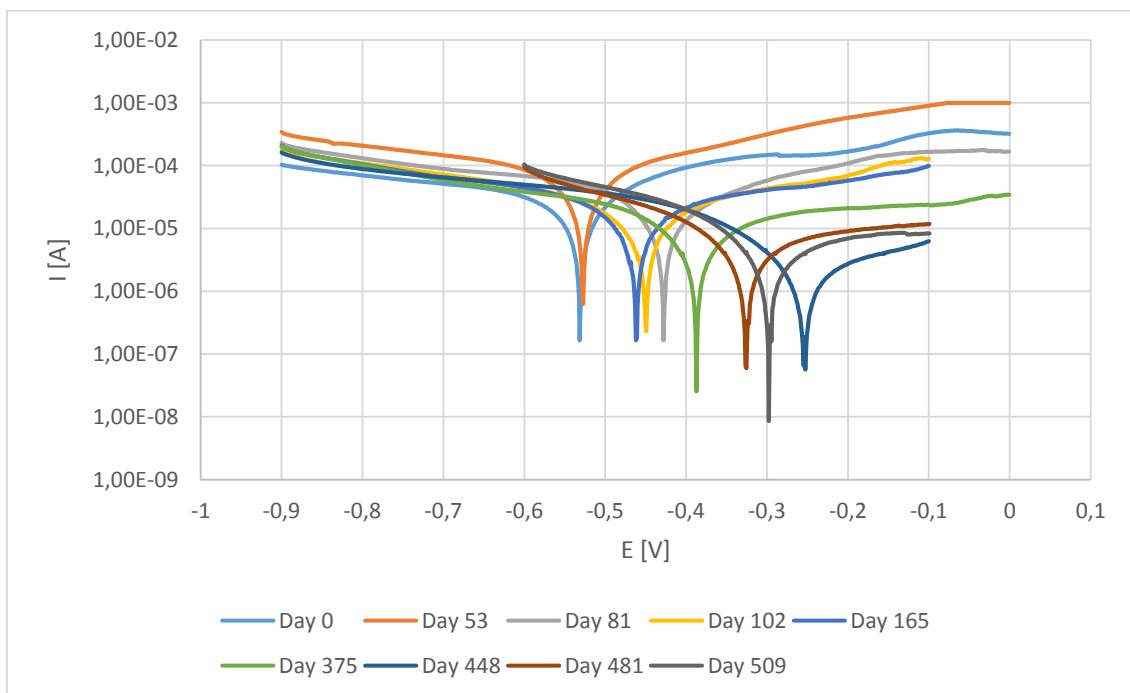


**Figure 2.** FeMg1 Sample in 0.9% NaCl

### Evaluation

In the previous graphical dependences (Tafel curves) the effect of Mg addition to the tested sample can be seen. The result is the fact that a few percent addition of the element significantly affects not only the size Corrosion potential, but also the magnitude of the current. This means the possibility of controlling the corrosion rate, so important for application in the field of bone implants.

From the resulting curves, certain anomalies in the shift of the corrosion potential and subsequently also changes in the corrosion current can be seen. The reason is probably the emergence of corrosion products, which can form pseudo-passivation layers on the surface of metal grains, which can affect corrosion reactions. The study of these parasitic corrosion phenomena will be the subject of subsequent research work.

### Acknowledgments

This work was supported by the grant FEKT-S-20-6206 "Materiály a technologie pro elektrotechniku III". This work was also supported by the grant AKTION 89p16 "Korozní procesy v materiálech na bázi Fe-Al a Fe – Mg".

### References

1. N. Perez, *Electrochemistry and Corrosion Science* (New York), (2004)
2. E. Zhang, H. Chen, F. Shen, *Biocorrosion Properties and Blood and Cell Compatibility of Pure Iron as a Biodegradable Biomaterial*, *J Mater Sci: Mater Med.*, 21(2151-2163), (2010)
3. M. Prakasam, J. Locs, K. Salma-Ancane, D. Loca, A. Largeteau, L. Berzina-Cimdina, *Review, Biodegradable Materials and Metallic Implants - A. Journal of Functional Biomaterials*, 8(4), (2017)
4. O. Veselý, *Ionty hořčíku a poruchy jejich bilance v organismu. Tvorba a ověření elearningového prostředí pro integraci výuky preklinických a klinických předmětů na LF a FZV UP Olomouc*, <http://pfyziolklin.upol.cz/?p=2285>, (2020)

## Corrosion of Sintered Materials Based on Fe.Si-Ag-Mg

M. Sedlaříková<sup>a</sup>, M. Zatloukal<sup>a</sup>, J. Bachmayer<sup>a</sup>, P. Čudek<sup>a</sup>

<sup>a</sup>Department Electrical and Electronic Technology, Brno University of Technology, Technická 10, 616 00 Brno, Czech Republic

The topic of this work is the solution of the problem of biomaterials and biocompatibility of metallic materials. The following is a procedure for the production of samples and the study of corrosion processes in various environments.

### Corrosion Processes

Electrochemical corrosion of metals is a spontaneous process of metal interaction with the surrounding electrically conductive medium, in which the ionization of the metal atom (oxidation) and reduction of the oxidizing component of the corrosive environment takes place simultaneously and their velocities depend on the electrode potential - the corrosion rate corresponds to the current flowing a corrosion cell between the cathode and the anode.

The essence of electrochemical corrosion is the formation of local electrical cells, caused by the difference of electrochemical potentials at the contact of two different metals, or due to different concentrations of metals. The primary precondition for electrochemical corrosion is, as with chemical corrosion, the thermodynamic instability of the metal in a given corrosive environment. The corroding metal loses its metallic character by the anodic reaction and becomes a cation which dissolves in solution or anodic compound is formed anodically from the metal. The anodic reaction is the exchange of an electric charge inextricably linked to the cathodic reaction, the reduction of some component of the corrosive environment. The corrosion rate corresponds to the magnitude of the current flowing through the corrosion cell between the cathode and the anode. The existence of separate cathodes and anodes on the surface of the corroded metal is caused by the inhomogeneity of the metal or liquid phase.

Factors influencing the rate and nature of electrochemical corrosion:

- position of the metal in the periodic table
- metal structure
- condition of the metal surface
- pH
- salt concentration in neutral solution
- content of corrosion inhibitors or stimulators
- temperature and pressure
- exposure to ultrasound
- radioactive radiation

### Preparation and Description of Samples

The experimental part of this work consisted of the preparation of samples for bone implants, which were then further examined. The basis of the prepared samples is a polymeric carrier material saturated with powdered metal. The procedure for the production of the sample was as follows: The

first step was to punch the desired piece of foam material with a punch and a hammer. The formed samples were 10 mm long and the diameter of the cylindrical cross-section was also 10 mm.

The next step was to weigh and mix the desired metal powder mixture (eg 95% Fe + 5% Si = 4.5 g Fe + 0.5 g Si), for proper homogeneity of the mixture, the metal powders were placed on a roller mixer after sealing in a test tube. Distilled water was then added to the tube. After mixing the mixture with water, one or more pre-prepared foam samples were placed in the tube. Shaking the tube ensured better filling of the pores of the foam material. The samples thus prepared were placed in corundum vessels for subsequent firing in a furnace under a nitrogen or argon atmosphere. Maximum temperature 1100 ° C with a delay of 10 minutes. When comparing, it was also found that for our interests, the best properties were BULPREN S 28089 foam, the foam with the highest porosity.

### Electrochemical Measurements

The measurements were performed using a three-electrode system - working, reference and auxiliary electrodes, on the potentiostat UTAUTOLAB TYPE II. The measurement was performed using the computer program GPES. Figure 1 shows the Tafel curves for the material Fe-Mg, resp. Fe-Si-Ag.

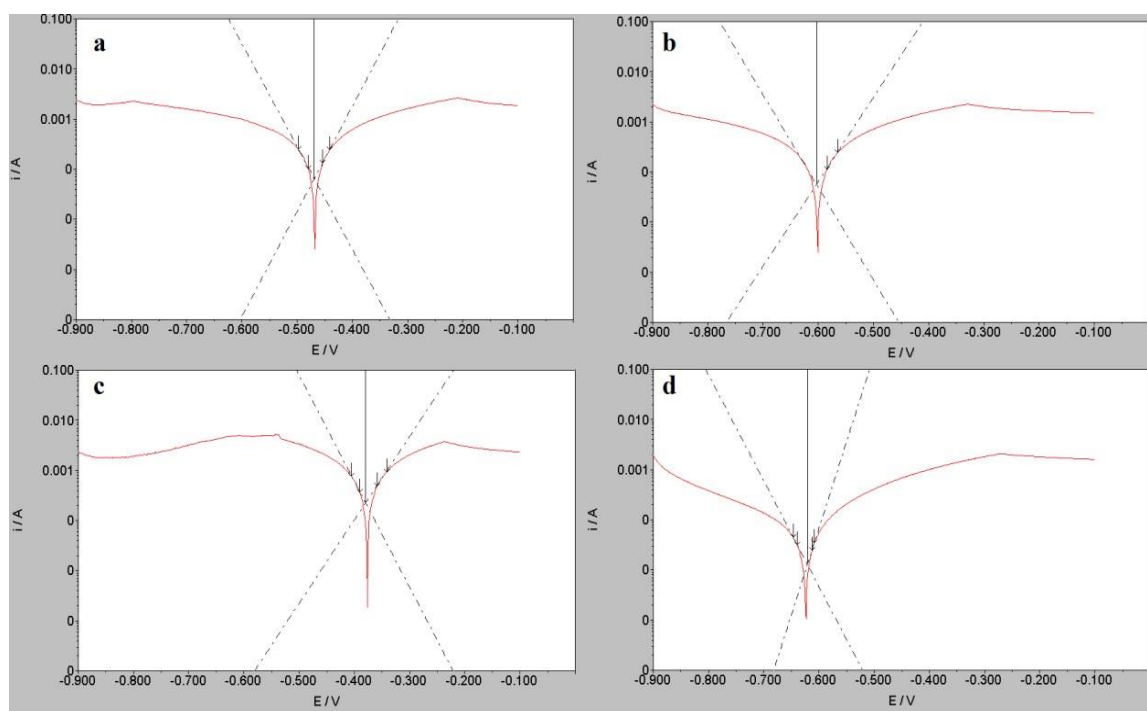


**Figure 1.** Comparison of graphs of corrosion potentials of a sample of 95% Fe 5% Mg after 56 days in solutions, a - standard saline solution + hydrogen peroxide; c and b - physiological Ringer's solution; d - saline + tartaric acid

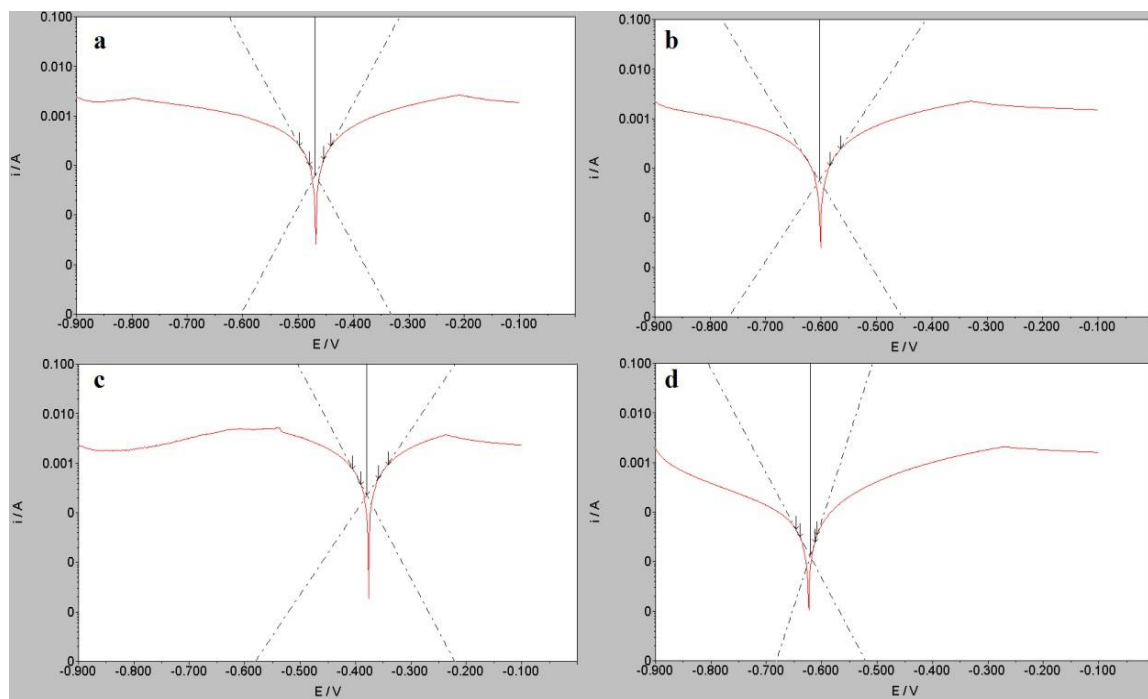


**Figure 2.** Comparison of graphs of corrosion potentials of a sample of 90% Fe 5% Si and 5% Ag after 86 days in solutions; a- standard saline; b - saline + hydrogen peroxide; c - Ringer's solution; d - saline + tartaric acid

## Conclusion

Results of electrochemical measurements of corrosion behavior of selected samples of iron-based material or its mixtures with other metals. Behavior in four different electrolytic environments was used as a criterion for their assessment. These solutions were selected both from common physiological solutions used in medicine and as models of different behavior of tissue fluids. In the latter group, it is a solution containing tartaric acid and a solution containing hydrogen peroxide. Tartaric acid was used for its ability to form coordination or complex compounds of iron and other metals and thus modify the corrosion properties of these solutions. Oxygen saturation of body fluids was simulated by the addition of hydrogen peroxide replacing the oxidative effect of oxygen molecules bound primarily to hemoglobin. The corrosion current, the position of the corrosion minimum and the Tafel directive  $b_a$  and  $b_k$  of the anodic and cathodic branches of the corrosion curve found by the potentiostatic method served as the assessed quantities.

The corrosion currents of the various composite materials in the pure electrolyte show that iron is the most corrosion resistant and, in addition, the mean values of the coefficients  $b$  have a value close to the expected, i.e. close to 50 mV per decade. This suggests that corrosion of this material is simple electrochemical oxidation. On the contrary, the lowest corrosion resistance appears to be a magnesium-containing substance. The corrosion current in the solution containing hydrogen peroxide is clearly greater, which results from the presumed oxidative action of this admixture.

## Acknowledgments

This work was supported by the grant FEKT-S-20-6206 "Materiály a technologie pro elektrotechniku III". This work was also supported by the grant AKTION 89p16 "Korozní procesy v materiálech na bázi Fe-Al a Fe-Mg".

### References

1. K. Dvořáčková, *Studium vlastností vybraných prostředků používaných pro ochranu kovů proti korozi*, Brno: Masarykova univerzita, Přírodovědecká fakulta, All About Electrochemistry, Electrochemical Corrosion, 53, (2007)
2. Z. Zhen, T. Xi, Y. Zheng, *A review on in vitro corrosion performance test of biodegradable metallic materials*, ScienceDirect, (2014)

## Impact of Electric Vehicles Charging on Electric Distribution Grids in Small Villages

V. Sít'ář<sup>a</sup>, T. Vysloužil<sup>a</sup>, L. Raková<sup>b</sup>, Z. Pazdera<sup>c</sup>

<sup>a</sup> Institute of Machines and Power Engineering, Faculty of Mechanical Engineering, UJEP, Na Okraji 1001/7, 400 01 Ústí nad Labem, Czech Republic

<sup>b</sup> Department of Electric Power and Environmental Engineering, Faculty of Electrical Engineering, UWB, Univerzitní 26, 301 00 Plzeň, Czech Republic

<sup>c</sup> ČEZ Distribuce, Teplická 874/8, 405 02 Děčín, Czech Republic

Current development of elektromobility leads to installations a huge amount of public electric vehicle charging stations (EVCSs) in cities and also along major roads. The electric distribution grids are relatively well dimensioned near shopping centres in cities or in localities, where great level of power is consumed by large industry customers. A significant portion of distribution grids is well dimensioned or it is after a recent reconstruction with a power reserve. Therefore, an installation of EVCSs doesn't bring relevant problems with their placement and negative influences of electric vehicles (EVs) don't cause complication through the increased power losses and voltage drops levels in the grids. The same applies for the EVCSs installed at the petrol stations along major roads which are mostly supplied directly from transformers connected to the high voltage grids.

Adverse conditions may occur when installation EVCSs in small villages, where electric distribution lines are poorly dimensioned and also in obsolete performance. The increased power consumptions when EVs charging may have an extreme negative influence on demanded voltage quality, active power losses level and also effect on total distribution grid operation.

In the paper, the authors deal with the influence of EVs charging on the electric distribution grid in a small village, where electric distribution lines are poorly dimensioned and out-of-date for current needs and also powered from low apparent power level transformers. The authors analyze in a paper mainly voltage deviations, active power losses, active and reactive power flows, and also distribution feeder loading at uncontrolled EVs charging from public and also homes EVCSs. The mentioned problems are solved in alternative simulation software DYNAST by means of EVCS power load model defined by demanded active and reactive power consumption when charging.

## Electromigration and Flux Residues

Jiří Starý

FEKT VUT Brno  
stary@feec.vutbr.cz

Assembly and interconnection structures and assemblies are characterized by a larger proportion of HDI structures (line/space < 100 μm), higher component density, a wide range of materials used and with a frequent absence of cleaning procedures after mass soldering and non-hermetic packages. On the electro-insulating surfaces, both atoms and molecules of flux residues and molecules of the polar liquid forming the electrolyte (most often water) are adsorbed. The interaction of metal materials with the polar environment and the ensuing electrical voltage is associated with chemical reactions and subsequent surface and volume diffusion. The acceleration of these electrochemical reactions is helped by higher working temperatures, higher humidity, size and frequency of electrical voltage between conductors. The result is often so-called electromigration, which is associated with the reduction of surface insulation resistance, corrosion, dendrite/fiber growth and the formation of subsequent short circuits.

### Types of Electromigration [1]

- 1) Dry electromigration = physical electromigration = movement of electron momentum
  - High temperatures (> 150 °C)
  - High current densities (> 10<sup>4</sup> A.cm<sup>-2</sup>)
- 2) Electrolytic (ionic) = electrochemical migration (ECM)
  - Ambient temperatures (< 100 °C)
  - Low current densities (< 1 mA.cm<sup>-2</sup>)
    - a) Normal conditions, no visible humidity ("Humid" or also silver electromigration)
    - b) Visible moisture on the PCB/traces ("Moisture" or wet electromigration).

This article demonstrates problems connected with ECM (Electrochemical Migration). Electrolytic electromigration mechanism is dependent on water and tends to occur whenever flux residues and surface moisture is formed on the base materials (typically FR4) that separates the conductive traces on/inside (CAF) PCB, flexible circuits, CC (chip carriers) and packages of integrated circuits) to allow electrolytic (ion) current conduction at applied electrical potential. Electrolytic electromigration is a phenomenon occurring mainly in DC and the direction of electromigration can be reversed by reversing the polarity of the applied electric field. Lower electromigration occurs when normal AC current is applied (with a frequency of 50/60 Hz) virtually no electromigration in higher frequencies. Conductive Anodic Filament (CAF) = growth of conductive anodic fibers between the cathode and anode - metal dendrites along the glass fibers of material FR4.

### Acceleration Factors Affecting the Speed of Ionic Migration:

- electrode material - metal and its solubility on ions Ag>Cu>Pb>SnPb>Sn>Au,
- electro-insulating surface – porosity, roughness, hygroscopicity FR2>FR4>PI>Al<sub>2</sub>O<sub>3</sub>

- level of surface humidity, suitable ions, e.g. Cl<sup>-</sup> and their concentration, pH < 7
  - condition with invisible layer of moisture on the surface or
  - visible condensed layer on the surface
- higher temperature.
- higher voltage, DC > AC,
- smaller distance between electrodes

### Flux and Flux Residues

Flux contains following ingredients: flux vehicle (RO, RE, OA), activators, solvents, ingredients and additives (surface tension modifiers, etc.). The most important for ECM is type and quantity of activators and their influence on SIR during temperature and humidity changes. Preferred are VOC free fluxes – more ecologic and water base solvent.

### Experiments and Results:

The practical part was focused on performing various test measurements. A series of surface insulation resistance (SIR) measurements were carried out on FR-4 plates with Cu comb structures acc. to IPC B-25 (preferred for evaluating electromigration). PCB structures were measured after contaminated by liquid fluxes, with and without isothermal process and PCB structures contaminated with flux passed through the soldering process. Furthermore, tests were carried out on PCB comb patterns with applied SAC pastes and patterns passed by soldering wave. Electromigration and SIR tests were carried out according to ANSI J STD 004 and IPC-TM-650. The plates were inserted into the climate chamber for 168 hours with a set relative humidity of 95 %, a temperature of 40 °C and voltage of 10 V. Each test was carried out on at least three test patterns according to the IPC-TM-650 standard. Results were averaged. Conductometric measurements of ionic contamination from fluxes were realised using the ROSE and SEC methods [2] [3]

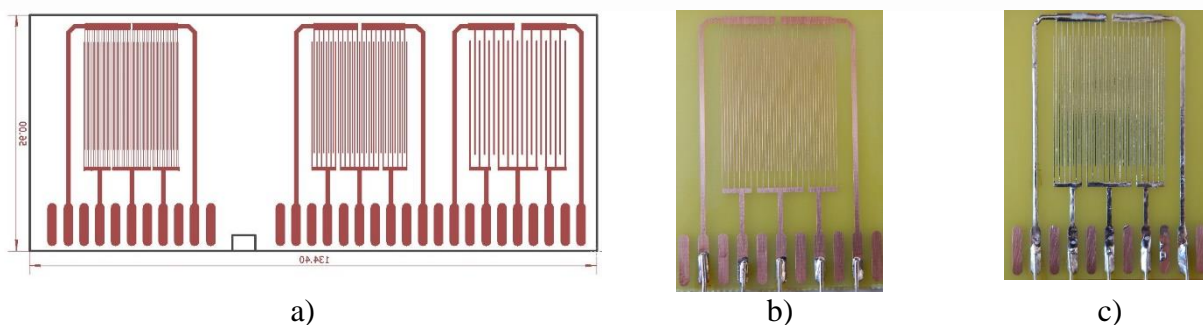


**Figure 1.** Designed structures a) FR-4 with Cu b) FR-4 with Cu covered with SAC surface finish c)

EIS (Electrochemical Impedance Spectroscopy) were used for fluxes and structures comparison acc. to 1b) and 1c). Measuring was realized at 10 mV in order to determine the corrosion rate from the polarisation resistance. VOC free flux and VOC flux were compared on Cu and SAC 305 structures.

Enclosed figures 3) and 4) with found dendrite received from SEM and EDAX.

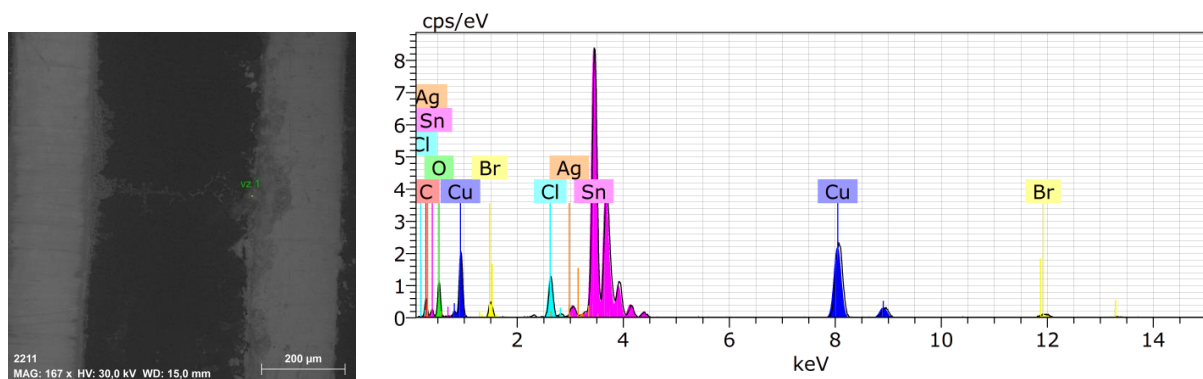


**Figure 3.** Dendrite with an area marked for evaluating the element analysis

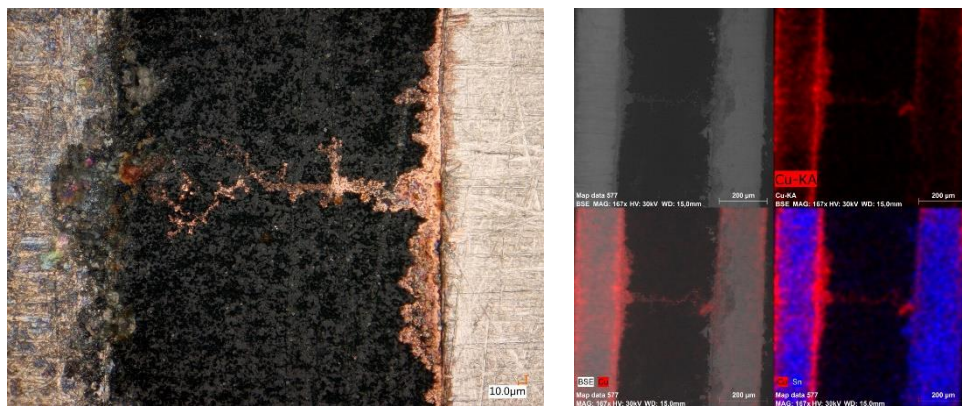


**Figure 4.** Images of the dendrite and elements analysis on the test DPS. (red copper, blue tin)

Relative humidity of 95 %, temperature of 40 °C and the attached voltage of 10 V on IPC B 25 shapes with Cu, Sn63Pb and SAC surfaces with residual no clean fluxes on the surface, only low electromigration appeared. During higher test voltage the dendrite growth was studied.

### Acknowledgements

This work was supported by the specific graduate research of the Brno University of Technology No. FEKT-S-20-6206.

### Literature

1. SIMEON J. KRUMBEIN, Metallic electromigration phenomena, IEEE Transactions on Components, Hybrids, and Manufacturing Technology ( Volume: 11, Issue: 1, Mar 1988).
2. TYLICH O., Electromigration of flux residues on the PCB surface, diploma thesis, Brno University of Technology 2016.
3. STOKLASEK L., Comparison of fluxes for wave soldering machine, bachelor thesis, Brno University of Technology 2017.

## Resistance of PLA material prepared by additive technology

Z. Studeny<sup>a</sup>, D. Dobrocky<sup>a</sup>, L. Dobsakova<sup>a</sup> and J. Prochazka<sup>a</sup>

<sup>a</sup> Department of Mechanical Engineering , University of Defence in Brno, Brno, Czech Republic

The article studies the surface properties of PLA material prepared by additive technology, i.e. 3D printing on equipment from Prusa company. Samples with a square test area were printed by FFF technology. After 3D printing, the surface texture of the samples was evaluated in terms of microgeometry. The TalySurf CLI1000 was used to evaluate the texture. The surface texture was measured with an inductive touch sensor.

Tribological tests were performed on the samples. The surface of the samples was cyclically stressed with the same load, always on the same path. Cyclic loading of the surface was performed on a UMT Bruker tribometer. The tribological properties between the sample surface and the test specimen in the shape of a ball were studied during the reciprocating motion. In particular, the coefficient of friction was measured and evaluated. The ball material was Nylon and PTFE.

Traces obtained during tribological testing were documented on an Olympus DSX 100 optical microscope. Trace parameters were verified by profilometric analysis on a TalySurf CLI1000. The wear parameters of samples and balls were also documented and evaluated. The results of the tests are the load dependences on the wear of the PLA material and the test specimens.

Keywords:

PLA, 3D printing, coefficient of friction

### Materials under Investigation

To measure the coefficient of friction, a material suitable for 3D printing from plastics - filament - was chosen. It is a PLA material - polylactic acid. The PLA is the most commonly used filament [11]. Said material is suitable for printing, has a low cost, is biodegradable and is characterized by good strength and durability. Its suitability is stated for static constructions because it has low thermal expansion. Melting point 175°C. It is also possible to print detailed structures. The nozzle temperature during printing was 210°C. A 50°C heated pad was used to ensure even cooling and to reduce deformation problems. The disadvantages of PLA material are, for example, low resistance to external influences. Furthermore, the PLA material loses its thermal mechanical resistance even at 55°C. Due to its low UV resistance, it is unsuitable for outdoor use. If post-printing requires surface treatment of the material after printing, it is usually done by wet grinding. The reason is the danger of melting due to friction and subsequent shape deformation.

The printing method FFF - Fused Filament Fabrication has been applied. The samples were printed on an Original Prusa i3 MK3S 3D printer. The samples were printed in the form of blocks (30

x 30) mm and 6 mm thick. The cubes to be measured had 70% internal filling. The surface was printed with 100% filling. Plates obtained by 3D printing technology were evaluated for surface microgeometry on a TalySurf CLI1000, see 3D model of surface in Fig. 1. The surface texture was measured by an inductive touch sensor [12]. The measurement took place on an area of (2 x 2) mm.

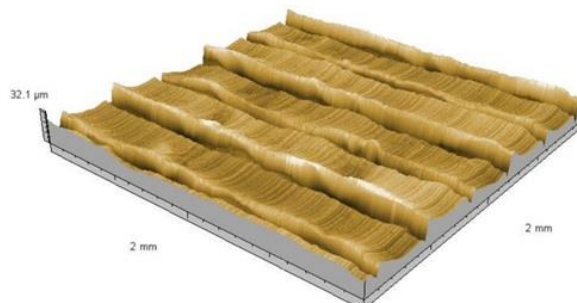


**Figure 1.** 3D PLA sample surface model

PTFE and Polypropylene (PP) balls with a diameter of 6.35 mm has been used as a counterpart for the tribological test.

### Tribological Tests

Tribological tests were performed by the Ball on Flat method [13]. The result of the test is a measurement of the coefficient of friction (COF). Ball on Flat was performed on samples made of PLA materials. This test was performed on a UMT-3 device. The Ball on Flat test is one of the basic methods for monitoring the abrasion of the material surface [14]. The principle of the method consists of loading the indenter, which moves horizontally, in our case reciprocally. The indenter was loaded with a constant force. Penetration of the indenter into the sample created a trace. Reciprocal motion took place on a constant path of 10 mm. The load during the test was always constant. However, different load levels were studied. The test took place at a constant time of 120 s.

The friction that arises between different surfaces, ie the sample and the ball, is expressed as a coefficient. This coefficient is the ratio of the friction force and the normal force. The normal force corresponds to the load acting perpendicularly across the ball to the specimen. The frictional force is then measured during movement and expresses the force required to overcome the resistance during movement. The aim of the experiment was to determine the real values of friction between the two materials.

The coefficient of friction can then be expressed [15]:

$$\mu = \frac{F_t}{F_N} \quad [1]$$

where:

$F_t$  is the friction force and  $F_N$  is the normal force.

The normal force value for the PTFE ball was at the following forces levels: (7, 20, 40, 60 and 100) N. On the other hand, for the PP ball, the load levels were shifted lower due to wear due to temperature rise during friction: (6, 7, 8 and 10) N. The frequency of reciprocal movement of the sample table was constant in all tests, 5 Hz.

### Measurement of thermal stress

The experimental Ball on Flat test was performed with dry friction, ie without lubricant. As a result, it was interesting to observe the temperature rise in the contact area. The measurement and validation of the measured data was performed using a FLIR T610 thermal imager, see Fig. 2. The increasing heat value significantly affects the overall wear, especially for PLA type material, which is one of the most printable softening materials due to temperature. Traces obtained during tribological testing were documented and measured on an Olympus DSX 100 optical microscope.

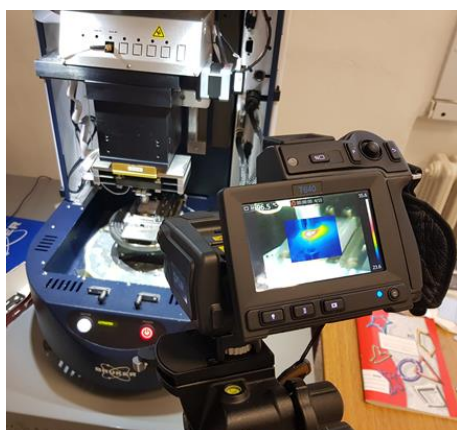


**Figure 2a.** Experimental design, UMT Bruker tribometer and FLIR T610 thermal imager on a tripod



**Figure 2b.** Example of heat measurement at the friction point during the experiment, load 8 N (PTFE ball)

### Evaluation of Tribological Testing

From the data obtained during the measurements, the dependences of the course of the COF in time, ie in the time of 120 s, were compiled. Each measurement at the respective level of normal force took place from three created tracks.

In addition to the COF values, attention was also focused on the condition of the surface of the PLA material sample on the one hand, as well as the condition of the ball and the area that was ground during the test on the other hand. The surface condition of the samples and beads was documented on an Olympus DSX 100 optical microscope. The material of the PLA sample, where the contact ball was PTFE, showed little signs of damage. On the other hand, with the PP ball, the wear of the PLA sample was significant even at orders of magnitude lower load values.

## Analysis of the effect of reflected shock waves in the experimental chamber

J. Maxa<sup>a</sup>, P. Šabacká<sup>a</sup>, R. Bayer<sup>a</sup>

<sup>a</sup> Department of Electrical and Electronic Technology, Brno University of Technology, Technická 10, 616 00 Brno, Czech Republic

As part of the research in the field of vacuum chamber pumping in the Environmental Electron Microscope, research on supersonic flow through apertures is being carried out at the Department of Electrical and Electronic Technology of Brno University of Technology in cooperation with the Institute of Scientific Instruments of the CAS. This paper deals with the influence of reflected shock waves on the resulting flow in the pumped part of the Experimental Chamber.

### Introduction

At the Department of Electrical and Electronic Technology of Brno University of Technology, in cooperation with Institute of Scientific Instruments of the CAS, research on supersonic flow at low pressures is being carried out (1, 2, 3). The results are used in the design of vacuum chambers of the Environmental Electron Microscope (4, 5, 6). The research will include static and total pressure measurements in the experimental chamber using a Pitot tube to determine the flow velocity, temperature reading in the supersonic flow and shock wave monitoring using the Schlieren optical method. Analysis of reflected shock waves in a closed chamber was performed to eliminate interference to the measurements.

### Experimental chamber

The current Experimental chamber consists of two chambers separated by a small aperture that simulates the condition created by differential pumping in an electron microscope (7, 8).

Figure 1 shows a schematic of the given chambers V1 and V2 separated by a 2 mm diameter nozzle as used for the Ansys Fluent calculation. This calculation was performed as 2D axisymmetric.

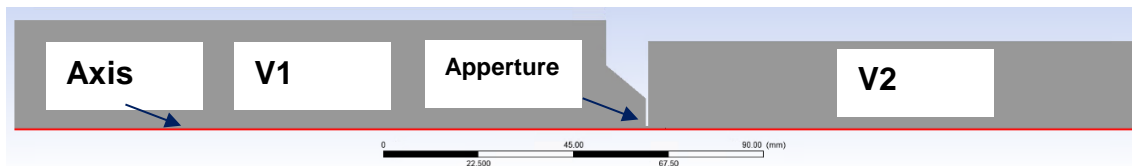


Figure 1. 2D axisymmetric model

### Results and Discussions

Pressure analysis was performed at four points on the chamber walls at the locations where the probes are planned to be mounted in practice (Figure 2). These points are marked in color. In the same colors, the pressure distribution during the pumping of the chambers from atmospheric pressure to operating pressures when the pressure is below 2000 Pa in chamber V1 and below 40 Pa in chamber V1 is plotted in Figure 3. It can be seen in Figure 3 that all the curves overlap because as can be seen in Figure 4 the differences are in tenths of Pa. These tiny differences are due to weak parallel-forming shock waves. However, their pressure gradient is very small, as can be seen in Figure 2.

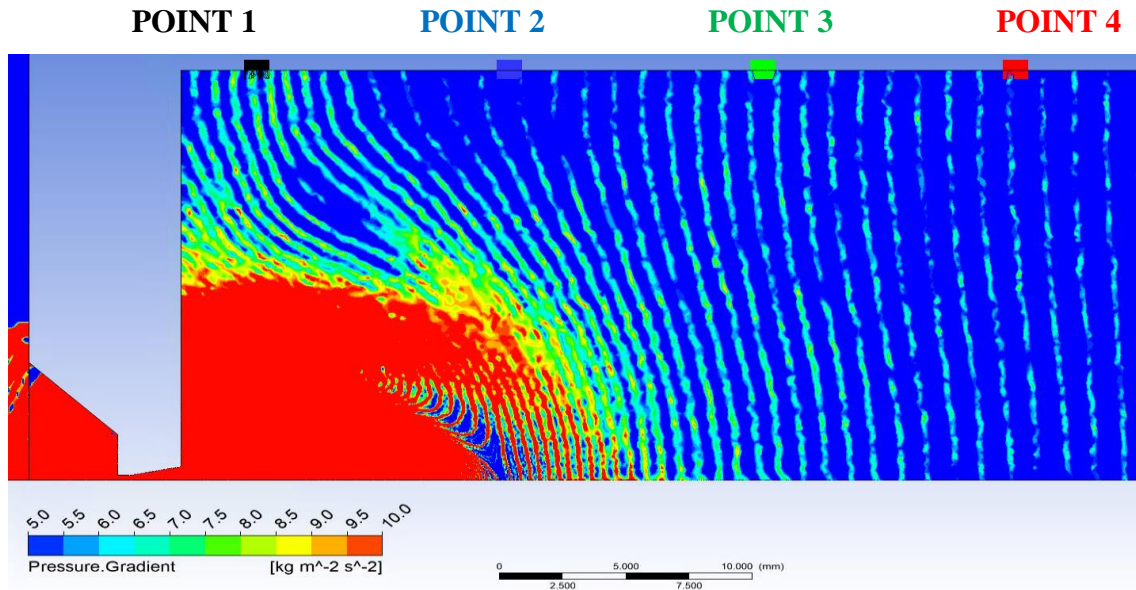


Figure 2. Pressure gradient and Sensed points

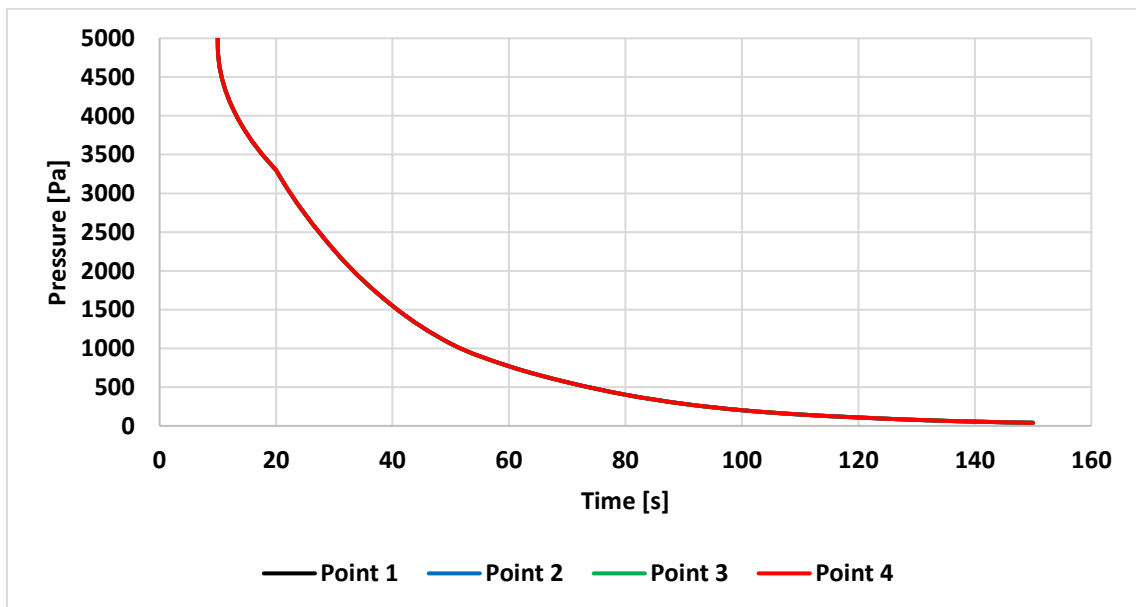
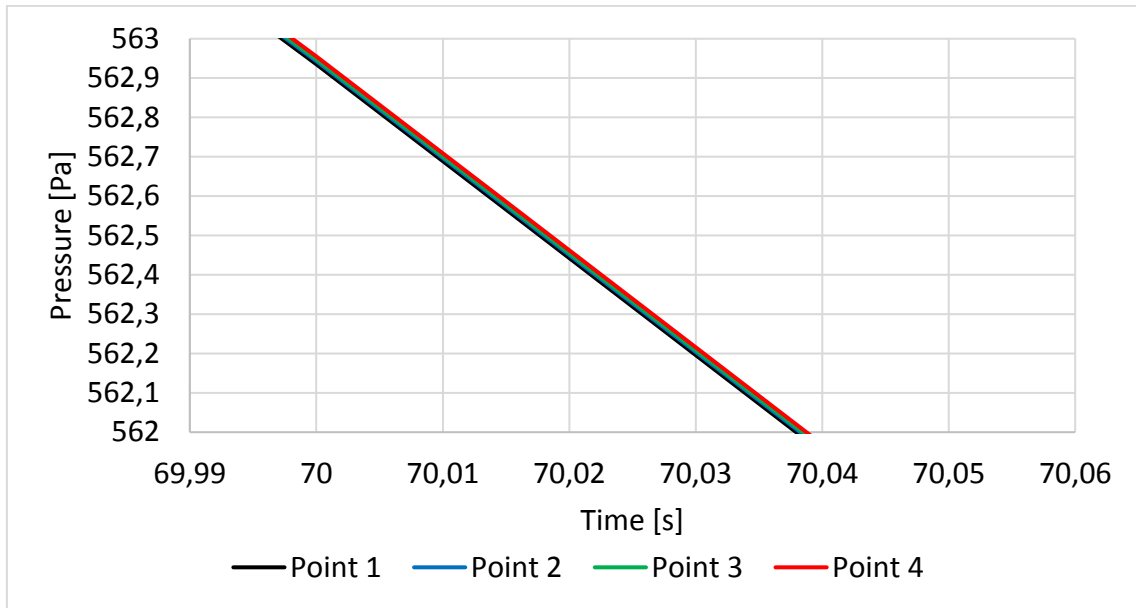
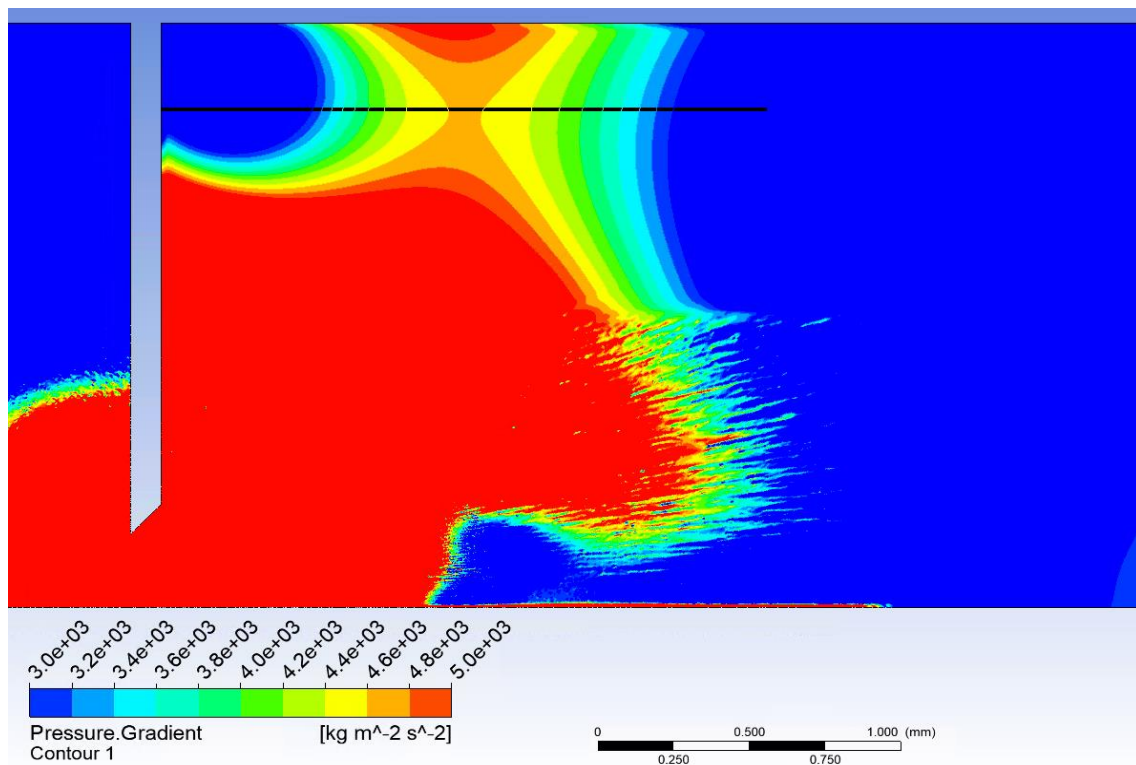


Figure 3. Pressure – Free variant



**Figure 4.** Pressure – Free variant – detail view

According to the performed analyses, the designed nozzle and the subsequent chamber have almost ideal proportions. On the other hand, Figure 5 shows an example of a case where a reflected shock wave is generated, on which a large pressure gradient is created, and a large pressure change occurs when passing through this wave (Figure 6).



**Figure 5.** Demonstration of reflected shock waves in case of improper chamber and aperture design

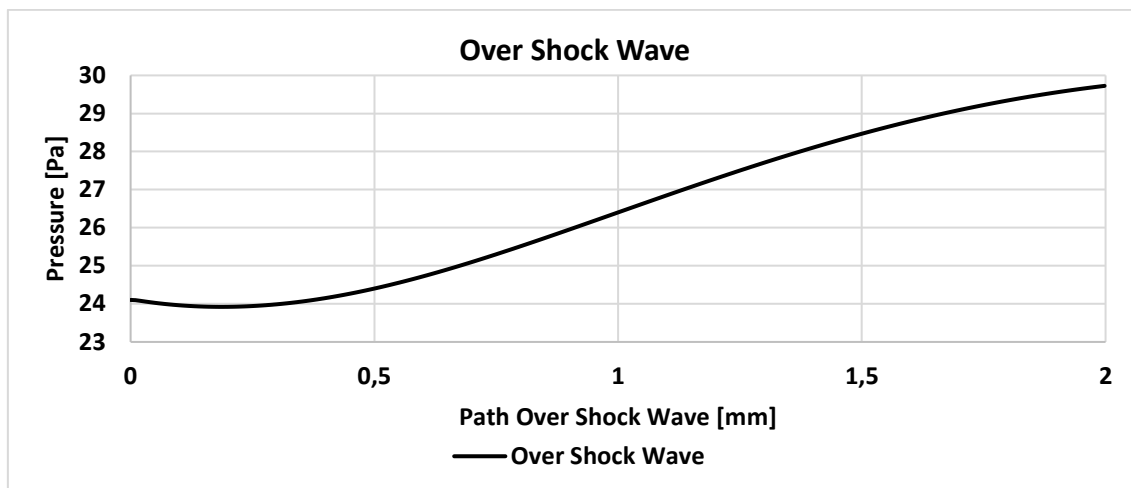


**Figure 6.** Pressure development during the transition of a reflected shock wave

### Acknowledgments

This research was supported by Brno University of Technology specific research program: Materials and technology for electrotechnics IV, reg. no. FEKT-S-20-6206.

### References

1. E. Tihlaříková, V. Neděla, and B. Dordevic, in In-situ preparation of plant samples in ESEM for energy dispersive x-ray microanalysis and repetitive observation in SEM and ESEM, *Scientific Reports*, 9(FEB), 2300. ISSN 2045-2322. doi: 10.1038/s41598-019-38835-w, (2019).
2. J. Maxa, V. Neděla, J. Jiráček, P. Vyroubal, and K. Hladká, in Analysis of gas flow in a secondary electron scintillation detector for ESEM with a new system of pressure limiting apertures, *Advances in Military Technology*, roč. 7, č. 2, s. 111-116. ISSN 1802-2308, (2012).
3. J. Maxa, M. Bílek, P. Hlavatá, P. Vyroubal, and K. Leptová, in Comparisons Using Methods of Continuum Mechanics and Monte Carlo at Differentially Pumped Chamber, *Advances in Military Technology*, 11, n. 2, p. 143-150. ISSN: 1802-2308, (2016).
4. M. Bílek, J. Maxa, P. Hlavatá, and R. Bayer, in Modelling and simulation of a velocity field within supersonic flows in low-pressure areas, *ECS Transactions*, 81(1), pp. 311–316, (2017).
5. P. Hlavatá, J. Maxa, M. Bílek, and V. Neděla, in Impact of the shape of the differentially pumped chamber on critical flow character, *ECS Transactions*, 81(1), pp. 317–322, (2017).
6. P. Hlavatá, J. Maxa, M. Bílek, P. Vyroubal, and R. Bayer, in Influence of critical flow in the differentially pumped chamber AQUASEM, *Advances in Military Technology*, 12(2), pp. 301–310, (2017).
7. A. Maxová, P. Šabacká, and J. MAXA, in Comparison of the Ansys Fluent system solvers for the possibility of supersonic flow solving at the low pressures, *ECS Transactions*, pp. 32-37, ISBN: 978-80-214-5109-4, (2019).
8. A. Maxová, J. Maxa, and P. Šabacká, in The Impact of Pumping Velocity on Temperature Running in Chambers of Experimental System, *ECS Transactions*, pp. 317-323, ISBN: 978-80-214-5109-4, ISSN: 1938-5862, (2021).

## Observation of environmental impact on HIPS material for 3D printing

P.Šafl<sup>a</sup>, J. Zimáková<sup>a</sup>, T.Binar<sup>a</sup>, M. Sedlaříková<sup>a</sup>

<sup>a</sup>Brno University of Technology, Technická 10, 616 00 Brno, Czech Republic

The aim of the work was estimating climatic influence on HIPS material used for 3D printing. This material undergoes rapid degradation and it can be used as a material suitable for setting the parameters of the climatic chamber for other materials. A climatic chamber was used for degradation, in which UV light, heat and increased humidity were applied to the material. The degree of degradation was then checked by a tensile test.

### Introduction

As Industry 4.0 intervenes and is increasingly being implemented in companies, it is slowly displacing traditional manufacturing and outdated principles. A part of a modern companies is also intelligent service, which includes additive production as well. Although additive manufacturing was developed several decades ago, it became important part of manufacturing and service processes recently. Unfortunately, the properties of the materials themselves and the fact that the materials have different properties when they are used for 3D printing and for conventional injection molding are often forgotten when implementing additive manufacturing. Therefore, studies must be carried out to determine the behavior of the materials after printing and how to adjust the properties of this material so that it is functional and trouble-free throughout its life. For the studies it is necessary to determine the environment where the device will be used and the influences contributing to its degradation. According to this information it is possible to set the climatic chamber and let the testing samples degrade. After finishing the controlled degradation, it is necessary to test the samples mechanically and compare them to the testing bodies which did not undergo degradation.

### Experiment

For the tensile tests, a testing bodies which corresponds to the standard which describes the tests have to be chosen. There is no standard dealing with testing for the needs of 3D printing, therefore the standard that determines the tensile properties for molded plastics was used. This is a standard under the designation ČSN EN ISO 527-2, from which a test body in the shape of a dog bone type 1A was selected. The body was printed using full perimeters, which means that the printheads draw the outline of the body from the outer wall towards the center. Bodies that have very similar mechanical properties, which is needed for the experiment, can be created using this procedure. Two sets of test specimens of four pieces were created in order to be able to average the measured values and evaluate the results. One of the sets was placed in a climatic chamber. After cycles in the climatic chamber both sets were mechanically tested.

### Measuring instruments

The A8 printer, which was created on the basis of the ANET A8 printer, was used for the production of test specimens. The entire printer is converted to 24 V and the electronics from

BIGTREE TECH company was used. The BigTreeTech SKR V1.3 board with TMC2209 drivers was chosen as a control unit, which ensures accurate and quiet operation of the printer.

A xenon chamber from Q-LAB company designated Q-SUN-Xe3 was used for the degradation (fig.1a). The chamber was chosen because it meets the standards for testing plastics for outdoor use (ASTM D2565) and for testing plastics for indoor use (ASTM D4459). Day-light-Q filters which simulate noon summer light was used.

The tests were performed on TEMPOS ZD20/200 kN tensile testing machine (fig.1b), which is connected to a PC via a control unit. The data were then processed in the program M TEST 1.7. The TEMPOS device is only able to record the force  $F$  [N] and the distance  $s$  [mm], which indicates how far the collets have moved apart during the measurement.



**Figure 1.** a) Climatic chamber Q-SUN-Xe3, b) TEMPOS ZD20/200 kN

## Measuring procedures

### Phase I:

1. The first step was to determine the glass transition temperature of the material to ensure that the material is not deformed by the high temperature. This step was performed experimentally using a Voltcraft DL-111K temperature data logger. The data logger has a type K temperature sensor that is able to measure the temperature range from  $-200$  to  $1370$  ° C. This sensor has a diameter of 2.5 mm, and therefore holes with a diameter of 2.5 mm were drilled into the measured object, into which the sensor was inserted.
2. After inserting the datalogger, the various heating temperatures in the oven were set and the glass transition temperature was determined to be  $95$  ° C.
3. After determining the glass transition temperature, a limit temperature of  $80$  ° C in the chamber during degradation was set.
4. Next was necessary to set the chamber cycles to match the required environment simulation.
5. After performing the degradation cycles in the chamber, the testing bodies were labeled and prepared for the tensile tests.

Degradation in the chamber simulated 15 days of direct sunlight with occasional precipitation. In South Moravia, around  $1122$  kW /  $m^2$  of energy is radiated per year. Unfortunately, in terms of time, it was not possible to approach this value, so a period of 15 sunny days in summer was chosen.

In the summer, the value of radiated energy per month is approximately 150.44 kWh / m<sup>2</sup>. When simulating radiated energy per half of month, the value of radiated energy is about 75.22 kWh/m<sup>2</sup>. The cycles in climatic chamber were set to 60 hours of total time. In 60 hours, the chamber was able to radiate energy of 34,243 kJ / m<sup>2</sup>, which is equal to 9,512 kWh / m<sup>2</sup>. This cycle was necessary to repeat 8 times in order to achieve simulation of the environment equal to 15 days. After finishing the simulation in the climatic chamber, a value of 76.096 kWh / m<sup>2</sup> was read, which roughly correspond to 15 days of direct sunlight. Already after the first cycle, which lasted 60 hours, the material started to turn yellow. The material turns yellow due to photooxidation, which leads to degradation of some polymer bonds.

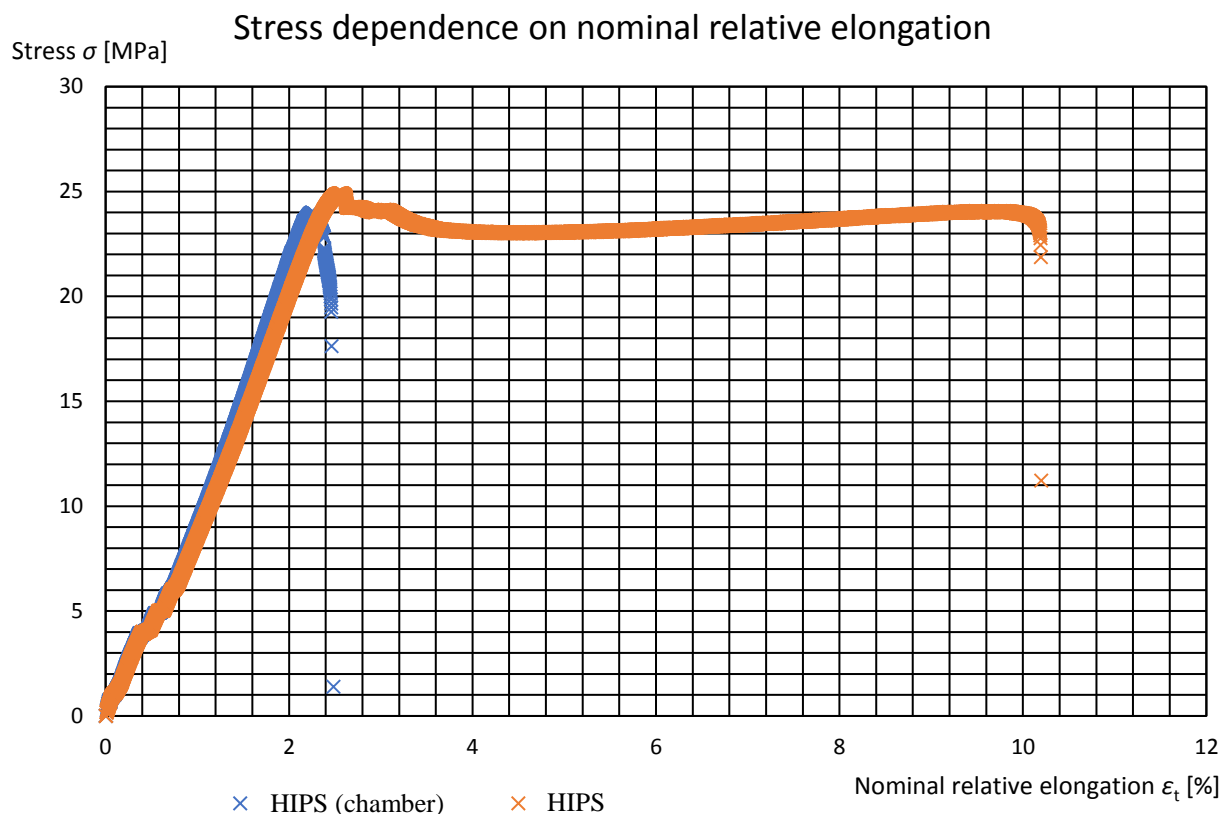
### Phase II:

1. The first step was to clamp the testing body in the collets and secure with tightening elements.
2. Then the M TEST 1.7 program was run and the initial position of the arm was set. When the arm is in the initial position, it is necessary to set the arm feed speed. The speed has been set to 5 mm / min.
3. The measured values of force and distance, which indicates how the collets moved apart were recorded.
4. A tensile diagram was plotted from the measured data and the yield strength, stretching at the yield point, maximum elongation at maximum stress, stress at break and elongation at break was subtracted.

From Table 1 it is possible to see that the bodies which were in the chamber were able to withstand elongation of only about 2.5% of the measured length. Bodies that have not been degraded in the chamber were much more flexible and were able to stretch up to 10% of the measured length. The Bodies that were not in the chamber have a significant yield strength, which was subtracted from the graph and recorded in Table 1. It can be seen in Graph 1 that both test specimens behave similarly up to about 2% of the nominal elongation and elastic deformation applies, and therefore Hooke's law. The approximate value of the proportionality point was set at 24 MPa for both testing bodies. After exceeding this point, the testing body, which has been degraded in climatic chamber ruptures. The testing body, which has not been degraded begins to plastically deform and ruptures up to about 10% of the nominal elongation. This difference was due to UV and IR radiation. UV radiation is dangerous for the material because it causes photolysis. UV radiation causes the macromolecules to break down to a smaller extent due to the breaking of the bond between two atoms in the chain. Furthermore, UV radiation causes photooxidation. The oxidation reaction first acts on the surface of the body, but gradually gets below the surface. Oxidation causes chemical changes in the structure of polymers and thus crosslinks of macromolecules. The material is then more brittle, loses its elasticity and cracks are starting to form in the material under stress.

**Table 1.** Measured and calculated values for the HIPS material

Chamber	Testing set	Sample number	Yield strength [MPa]	Stretching at the yield point [%]	Maximum stress [MPa]	Elongation at maximum stress [%]	Stress at break [MPa]	Elongation at break [%]
NO	1	A1	25,8	2,8	25,8	2,6	24,0	10,1
		A2	25,1	2,6	25,1	2,5	21,7	10,6
		A3	24,3	2,2	24,6	2,4	23,2	10,3
YES	5	E1	N	N	24,0	2,4	22,2	2,6
		E2	N	N	24,0	2,5	17,8	2,7
		E3	N	N	24,7	2,4	17,6	2,5



**Graph 1.** Display of average values of the tensile diagram for the material HIPS and HIPS with chamber

### Acknowledgements

This work was supported by the specific graduate research of the Brno University of Technology No. FEKT-S-20-6206.

### References

1. ČSN EN ISO 527-1. Plastics – Determination of tensile properties – Part 1: General principles (ISO 527-1:2019).
2. ČSN EN ISO 527-2. Plastics – Determination of tensile properties – Part 2: Test conditions for moulding and extrusion plastics (ISO 527-2:2012).
3. ČSN ISO 2768-1. General tolerances – Part 1: Tolerances for linear and angular dimensions without individual tolerance indications.
4. Xe-3 Xenon Test Chamber [online]. 2015. web: Q-SUN, 2015 [cit. 2021-5-24]. <https://www.q-lab.com/en-gb/products/q-sun-xenon-arc-test-chambers>.
5. Degradace polymerů [online]. 2013. [cit. 2021-5-24]. [http://tpm.fsv.cvut.cz/student/documents/files/IMP/IMP\\_10.pdf](http://tpm.fsv.cvut.cz/student/documents/files/IMP/IMP_10.pdf)
6. Účinky a užití optického záření [online]. 2011 [cit. 2021-5-24]. <http://www.odbornecasopisy.cz/res/pdf/44295.pdf>
7. SEPE, Mike. MICHAEL P. SEPE, LLC. *Annealing Tips for Thermoplastic Polyurethanes* [online]. 2020. 6/7. *Plastics Technology*, 2020, [cit. 2021-7-13].
8. ŠAFL, Pavel. *Použití technologie 3D tisku pro návrh výroby náhradních dílů* [online]. 2021 [cit. 2021-07-13].

## Reducing internal stress by annealing

P.Šafl<sup>a</sup>, J. Zimáková<sup>a</sup>, T.Binar<sup>a</sup>, M. Sedlaříková<sup>a</sup>

<sup>a</sup>Brno University of Technology, Technická 10, 616 00 Brno, Czech Republic

The aim of the work was to reduce internal stress by annealing. For this work, the classic PLA was chosen, which is the most used material for 3D printing. Stress reduction was performed by drying oven, which is able to gradually increase the temperature, and thus no undesired heat shock occurs. The testing samples were inserted into the UV chamber and then the deformation was monitored.

### Introduction

Annealing of plastics is a method that has been taken from metallurgy in order to improve some properties of plastics. It is a method of heat treatment of printed products in the final adjustment, where the state of the structure changes, and thus the properties change due to controlled heating. The process of annealing plastics is the same as for metallic materials, but plastics are heated to much lower temperatures. The procedure is divided into three parts. The first part is heating to the prescribed temperature  $T_a$ . The second part is staying at the prescribed temperature and the last one is gradual cooling. Each plastic is specific, and therefore needs a specific setting of temperature and residence time at a given temperature. Thermoplastics can be divided into two groups, amorphous and crystallizing. Thermoplastics with an amorphous structure are annealed to a temperature close to their glass transition because strong deformation occurs after exceeding this point. For crystalline thermoplastics, the heating is carried out up to the melting point  $T_g$ . The use of annealing in the field of 3D printing is very useful, because annealing reduces the internal stress of the material, and thus prevents the formation of creases. The body created by 3D printing is created by applying thin layers of molten material. However, this molten material is laid on an already cooled layer of material, and due to different temperatures, the layers expand and shrink. This expansion creates an internal stress in the material.

### Experiment

It was necessary to make the testing bodies, which were selected according to the ČSN EN ISO 527-2 standard. Testing body in the shape of a dog bone type 1A was chosen for the tests. Twelve samples from PLA material were placed into the chamber. The first 3 samples were not annealed, and the others always went through a half-hour annealing process. The annealing of the plastic took place in a drying chamber, which was fully sufficient for the needs of annealing. The Venticell ECO line chamber, which was able to anneal plastics up to a temperature of 250 °C was selected. The chamber has a timer, on which was necessary to set 30 minutes, because it takes 30 minutes to heat the entire volume of the body. The testing bodies were always placed in a heated chamber at a temperature of 40 °C. After inserting the bodies into the chamber, a delay of two minutes was set to stabilize the selected temperature. Temperature stabilization was necessary for more accurate measurements because the space inside the chamber cooled when the chamber door was opened. After annealing, the bodies were removed from the chamber and cooled to a room temperature of 21.5 °C. The bodies

were then measured in all axes and the measured values were evaluated. In the next step, the bodies were exposed to UV radiation and deformation in all axes was monitored.

### Measuring procedures

Before the work procedure was created, cyclic voltammetry measurements were made to determine the glass transition temperature of the material, to be able to set the highest possible annealing temperature. This value was determined experimentally using a Voltcraft DL-111K temperature data logger, which was inserted into the test specimen. Then the body with the data logger were placed in a drying oven (Fig.1).



*Figure 1. Example of an constructed measuring device*

#### Procedure I:

1. In the first step, it is necessary to prepare the testing bodies. The bodies were printed on a modified 3D printer of the Ender 3 PRO brand, only with the help of perimeters, for the closest possible imitation of the injected parts.
2. According to the previous glass transition temperature measurement, the annealing temperatures were set at 80 °C, 110 °C, 130 °C for 30 minutes.
3. After 30 minutes, the test specimens were removed from the drying oven and placed on a mat where they were cooled to room temperature.

When the bodies cooled down, a description of the test bodies and measurement of deformation in all axes was made. The measured values were recorded in Table 1. The dimensions of the measured test specimen in three axes were recorded and the average value and the percentage change were calculated from the measured values.

Dimensional deformation can be observed in Table 1, where can be seen a comparison of all dimensions. From the table it is possible to determine if the body still meets the dimensional accuracy, according to the ISO 2768-1 standard. From the table it is possible to see that the dimension change in the x-axis, which forms the longest part of the test specimen, occurs at all temperatures. The body is printed only from perimeters (walls without filling), and therefore, before the nozzle applies another layer of material, the previous layer is already cooled to ambient temperature and a temperature difference, which causes internal stress due to thermal expansion occurs. Due to internal stress, the test specimen tends to shrink the most in this axis. Changes in the y-axis already occur at 80 °C, but at this temperature there is still no deformation that would exceed the standard. This is due to the fact that in the y-axis the tested object had only 20 mm, and therefore there is no such large temperature difference between the layers and no greater internal stress is visible. The material tends to shrink further with increasing temperature until the melting point occurs. When the melting point is reached, the material collapses mainly in the y-axis. The change in the z-axis is opposite to change in the y-

axis because there is almost no internal stress in the z-axis. Due to the absence of internal stress, the material tends to expand in the z-axis.

**Table 1.**

PLA HTPRO Plastika Trček				PLA HTPRO Plastika Trček			
Temperature [°C]	Dimension change in the axis [mm]			Temperature [°C]	Dimension change in the axis [mm]		
	x-axis	y-axis	z-axis		x-axis	y-axis	z-axis
0	170,3	19,93	3,71	0	170,33	19,93	3,68
	170,5	19,93	3,68	80	169,37	19,92	3,72
	170,2	19,94	3,66	110	168,87	19,86	3,79
80	169,2	19,91	3,71	130	167,50	19,80	3,82
	169,4	19,92	3,72				
	169,5	19,92	3,73				
110	168,9	19,84	3,79	Temperature [°C]	Dimension change in the axis [%]		
	168,8	19,85	3,78		x-axis	y-axis	z-axis
	168,9	19,9	3,79	0	100,00	100,00	100,00
130	167,7	19,82	3,81	80	99,43	99,92	101,00
	167,2	19,82	3,82	110	99,14	99,65	102,81
	167,6	19,77	3,82	130	98,34	99,35	103,62

### Procedure II:

1. After the annealing is finished, the testing bodies are placed into the climatic chamber, where the resistance to sunlight is tested.
2. Before setting the program, it is necessary to insert a special filter in front of the lamps, which imitates midday light through clear glass (Window - Q).
3. The climate chamber is set to 100 W of lamp power. Next, a sensor is set for the maximum temperature of the black body, which simulates the temperature on the surface of the test body.

After setting, a twelve-hour cycle consisting of two modes starts. The first mode, during which the test specimens are illuminated is 5 hours long. In the second mode the lamps are switched off and the specimens are cooled down.

Figure 2 shows test specimens that have not been annealed. The unannealed body is affected by internal stresses which deform the body. This deformation was caused by heat radiation from lamps in the chamber. The testing bodies were placed on a steel plate of the chamber, which is cooled by a blower. The bodies were cooled from the bottom and heated from the top, which resulted in softening of the upper layers of the test specimen, which began to shrink. Fig. 3 shows test specimens annealed at 80 °C. Due to annealing the internal stress was reduced, and therefore no major deflections occurred. The deflection measured by the caliper was 1.6-1.9 mm and the dimensions of the testing body remained unchanged. The best results were obtained by the test body during annealing at 110 °C. The internal stress was significantly reduced, and the body showed no signs of deflection, which can be seen in Fig. 4. The higher annealing temperature then had the same results as the temperature of 110 °C, but at a higher temperature there is a risk of deformation of the body.



**Figure 2.** Example of an unannealed testing bodies



**Figure 3.** Example of an annealed testing bodies at 80 ° C



**Figure 4.** Example of an annealed testing body at 100 ° C

### Acknowledgements

This work was supported by the specific graduate research of the Brno University of Technology No. FEKT-S-20-6206.

### References

1. ČSN ISO 2768-1. *General tolerances – Part 1: Tolerances for linear and angular dimensions without individual tolerance indications.*
2. *Xe-3 Xenon Test Chamber* [online]. 2015. web: Q-SUN, 2015 [cit. 2021-5-24]
3. *Degradation of polymers* [online]. 2013. [cit. 2021-5-24]. [http://tpm.fsv.cvut.cz/student/documents/files/IMP/IMP\\_10.pdf](http://tpm.fsv.cvut.cz/student/documents/files/IMP/IMP_10.pdf)
4. *Žihání termoplastů.* online: 1.4.2020 [cit. 2021-5-24] <https://www.mmspektrum.com/clanek/zhani-termoplastu>
5. ŠAFL, Pavel. *Použití technologie 3D tisku pro návrh výroby náhradních dílů* [online]. 2021 [cit. 2021-07-13]
6. *Účinky a užití optického záření* [online]. 2011 [cit. 2021-5-24] <http://www.odbornecasopisy.cz/res/pdf/44295.pdf>
7. Di Vona M.L. (2014) *Annealing of Polymer Membranes.* In: Drioli E., Giorno L. (eds) *Encyclopedia of Membranes.*

## Battery Powered Lawn Mower

P. Vorel<sup>a</sup>, J. Martis<sup>a</sup>

<sup>a</sup> Department of Power Electrical and Electronic Engineering, Brno University of Technology, Brno 61600, Czech Republic

### Introduction

Electric lawn mowers have certain advantages in comparison with the combustion engine powered machines. The combustion engine produces exhaust fumes and its vibrations can damage the chassis of the mower. Also the noise level is much higher at the combustion engine compared with the electric motor. There is the necessity of regular oil change at the four-stroke engines. The fuel smell can be unpleasant when storing the combustion engine lawn mower. The combustion engine does not allow to slow down the speed under a certain value (too high load torque caused with the mowed grass) - the engine torque dramatically decreases and the engine stops. Then a new starting is necessary. The electric machine can produce a torque at zero speed what means it does never stop because of torque overload – it only decreases the speed to zero and after decrease of the load torque (moving or lifting the mower slightly etc.) the speed of the machine again rises.

However there is a problem with the energy source in the electric lawn mowers. The plug-in concept using a cable connected to a standard grid is not practical as the cable often gets in the way during the mowing. Also it is not suitable for mowing large areas. This is why only a conception with battery placed directly on the mower is an adequate replacement of the combustion engine. The contemporary Li-ion batteries with high energy volume density enable to achieve satisfactory working time of the lawn mower.

### Design parameters of the proposed lawn mower

In the speed range from 0 to 1130 rpm the main knife motor is able to provide a constant torque of 17 Nm. In this speed range and this maximum torque the power increases from 0 to 2 kW. In the speed range from 1130 rpm to maximum speed of 3000 rpm the available torque hyperbolically decreases from 17 Nm to 6.4 Nm to keep the power on the constant value of 2000 W. This torque-speed characteristics is satisfactory for mowing the grass with the knife length of 47 cm.



*Figure 1. View of the mower prototype.*

The mower has a separate motor for the traction. Maximum traction speed is 5 km/h and maximum climb is 12 degrees. The weight of the mower is 45 kg. The battery voltage (fully charged) is ca. 29 V and its energy capacity is 1600 Wh.

### Battery construction

The battery contains 147 cells type NCR18650A from Panasonic. There are 7 blocks connected to series. Each of these blocks consists of 21 parallel cells. The battery pack is split into 2 separate cases because of better distribution of the weight of cells on the mower. The first case with dimensions 140x85x295 mm contains 4 serial blocks. The second case with dimensions 134x79x289mm contains 3 serial blocks. The view of both packs (without enclosures) is in Figure 2.

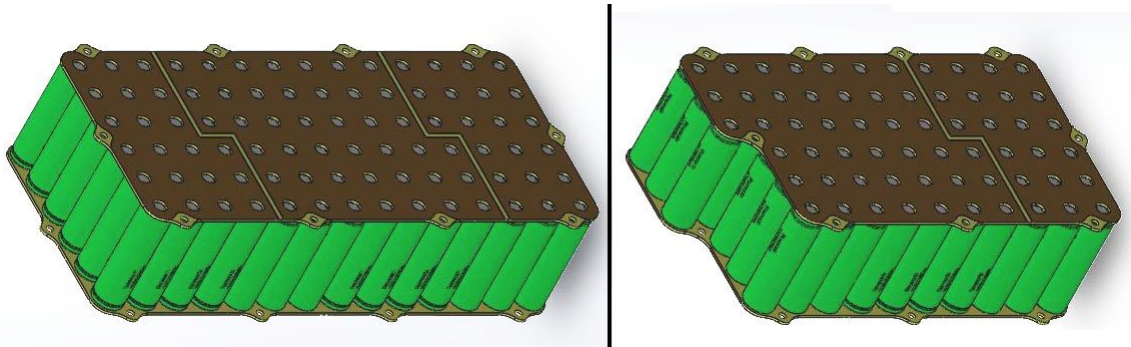


*Figure 2. View of the battery packs.*

### Knife motor and traction motor

The main drive of the knife as well as the traction drive are based on BLDC motors with 3phase inverters. The knife motor Flipsky has a nominal torque 17 Nm, its voltage constant is 130 rpm/V, maximum phase current 148 A and weight 1,82 kg. The knife motor is constructed as an outrunner and is very lightweight. The high torque/weight ratio is the main advantage of synchronous motors with permanent magnets (including BLDC). Because of the open construction of the knife motor it was necessary to place it into a dustproof metallic cover. There is a fan placed on the end of the motor shaft in order to circulate the air inside the cover (see Figure 3). This way of motor cooling is sufficient.



*Figure 3. Inside space of the dustproof cover of the knife motor.*

The traction motor is BLS043.240 from INTECNO. Its nominal torque is 0.43 Nm, voltage constant 125 rpm/V, maximum phase current 6 A and weight 1.25 kg. We can see the torque/weight ratio of this motor is much worse than at the knife motor. The reason is the dustproof robust construction of the traction motor. This is why it needs not be placed into any protecting cover. In order to decrease the weight of the travel drive there is a motor with a low torque and high speed (maximum 3000 rpm). It means a gearbox is necessary. A gearbox from company INTECNO is used. Its transfer ratio is 22.2 and maximum allowed secondary torque is 12 Nm. At the primary speed of 3000 rpm it creates the secondary speed of 135 rpm. From the primary motor torque of 0.43 Nm it creates the secondary torque of 9.5 Nm which is less than the maximum allowed 12 Nm and it is sufficient for the wheel drive.

### Drive conception

The block diagram of the main (knife) drive is in Figure 4. The battery, MOSFET bridge and BLDC motor represent the power chain. The rotor position is sensed with three Hall sensors. Signals from them influence the PWM block to switch the appropriate transistors. A cascade control structure is used. There is a slave inside current control loop. Therefore the motor current must be measured. The desired current value is set with the master outside speed control loop. The real motor speed is detected of the signals from Hall sensors. This cascade structure provides a good stability of the control system and its sufficient dynamics.

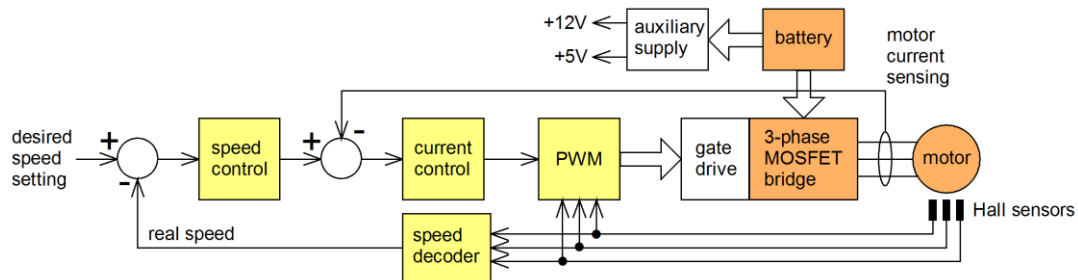


**Figure 4.** Block diagram of the knife drive.

The traction drive conception is very similar to the knife drive conception. However there is no cascade control structure but only one speed control loop without the inside current loop. It is sufficient here because of low power and low dynamics requirements on the traction drive.

### Conclusion

The battery powered lawn mowers are becoming quite common nowadays. The practical test with our prototype showed that the cooling of the motors and the battery is sufficient. The power during mowing the grass is not always 2 kW but we can guess the average power about 500 W. Then at the battery energy capacity of 1600 Wh we can expect the mower will be able to work for 3.2 hours – after that the battery has to be charged. Maybe a lower battery capacity would be sufficient. This way the price and weight of the mower could be reduced.

### Acknowledgment

This research work has been carried out in the Centre for Research and Utilization of Renewable Energy (CVVOZE). Authors gratefully acknowledge financial support from the Ministry of Education, Youth and Sports under institutional support.

### References

1. PICMAUS, Jan. Akumulátorová sekačka na trávu. Brno: Brno University of Technology, Faculty of electrical engineering and communication, Department of power electrical and electronic engineering, 2021, 83 pages. Master's thesis.
2. Brushless DC motor 80100 130KV 7000W for Electric Bike and Electric Skateboard Flipsky [online]. Dongguan City: Flipsky technology, 2018 <https://flipsky.net/collections/e-skateboard/products/brushlessdc-motor-80100-130kv-7000w-for-electric-bike-electric-skateboard-go-cart>

## CFD Simulation of Thermal Abuse in Lithium-Ion Battery Pack

P. Vyroubal<sup>a</sup>, T. Kazda<sup>a</sup>, M. Mačák<sup>a</sup>

<sup>a</sup> Department of Electrical and Electronic Technology, Brno University of Technology, Technická 10, 616 00 Brno, Czech Republic

This article deals with the possibility of modeling thermal abuse, which subsequently leads to the thermal runaway effect in lithium-ion battery pack. The simulation is accompanied by experimental measurements and comparison of the original results from the real test and simulation. The model of each battery cell was created as homogenous, using MSMD modelling approach.

### Introduction

Safety is a major obstacle to the wider use of lithium-ion batteries in electric vehicles. With the constant improvement of lithium-ion batteries in energy density, increasing their safety for the development of electric vehicles is an increasingly relevant topic. Thermal runaway is a key scientific issue in battery safety research. This article provides an insight into the possibility of numerical simulation of the thermal runaway effect.

The mechanisms that lead to the thermal runaway effect can be of the mechanical, electrical or thermal type.

The consequence of these factors is an internal short circuit in the battery and the formation of subsequent chain exothermic reactions, which lead to decomposition reactions of the materials of which the battery is composed.

#### Mechanical initiation

Destructive deformation or displacement of a structure under the action of force are two common features of a mechanical type of damage [1]. Collisions and subsequent crushing or penetration of a foreign body into the battery are typical factors. If the battery is deformed, the separator may rupture and thus an internal short circuit may occur, or the electrolyte may leak, causing a subsequent fire. During penetration, a foreign body penetrates into the battery structure (e.g. in the event of an accident) and in the case of a conductive body, the internal structure of the battery is short-circuited.

#### Electrical initiation

In the case of electrical initiation, it is mainly a short conductive connection of the battery electrodes, so we speak of an external short circuit. Furthermore, overcharging the battery, for example by a failure of the BMS, which has the task of monitoring and stopping the charging process [2]. This is then accompanied by gassing and heat generation (Joule heat and heat generated by electrochemical reactions). Another factor can be excessive battery discharge (BMS failure).

#### Thermal initiation

Local overheating of the battery can be caused by either mechanical and electrical initiation or poor thermal management of the entire system, when the battery is excessively burned by its

surroundings [3]. Overheating is then associated with an internal short circuit in the battery and the breakdown of the separator and the ingress of spontaneous exothermic reactions.

### Results and discussions

The numerical model was compiled on the basis of findings from previous measurements. It was necessary to measure the charging and discharging curves of one cell and implement them together with the geometry and boundary conditions into ANSYS Fluent [4]. The following Figure 1 illustrates the geometric model of a 1/4 e-bike battery pack (left) and a comparison of the measured and simulated discharge curve (at current 1C) of one cell (right). Here was the MSMD simulation approach used [5].

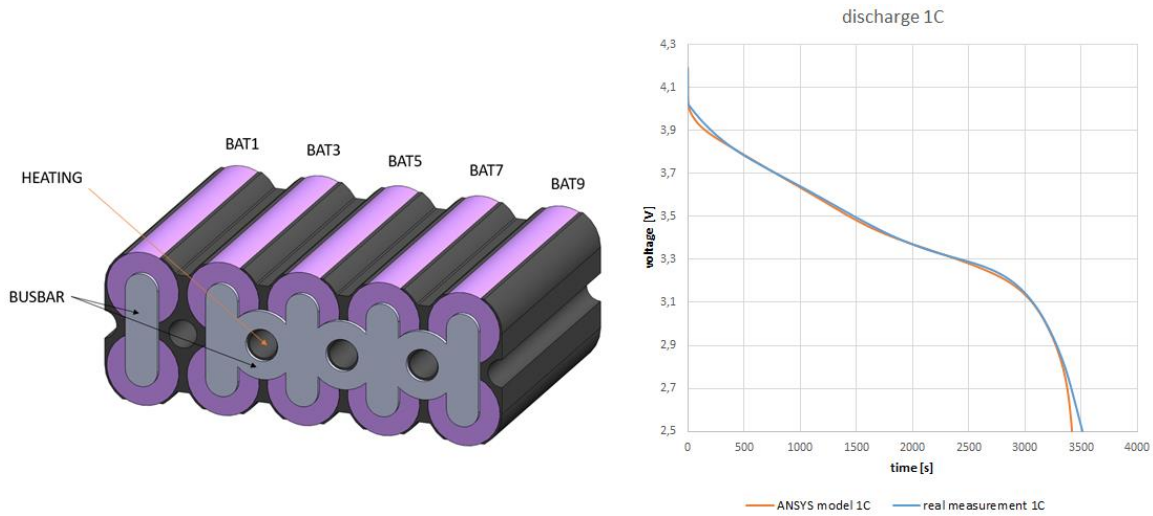


**Figure 1.** Temperature map on the battery pack.

The next Figure 2 shows a color temperature map of the whole battery pack, with constant heating. Simulation is steady-state, without considering startup thermal mechanisms.

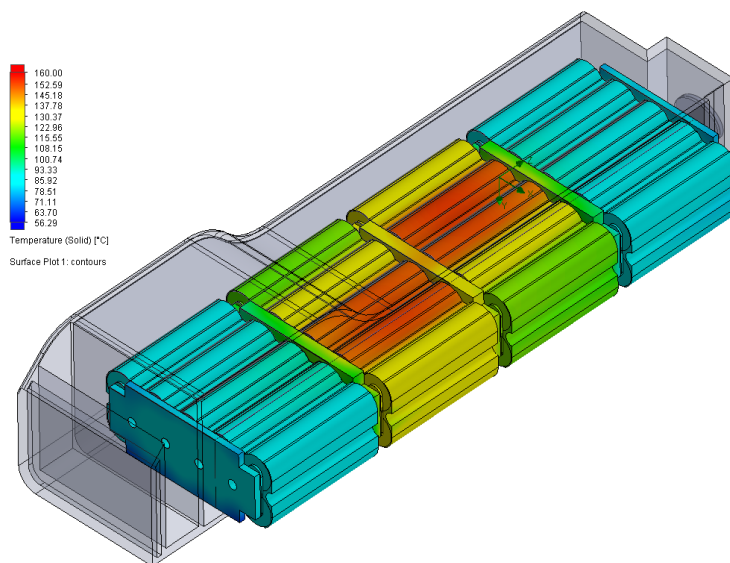


**Figure 2.** Temperature map on the battery pack.

The following graph shows the temperature profile on the individual cells (as they are named in Figure 1 on the left site). This simulation is already transient (time-dependent) and considers the thermal processes, that occur when the battery overheats. It is clear from the figure, how the temperature rises uncontrollably on cells near the heating system and the subsequent triggering of exothermic reactions in other cells.

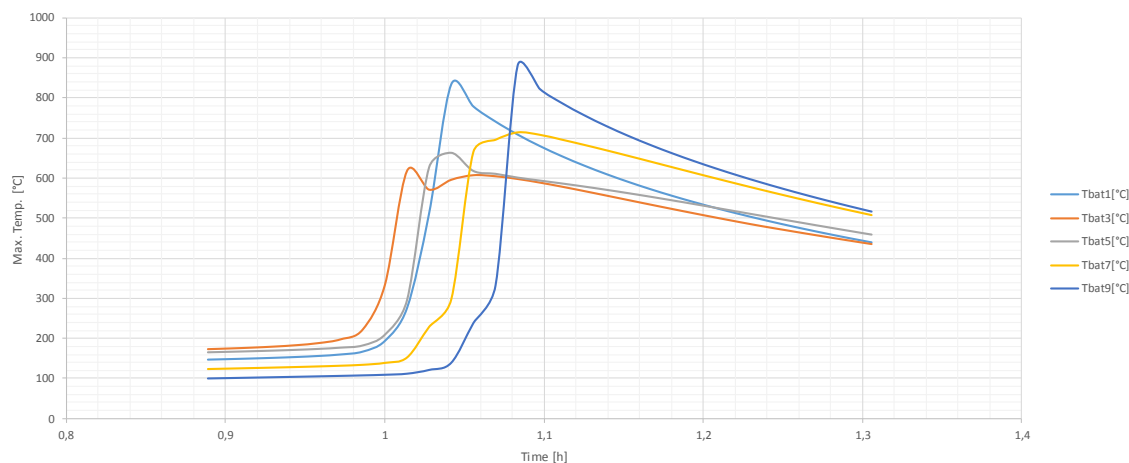


**Figure 3.** Temperature profiles on individual cells of the battery pack.

### Acknowledgments

This work was supported by the specific graduate research of the Brno University of Technology No. FEKT-S-20-6206 and National Centre for Energy TN01000007.

### References

1. X. Feng and X. Minggao, *Energy Storage Materials*, **10**, (2018).
2. ANSYS Fluent Theory Guide, (2019).
3. ANSYS Fluent Customization Manual, (2019).
4. P. Vyroubal and T. Kazda, *Journal of Energy Storage*, **11** (2018).
5. P. Vyroubal, T. Kazda and M. Mačák, *ECS Transactions*, **87**(1) (2018).

## Numerical Modeling of Reactions at the Level of an Electrochemical Cell

P. Vyroubal<sup>a</sup>, M. Mačák<sup>a</sup>, T. Kazda<sup>a</sup>

<sup>a</sup> Department of Electrical and Electronic Technology, Brno University of Technology, Technická 10, 616 00 Brno, Czech Republic

This paper deals with the implementation and verification of a mathematical model of electrochemical reactions for the CFD solver ANSYS Fluent. The resulting model can then be used to calculate, for example, the CV of the characteristic of the electrochemical cell and thus expands the existing possibilities of this solver.

### Introduction

At present, great emphasis is placed on the study of electrochemical power sources in the world. In modern energy, energy storage in general is of great importance, especially due to the transition to renewable sources and electromobility.

All battery systems have a common feature and that is their basic structure. The elementary part of the battery is one cell, which consists of a positive and a negative electrode, between which there is an electrolyte, which can be liquid or solid.

The Institute of Electrotechnology has been researching electrochemical cells and batteries for many years, and numerical modeling has become part of it.

Battery models, has their application in the study of temperature fields that are generated during their operation (discharge, charging or failure). Such models are based on the homogenization of the whole battery, where we model the battery as a homogeneous continuum and its parameters, i.e., how the battery behaves electrically, are fitted into it with the help of real experiments.

Real measurements can only include measurements of charging and discharging curves (published in [1] and [2]) or they can be sophisticated measurements where we fit the battery to an electrical circuit using impedance spectroscopy (published in [3]). In the case of failure (short circuit or breakdown), tests are relatively expensive and dangerous, and here computer models find their application again (published in [4]).

Modeling of electrochemical cells at the level of reactions is important in the selection and testing of basic materials. This is a method in which we define the reactants and reactions that are to take place in the solver. However, these models are still at a relatively basic level. This is because commercial solvers are limited to certain types of applications. These are mainly complex tasks, where it is possible to neglect some phenomena that play a significant role at the elementary level. Thus, simpler mathematical models are implemented in them, which has the advantage that the calculation is less demanding and therefore faster.

However, the disadvantage is that at different concentrations of ions in the electrolyte the course of the potential in the cell has a linear course (i.e., impossibility of modeling the double layer), the calculation is unstable at low concentrations of reactants (it is necessary to consider concentrated and well-mixed electrolytes) and a large part of calculations is necessary to implement as transient (time variable).

The contribution of this paper is the implementation of a more robust mathematical model in the FLUENT solver and the demonstration of its functionality.

## Experimental

Cyclic voltammetry (CV) belongs to the group of potentiodynamic experimental methods, thanks to which it is possible to obtain relatively quickly the basic characteristics of the studied system, especially about the mechanism of the electrode process and its kinetic parameters. Cyclic voltammetry is characterized by a gradual increase in the potential of the working electrode from one limit value to another and back to the starting point. It follows that the basic adjustable parameters of the experiment are the limits and the speed of the potential shift. The properties of the electrolyte can also be influenced, in particular the concentration of the electro-active substance and the temperature. The response of the system is the so-called polarization curve or the dependence of the current flowing through the electrode on its potential. There are generally two limit cases of the studied systems, namely the reversible and irreversible electrode processes. Next, we will deal with reversible (reversible) events [5].

Due to the high concentration of the electrolyte, it is possible to neglect the potential differences in it, i.e., the ions move only due to diffusion (migration is neglected) and the electrolyte is constant zero potential, thus the bias voltage is determined only by the applied voltage at the electrode.

The electrochemical model, which will be presented in full, was based on the Current Distribution methods described in the above chapters. They are based on the definition of the electrode potential and the electrolyte potential. The reactions are then described using the Butler-Volmer equation. The FLUENT solver will implement the secondary method together with the transport of chemicals.

This description was chosen because the primary description is not suitable for this case at all (it was mentioned above) and the tertiary method is too impractical and complex to implement in FLUENT.

The description of the electric potential and the motion of ions could be numerically realized using Poisson-Nernst-Planck equations, but in this case, it is relatively difficult to add electrochemical reactions to the model (it is difficult to get the value of the potential difference at the interface where the reaction takes place).

## Results and discussions

For example, a single-electrode, reversible reaction with an equilibrium potential  $E_{eq} = -0.45$  V and an exchange current density of  $10$  A/m<sup>2</sup> was defined. The diffusion coefficients of the reactant and the product were set at  $1 \cdot 10^{-9}$  m<sup>2</sup>/s, which represents the standard values of the coefficients in aqueous solutions. The initial reactant concentration was set at 1 mmol/l and for the product 0 mmol/l.

A signal with a triangular waveform from 0 V to -0.65 V and back at a speed of 25 mV/s was chosen as the excitation signal on the working electrode.

In the case of simulation, it is not necessary to work with the reference electrode, as is the case with real measurements.

The DigiSim program, which is used in electrochemistry to simulate CV characteristics, was also used to compare the results of this model. Results from both programs illustrates Figure 1.

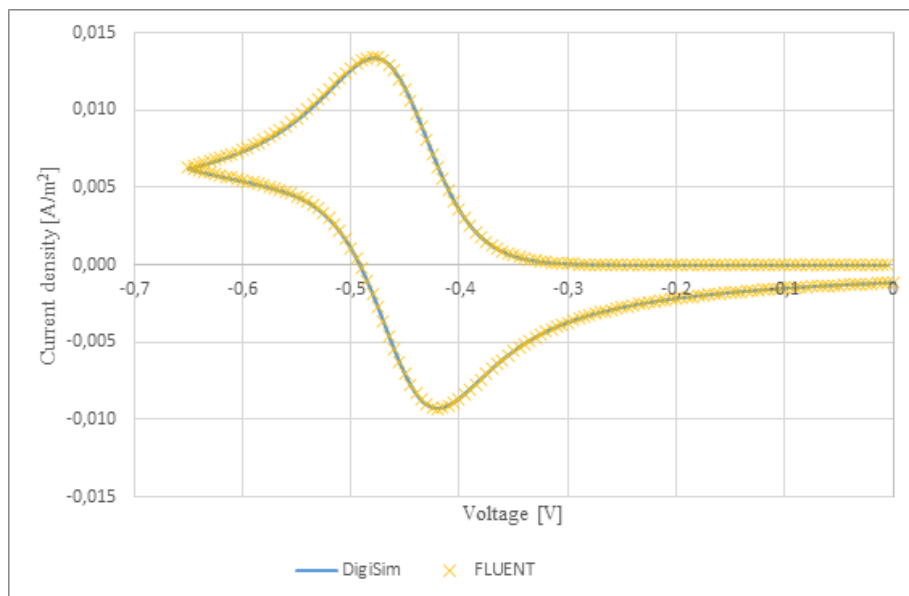


**Figure 1.** Comparison of results from the newly implemented model in FLUENT and results from DigiSim software.

## Conclusion

It is not possible to perform voltammetry simulation in FLUENT (in its built-in module) for several reasons. The first problem is the numerical instability in the region of low concentration of reactants. If the concentration of the reactant is close to zero and the reaction rate depends on it, the calculation diverges, and it is not possible to continue it.

The second problem is the fact that FLUENT always calculates the potential of the electrolyte, which is not suitable for simulating voltammetry. Because this potential is also determined by Ohm's law and the presence of the "supporting" electrolyte, and thus the high electrical conductivity, leads to an unrealistically high current density, which prevents the calculation.

## Acknowledgments

This work was supported by the specific graduate research of the Brno University of Technology No. FEKT-S-20-6206.

## References

1. P. Vyroubal and T. Kazda, *Journal of Energy Storage* **14** (2017).
2. P. Vyroubal and T. Kazda, *ECS Transactions* **81**(1) (2017).
3. P. Vyroubal and T. Kazda, *Journal of Energy Storage* **15** (2018).
4. P. Vyroubal and T. Kazda, *Journal of Energy Storage* **20** (2018).
5. Pérez-Brokate, Cristian Felipe et al., *Journal of Computational Science* **11** (2015).

## **Analysis of Time Delays in the Supply of Rechargeable Batteries in a Specific Inventory System**

Robert Kutil<sup>1</sup>, Tomáš Binar<sup>1</sup>, Marie Sedlaříková<sup>2</sup>, Jana Zimáková<sup>2</sup>

<sup>1</sup>Faculty of Military Leadership, University of Defence, Brno, Czech Republic

<sup>2</sup>Brno University of Technology, Technická 3058/10, 616 00 Brno, Czech Republic

Inventory creation of rechargeable batteries and optimization of this creation is a complicated task entirely dependent on knowledge of past and future stock flows data, material service life and knowledge of mathematical models. The input data for each specific subject reflects not only the business task, but also its concept and position in the sales or production market. It is obvious that the concept of inventory creation will be different for a manufacturing company, different for a commercial subject and different for a state-financed entity. The state-financed and managed entities have specific requirements for the creation of inventories arising from the purpose of their existence and concurrently from the restrictions given by the management systems and regulation of financial flows. It is the limitation resulting on the one hand from the methodologies and laws governing the principles of public procurement that may be in partial conflict with internal normative acts. The result can be an inventory creation system that is not completely flexible and does not always comply the principles of optimizing the quantity of inventories held. The need to hold more stocks from a tactical or strategic point of view can then prevail over the economy scale. The difference in the speed and completeness of deliveries is shown on the selected type subject, using the analysis of input parameters of purchases with subsequent application to a specific model of inventory creation from inventory theory, and the resulting level of the maximum required amount of the inventory held.

### **Introduction**

The task of the inventory creation theory is to evaluate the possibilities of using some already known model from inventory theory based on the selected priority parameters obtained from the analysis of a specific logistics chain of a particular entity. It is often necessary to adjust a specific model for the use with slightly modified parameters. All these processes aims to optimize the level of stocks held and acquired, deliveries and material flows in supply and storage processes.

The size of stocks is currently paid considerable attention in all companies, as optimizing stock and supply processes can save 15-25% of costs in the supply system. These costs do not only constitute the sum of the costs of direct stocks in the material stored, but also the costs of holding and operating the storage premises, the work of the storekeepers or the costs of disposing of unused stocks [1].

The task of inventory optimization is to bring financial cost savings. This task is done primarily through the calculation of exact minimum stocks, emergency stocks and the determination of other maximum accurate levels and deadlines for performing operations in the material flow system.

There are situations when it is not possible to optimize stocks in terms of minimizing them or, for example, accelerating the turnover of deliveries to the warehouse. There are selected subjects for which the creation of stocks is of a strategic character. Our model subject operates a large number of parameter-specific techniques. The necessary service in the maintenance and repair system is therefore done by its own means in its own service and repair facilities. A specific technique is in our case also a technique whose numbers are small on world market or whose sales are strategically limited. The same applies to the quantity or actual availability of rechargeable batteries on the free market at a particular time. Spare parts or components with a limited service life, such as rechargeable batteries, may not be realistically available at all or it is difficult to ensure their replenishment with the classic system of tenders and public contracts. Therefore, it is necessary to build up the necessary stocks even with the risk of higher costs of holding stocks [2].

### **Materials and Methods**

The primary task was to determine the input parameters of the searched logistics chain for a particular monitored subject using the analytical methods. The documents were obtained within the initial analysis of the current state of logistical support of the Ministry of Defense within the project Technical Maintenance System in the Ministry of Defense (USYS) [3, 4]. General data of several internal subjects were analyzed, evaluated and compared.

The main evaluation aspect of the supply system in this particular case was the requirement to have spare parts available in a short term of several weeks, ideally within a maximum of one month from the request. Based on this main evaluation criterion, the reality of compliance with this parameter was assessed by comparing the parameters set by laws and internal normative acts. At the same time, the previous processes of material flows already applied or realized for the selected material class, i.e. accumulator batteries for communication and information technology, were analyzed.

It is the specifics of financing and the uniqueness of the operated technology, as well as the uniqueness of the accessories of this technology, that makes the monitored subject a suitable study object, which differs from most common commercial entities on the market. The striking point is the limited ability of the market to cover the demand for spare parts for special military equipment, including rechargeable batteries.

The identified generally used practices for material flow management were then grafically reflected, and an evaluation was made about the meaning in this particular case for this particular subject to create long-term framework central contracts for a limited or complete range of monitored and used material in the maintenance and repair system by the entity of used technique.

### **Expected results**

The aim of the solution is to devise an optimal inventory management system for the monitored entity as a part of supply optimization and to determine the limit principles of operation of the system for minimization of emergency reserves held. The aim is the maximum optimization of the amount of stocks held, their regular replacement and compliance with the maximum speed of satisfaction of the demand for the part in the system of own maintenance and repairs of the monitored entity's equipment.

The criteria for the decision-making process will be displayed in graphical form with an explanation. When eliminating the possibility of a complete shortage of stocks on the market due to

the blockade of commodity exports, the main limiting factor influencing the length of the supply cycle of a particular commodity appears to be the possibility that the commodity will not be subject to a contractual spare parts list. This difference is shown in Diagram 2.

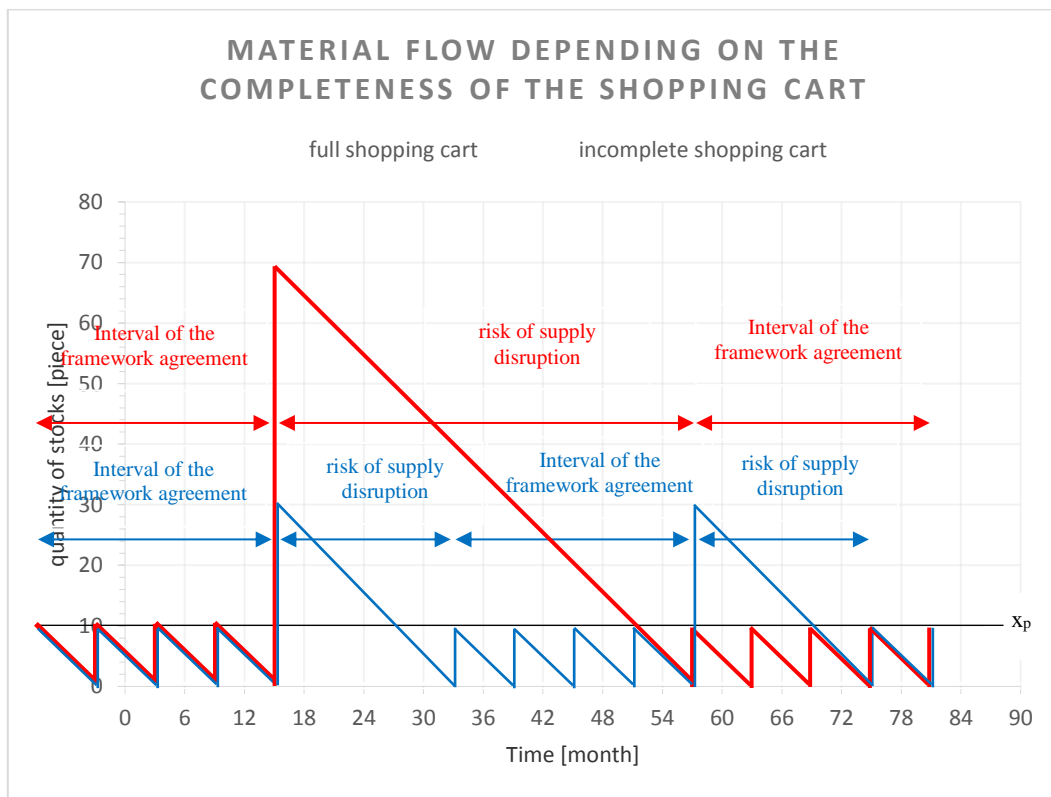


**Diagram 2.** The difference in the maximum level of stock held for complete and incomplete spare parts list

The diagram is a model example showing the flows of a particular inventory item for the case where the framework contract contains this item and when it does not. Then the item will be included in the new contract. The example relates to one type of technique acquired over 5 years in a 100-piece series with an expected service life of 20 years. The rechargeable battery has a standard service life of 5 years. The emergency stock  $x_p$  was determined for optimal P-system of inventory management for 10 pcs. The supply cycle is optimally 6 months, while the values from Diagram 1 for individual cases were accepted for the further course of the graph. In the case of prediction of supply fluctuations for a non-standard commodity on the market, it is possible to increase the emergency stock before the planned outage and thus avoid the possibility that there will not be enough pieces of this commodity on the market in the event of subsequent demand for a large quantity of commodities in a single supply.

## Conclusion

The acquisition of accumulator batteries through central framework agreements pursuant to Public Procurement Act 134/2016 Coll., as amended, will limit the possibility of corrupt practices of the persons managing billions budgets. Unfortunately, for material whose availability on the market is limited or restricted, it has proved as necessary to adhere to certain principles accompanying the purchasing system and public procurement system, which would eliminate the possibility of a complete shortage of stocks due to the disappearance of stock anytime during the life cycle. The

opposite would mean the need to hold an emergency stock in the amount of the real need for the entire life cycle of all pieces of technique.

Based on the information obtained on the functioning of the system, financing purchases, concluding contracts, laws and internal normative acts set by the rules of these legal and financial operations, the optimal inventory management model was selected and rules were set to optimize the functioning of material flows and material acquisition for the monitored subject.

### Acknowledgements

The paper was written with the support of the project of long-term strategy of organization development: ROZVOLOG: Development of Capabilities and Sustainability of Logistics Support (DZRO ROZVOLOG 2016–2020), funded by the Ministry of Defense of the Czech Republic and the publication was created within the project of specific research at BUT (No. FEKT-S-20-6206).

### References

1. SIXTA, J., MAČÁT., V. Logistika: teorie a praxe. Brno: CP Books, 2005. Business books (CP Books). ISBN 80-251-0573-3.
2. KUTIL, R. Analýza metod používaných pro optimalizaci tvorby zásob materiálu. *Seminární práce z managementu údržby a oprav*. Univerzita obrany, Brno, 2016.
3. KUTIL, R. Analýza aktuálního stavu logistické podpory techniky v resortu Ministerstva obrany. *Projekt obraného výzkumu USYS*. VTÚ s.p., Vyškov, 2017, VTÚ/VTÚPV-1187-10/2017.
4. KUTIL, R. Model tvorby provozních rezerv technického materiálu v Armádě České republiky. *Disertační práce*. Univerzita obrany, Brno, 2020.
5. ŠEFČÍK, V. *Ekonomika a obrana státu*. Praha: Ministerstvo obrany České republiky - AVIS, 1999. ISBN 80-7278-014-X.
6. SIXTA, J., ŽIŽKA, M. Logistika: metody používané pro řešení logistických projektů. Brno: Computer Press, 2009. *Praxe manažera (Computer Press)*. ISBN 978-80-251-2563-2.
7. JABLONSKÝ, J. *Operační výzkum: kvantitativní modely pro ekonomické rozhodování*. Brno: Professional Publishing, 2002. ISBN 80-86419-23-1.

**Title:** Advanced Batteries Accumulators and Fuel Cells – 22<sup>nd</sup> ABAF

**Edited:** Marie Sedlaříková  
Vítězslav Novák  
Tomáš Kazda  
Petr Bača

**Publishing Office:** Marie Sedlaříková  
Vítězslav Novák  
Tomáš Kazda  
Petr Bača

**Deadline:** July 17<sup>th</sup> 2021

**Publisher:** Brno University of Technology  
Faculty of Electrical Engineering and Communication  
Department of Electrical and Electronic Technology

**Year:** 2021

The authors are fully responsible for the content and language of their contribution

**ISBN 978-80-214-5975-5**